Can local adaptation measures compensate for regional climate change in Hamburg Metropolitan Region?

Dissertation

zur Erlangung des Doktorgrades der Naturwissenschaften im Fachbereich Geowissenschaften der Universität Hamburg

vorgelegt von

Robert Schoetter
aus Esch-sur-Alzette

Hamburg

2013

Als Dissertation angenommen vom Fachbereich Geowissenschaften der Universität Hamburg

auf Grund der Gutachten von Prof. Dr. K. Heinke Schlünzen

und Prof. Dr. Felix Ament

Hamburg, den 21.06.2013

Prof. Dr. Jürgen Oßenbrügge

Sprecher des Fachbereichs Geowissenschaften

Abstract

In this thesis, it is investigated whether local adaptation measures can compensate for regional climate change in Hamburg Metropolitan Region. The focus is set on the summer season and the target variables "perceived temperature" (PT) and "heavy precipitation". PT is a measure for human thermal comfort developed by the German Meteorological Service. Heavy precipitation is defined in this thesis as a daily precipitation amount exceeding 25 mm.

Simulation results of the regional climate models CLM and REMO are evaluated to determine if the models simulate the meteorological input data for PT within the uncertainty of the observation based data. The sensitivity of PT on meteorological variables and urban morphology data is determined for meteorological situations in the summer season. The modification of radiation due to the presence of buildings is calculated with the Building Effect Parameterisation BEP. With the sensitivities, the potential impact of adaptation measures can be estimated. The sensitivity of PT is higher for situations with heat stress and humid conditions than for situations with thermal comfort. The highest sensitivity of PT on wind speed is obtained for small wind speed. The sensitivities of PT on mean radiant temperature, wind speed and building height indicate that there exist good options to compensate for regional climate change by local adaptation measures in the city of Hamburg.

Meteorological situations with observed heavy summer precipitation are downscaled with the mesoscale atmospheric model METRAS. The setup and adaptation of METRAS is described. Simulated daily precipitation amounts are evaluated against rain gauge observations made by DWD. METRAS simulates heavy precipitation in 60% of the selected meteorological situations. The impact of topography on the downscaled heavy summer precipitation is investigated for two plausible urban development scenarios, one scenario without orography, and one scenario with all non-natural surface covers replaced by natural surface covers. No statistically significant change of heavy precipitation is obtained in Hamburg or downwind of Hamburg for the scenarios with changed surface cover. A statistically significant decrease of heavy precipitation is obtained in Hamburg for the scenario without orography. Based on the obtained results, a compensation of the projected increase of heavy summer precipitation in future climate by local adaptation measures is not promising.

Zusammenfassung

In dieser Arbeit wird untersucht, inwiefern lokale Anpassungsmaßnahmen regionale Klimaänderungen in der Metropolregion Hamburg ausgleichen können. Die Fragestellung wird für die Sommerjahreszeit und die Zielgrößen „Gefühlte Temperatur" (GT) und „Starkniederschläge" untersucht. Die GT ist eine vom Deutschen Wetterdienst entwickelte Kennzahl zur Quantifizierung des thermischen Wohlbefindens des Menschen. Starkniederschläge werden in dieser Arbeit als Tagesniederschläge größer als 25 mm definiert.

Simulationsergebnisse der regionalen Klimamodelle CLM und REMO werden evaluiert um zu bestimmen, ob die Modelle die Eingabedaten für die GT im Rahmen der Unsicherheit der verwendeten Beobachtungsdatensätze berechnen. Die Sensitivität der GT bezüglich meteorologischer Eingangsdaten sowie stadtmorphologischer Daten wird für meteorologische Situationen im Sommer berechnet. Die Modifikation der Strahlung durch die Gebäude wird mit Hilfe der Stadtparametrisierung BEP berechnet. Anhand der Sensitivitäten kann der Einfluss von möglichen Anpassungsmaßnahmen auf die Zielgröße GT abgeschätzt werden. Die Sensitivität der GT ist in meteorologischen Situationen mit Hitzestress und hoher Luftfeuchtigkeit größer als in meteorologischen Situationen in denen thermisches Wohlbefinden vorliegt. Die Sensitivität der GT bezüglich der Windgeschwindigkeit ist bei niedriger Windgeschwindigkeit am höchsten. Die Sensitivitäten bezüglich der Strahlungstemperatur, der Windgeschwindigkeit, sowie der Gebäudehöhen zeigen, dass in der Stadt Hamburg gute Möglichkeiten bestehen, anhand lokaler Anpassungsmaßnahmen die regionalen Klimaänderungen zu kompensieren.

Meteorologische Situationen mit Starkniederschlagsereignissen werden mit dem mesoskaligen Atmosphärenmodell METRAS verfeinert. Die Konfiguration des Modells, sowie die vorgenommenen Modellanpassungen werden beschrieben. Die simulierten Tagesniederschläge werden gegen Stationsdaten des DWD evaluiert. METRAS berechnet in 60% der ausgewählten meteorologischen Situationen Starkniederschläge. Der Einfluss der Topographie auf die simulierten Starkniederschlagsereignisse wird quantifiziert. Zwei plausible Stadtentwicklungsszenarien, ein Szenario ohne Orographie, und ein Szenario in dem die künstlichen Oberflächenbedeckungen durch natürliche Oberflächenbedeckungen ersetzt wurden, werden untersucht. Für die Szenarien mit geänderten Oberflächenbedeckungen ergeben sich keine statistisch signifikanten Änderungen des Starkniederschlags in Hamburg oder im windabgewandten Bereich von Hamburg. Für das Szenario ohne Orographie ergibt sich eine statistisch signifikante Reduktion des Starkniederschlags in Hamburg. Auf Basis der Ergebnisse erscheint es nicht vielversprechend, die projizierte Zunahme von Starkniederschlägen im zukünftigen Klima anhand von lokalen Anpassungsmaßnahmen auszugleichen.

Contents

iv

1 Introduction

The scientific knowledge on climate change is continuously documented by the Intergovernmental Panel on Climate Change (IPCC) with the last summary report published in 2007. The observed increase of globally averaged air temperature within the second half of the 20th century can "very likely" be attributed to greenhouse gas forcing (Hegerl et al., 2007). Ensembles of coupled atmosphere-ocean general circulation models project a global near-surface averaged air temperature increase of 1.1 K to 2.9 K, 1.7 K to 4.4 K and 2.0 K to 5.4 K until the end of the 21th century for the SRES scenarios B1, A1B and A2, respectively (Meehl et al., 2007b). The SRES (Special Report on Emissions Scenarios; Nakicenovic et al., 2000) scenarios have been developed by the IPCC to account for possible future demographical, technological and socio-economic pathways leading to different levels of greenhouse gas emissions and concentrations in the atmosphere. The simulations with general circulation models (GCMs) are dynamically downscaled with regional climate models (RCMs) in order to obtain more detailed information on regional climate change. For Europe, the air temperature is "likely" to increase more than the global average (Christensen et al., 2007). A decrease of summer precipitation and an increase of winter precipitation is "likely" in Central Europe.

The projected climate change will affect sectors like hydrology (Kay et al., 2009; Hellmers and Pasche, 2011), agriculture and forestry (Spittlehouse and Stewart, 2003), ecosystems (Huntley et al., 2008), health (Muthers et al., 2010), tourism (Matzarakis et al., 2012) and transport (Scholten et al., 2011). These sectors can benefit from integration of knowledge provided by climate science into long-term planning. Adaptation measures to climate change should be developed in order to optimise the relevant systems and processes for possible future climate conditions. For this purpose, the German Federal Ministry of Education and Research (BMBF) supports seven regions in Germany: the KLIMZUG projects (BMBF, 2011).

This thesis has been conducted in the framework of the project KLIMZUG-NORD, which has its focus on Hamburg Metropolitan Region in Northern Germany (Thamer et al., 2009). The main goal of the thesis is to determine whether local adaptation measures can compensate for regional climate change. The investigations are focussed on the summer season and the target variables "perceived temperature" and "heavy precipitation".

The "perceived temperature" PT (Jendritzky et al., 2000; Staiger et al., 2011) is a measure for outdoor human thermal comfort that was developed by the German Meteorological Service (DWD). PT is the temperature, which would be perceived by a reference human being in a reference environment with the mean radiant temperature equal to air temperature, a wind speed of 0.1 m/s and a relative humidity of 50%. PT is based on a heat budget equation of the human

body accounting for the metabolic heat production, the radiative heat transfer at the skin as well as the sensible and latent heat exchange by respiration and by the skin. The human body experiences thermal stress if its heat budget is not at equilibrium. The thermal stress can result in increased morbidity, decreased labour productivity and so on. The thermo-physiological meaning of PT (e.g. "moderate heat stress") is expressed by a 9-point thermal sensation scale defined by Staiger et al. (2011). Air temperature, water vapour pressure, wind speed and mean radiant temperature need to be known for the calculation of PT.

Several simplifications are made by choosing the target PT. A steady state is assumed in the heat budget equation. This causes errors if the environmental conditions change rapidly. Further, it is assumed that the reference human being adapts its clothing within certain limits in order to achieve thermal comfort. Here a reasonable human behaviour is assumed. Situations with cold or heat stress might occur in the case of non-reasonable human behaviour even though PT indicates that thermal comfort is achievable. PT neglects differences between humans: the heat budget is calculated assuming a male person of 35 years, 75 kg weight and 1.75 m tall, walking with 4 km/h on flat ground. Persons deviating from this reference human being will experience a different thermal comfort under the same meteorological conditions than expressed by PT. Finally, PT depends only on the actual meteorological conditions. It is thus ignored that the human body might adapt within certain limits to the prevailing thermal environment (e.g. Cheng et al., 2012).

The target variable "heavy precipitation" is defined in this thesis as a daily precipitation amount exceeding 25 mm. Events with precipitation exceeding 25 mm/d can lead to flooding within the city of Hamburg due to limitations of the drainage system and therefore cause high economic damage. The focus lies on daily precipitation amounts, because in situ measurements of sub-daily precipitation amounts are rare in Hamburg Metropolitan Region. Further, the spatial and temporal representativity of sub-daily precipitation amounts is very low, especially in the summer season (Ertl, 2010; Bohnenstengel et al., 2011). Only simulated daily precipitation amounts can therefore be evaluated against in situ measurements.

Studies dealing with adaptation to climate change are subject to uncertainties of future greenhouse gas emissions, the internal climate variability as well as uncertainties of data, models and methods (Jones, 2000; Christensen and Christensen, 2007; Murphy et al., 2007; Swart et al., 2009; Foley, 2010).

In this thesis, the uncertainty of future greenhouse gas emissions is accounted for by analysing results for the SRES B1, A1B and A2 scenarios. The assumptions made by the IPCC for these scenarios are described in Nakicenovic et al. (2000). The scenarios start with identical greenhouse gas emissions in 2000. The A2 scenario is characterised by continuously increasing

emissions between 2000 and 2100. In the A1B scenario, emissions are increasing similar to the A2 scenario until 2040. After 2040 however, emissions decrease slightly until 2100. In the B1 scenario, emissions increase only slightly until 2040, then they are decreasing rapidly towards levels below the value in 2000.

Internal climate variability is accounted for by analysing three realisations of simulated climate for each greenhouse gas scenario. The realisations are distinguished by different initial conditions in the preindustrial control simulation of the GCM. Using results of three realisations gives a basic guess on how statistical properties of the investigated meteorological variables are influenced by internal climate variability. A larger number of realisations (30-100) would be needed in order to make more detailed investigations on internal climate variability.

The uncertainties of the projected climate change signals related to the characteristics of the applied climate models are quantified by multi model ensembles of GCMs and RCMs. The multi model ensemble approach has been used to quantify the uncertainty of global climate change signals in the context of the Coupled Model Intercomparison Projects (CMIP3: Meehl et al., 2007a; CMIP5: Taylor et al., 2012), and the uncertainty of the regional climate change signals in the projects PRUDENCE (Christensen and Christensen, 2007), ENSEMBLES (Jacob et al., 2012) and CORDEX (Giorgi et al., 2009). In this thesis, the ensemble of RCMs analysed is reduced to the simulations conducted with the "Climate Local Model" (CLM; Rockel et al., 2008) at 0.165° (~18 km horizontal resolution) and the "Regional Model" (REMO; Jacob, 2001) at 0.088° (~10 km horizontal resolution). Both RCMs are forced by simulation results of the GCM ECHAM5-MPIOM (Roeckner et al., 2003; Jungclaus et al., 2006) at T63 resolution (~200 km at 0° latitude). The uncertainty of the climate change signals arising from the choice of the GCM is therefore neglected. However, no extreme climate change path is chosen with the selected GCM, because the equilibrium climate sensitivity of ECHAM5-MPIOM is close to the ensemble average of the CMIP3 models (Randall et al., 2007).

Apart from the uncertainties of the climate change signals, the output of the RCMs can be subject to biases. Therefore, the simulation results of the RCMs should be evaluated before they are used in studies dealing with adaptation to climate change. In Chapter 2 of this thesis, the meteorological variables air temperature, precipitation, total cloud cover, relative humidity and wind speed simulated by the RCMs CLM and REMO are evaluated against observation based data for a domain covering Hamburg Metropolitan Region. Prior to model evaluation, the uncertainty of the observation based data is quantified. With the evaluation, it is determined which RCM simulates the input variables of PT as well as precipitation within the uncertainty of the observation based data.

In Chapter 3, the sensitivities of PT on meteorological variables and urban morphology data are

calculated for meteorological situations in the summer season. With these sensitivities, the impact of local adaptation measures on the target variable PT is quantified. Further, the sensitivities indicate how accurate the different input variables need to be known in order to achieve a desired accuracy in the target variable PT.

In Chapter 4, the projected change of PT in future climate is determined. The climate change signal of PT is compared to the climate change signal of air temperature. The change in the frequency of PT with respect to the thermal sensation scale is quantified. The results indicate in which season and at which time of day, outdoor human thermal comfort is improved or deteriorated in future climate compared to present climate.

In order to quantify the impact of relatively small-scale changes in surface cover on heavy precipitation, the surface characteristics have to be properly resolved and the heavy precipitation needs to be simulated in a realistic manner with an atmospheric model at horizontal resolutions in the order of 1 km. Therefore, in Chapter 5, heavy summer precipitation for present climate and present surface cover is downscaled with the mesoscale atmospheric model METRAS from the ERA-Interim reanalysis to a domain with 2 km horizontal resolution covering Hamburg Metropolitan Region. The setup and adaptation of METRAS is described. Simulated hourly values of air temperature, specific humidity, wind speed, wind direction and simulated daily precipitation amounts are evaluated against routine observations made by DWD.

In Chapter 6, the impact of topography on heavy summer precipitation downscaled in Chapter 5 is determined. Four scenarios are investigated: one without orography, one with all non-natural surface covers replaced by natural surface covers and two plausible urban development scenarios. The results indicate to which degree local adaptation measures can compensate for the projected increase of heavy summer precipitation due to regional climate change.

The final conclusions of the thesis are drawn in Chapter 7.

Parts of this thesis have already been published (Chapter 2; Schoetter et al., 2012), are accepted (Chapter 3; Schoetter et al., 2013) or intended for publication (Chapters 4 to 6). The journal articles are reproduced here. To facilitate the reading, the abstracts are left out and all references are summarised at the end of the thesis. Furthermore, some figures are replaced by their coloured counterpart, all texts are written in British English and cross references to published papers, that are chapters of this thesis, are accomplished by using the chapter numbers.

2 Evaluation and bias correction of regional climate model results using model evaluation measures

Preface

This chapter has been published by Schoetter, Robert, Peter Hoffmann, Diana Rechid and K. Heinke Schlünzen, 2012: Evaluation and Bias Correction of Regional Climate Model Results Using Model Evaluation Measures. Journal of Applied Meteorology and Climatology, 51, 1670–1684. © Copyright 2012 American Meteorological Society (AMS)[1]. The abstract has been left out, some figures have been replaced by their coloured counterpart, the American English is changed to British English and the references are summarised at the end of the thesis. The Section 2.2.1 has been contributed by Diana Rechid, the Figures 2-1 and 2-12 have been contributed by Peter Hoffmann.

2.1 Introduction

Climate model output is increasingly used in climate change impact, vulnerability and adaptation studies for statistical downscaling (Wilby, 2003; Hoffmann et al., 2012), statistical-dynamical downscaling (Fuentes and Heimann, 2000) and for the provision of physically consistent forcing data for impact models like hydrological models (van Pelt et al., 2009), ecosystem models (Huntley et al., 2008) and biometeorological models (Muthers et al., 2010). Results of impact studies can be very sensitive to the meteorological data used. For this reason, the evaluation of RCM results is crucial for the interpretation of results of impact studies (Dibike et al., 2008).

Biases in RCM simulation results can arise from shortcomings of the RCMs themselves, but also from erroneous forcing data. RCM evaluations are mostly done for RCMs forced with reanalysis data over a given time period; the RCM results are then compared to observation data (e.g. Kotlarski et al., 2005; Christensen et al., 2008). This evaluation approach is not within the scope of the present study, because transient simulations of RCMs forced by GCMs are needed for studies that deal with regional climate change impacts. Transient RCM integrations have, for

---

example, been evaluated by Jacob et al. (2007) with the focus on seasonal and annual averages of air temperature and precipitation. In the present study, we evaluate results of the RCMs CLM (Rockel et al., 2008) at 0.165° (~18 km horizontal resolution) and REMO (Jacob, 2001) at 0.088° (~10 km horizontal resolution), both forced by simulation results of the GCM ECHAM5-MPIOM (Roeckner et al., 2003, Jungclaus et al., 2006) at T63 resolution (~200 km at 0° latitude). The results of ECHAM5-MPIOM, CLM and REMO are evaluated for Hamburg Metropolitan Region in Northern Germany for the period 1961-2000. This area (Figure 2-1a) is located close to the coast and it is one of the areas selected by the German Federal Ministry of Education and Research to develop adaptation measures to climate change within the project KLIMZUG-NORD. Thus, the RCM results are used for various purposes in the framework of the development of adaptation measures to climate change. The meteorological variables air temperature, precipitation, total cloud cover, relative humidity and wind speed are evaluated.

The evaluation of a climate model operating in climate mode needs to be based on the comparison of statistical properties of simulated and observed variables. In the present study, the climatological annual cycle, the variance of time series of monthly averages and the empirical probability density function (PDF) of daily averages are evaluated. The degree of agreement between simulated and observed climate is quantified by model evaluation measures. Model evaluation measures introduced by Keuler (2006) are used for evaluation of the climatological annual cycles. The Skill-Score (SSC) introduced by Perkins et al. (2007) and an additional model evaluation measure, the Hit-Rate of the percentiles (HRP), newly introduced in this study, are used for evaluation of the PDFs of daily averages.

Two major issues have to be addressed in the evaluation: uncertainties of the observational data and internal climate variability. The issue of uncertainties of the observational data is addressed by using more than one observational dataset for evaluation. The issue of interannual climate variability is addressed by calculating confidence intervals for the model evaluation measures by bootstrap resampling.

The quantitative climate model evaluation is carried out in order to determine if it is reasonable to apply a bias correction to the RCM data before it is used in impact studies. For the RCMs evaluated here, recommendations will be given which meteorological variables should be bias corrected.

The structure of this chapter is the following: the setup of the climate model simulations to be evaluated and the data processing are described in Section 2.2. The observational datasets used for model evaluation are described in Section 2.3. The evaluation method is described in Section 2.4. Evaluation results are discussed in Section 2.5. In Section 2.6, an example for using model evaluation measures to determine whether bias correction is reasonable is presented.

Conclusions are drawn in Section 2.7.

2.2 Regional climate model simulations

2.2.1 Setup of the regional climate models

The global GCM datasets are taken from the ECHAM5-MPIOM simulations for the IPCC Assessment Report Four (AR4) (Roeckner, 2004; Roeckner et al., 2006a,b). The ECHAM5-MPIOM control climate simulations include observed anthropogenic forcing (CO_2, CH_4, N_2O, CFCs, O_3 and sulphate) for the period 1860-2000. These simulations neglect natural forcing from volcanic aerosols and variable solar activity. The three different members of the control period were initialised in different years from a 500 year preindustrial control simulation to account for internal climate variability.

The global ECHAM5-MPIOM ensemble was used to force the RCM REMO first for Europe at 0.44° horizontal resolution. In a second nesting step, the ensemble is further downscaled to 0.088° for Germany with 27 vertical levels (Jacob, 2005a; Jacob et al., 2008; Jacob et al., 2009a). A different version of the REMO model was used for the third realisation (REMO-3). The REMO-3 data have been directly provided for usage within KLIMZUG-NORD (Rechid, 2010; personal communication). The RCM CLM was directly nested into the global ECHAM5-MPIOM simulations for Europe at 0.165° horizontal resolution with 32 vertical levels (Hollweg et al., 2008; Keuler et al., 2009a/b; Lautenschlager et al., 2009).

2.2.2 Data processing

For REMO, hourly values of 2 m air temperature, 2 m dew point temperature, total cloud cover, 10 m wind speed as well as convective and stratiform precipitation sums are available. Hourly total precipitation sums are calculated by adding convective and stratiform precipitation sums. Hourly relative humidity is calculated from 2 m temperature and 2 m dew point temperature by using the Magnus formula (Hupfer and Kuttler, 2006). From hourly values, daily and monthly averages (2 m temperature, 2 m relative humidity, 10 m wind speed and total cloud cover) are calculated. The integrated values are calculated for precipitation.

For CLM, 3-hourly values of 2 m temperature, 2 m dew point temperature, total cloud cover and hourly values of 10 m wind speed in West-East and South-North directions as well as convective and stratiform liquid and solid precipitation sums are available. Hourly values of 10 m wind speed and total precipitation are derived; 3-hourly values of relative humidity are calculated from 2 m temperature and 2 m dew point temperature. Again, daily and monthly averages are calculated from hourly or 3-hourly values.

For ECHAM5, 6-hourly values of 2 m temperature, 2 m dew point temperature, total cloud cover, 10 m wind speed in West-East and South-North directions and convective and stratiform precipitation are available. Daily and monthly averages are derived with the same methods as for CLM and REMO.

2.3 Observation based data

2.3.1 Datasets

The ERA-40 reanalysis (Uppala et al., 2005) covers the period from September 1957 to August 2002. The spatial resolution is about 1.125°. The values for 2 m air temperature, total cloud cover, 2 m relative humidity and 10 m wind speed are taken from the 6-hourly instantaneous fields. Precipitation is taken as the integrated value from the first 6 hours after each assimilation step. It has to be kept in mind that a general underestimation of precipitation in the ERA-40 reanalysis data for the extratropical regions has been found by Uppala et al. (2005).

The CRU TS 2.1 data (Mitchell and Jones, 2005) cover the period from 1901 to 2002. Data is provided on a 0.5° regular grid. The monthly values of 2 m air temperature, precipitation and total cloud cover are used in the present study. New et al. (1999) report a mean square cross validation error of about 15% for precipitation, 0.5 K for summer air temperature, 1.0 K for winter air temperature, 0.3 oktas (3.75 %) for total cloud cover and 1 m/s for wind speed in the CRU 1961-1990 climatology for Northern Europe.

Among the various GPCC products (Rudolf and Schneider, 2005; Rudolf et al., 2010) the "Full Data Reanalysis Version 4" (GPCC-V4), which covers the period from 1901 to 2009, is used in the present study. The monthly precipitation sums are available on a 0.5° regular grid. More than 300 rain gauges were used for interpolation in the evaluation domain for all months of the evaluation period. This indicates that the interpolation error is below 10% (Rudolf and Schneider, 2005). The GPCC-V4 data are not corrected for the systematic undercatch of precipitation. Estimates of the climatological correction factors derived by the method of Legates and Willmott (1990) are provided with the data. Correction factors are substantial for precipitation evaluation: during the winter season they reach a value of up to 1.6 in the evaluation domain. Correction factors delivered with the GPCC data appear to range at the upper bound of published precipitation correction factors. For example, correction factors derived by Adam and Lettenmaier (2003) and by Yang et al. (2005) are about 1.2 to 1.3 in the winter season, thus much below the GPCC-V4 correction factors.

The European Climate Assessment and Data (ECA&D-3.0; Haylock et al., 2008) cover the period from 1950 to 2009. Daily average 2 m air temperature and daily precipitation sums are used in the present study. ECA&D-3.0 consists of station data interpolated on a 0.25° regular

grid. Precipitation is not corrected for systematic undercatch.

The REGNIE gridded daily precipitation sums have been provided for the period 1961-2000 by the German Meteorological Service (DWD) (Köcher, 2010; personal communication) for the purpose of the present evaluation study. The precipitation data are on a regular 30" x 60" grid. REGNIE data have been created by DWD in three steps. The climatological spatial distribution of the monthly precipitation sum for the period 1961-1990 has been interpolated to the target grid by multiple linear regression using height above sea level, longitude, latitude and the slope of the terrain in relation to the prevailing wind. The precipitation anomalies at the stations have then been interpolated onto the REGNIE grid. Finally, the anomalies have been multiplied with the background field values to give the final value for precipitation. REGNIE precipitation values used in the present study are not corrected for systematic undercatch.

The DWD routine observations (ROD) are station data. From these, daily averages of total cloud cover, 2 m relative humidity and 10 m wind speed are used in the present study. The location of the stations within the domain is shown in Figure 2-1b. The average of all available station records is calculated for every day during the evaluation period.

(a)   (b)
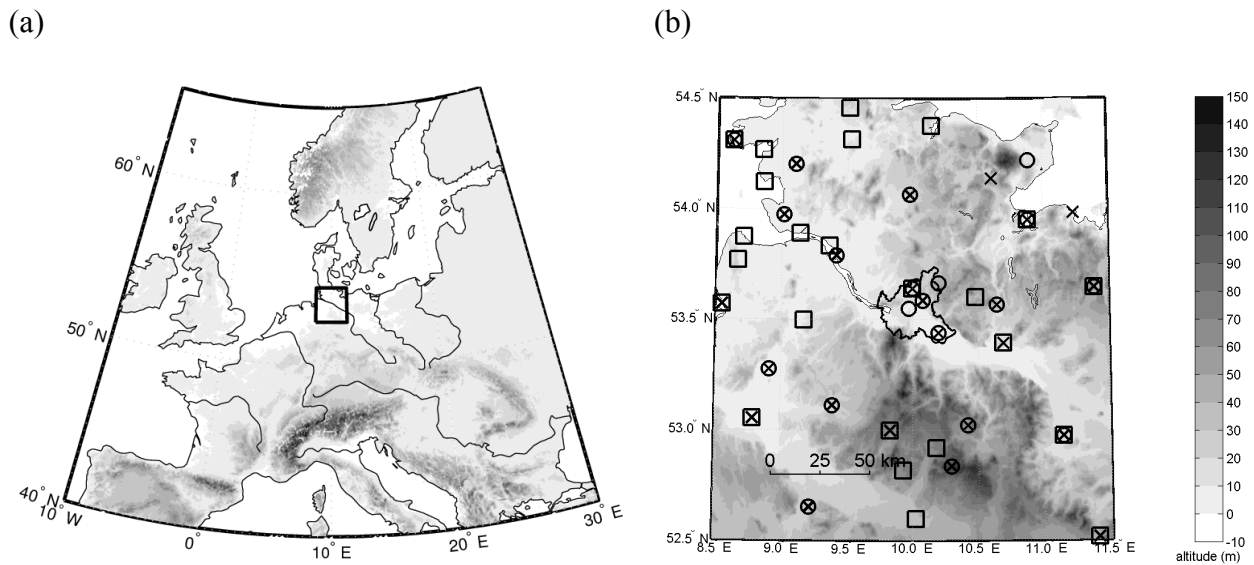
Figure 2-1: (a) Map of Europe with the evaluation domain in Northern Germany and (b) location of the stations within the evaluation domain. In (b), the stations with observations of total cloud cover, wind speed and relative humidity are marked with a circle, a square and a cross respectively. The black line indicates the border of the federal state Hamburg.

2.3.2 Uncertainties of data

Datasets used in the present study are gridded station data, the ERA-40 reanalysis data and the ROD which are area-averaged station data. Gridded station data are created by spatial interpolation of point measurements. Uncertainties in these datasets arise mainly from measurement errors and the method used for spatial interpolation. The contribution of both types of uncertainties to the total uncertainty is different for each meteorological variable. For example, station measurements of air temperature are accurate to tenth of a degree (Haylock et al., 2008), whereas observations of total cloud cover are quite uncertain. Different methods used for spatial interpolation can lead to strongly different results if the interpolated meteorological field has large gradients (e.g. the station data have low spatial representativity). The spatial representativity of point measurements depends on the meteorological variable. The gridded datasets used are created with (slightly) different interpolation methods but are mainly based on the same measurement dataset. For this reason, usage of different gridded datasets helps to capture the interpolation uncertainty but not necessarily the measurement uncertainty.

The ERA-40 data can be assumed to be more independent of the gridded station data, because they use also other sources such as radiosonde and satellite data. Additionally, ERA-40 data are subject to characteristics of the ECMWF model and the method used for data assimilation. Precipitation is the result of 6 hours model integration and therefore very sensitive not only to initial data but also to model characteristics.

Differences between ERA-40 data and gridded station data capture many different types of uncertainties. However, one has to keep in mind that the station data do influence the ERA-40 data and shortcomings of the ECMWF model introduce new uncertainties.

The described observational datasets are not suitable for trend detection due to the changing number of stations contributing to the interpolated fields and due to the inhomogeneities in the records of single stations. Therefore, trends in RCMs cannot be evaluated using these datasets.

2.3.3 Evaluation domain

As mentioned, the focus of the evaluation is on Northern Germany. Since the CRU TS 2.1, ECA&D-3.0, GPCC-V4 and DWD-REGNIE data are only defined for land points, the evaluation domain is chosen to be a rectangular area situated at 52.5°N to 54.5°N and 8.5°E to 11.5°E, with the water surfaces excluded. The ERA-40 data are selected in a way to best fit this evaluation domain. The climate model data are averaged over the whole domain; all model grid points with a land fraction below 0.5 are omitted. The gridded observation data as well as the station data are also averaged over the evaluation domain.

2.4 Evaluation method

2.4.1 Evaluation method for monthly averages

Measures for the evaluation of monthly averages (Table 2-1) have been suggested by Keuler (2006). These model evaluation measures are calculated for every pair of climate model and observational dataset. One value for the BIAS is calculated for every month of the year. All realisations of simulated climate by one given climate model version are merged, because they represent equally probable estimates of the average simulated climate. REMO-3 is here not merged with REMO-2 and REMO-1 due to the different model version.

Table 2-1: Model evaluation measures for monthly averages as introduced by Keuler (2006). M_m denotes the model result for the mth month of the year, O_m the observational data for the mth month of the year. M_i denotes the ith monthly averaged model result of the time series, O_i the ith monthly averaged observation of the time series. The overbar denotes a climatological average. $\bar{M}$ denotes the climatological average over all months of the year.

Abbreviation	Denomination	Formula	Optimum value
BIAS	Bias	$BIAS_m = \overline{M_m} - \overline{O_m}$	0
MAMD	Mean absolute monthly difference	$MAMD = \dfrac{1}{12} \sum_{m=1}^{12} \lvert \overline{M_m} - \overline{O_m} \rvert$	0
ROYA	Ratio of yearly amplitudes	$ROYA = \dfrac{max(\overline{M_m}) - min(\overline{M_m})}{max(\overline{O_m}) - min(\overline{O_m})}$	1
CTCO	Climatological temporal correlation	$CTCO = \dfrac{\sum_{m=1}^{12}(\overline{M_m} - \bar{M})\,(\overline{O_m} - \bar{O})}{\sqrt{\sum_{m=1}^{12}(\overline{M_m} - \bar{M})^2 \sum_{m=1}^{12}(\overline{O_m} - \bar{O})^2}}$	1
RATV	Ratio of temporal variances	$RATV = \dfrac{\sum_{i=1}^{N}(M_i - \bar{M})^2}{\sum_{i=1}^{N}(O_i - \bar{O})^2}$	1

The model evaluation measures suggested by Keuler (2006) are applicable to every meteorological variable of interest. However, some shortcomings have to be mentioned. All model evaluation measures deal with the average or the standard deviation of monthly averages. It is well known (e.g. Wilks, 1995) that these are not robust statistical measures, and therefore very sensitive to climate variability. Furthermore, the model evaluation measures "climatological

temporal correlation" (CTCO) and "ratio of yearly amplitudes" (ROYA) have different effective ranges for different meteorological variables. For example, biases of air temperature will hardly become larger than the yearly amplitude of air temperature in the studied evaluation domain. Therefore, CTCO and ROYA tend to yield values near the optimum value of 1 for air temperature even though considerable biases are simulated.

2.4.2 Evaluation method for daily averages

The agreement between simulated and observed PDFs of daily averages is quantified with the model evaluation measures displayed in Table 2-2. The Skill-Score (SCC) has been introduced by Perkins et al. (2007). The Hit-Rate of the percentiles is newly introduced in the present study. The model evaluation measures are calculated for every pair of climate model and observational dataset for each of the four seasons December, January, February (DJF), March, April, May (MAM), June, July, August (JJA) and September, October, November (SON). Again, all realisations of simulated climate are merged for every climate model. Bin widths used for the construction of the empirical PDFs which in turn are needed to calculate the SSC are chosen to be 1 K for air temperature, 10% for total cloud cover, 4% for relative humidity and 1 m/s for wind speed. The bin widths have been chosen to equal the order of the uncertainty of the observational data, because it does not make sense to discriminate the data with a higher accuracy than they can be observed.

Table 2-2: Model evaluation measures for daily averages. The SSC has been introduced by Perkins et al. (2007). $PDF_{M,i}$ is the relative frequency of the climate model data in the ith bin, $P_{M,i}$ is the ith percentile of the climate model data, $U(P_{O,i})$ is the allowed deviation for the ith percentile of the observational data.

Abbreviation	Denomination	Formula	Optimum value
SSC	Skill-score	$SCC = \sum_i min(PDF_{M,i}, PDF_{O,i})$	1
HRP	Hit-Rate of the percentiles	$HRP = \sum_{i=1}^{99} \begin{cases} \frac{1}{99} & if \quad |P_{M,i} - P_{O,i}| \leq U(P_{O,i}) \\ 0 & else \end{cases}$	1

The value of the SSC is 1 for a perfect overlap of simulated and observed PDFs. However, a perfect agreement of the empirical PDFs is very improbable due to the limited sample size. Therefore, the effective optimum value for the SSC is lower than 1. The value of the SSC is 0 if the PDFs have no overlap at all. This is very improbable for most meteorological variables, because the PDFs will overlap to some degree even for large model deficiencies. The SSC is

therefore easy to calculate but not very selective, because neither the optimum value of 1 nor the weakest possible score of 0 are in the effective range of this model evaluation measure.

The motivation to newly introduce the Hit-Rate of the percentiles (HRP) is twofold: at first, this model evaluation measure has an effective range between 0 and 1 independent of the meteorological variable to be evaluated. At second, HRP allows to account for an "allowed deviation" between the percentiles of simulated and observed data. For the calculation of the HRP, the 1st to 99th percentiles of simulated and observed daily averages are calculated using the "prctile" function of the MATLAB software. The HRP is then defined as the fraction of percentiles with a difference between the percentiles of simulated and observed data below the allowed deviation.

The choice of the allowed deviation depends on the purpose and the type of the evaluation study. If RCMs forced with reanalysis data are evaluated, the allowed deviation should be an estimate of the uncertainty of the observational data. In the present study, the allowed deviation should account for both uncertainty of observational data and internal climate variability. In the following, we describe how we determine the value for the allowed deviation.

In a first step, one has to decide if the allowed deviation shall depend on the percentile. In the present study, the allowed deviation for air temperature, wind speed and relative humidity is chosen to be independent of the actual percentile ($U(P_{O,i}) = U$). Thus, for example it is assumed that air temperatures of -5°C have the same uncertainty as air temperatures of +25°C. For total cloud cover, we assume that the allowed deviation is twice as large for a total cloud cover of 50% than for a total cloud cover of 0% and 100%, with a linear scaling between the minimum and maximum value.

In a second step, the value of the allowed deviation is calculated by considering the interannual climate variability and the uncertainty of the observational data. The contribution of both uncertainties to the allowed deviation is estimated by a learning process based on the available observational datasets.

The contribution of the interannual climate variability to the allowed deviation is determined by calculation of the HRP for different bootstrap resamples (Efron, 1979) of the observational data as a function of the chosen allowed deviation. The daily data are resampled as blocks to account for temporal correlation. One block contains all daily averages belonging to one specific season (e.g. all daily data from JJA-1965). The median of the HRP is 0 if the allowed deviation is 0 due to statistical variability and increases to 1 for large allowed deviations. This behaviour is displayed in Figure 2-2 for the example of air temperature in MAM (red crosses). The contribution of interannual climate variability to the allowed deviation is defined as the allowed

deviation where the median of the HRP is 0.95 (U_{VAR}, red line in Figure 2-2). As shown in Figure 2-2, the ECA&D data have been used to estimate U_{VAR} for air temperature. For total cloud cover, relative humidity and wind speed, the ROD data have been used.

The contribution of the uncertainty of the observational data to the allowed deviation is obtained by calculating the HRP as a function of the allowed deviation for two observational datasets (blue crosses in Figure 2-2). The contribution of the uncertainty of the observational data to the allowed deviation is defined as the allowed deviation, for which the HRP is 0.95 (U_{OBS}, blue line in Figure 2-2). For air temperature, the ECA&D and the ERA-40 data have been used to estimate the value for U_{OBS}. For total cloud cover, relative humidity and wind speed, the ROD and the ERA-40 have been used.
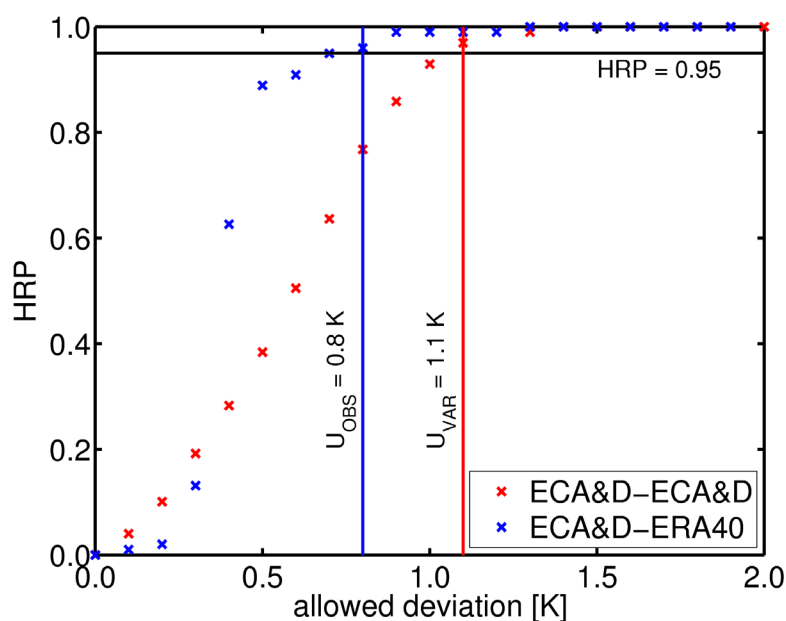
Figure 2-2: Determination of the allowed deviation for the example of air temperature in MAM. Red crosses: model evaluation measure HRP as a function of the allowed deviation for evaluation of different resamples of the ECA&D-3.0 data against themselves to capture interannual climate variability. Blue crosses: HRP as a function of the allowed deviation for evaluation of the ECA&D3.0 data against the ERA-40 data to capture the uncertainty of the observations. In this example, the obtained allowed deviations are 0.8 K for the observation uncertainty (U_{OBS}) and 1.1 K for the interannual variability (U_{VAR}).

With the described method, one value for U_{OBS} and U_{VAR} is obtained for each season. The evaluation could be performed with a different allowed deviation for each season, but in the present study, we choose to use the maximum of the U_{OBS} and the U_{VAR} obtained for the different seasons to avoid time dependent changes in the allowed deviation. The allowed deviation is defined in a pragmatic way as the square root of the sum of the squares of U_{OBS} and U_{VAR}. The

allowed deviations obtained by this method are 1.4 K for air temperature, 6% for total cloud cover, 4% for relative humidity and 0.6 m/s for wind speed. The allowed deviation for wind speed appears lower than published estimates. For this reason, it is set to 1 m/s, consistent with the value in New et al. (1999).

2.4.3 Confidence intervals for the model evaluation measures

The few realisations of simulated climate and the one realisation of past climate provide only a small sample of the statistical population of climate model results and observations. For this reason, model evaluation measures are only representative for the samples of model results and observations used in the present study, but not necessarily for the basic population. Confidence intervals for the model evaluation measures are calculated by bootstrap resampling to get an estimate of their statistical spread with respect to interannual climate variability. By resampling of blocks containing all daily data in one specific season in simulated and observed data, 10^5 bootstrap resamples are drawn and then the model evaluation measures are calculated for each. With this method, 10^5 values are obtained for each model evaluation measure. From these values, the 5th, 50th and 95th percentiles are calculated and graphically presented in Section 2.5 as the median and the 90% confidence interval of the model evaluation measures.

The serial correlation of the data is a major issue when dealing with bootstrap resampling (e.g. Wilks, 1995). The higher the serial correlation, the more the confidence intervals are underestimated. The issue of serial correlation is reduced to serial correlations over a lag of one year or more by resampling of blocks containing all daily data in one season. Even then, the serial correlation cannot be neglected (Kendon et al., 2008). Therefore, different realisations of simulated climate from the same climate model are evaluated against each other in Section 2.5.6. The HRP can be expected to yield low values if the estimated allowed deviations are too small.

In Section 2.5, a BIAS is called significantly positive if the 5th percentile of the BIAS values obtained by resampling of the data is positive, and significantly negative, if the 95th percentile of the BIAS values obtained by resampling is negative.

2.5 Results

2.5.1 Air temperature

The climatological annual cycle of air temperature is shown in Figure 2-3a. Differences between the observational datasets (black lines) are small. Simulated annual cycles of air temperature agree well with the observed ones at a first glance, meaning they reflect the large annual amplitude. However, a significant negative BIAS is found for ECHAM5 in SON and DJF, whereas a significant negative BIAS appears for CLM in JJA and SON. The fact that no

significant BIAS is found for REMO is reflected by the values for the "mean absolute monthly difference" (MAMD), which yields lower values for REMO than for ECHAM5 and CLM (Figure 2-3b).

(a)   (b)
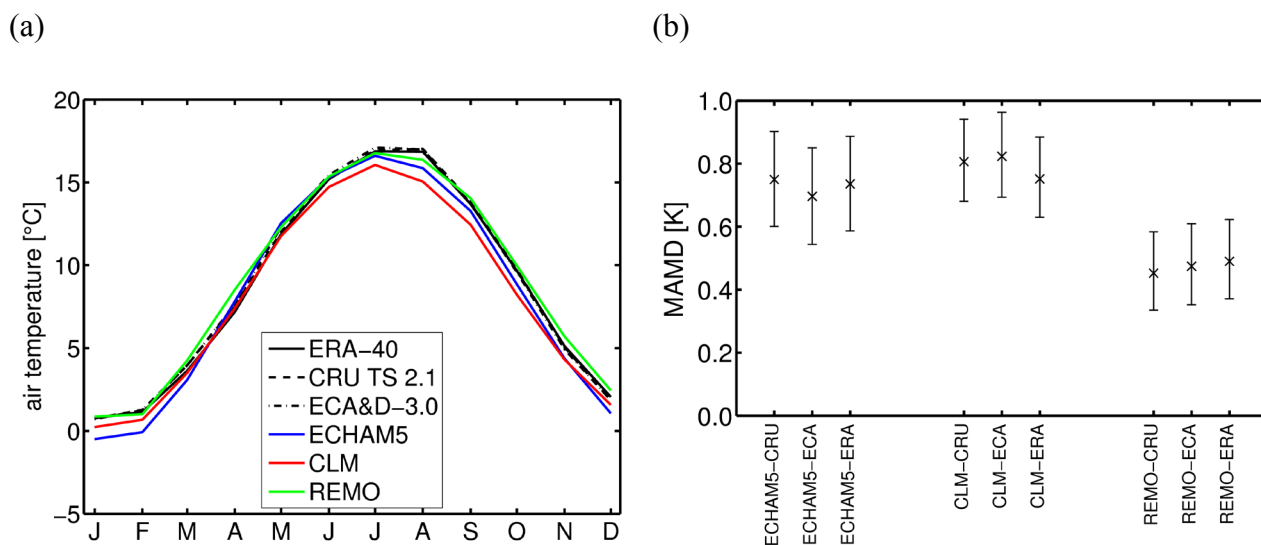
Figure 2-3: (a) Simulated and observed climatological annual cycle of air temperature for 1961-2000 and (b) the corresponding MAMD. In (b), CRU-2.1 is abbreviated by CRU, ECA&D-3.0 by ECA and ERA-40 by ERA.

Observed and simulated PDFs of air temperature are displayed for DJF in Figure 2-4a. The PDFs of the observational data are skewed to the left and therefore large negative daily air temperature anomalies occur with a higher probability than large positive daily air temperature anomalies. Climate models are able to capture this skewed PDF pattern. The RCMs CLM and REMO simulate the major part of the PDF better than ECHAM5, but both RCMs produce a maximum in the PDF at 0 °C. This unrealistic maximum can cause problems when dealing with the data (e.g. calculation of the number of frost days). The problem of the maximum in the PDF at 0 °C is present in results from older versions of CLM and REMO but it is eliminated in the new versions (e.g. the REMO version used to create the REMO-3 data). The SSC and the HRP (Figure 2-4b) are of limited help in the evaluation of air temperature in DJF. SSC is nearly the same for the three models, because a slightly better simulation of the shape of the PDF by the RCMs compared to ECHAM5 cancels out the negative effect of the maximum at 0 °C. HRP yields higher values for the RCMs than for ECHAM5 because the maximum at 0 °C does not cause many percentiles of the PDF to be shifted by more than the allowed deviation. This example shows that singularities in climate data, that may appear, are not always detectable by model evaluation measures.

A bias correction of CLM temperature in JJA and SON can be recommended from the viewpoint of model evaluation due to the negative BIAS in these seasons. For REMO, the original model output should be used. However, the unrealistic maximum in the PDF at 0 °C needs to be kept in mind.

(a)   (b)
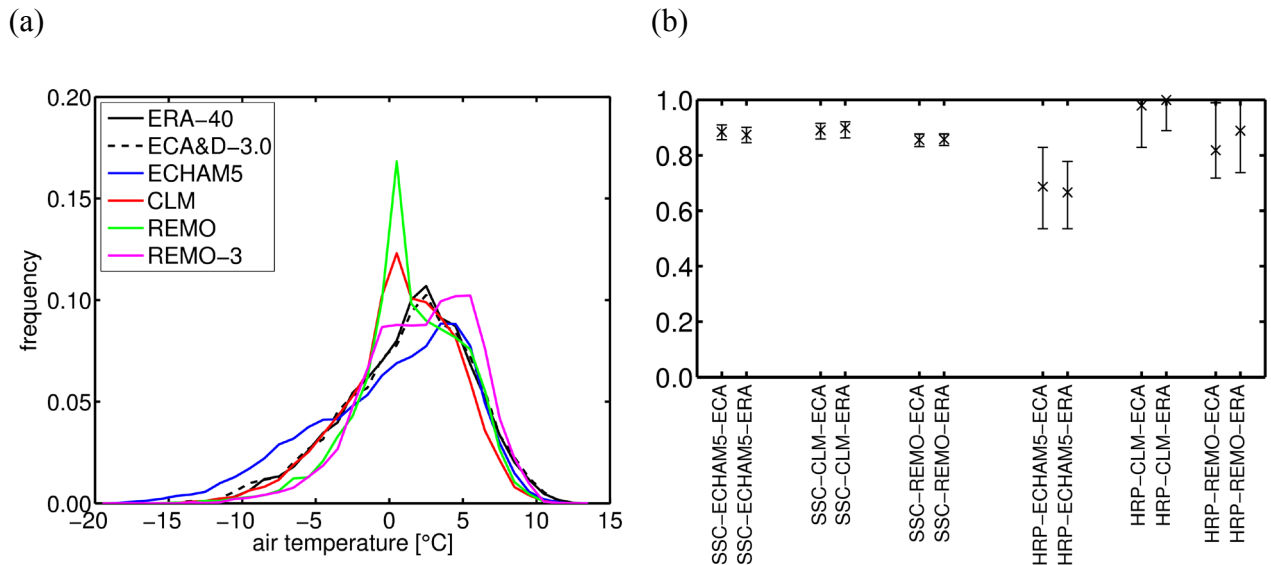
Figure 2-4: (a) PDFs of simulated and observed daily average air temperature in DJF for 1961-2000 and (b) the corresponding SSC and HRP. The bin width used for construction of the PDFs is 1 K.

2.5.2   Precipitation

Six observational datasets are available for evaluation of monthly precipitation sums: four gridded datasets based on rain gauge measurements without undercatch correction, one gridded dataset with corrected precipitations and the ERA-40 reanalysis data. The climatological annual cycles of all observations are displayed in Figure 2-5. All uncorrected gridded datasets exhibit nearly the same climatological annual cycle. The reasons are the large number of stations in the evaluation domain and the good spatial representativity of monthly precipitation sums. Therefore, the interpolation error is small. The corrected gridded dataset differs a lot from the four uncorrected gridded datasets. Even if the correction factors provided by GPCC are large compared to correction factors derived by other authors, this example indicates that using different observational datasets capturing only one type of uncertainty (in this case the interpolation uncertainty) can lead to the wrong conclusion that the uncertainty of the observation based data is small. The precipitation from ERA-40 is lower than the uncorrected gridded precipitation data, especially in JJA. This is consistent with Uppala et al. (2005). As precipitation overcatch by rain gauges is very improbable, the ERA-40 precipitation data are assumed to be too low and not further used for model evaluation.
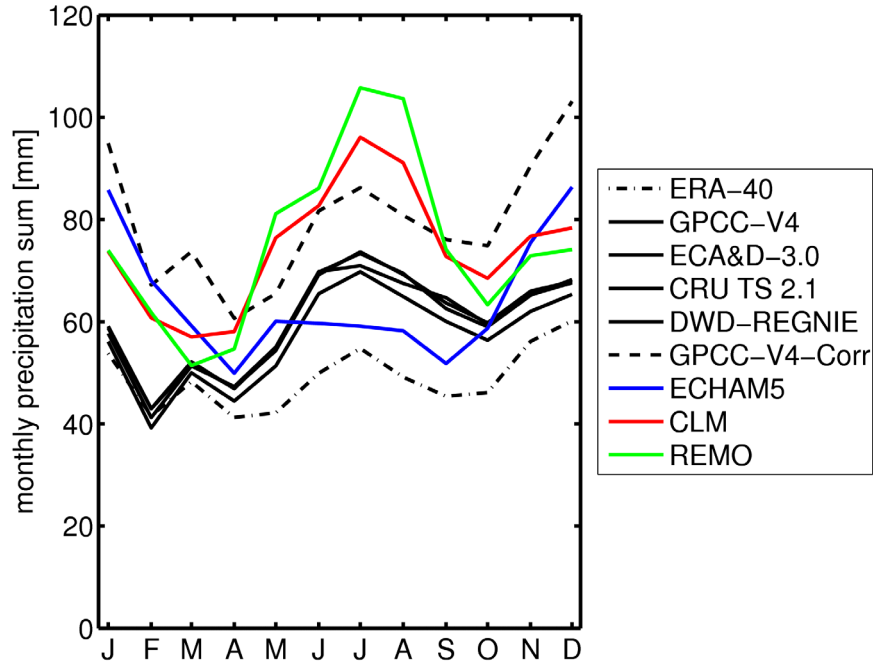
Figure 2-5: Climatological annual cycle of precipitation for 1961-2000. The four gridded precipitation datasets using uncorrected rain gauge data are only slightly different (4 black straight lines), whereas the gridded precipitation dataset based on corrected rain gauge data yields much higher values (black dashed line). ERA-40 underestimates precipitation (black dash-dotted line).

Simulated precipitation lies between corrected and uncorrected observational data except from spring to early autumn. ECHAM5 significantly underestimates precipitation in JJA, whereas both RCMs significantly overestimate precipitation. The BIAS of the RCMs depends on the region. Feldmann et al. (2008) report no overestimation of precipitation in JJA for a mountainous region in Southwestern Germany in the same RCM simulations. Figure 2-5 also indicates that the decision whether a climate model has a positive or negative precipitation BIAS in DJF mainly depends on the choice between corrected and uncorrected precipitation data. In impact studies, problems might arise when hydrological models are calibrated with uncorrected precipitation data.

From the viewpoint of model evaluation, bias correction of precipitation can only be recommended in the summer season.

An evaluation of daily precipitation is not conducted in the present study because no corrected daily precipitation data have been available for the present study.

2.5.3 Total cloud cover

The climatological annual cycle of total cloud cover is displayed in Figure 2-6a. The total cloud cover has a maximum in DJF and a minimum in JJA in the observation based data (black lines). This pattern is reproduced by the climate models but the amplitude of the annual cycle is underestimated by CLM resulting in a significant positive BIAS of total cloud cover for the period May to September. A significant positive BIAS is found in MAM for ECHAM5. No significant BIAS is found for REMO.
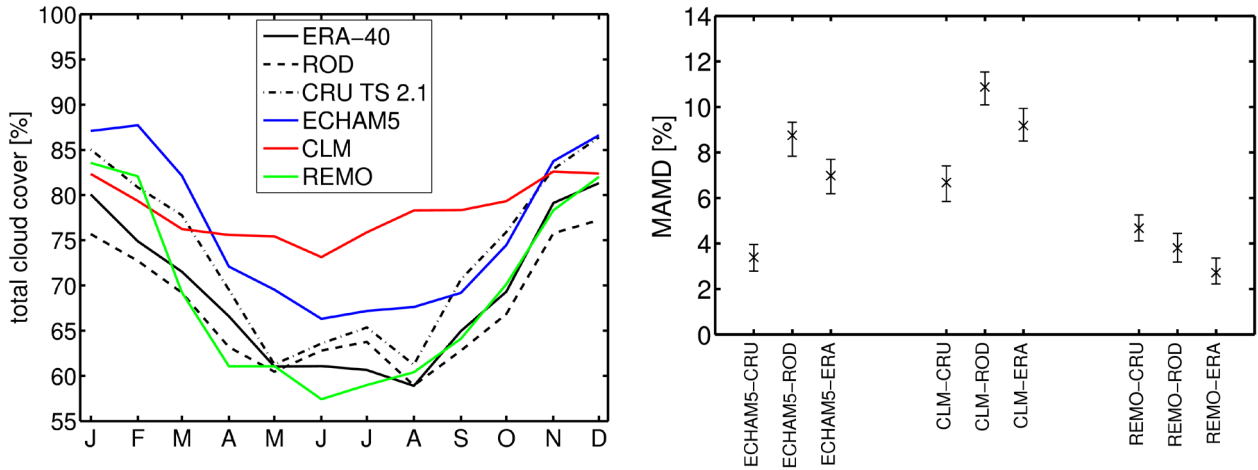
Figure 2-6: (a) Climatological annual cycle of total cloud cover for 1961-2000 and (b) the corresponding MAMD.

The differences among the observational datasets are quite large. Therefore, the same model evaluated against different observational datasets yields quite different values for MAMD (Figure 2-6b). The large BIAS of CLM in JJA and SON causes higher MAMD values for CLM than for REMO. The too high values for total cloud cover simulated by CLM for the period May to September might be the physical reason for the underestimation of air temperature in JJA and SON (Figure 2-3a).

The PDFs of daily average total cloud cover in JJA are shown in Figure 2-7a. In ECHAM5 and CLM, days with total cloud cover above 90% are too frequently simulated, while the frequency of intermediate values of total cloud cover is underestimated. REMO is able to reproduce the observed PDF. The SSC and the HRP confirm this subjective impression (Figure 2-7b). However, the SSC is less selective than the HRP. For example, the PDF simulated by CLM still obtains a median value of the SSC of 0.64 when compared to the ERA-40 reanalysis data and a median value of the SSC of 0.67 when compared to the ROD data. The simulated values of total cloud cover from CLM might lead to unrealistic results in adaptation studies, especially in JJA.

REMO results are within the allowed deviation. Therefore, bias correction is recommended for CLM but not for REMO.

(a)   (b)
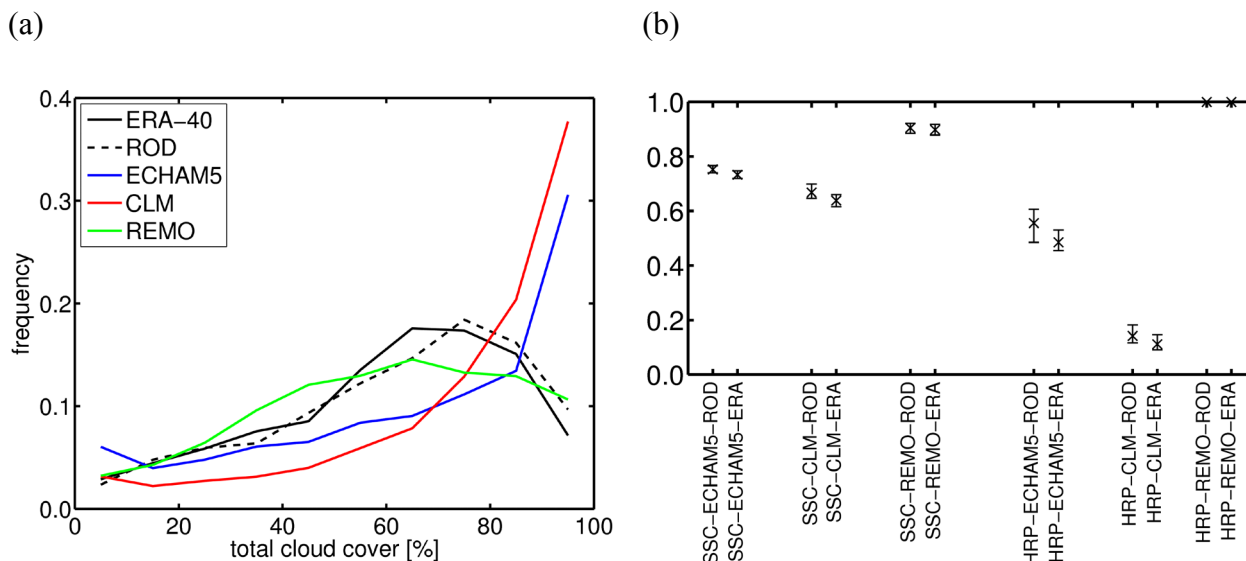
Figure 2-7: (a) PDFs of simulated and observed daily average total cloud cover in JJA for 1961-2000 and (b) the corresponding SSC and HRP. The bin width used for construction of the PDFs is 10%.

2.5.4 Relative humidity

The simulated and observed climatological annual cycle of relative humidity is displayed in Figure 2-8a and the corresponding MAMD evaluation measures in Figure 2-8b. The maximum in DJF and the minimum in JJA are captured by the climate models but the simulated relative humidity is generally higher than the observed relative humidity. A significant positive BIAS is found for all models and all seasons except in SON for ECHAM5, and in both transition seasons for REMO.

The PDFs of relative humidity in JJA are presented in Figure 2-9a, with the corresponding model evaluation measures in Figure 2-9b. The observed PDF is reproduced well by ECHAM5 whereas both RCMs have deficiencies. This behaviour is captured by both model evaluation measures. The HRP is much more subject to interannual climate variability than the SSC, especially for REMO. The reason is that the whole PDF simulated by REMO is shifted by a constant offset towards higher values of relative humidity compared with observations. The offset is of similar magnitude than the allowed deviation. Resampling of the data can lead to a wide range of values for the HRP in such cases. This behaviour is the trade-off for the higher selectiveness of the HRP evaluation measure.

(a)   (b)
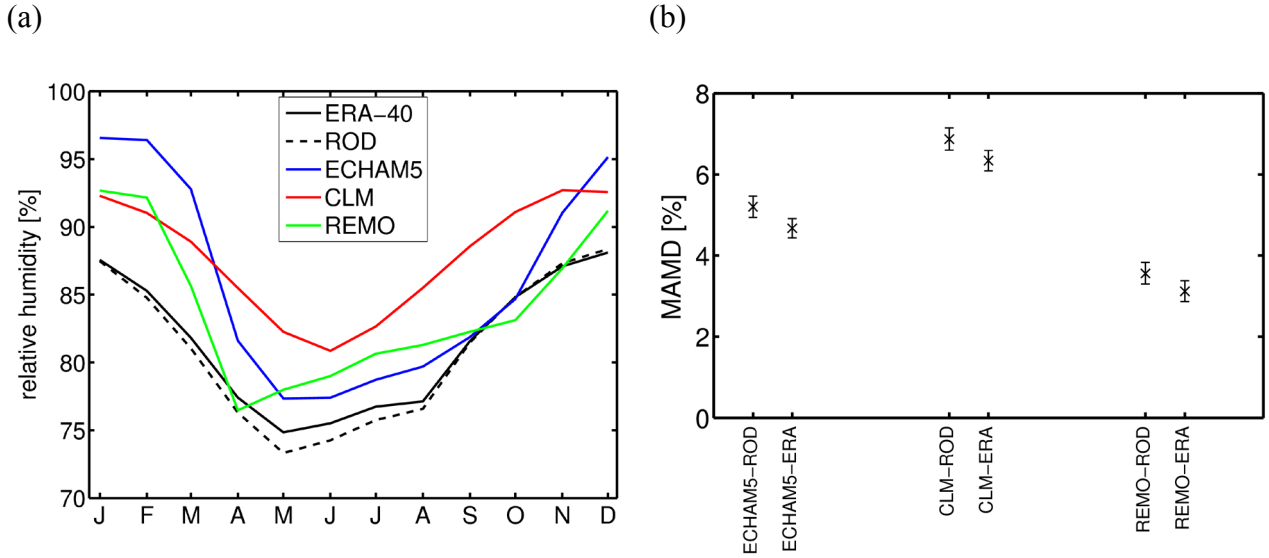
Figure 2-8: (a) Climatological annual cycle of relative humidity for 1961-2000 and (b) the corresponding MAMD.

(a)   (b)
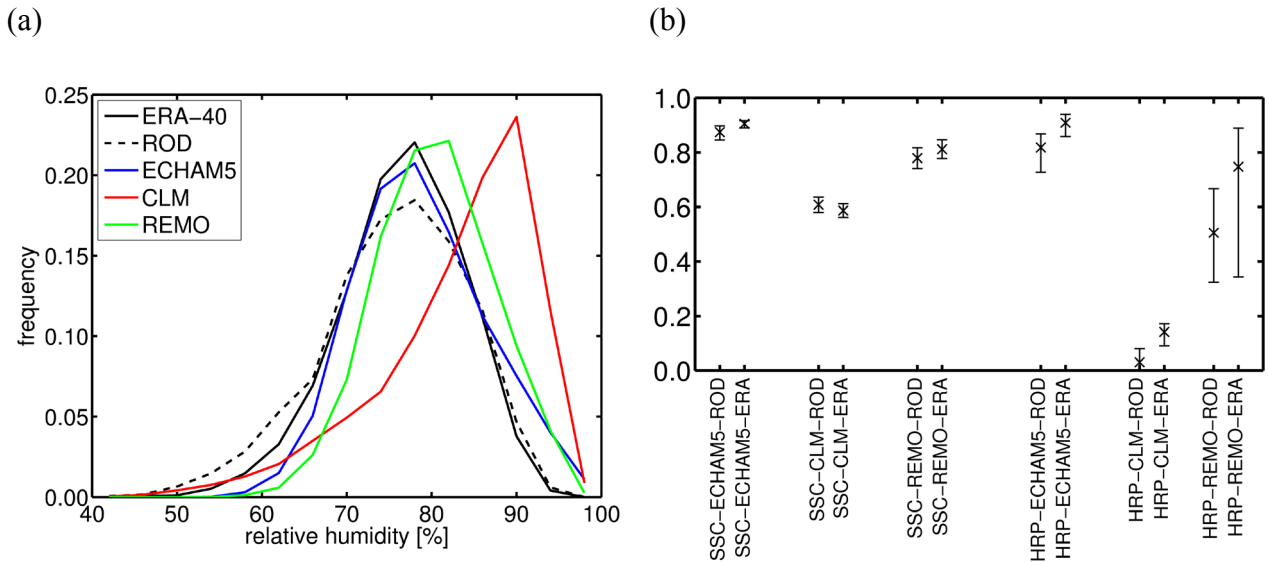
Figure 2-9: (a) PDFs of simulated and observed daily average relative humidity in JJA for 1961-2000 and (b) the corresponding SSC and HRP. The bin width used for construction of the PDFs is 4%.

The use of uncorrected values of relative humidity might lead to unrealistic results in studies dealing with adaptation to climate change. The fact that CLM simulates too high a frequency of high relative humidity in JJA is physically consistent with the too high frequency of high total cloud covers. This type of physical consistency is not found for ECHAM5: the PDF of relative humidity is simulated well in JJA, while the PDF of total cloud cover is not.

2.5.5 Wind speed

The evaluation period is reduced to 1981-2000 for wind speed, because the number of station records in the ROD dataset available for this thesis before 1980 is low. Average wind speed is higher in DJF than in JJA due to the higher number of passing low pressure systems in DJF. Climate models reproduce this annual cycle, but with smaller annual amplitude (Figure 2-10a). ECHAM5 and CLM exhibit a significant positive BIAS in JJA, whereas REMO has a significant negative BIAS in DJF. The variance of the time series of monthly averages is underestimated in both RCMs, a behaviour that is reflected by the "ratio of temporal variances" RATV evaluation measure (Figure 2-10b). This was not found for the other meteorological variables (not shown). This example shows that, even for monthly averages, RCMs can produce characteristics of the time series that are different from the forcing GCM.

(a)   (b)
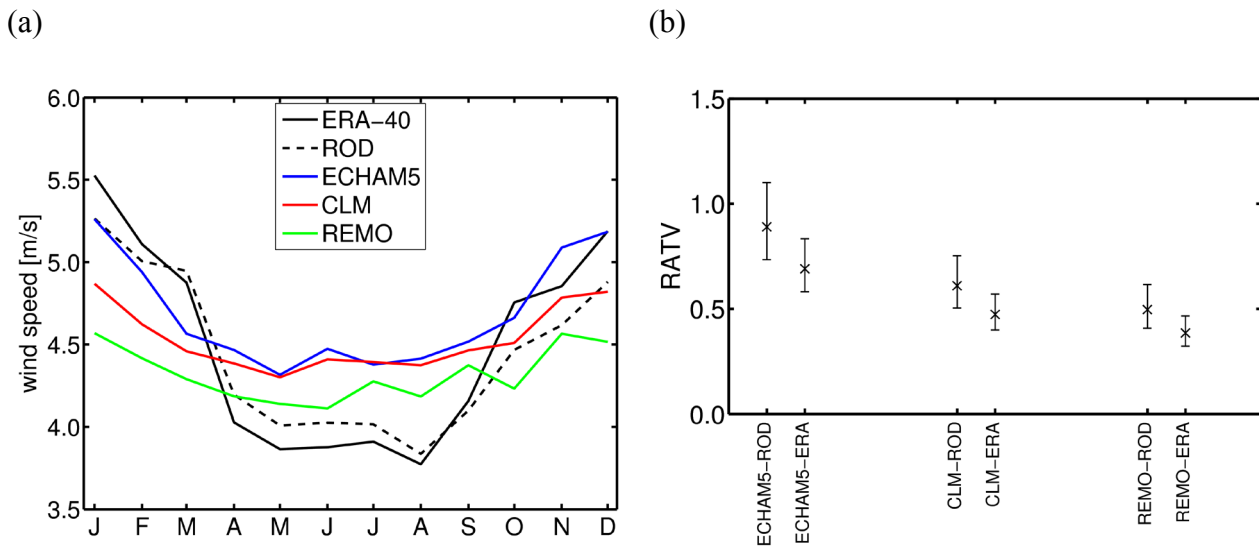
Figure 2-10: (a) Climatological annual cycle of wind speed for 1981-2000 and (b) the corresponding RATV.

The PDFs of daily averages are well simulated by both RCMs in all four seasons (the median value of the HRP is above 0.95). The only exception is obtained for REMO in DJF and JJA. Here, the HRP yields values lower than 0.95. ECHAM5 performs well, except for JJA. The PDF for JJA is shown as an example in Figure 2-11a and the corresponding model evaluation measures in Figure 2-11b. The conclusion of wind speed evaluation is that the amplitude of the annual cycle is slightly underestimated by the climate models. However, a bias correction of the RCM results is not recommended, because the simulated PDFs are mainly within the allowed deviation.
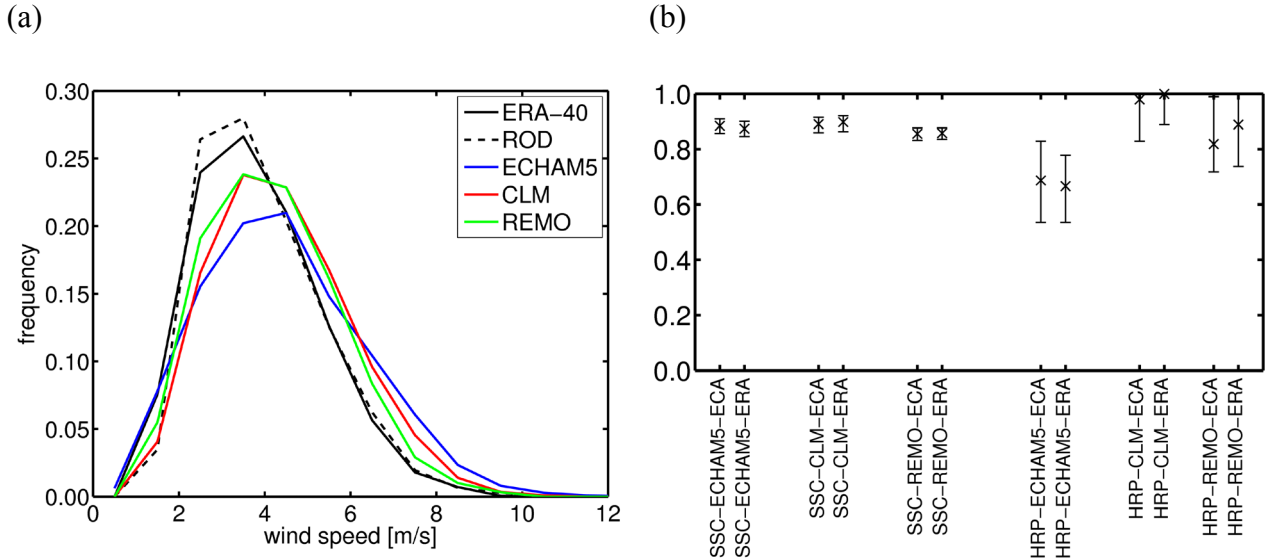
Figure 2-11: (a) PDFs of simulated and observed daily average wind speed in JJA for 1981-2000 and (b) the corresponding SSC and HRP. The bin width used for construction of the PDFs is 1 m/s.

2.5.6 Influence of long-term climate variability

The influence of long-term climate variability on the evaluation results is investigated by the calculation of the HRP for one realisation against another realisation of control climate simulations of the same climate model. For example, the PDF of air temperature in JJA from CLM-1 is compared to the corresponding PDFs from CLM-2 and CLM-3.

The median values of the HRP are between 0.97 and 1.00 for total cloud cover, between 0.96 and 1.00 for relative humidity, between 0.99 and 1.00 for wind speed and between 0.87 and 1.00 for air temperature. The largest deviations of the HRP from the optimum value 1 are obtained for air temperature in DJF and MAM. This result is not surprising, because time series of air temperature can be expected to be subject to higher serial correlation than time series of the other meteorological variables evaluated in the present study. However, the HRP also yields high values for air temperature. Evaluation of model results from different realisations of simulated climate from the same climate model indicate that the issue of long-term climate variability is not as important for model evaluation as for the detection of climate change signals when the HRP model evaluation measure is used. The main reason is that the allowed deviation used for HRP calculation considers not only the interannual climate variability but also the uncertainty of the observational data. Therefore, systematic underestimation of the confidence intervals due to serial correlation is not as important as in the case where only the uncertainty due to internal climate variability is investigated. The latter is relevant to detect climate change signals.

It has to be mentioned that the number of realisations available for testing the influence of

climate variability is very small and the three available realisations might not capture the whole spectrum of climate variability. A larger number of realisations would therefore be needed for detailed studies on simulated climate variability.

2.6   Application of HRP to decide if bias correction is reasonable

In this section, an example of applying HRP as a basis to decide if bias correction is reasonable, is presented. Hoffmann et al. (2012) developed a statistical model for the urban heat island (UHI) of Hamburg in Northern Germany. The statistical model is based on relationships between the nocturnal UHI and daily averages of total cloud cover, relative humidity and wind speed. Considerable differences between observed UHI and statistically calculated UHI appear for 1971-2000 when using the CLM simulation results as input for the statistical model (Figure 2-12). Evaluation results presented in Section 2.5 indicate that significant BIASes are found in CLM results for total cloud cover and relative humidity. Bias correction of CLM output seems a promising approach for obtaining better results from the statistical model for present climate.

The UHI climatology was determined for every month of the year by Hoffmann et al. (2012). Therefore, the monthly PDFs of relative humidity and total cloud cover are bias corrected. In this example, a bias correction is recommended if the median value of the HRP is below 0.95 for comparison of model results with both observation based datasets available for relative humidity and total cloud cover (ERA-40 and ROD). With this criterion it is made sure not to bias correct RCM results with differences between simulated and observed percentiles that are within the allowed deviation.

The ERA-40 reanalysis data have been used as a reference dataset for the derivation of the bias correction. The statistical bias correction method which we apply is described in Piani et al. (2010a). Instead of the gamma distribution used for precipitation by Piani et al. (2010a), a beta distribution is fitted to the PDFs of daily data from ERA-40 and CLM. The beta distribution is the theoretical PDF that is best suited to fit the empirical PDFs of total cloud cover and relative humidity (Wilks, 1995). The domain of definition of the beta distribution between 0 and 1 helps to assure that corrected total cloud cover and relative humidity are in the range between 0% and 100%.
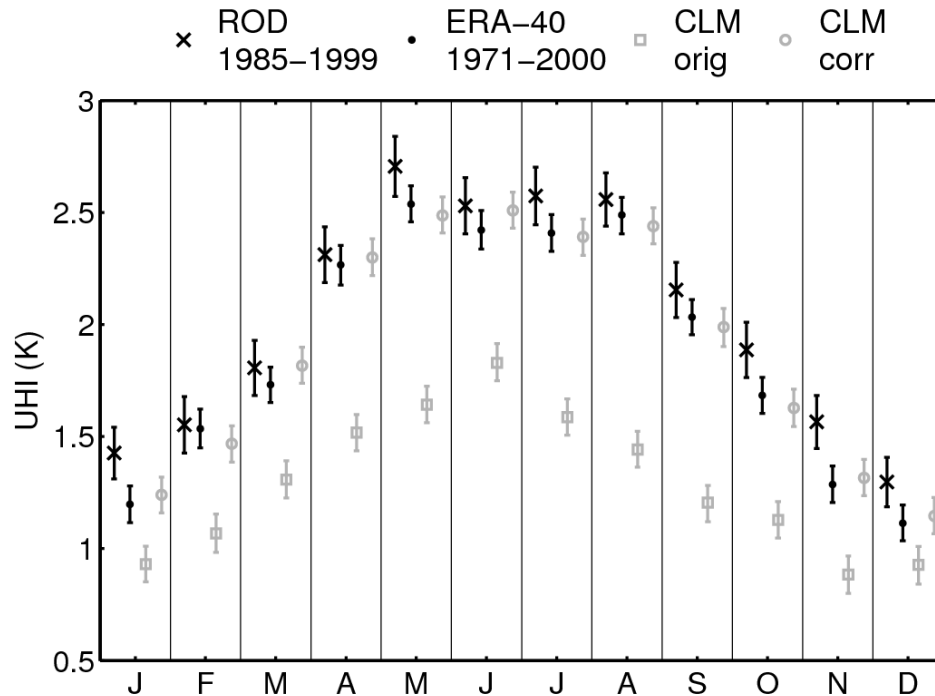
Figure 2-12: Climatological annual cycle of the urban heat island (UHI) of Hamburg calculated with the statistical model described in Hoffmann et al. (2012). In black: statistical model driven with routine observation data (ROD) (crosses) and ERA-40 reanalysis data (dots). In gray: statistical model driven with original (squares) and with bias corrected (circles) CLM data for 1971-2000.

The model output does not agree exactly with observations after the bias correction, because the theoretical PDFs fitted to the data do not exactly match the empirical PDFs. Therefore, an important question is whether the bias correction really has improved the data. This is quantified by the HRP. The HRP values for relative humidity and for total cloud cover before and after the bias correction are displayed in Table 2-3 and Table 2-4. After the bias correction, the HRP is above or equal to 0.95 for every month of the year for both meteorological variables. This indicates that bias correction sufficiently improves the CLM output. A further correction of the data is not necessary, because at least 95% of the percentiles are within the allowed deviation after bias correction. Unrealistic jumps in the time series of bias-corrected data might appear, because the correction employed is different for every month of the year (Piani et al., 2010b). We decided not to apply special transition functions to remove month-to-month jumps in the bias-corrected time series because these are not important for the results obtained in Hoffmann et al. (2012).

Table 2-3: Model evaluation measure HRP for relative humidity simulated by CLM compared with the ERA-40 reanalysis data before and after bias correction.

	Jan.	Feb.	Mar.	Apr.	May	Jun.	Jul.	Aug.	Sep.	Oct.	Nov.	Dec.
Before correction	0.15	0.05	0.02	0.02	0.00	0.12	0.09	0.00	0.04	0.15	0.24	0.23
After correction	1.00	1.00	1.00	0.96	0.97	0.95	1.00	1.00	0.98	1.00	0.98	1.00

The statistical model of the UHI driven by bias-corrected CLM output (Figure 2-12) yields much better results for the UHI than those with uncorrected data. It should be noted that the climate change signals for the UHI of Hamburg do not change considerably when bias-corrected data are used (not shown). However, the bias correction presented in this section does not conserve the physical consistency of meteorological data. This is not a serious constraint for the statistical model of the UHI. However, physical inconsistencies in the bias-corrected data could lead to problems in the case of a dynamical downscaling with a complex high-resolution numerical model.

Table 2-4: Model evaluation measure HRP for total cloud cover simulated by CLM compared with the ERA-40 reanalysis data before and after bias correction.

	Jan.	Feb.	Mar.	Apr.	May	Jun.	Jul.	Aug.	Sep.	Oct.	Nov.	Dec.
Before correction	1.00	0.73	0.68	0.45	0.21	0.31	0.12	0.10	0.22	0.30	0.86	0.97
After correction	1.00	1.00	1.00	1.00	1.00	1.00	1.00	1.00	1.00	1.00	1.00	0.97

2.7 Conclusions

Air temperature, precipitation, total cloud cover, relative humidity and wind speed simulated by the GCM ECHAM5 and the RCMs CLM and REMO have been evaluated for Hamburg Metropolitan Region. All models are able to reproduce general characteristics of the climatologies. The best model performance was found for wind speed, the weakest model performance for relative humidity. Summer precipitation is underestimated by the GCM and overestimated by both RCMs. Winter precipitation is simulated well; it lies between corrected and uncorrected precipitation data. The PDFs of air temperature are generally well simulated, with the exception of the maximum in the PDF at 0 °C in the RCM data used in the present study, but removed in the more recent versions of the RCMs. The RCM results mostly agree better with observation based data than do the results of the forcing GCM. Thus, they improve the GCM result and provide additional value. However, the improvement is not found for all seasons and

all meteorological variables. One example is relative humidity in JJA.

Evaluation measures can help to evaluate the regional climate models in an objective manner. The newly introduced Hit-Rate of the percentiles (HRP) is more selective than the Skill-Score (SSC), but also more sensitive towards climate variability. HRP can be used to decide if bias correction can be recommended from the viewpoint of model evaluation. Whether bias correction is useful depends on the application. Furthermore, the evaluation measures can be used for evaluation of the bias correction itself. Evaluation of different realisations of simulated climate from the same climate model against themselves using HRP indicates that the issue of long-term climate variability has no large impact on evaluation results. However, when focussing on the detection of climate change signals, the issue of long-term climate variability can be expected to be larger.

Finally, it has to be mentioned that the climate model evaluation presented in this chapter is based on the evaluation of the statistics of time series and is done from the viewpoint of a climate model data user. A more detailed analysis of the representation of physical processes or of single weather types that occur might be a promising model evaluation strategy from the viewpoint of a climate model developer to improve the skill of the model.

3 Impact of local adaptation measures and regional climate change on perceived temperature

Preface

This chapter has been published by Schoetter, Robert, David Grawe, Peter Hoffmann, Peter Kirschner, Angelika Grätz and K. Heinke Schlünzen, 2013: Impact of local adaptation measures and regional climate change on perceived temperature, Meteorologische Zeitschrift, 22 (2), 117-130, DOI: 10.1127/0941-2948/2013/0381. For this thesis, the abstract has been left out, some figures are redrawn in colour and the references are summarised at the end of the thesis. Parts of Section 3.2.3 have been contributed by David Grawe. Peter Hoffmann selected the meteorological situations. Peter Kirschner prepared the data characterising the urban morphology. Angelika Grätz prepared the program for calculation of PT.

3.1 Introduction

Average summer air temperature in Hamburg Metropolitan Region is projected to increase by 2.5 K to 3.0 K for the SRES (Nakicenovic et al., 2000) A1B and A2 scenarios and by 1.5 K to 2.0 K for the SRES B1 scenario for the period 2071-2100 compared to the reference period 1961-1990 (Daschkeit, 2011). The number of hot days per year (3 to 5 in the reference period) is projected to increase by 3 to 12 days per year in future climate. Hamburg Metropolitan Region should therefore adapt to these climate changes.

Adaptation measures to climate change are developed in the framework of the project KLIMZUG-NORD. One of the goals is the optimisation of human thermal comfort. The perceived temperature (PT) (Jendritzky et al., 2000; Staiger et al., 2011) is a physically based measure for the quantification of human thermal comfort based on a heat budget of the human body. The goal of this study is to quantify the sensitivity of PT on air temperature, water vapour pressure, wind speed, mean radiant temperature, street canyon width and building height, using the city of Hamburg as an example. Meteorological input data for PT are provided by integration of the mesoscale atmospheric model METRAS (Schlünzen, 1990; Schlünzen et al., 2012b) at 250 m horizontal resolution. Modification of shortwave and longwave radiation due to buildings is calculated offline with the radiation modification routines from the "Building Effect Parameterisation" (BEP; Martilli et al., 2002). The sensitivities of PT are obtained by automatic differentiation of the program that calculates PT and the radiation modification routines from BEP using the "Transformation of Algorithms in Fortran" precompiler TAF (Giering and Kaminski, 1998; Giering et al., 2005).

Our motivation is twofold. The sensitivities indicate how the target variable PT can be influenced most effectively. This helps to estimate the impact of adaptation measures at low computational costs. Furthermore, the sensitivities indicate how accurate the different input variables need to be known in order to achieve a desired accuracy of the target variable PT. This might help to better deal with uncertainties in climate change projections as well as biases in climate model output (Chapter 2; Schoetter et al., 2012).

This chapter is structured as follows: In Section 3.2, the methodology is described. Results for the sensitivities of PT are shown in Section 3.3 and discussed in Section 3.4. Conclusions are drawn in Section 3.5.

3.2   Methodology

3.2.1   Perceived temperature PT

There exist a variety of measures for the quantification of human thermal comfort (Jendritzky et al., 2000; Blazejczyk et al., 2011). Both the "Physiological Equivalent Temperature" PET (Höppe, 1999) and the "Perceived Temperature" PT (Jendritzky et al., 2000; Staiger et al., 2011) are based on a heat budget of a reference human body. PET is designed for indoor office-work conditions with fixed clothing whereas PT is designed for staying outdoors and considers the adjustment of clothing by the reference person within certain limits. Mayer et al. (2008) used PET for quantification of thermal comfort in a street canyon during a hot summer day. Kim et al. (2009) used PT for quantification of human thermal comfort in Korea for long-term records of routine observation data.

In this study, the focus is set on PT, because outdoor conditions shall be assessed. PT is the temperature that a reference person would perceive in a reference environment with a mean radiant temperature equal to air temperature, a wind speed of 0.1 m/s and in the case of warm/humid conditions a relative humidity of 50%. The German Meteorological Service (DWD) developed a program for the calculation of PT (DWD, 2011; personal communication). Required meteorological input data are 2 m air temperature, 2 m water vapour pressure, 1 m wind speed and the mean radiant temperature. The mean radiant temperature for an upright standing person is calculated by the program from the total incoming shortwave radiation, the incoming longwave radiation, the longwave emission of the surface and the elevation angle of the sun. The incoming longwave radiation and the longwave emission are equally weighted.

3.2.2 METRAS model

The meteorological input data required for PT are obtained by integration of the mesoscale atmospheric model METRAS (Schlünzen, 1990; Schlünzen et al., 2012b). A total of 13 simulations have been carried out in the framework of a statistical-dynamical downscaling for the nocturnal UHI of Hamburg (Hoffmann, 2012). These 13 situations have been chosen by Hoffmann and Schlünzen (2012) in order to represent a strong UHI for Hamburg resulting from different weather patterns. All selected situations represent the summer season.

A nested model system is applied. METRAS is integrated at 4 km horizontal resolution for a domain covering Northern Germany and parts of the North Sea, the Baltic Sea and Southern Scandinavia. ECMWF analysis data at T799 (about 25 km horizontal resolution; ECMWF, 2009b; ECMWF, 2010) are used for lateral forcing. In the next nesting step, the simulations are downscaled to 1 km horizontal resolution for a domain covering Hamburg Metropolitan Region. The simulations have been carried out and evaluated against DWD routine observations by Hoffmann (2012). The results from Hoffmann (2012) have been used in the framework of the present study to force a 250 m horizontal resolution simulation for a domain covering the city of Hamburg.

In METRAS, the urban areas are parameterised by higher roughness, lower water availability, increased thermal conductivity and increased thermal diffusivity compared to rural areas. However, no urban canopy scheme is used that would take into account the influence of buildings on the meteorological fields at higher model levels or the modification of radiation by shading and radiation trapping. Simulated air temperature, water vapour pressure and wind speed in 10 m above ground are used directly. A calculation of these variables in 2 m above ground from the simulated variables in 10 m above ground using Monin-Obukhov Similarity Theory (MOST, e.g. Garratt, 1992) is not made here, because the MOST is not applicable in the street canyons that are the focus of the present study.

The total incoming shortwave radiation, the incoming longwave radiation and the longwave emission simulated by METRAS are used as input for the Building Effect Parameterisation.

3.2.3 Building Effect Parameterisation BEP

The "Building Effect Parameterisation" (BEP) (Martilli et al., 2002) has been developed in order to parameterise the effect of buildings on the grid cell averaged variables simulated by a mesoscale atmospheric model. The urban morphology is described by a probability distribution of building heights and building widths, as well as of street canyons with their orientation and specific width. Only the radiation modification routines from BEP are used in the present study. They allow for calculation of the modification of the shortwave radiation due to shading and

30

reflection by the buildings as well as the modification of the longwave radiation due to radiative trapping. The corrections to ensure energy conservation in the shading calculation introduced by Schubert et al. (2012) have been implemented. In contrast to Grawe et al. (2012), BEP is not implemented into METRAS in the current study but used offline for the calculation of the grid cell averaged effect of shading and radiation trapping due to buildings.

Data that characterises the urban morphology are required as input for BEP. For the city of Hamburg, datasets of building heights, street directions and street canyon widths have been created based on two datasets: the digital town map depicting the outlines of the structures ("Digitale Stadtgrundkarte"; LGV, 2009) and the sealing data ("Versiegelungsdaten Hamburg"; BSU, 2008). Street directions have been derived directly from shape information of each individual street segment. Street canyon widths have been obtained for each street segment from the respective building outlines. Direct information on the building heights has not been available. However, available data includes the number of floors for each building (or parts thereof for complex buildings), the type of building (e.g. industrial, commercial or residential) and the period of construction. Based on this information, a height has been estimated consistently for each building. All BEP input data have been converted to a 250 m raster, from which statistical information for each METRAS grid cell has been calculated.

The vertical resolution of the "urban grid" in BEP is set to 5 m. The fraction of buildings with heights in the bins 2.5 m to 7.5 m up to 67.5 m to 72.5 m is calculated. All buildings higher than 70 m are treated as having a height of 70 m. Four street direction classes are considered: street directions from 0° to 22.5° and from 157.5° to 179° (0° assumed as direction), from 22.5° to 67.5° (45° assumed as direction), from 67.5° to 112.5° (90° assumed as direction) and from 112.5° to 157.5° (135° assumed as direction). Again, 5 m bins are used for the width of the street canyons: 2.5 m to 7.5 m and so on. The most frequent street canyon width is determined for every street direction class at each grid point. The values for the albedo of the wall and the ground are set to 0.18 and 0.09 respectively, consistent with the values used in METRAS for the surface cover classes "buildings" and "asphalt" (Schlünzen et al., 2012a). The emissivity of the wall and the ground is set to 0.95 consistent with the emissivity used by METRAS. The temperature of the walls and the ground is set to the skin surface temperature calculated by METRAS.

The incoming shortwave radiation as well as the incoming longwave radiation calculated by METRAS are modified by the radiation modification routines of BEP at each grid cell with data characterising urban morphology. With this methodology, the average conditions within the street canyons in the respective METRAS grid cell are accounted for. Modification of radiation due to urban canopy vegetation (e.g. street trees) is neglected here.

3.2.4 Transformation of Algorithms in Fortran TAF

The "Transformation of Algorithms in Fortran" precompiler TAF (Giering and Kaminski, 1998; Giering et al., 2005) is used to calculate the tangent linear sensitivities (partial derivatives) of PT on the input variables air temperature, water vapour pressure, wind speed, mean radiant temperature and the width of the street canyons. An adjoint version of the code has been derived with relative differences between adjoint sensitivities and tangent linear sensitivities below 10^{-4}. However, the calculation of the tangent linear sensitivities turned out to be faster than the calculation of the adjoint sensitivities due to the structure of the code calculating PT grid point per grid point.

The tangent linear sensitivities are the partial derivatives of PT with respect to its input variables. For the interpretation of the results, it is important to note that the partial derivatives themselves depend on the input variables, meaning the actual meteorological conditions. For example, the sensitivity of PT on air temperature depends on air temperature, wind speed, water vapour pressure and mean radiant temperature. The sensitivities are therefore only valid for the particular meteorological conditions for which they have been calculated.

The sensitivities of PT obtained from automatic differentiation are validated by comparison with results obtained when approximating the partial derivatives with finite differences. The percentage of grid points with an absolute value of the relative difference between the sensitivity obtained from automatic differentiation and the sensitivity obtained from finite differences smaller than 0.05 is shown in Table 3-1. Larger deviations between the sensitivities are found for a small percentage of the grid points. The reason is the non-differentiability of the code calculating PT, because the control flow (e.g. "if-statements") depends on the input variables. Therefore, a relatively small variation of the input variables can lead to a relatively large difference in PT; an unrealistic sensitivity is then obtained from finite differences. The sensitivities obtained from automatic differentiation are in these cases physically more reasonable than the sensitivities approximated with finite differences. The PT code could be rendered differentiable by slight modifications of the solution, but this has not been made here, because we wanted to keep PT in its original form.

Table 3-1: Percentage of grid points with an absolute value of the relative difference between the sensitivity obtained from automatic differentiation and the sensitivity obtained from finite differences below 0.05. The increment used for the calculation of the sensitivities from finite differences is also shown.

variable	air temperature	water vapour pressure	wind speed	mean radiant temperature	street canyon width
increment	0.01 K	0.1 hPa	0.01 m/s	0.1 K	0.5 m
percentage	99.2%	97.6%	99.0%	99.1%	94.2%

It has to be pointed out that the sensitivities calculated in the present study do not account for complex physical interactions, because only the PT program and the radiation modification routines from BEP, but not the METRAS code are subject to automatic differentiation. For example, a change of the street canyon width would not act on PT by the modification of radiation only but also by a change in the wind field and the other meteorological variables influencing PT. This effect is not considered in the present study. The advantage of the presented partial derivatives is that they can be computed with very low computational costs compared to a full integration of the mesoscale model METRAS. This would be required for consideration of all implemented physical processes. Another advantage is that the chosen approach allows a clear distinction between the impacts of changes in different influential factors.

3.3 Results

Detailed results are shown for the simulated meteorological variables, PT and its sensitivities in the Sections 3.3.1 to 3.3.4. The selected day is 10 June 2007. The meteorological situation is determined according to Hoffmann and Schlünzen (2012) by a "weak east-west gradient with a ridge to the east, advection of warm air masses from south-east". METRAS is initialised for 8 June 2007 at 22:00 local time. The analysis is carried out for the time periods 10 June 2007 10:00 to 16:00 local time (NOON) and 21:00 to 24:00 local time (LATE). The LATE time period starts after sunset. METRAS output is written every half hour. The results are thus averaged over 13 and 7 output times for NOON and LATE, respectively. PT and its sensitivities are first calculated separately for each output time and then averaged over NOON and LATE. In Section 3.3.5, the results are briefly compared with the results from the other 12 meteorological situations selected by Hoffmann (2012).

3.3.1 Model domain

The characteristics of the model domain including the city of Hamburg and its surroundings are presented. The orography (Figure 3-1a) is characterised by the valley of the river Elbe (at sea level height or slightly below sea level height) and the surrounding "Geest", low hills formed by glaciers during the ice ages. In the southwest of the domain, the hills called "Harburger Berge" reach heights of up to 150 m above sea level. A summarised surface cover classification for the domain is shown in Figure 3-1b. The original 36 surface cover classes used in METRAS are mapped for presentation purposes into 4 surface cover groups (water, cropland/grassland, forest, sealed surfaces). The most abundant of these groups is displayed for each grid point. The main water bodies in the domain are the river Elbe with a width of more than 1 km in the western part of the domain and the lake Außenalster within the city. Outside the city, the valley of the river Elbe is mainly covered by grassland, cropland and orchards. Cropland and forests dominate the other surroundings of the city of Hamburg. The aspect ratio of the street canyons is shown in

Figure 3-2. It is defined as the average building height divided by the most frequent width of the street canyons. The aspect ratio is highest (between 1 and 2) near the centre of the city, because the buildings are relatively high in this region, but also in the urban quarter Blankenese in the western part of Hamburg, where the street canyons are relatively narrow. No data characterising urban morphology is available outside the city of Hamburg. The domain shown in the figures is smaller than the domain simulated with METRAS at 250 m horizontal resolution. At least 20 grid points (5 km) have been omitted at each of the lateral boundaries.

(a)   (b)
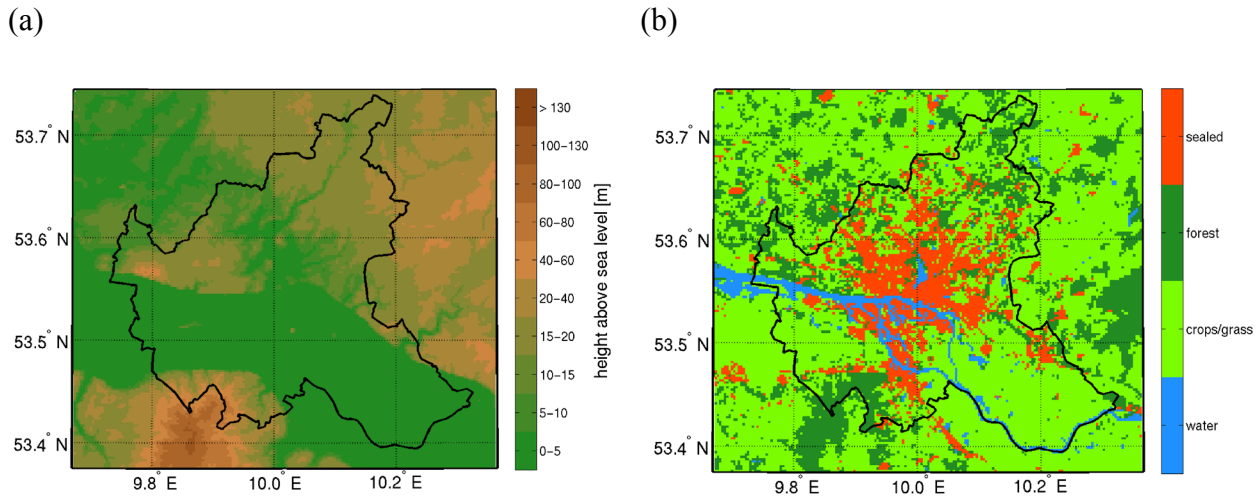
Figure 3-1: (a) Height above sea level for the domain of investigation and (b) simple surface cover classification. Note that a more detailed surface cover classification with a total number of 36 surface cover classes is used by METRAS. The black contour line depicts the border of the federal state Hamburg.
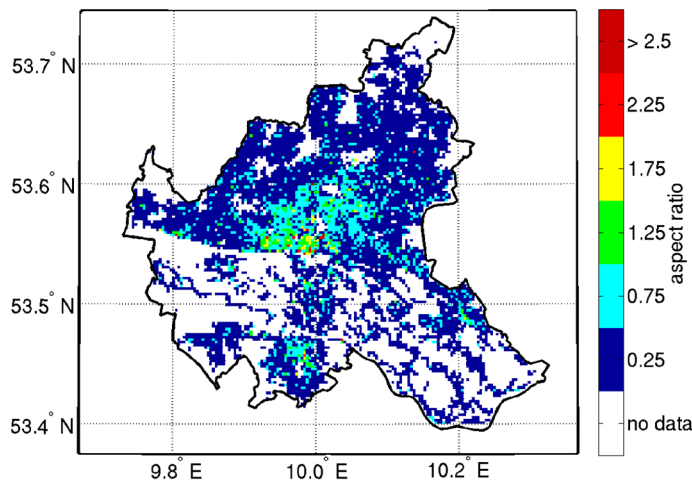
Figure 3-2: Aspect ratio of the street canyons defined as the average building height divided by the most frequent width of the street canyons in the respective METRAS grid cell (250 m x 250 m). Note that all grid points with no data on urban morphology are in white.

34

3.3.2 Simulated meteorological variables

In this section, the simulated meteorological variables, which influence PT the most, are shown and the most important features are discussed. All results are displayed as average over all output times separately for NOON and LATE.

The horizontal cross section of air temperature in 10 m above ground is displayed in Figure 3-3. For NOON (Figure 3-3a), air temperature is lowest in the region of "Harburger Berge" and over the large water surfaces in the western part of the domain. Air temperature is higher within the city of Hamburg than in the eastern surroundings of the city covered mainly by forests and cropland. This is due to the high evaporation over these surface cover classes. For LATE (Figure 3-3b), air temperature is higher within the city and the harbour area than in the surrounding rural areas. Air temperature is noticeably lower in the valley of the river Alster in the north of the city compared to the city centre.
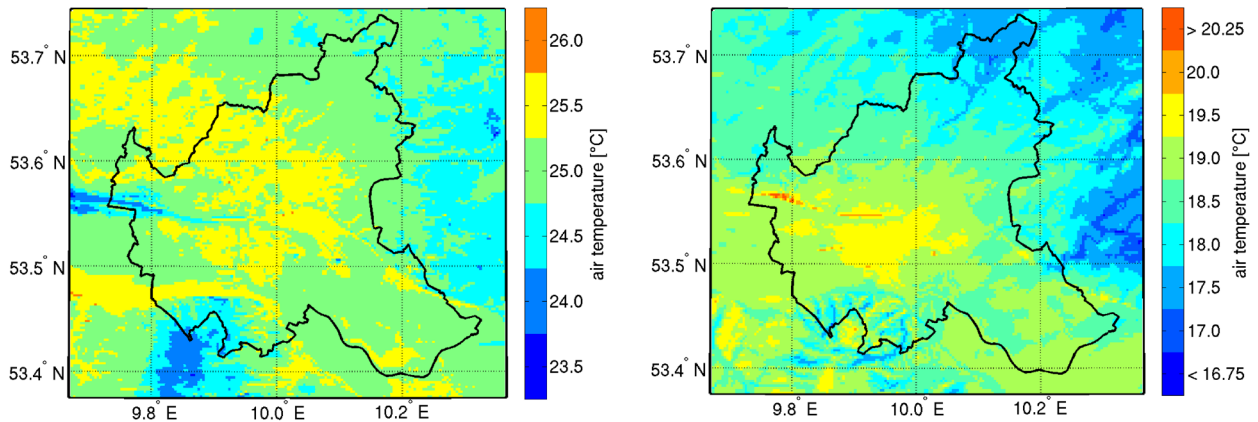
Figure 3-3: Horizontal cross section of simulated air temperature in 10 m above ground. (a): average over NOON, (b): average over LATE. Note the different colour scales.

The horizontal cross section of water vapour pressure in 10 m above ground is displayed in Figure 3-4. Water vapour pressure is highest over the forested areas for NOON (Figure 3-4a) and LATE (Figure 3-4b) and at least for NOON slightly lower in the urban areas than in the rural areas.

The horizontal cross section of wind speed in 10 m above ground is displayed in Figure 3-5. For NOON (Figure 3-5a), the lowest wind speeds appear in areas with relatively high roughness (forests and urban areas) and the highest wind speeds in areas with relatively low roughness (water, grassland and cropland). For LATE, the wind speeds are particularly low in the valley of the river Elbe (Figure 3-5b).

(a)   (b)
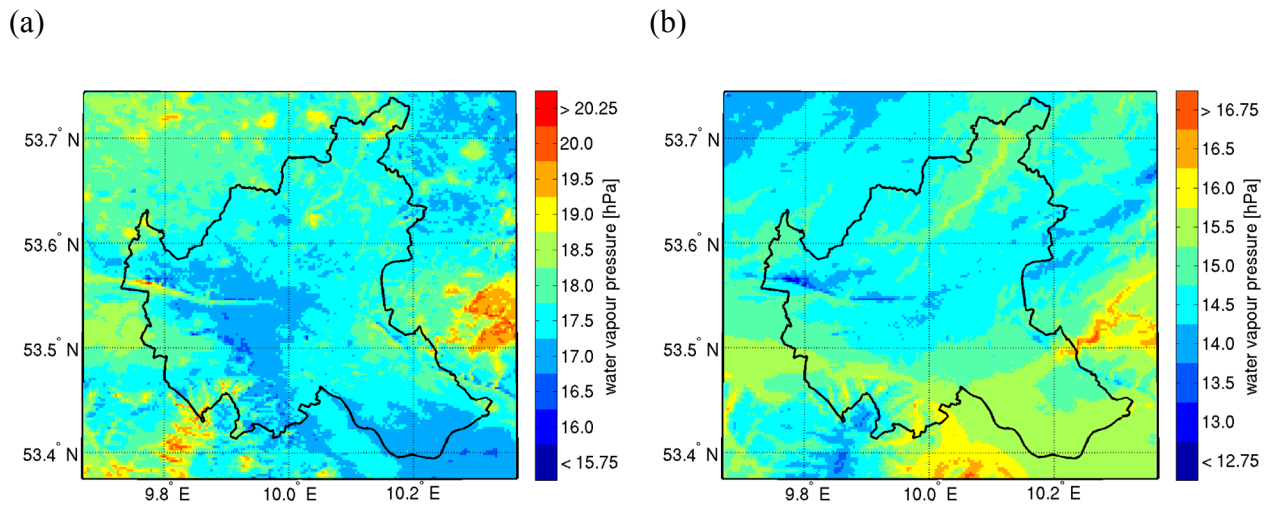
Figure 3-4: Horizontal cross section of simulated water vapour pressure in 10 m above ground. (a): average over NOON, (b): average over LATE. Note the different colour scales.

(a)   (b)
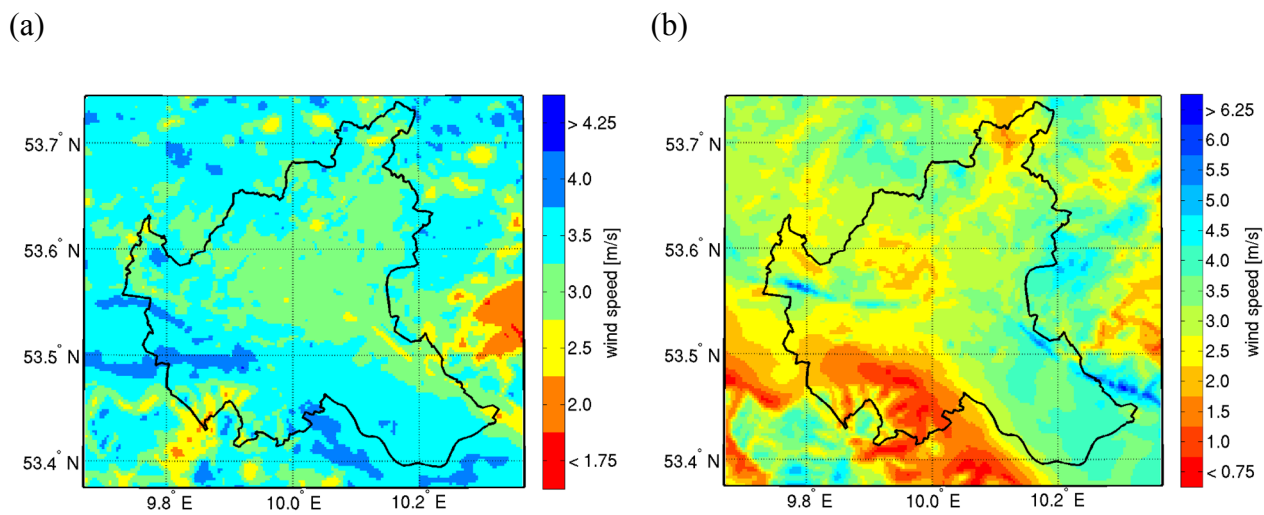
Figure 3-5: Horizontal cross section of simulated wind speed in 10 m above ground. (a): average over NOON, (b): average over LATE. Note the different colour scales.

For NOON, the emission of longwave radiation from the surface exhibits large spatial differences (Figure 3-6a). This is due to large differences in the skin surface temperature of different surface cover classes. The highest values are simulated in the dense urban quarters and especially for the large streets, airports and railroad tracks. The lowest values are simulated for the water surfaces and the forests. The gradients of the longwave emission are smaller for LATE (Figure 3-6b). Again, the highest values are simulated in the dense urban quarters, but not for the large streets, airports and railroad tracks, whose skin surface temperature has decreased after sunset.

The incoming shortwave radiation is zero for LATE (after sunset) and very homogenous for NOON, because no clouds form within the domain (not shown).

(a)   (b)
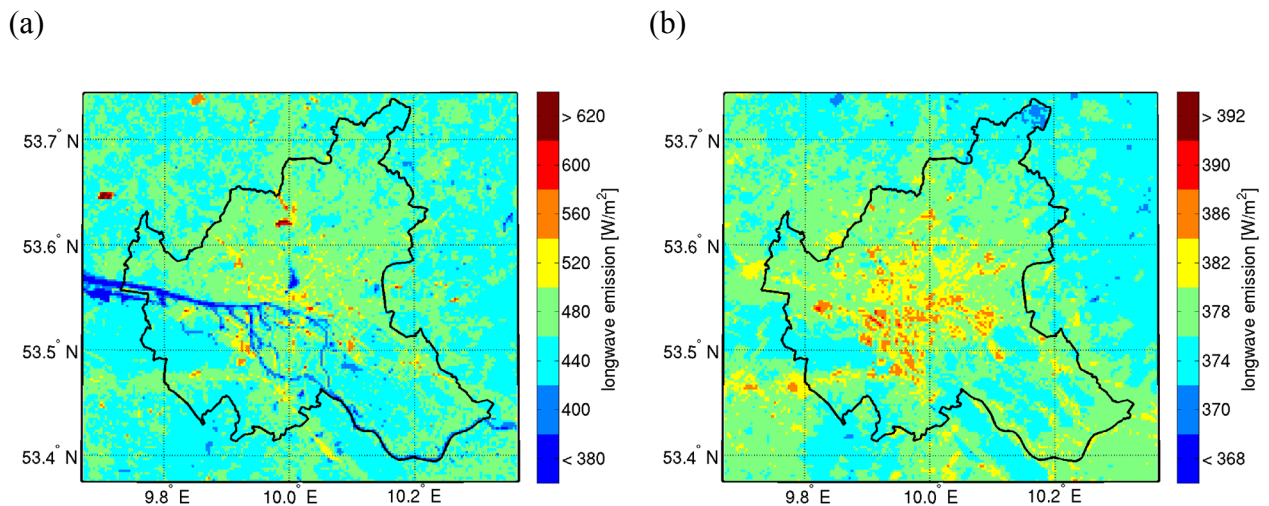
Figure 3-6: Simulated emission of longwave radiation from the surface. (a): average over NOON, (b): average over LATE. Note the different colour scales.

The mean radiant temperature calculated by the PT program after the radiation modification from BEP is displayed in Figure 3-7. For NOON (Figure 3-7a), the highest values are simulated at grid points with low aspect ratio of the street canyons and with high skin surface temperature. The lowest values are simulated in regions with the highest aspect ratio of the street canyons, because the shading due to the buildings reduces the incoming shortwave radiation. For LATE (Figure 3-7b), the mean radiant temperature is highest in the regions with highest aspect ratio of the street canyons, because the incoming longwave radiation is increased there due to the presence of the buildings.

(a)   (b)
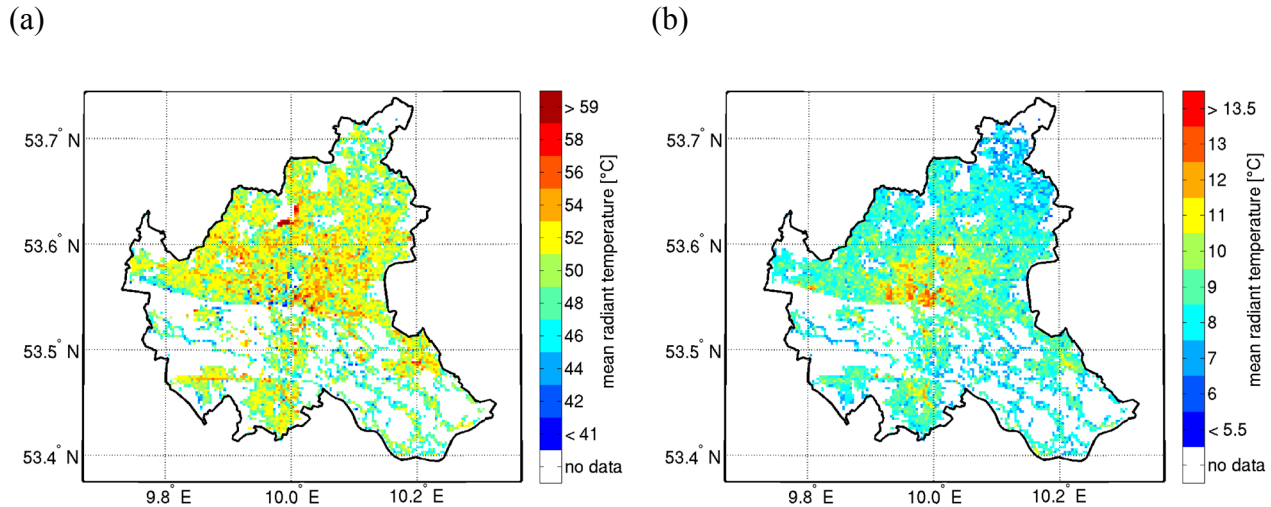
Figure 3-7: Mean radiant temperature calculated by the PT program from the total incoming shortwave radiation, the incoming longwave radiation, the longwave emission of the surface and the elevation angle of the sun. The radiation fluxes are calculated by METRAS and then modified by BEP to consider the average situation in a street canyon within each grid cell. The data are therefore only displayed at grid points with data characterising urban morphology available, the remaining grid points are in white. (a): average over NOON, (b): average over LATE. Note the different colour scales.

3.3.3   PT with original and building modified radiation fields

The spatial distribution of PT obtained when using the original radiation fields from METRAS is displayed in Figure 3-8. For NOON (Figure 3-8a), PT is in the classes "slight heat stress" and "moderate heat stress" according to the thermal sensation scale defined by Staiger et al. (2011). PT is highest in the regions with highest air temperature and highest emission of longwave radiation from the surface. For LATE (Figure 3-8b), PT is in the "comfort possible" class. The values of PT are highest in the areas with highest air temperature and lowest wind speed.

The difference between PT calculated using the radiation fields modified by BEP and PT calculated using the original radiation fields simulated by METRAS is displayed in Figure 3-9. Only the modification of longwave radiation needs to be considered for LATE (Figure 3-9b). The presence of buildings leads to an increase of PT at each grid point, because the longwave radiation from the walls is higher than the incoming longwave radiation in an open area (as it is assumed by METRAS). The differences are highest (about 0.8 K to 1.4 K) in the regions with the highest aspect ratio of the street canyons. The situation is more complex for NOON (Figure 3-9a). On the one side, the shading due to the presence of buildings reduces the incoming shortwave radiation tending to decrease PT. On the other side, the presence of buildings increases the incoming longwave radiation tending to increase PT. Results indicate that the shading effect dominates near the centre of the city: PT is reduced by up to 3.5 K if the modified radiation is

used. A similar situation is found for the regions in the vicinity of the river Elbe in the western part of the domain. Here, many streets are oriented in West-East direction following the course of the river. These are mostly affected by shading for NOON. The absolute values of the differences of PT are smaller in the other parts of the city. At some grid points, PT even increases by up to 1.5 K due to the presence of buildings. This is because the increased longwave radiation dominates over the shading.

To avoid confusion it has to be mentioned that the values shown in the Figures 3-3 to 3-6 and 3-8 are representative for the average over the whole METRAS grid cell whereas the values shown in the Figures 3-7 and 3-9 to 3-15 are only representative for the average street canyon within the METRAS grid cell.

(a)   (b)
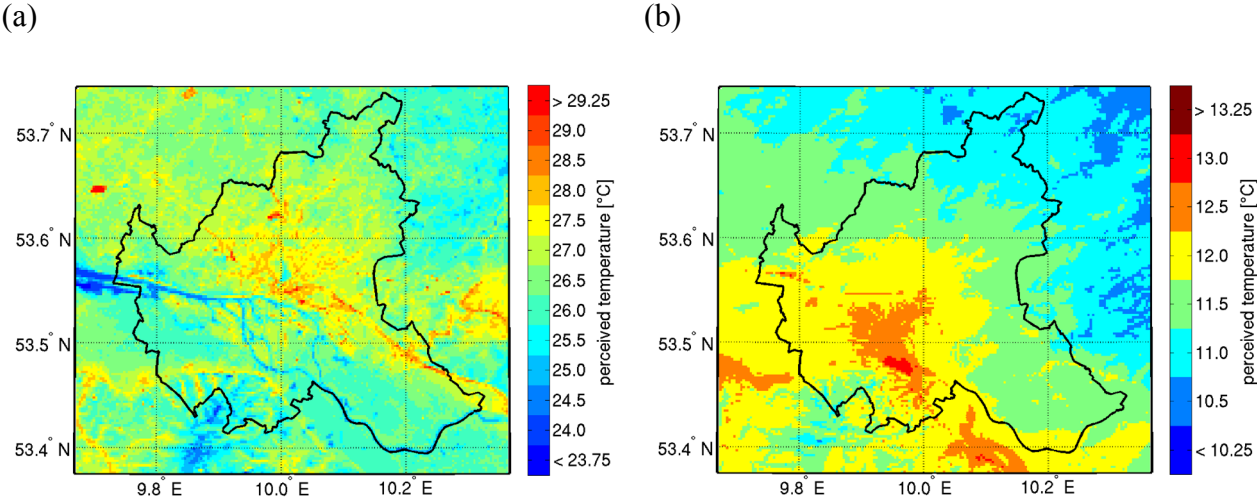
Figure 3-8: PT calculated with the original radiation fields simulated by METRAS. (a): average over NOON, (b): average over LATE. Note the different colour scales.

(a)   (b)
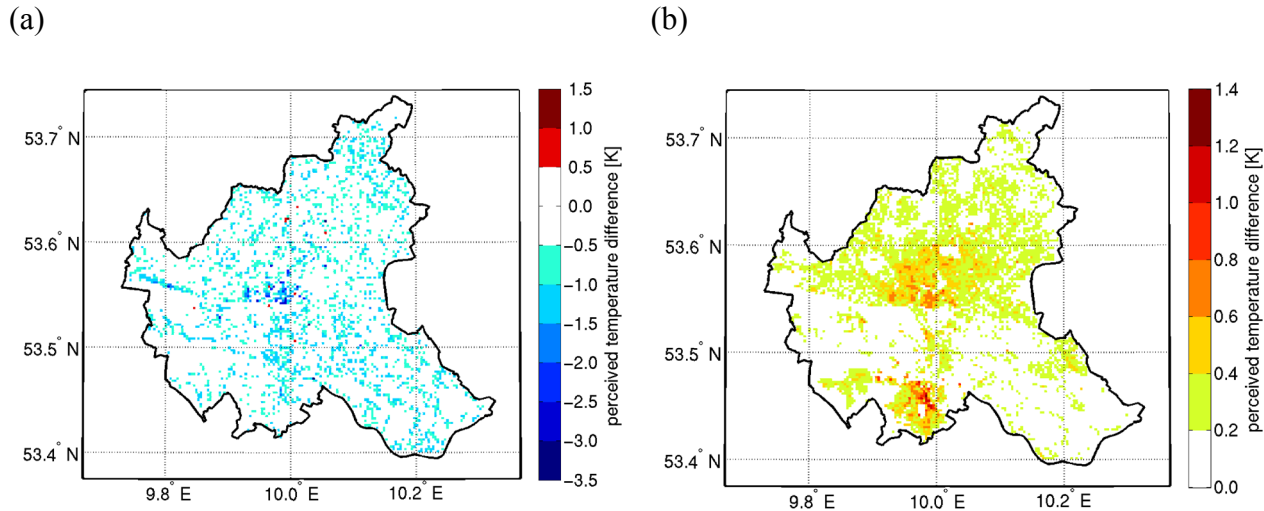
Figure 3-9: Difference between PT calculated with the radiation fields modified by BEP and PT calculated with the original radiation fields simulated by METRAS. (a): average over NOON, (b): average over LATE. Note the different colour scales.

3.3.4   Sensitivities of PT

In this section, the results for the tangent linear sensitivities (partial derivatives) of PT are presented.

The tangent linear sensitivity of PT on air temperature is displayed in Figure 3-10. The sensitivity is always positive indicating an increase of PT with increasing air temperature. The sensitivity is higher for NOON (Figure 3-10a; slight to moderate heat stress) than for LATE (Figure 3-10b; comfort possible). Spatial differences between the sensitivities are small.

The tangent linear sensitivity of PT on water vapour pressure is displayed in Figure 3-11. Again, the sensitivity is always positive. For NOON (Figure 3-11a; slight to moderate heat stress), the sensitivity of PT on water vapour pressure is higher than for LATE (Figure 3-11b; comfort possible). Spatial differences between the sensitivities are small.

40
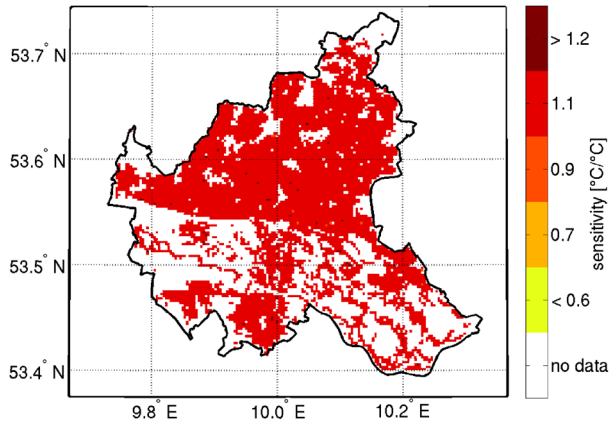
(a)   (b)
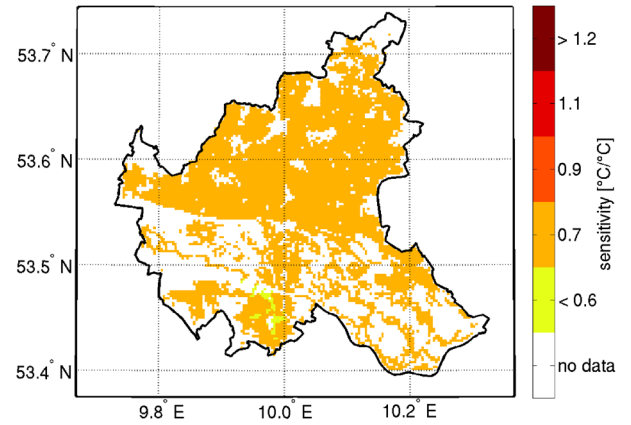
Figure 3-10: Tangent linear sensitivity of PT on air temperature. (a): average over NOON, (b): average
over LATE.
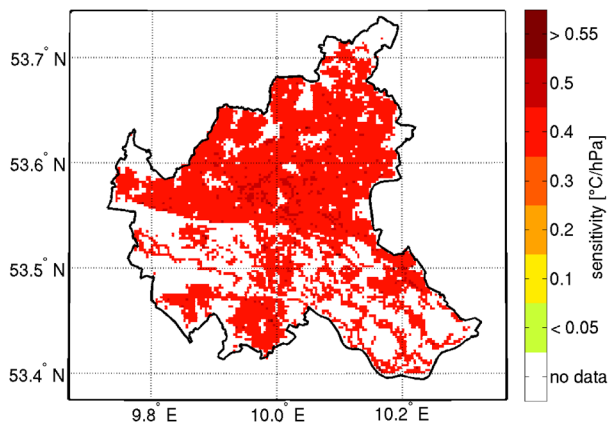
(a)   (b)
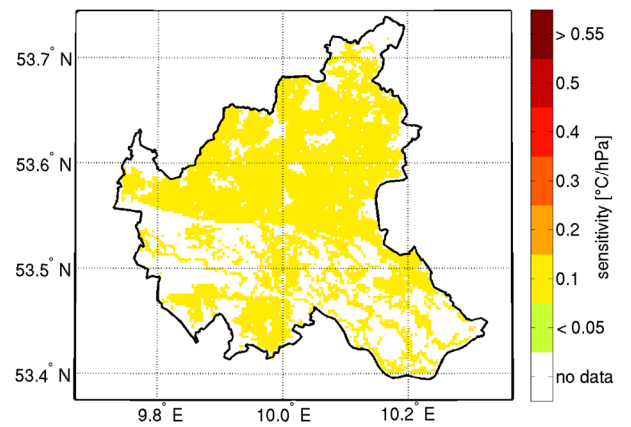
Figure 3-11: Tangent linear sensitivity of PT on water vapour pressure. (a): average over NOON, (b):
average over LATE.

The tangent linear sensitivity of PT on wind speed is displayed in Figure 3-12. The sensitivity is negative indicating a decrease of PT with increasing wind speed. For NOON (Figure 3-12a; slight to moderate heat stress), the absolute values of the sensitivities are mostly larger than for LATE (Figure 3-12b; comfort possible). For LATE, the absolute values of the sensitivities are relatively small in regions with high wind speeds and relatively high in regions with low wind speeds (Figure 3-5b).

(a)   (b)
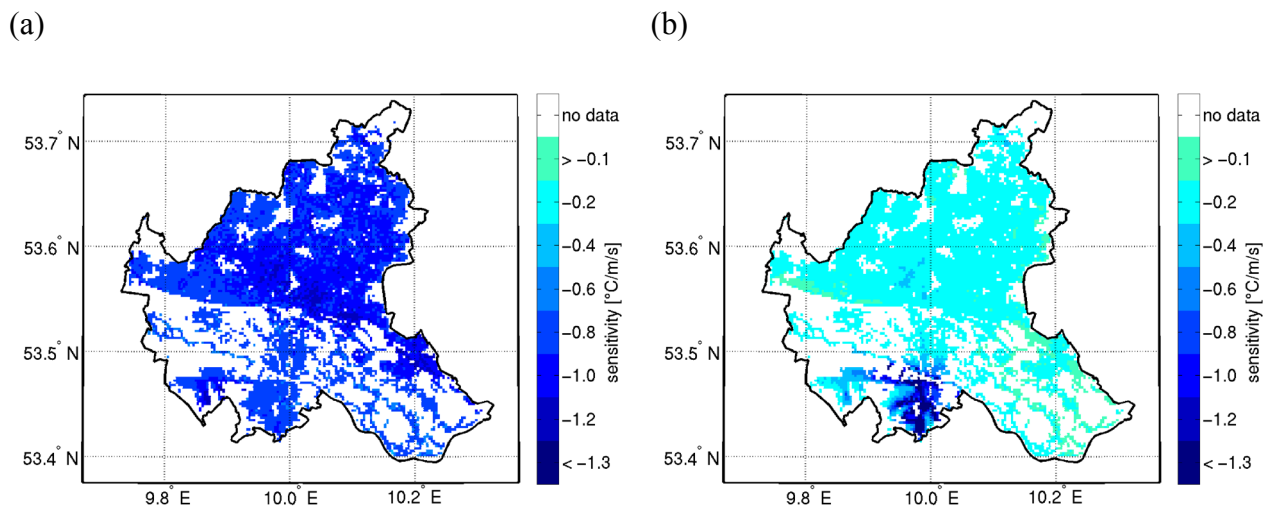
Figure 3-12: Tangent linear sensitivity of PT on wind speed. (a): average over NOON, (b): average over LATE.

The tangent linear sensitivity of PT on mean radiant temperature is displayed in Figure 3-13. The sensitivity is higher for NOON (Figure 3-13a) than for LATE (Figure 3-13b). This indicates a higher influence of a change in the mean radiant temperature, if PT is in the range of slight to moderate heat stress compared to situations with comfort possible. For NOON, the sensitivity of PT on mean radiant temperature (0.25 °C/°C to 0.35 °C/°C) is about a factor of four lower than the sensitivity of PT on air temperature. However, one has to keep in mind the higher spatial variability of the mean radiant temperature (Figure 3-7a) compared with the spatial variability of air temperature (Figure 3-3a). Also, the mean radiant temperature can be influenced more efficiently by adaptation measures (e.g. shading during the day) than air temperature.
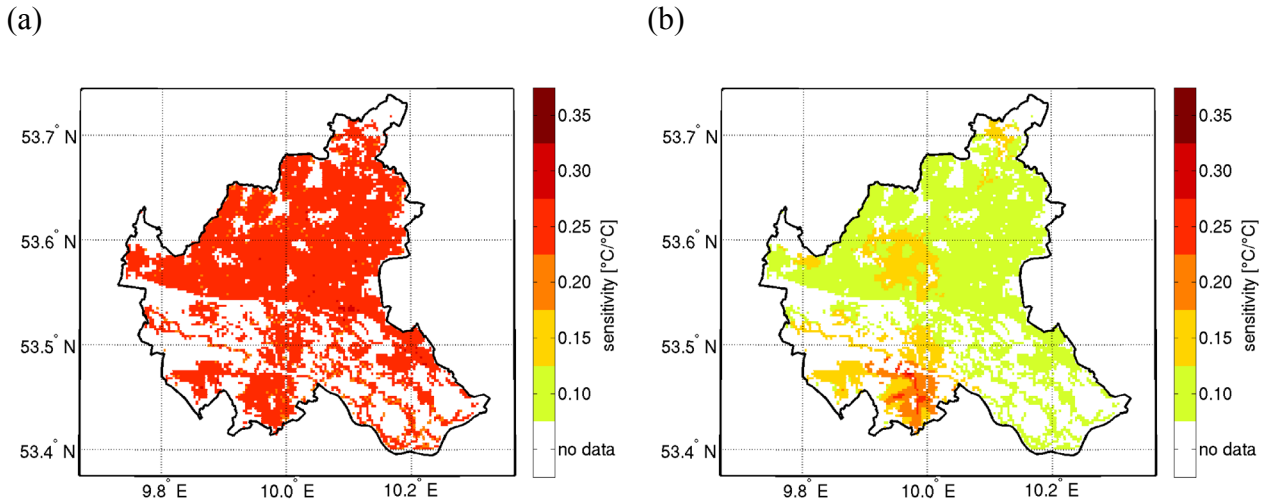
Figure 3-13: Tangent linear sensitivity of PT on mean radiant temperature. (a): average over NOON, (b): average over LATE.

The tangent linear sensitivity of PT on the street canyon width is displayed in Figure 3-14. The sensitivity is negative for LATE (Figure 3-14b, no shortwave radiation), because a broadening of the street canyons leads to a reduction of the incoming longwave radiation at the surface. The absolute values of the sensitivities are small (0 °C/m to -0.30 °C/m). Only at a few grid points the sensitivities are lower than -0.1 °C/m. This result is not surprising, because the total effect of the buildings on PT is below 1.4 K for the given meteorological situation (Figure 3-9b). The situation is more complex for NOON (Figure 3-14a), because a broadening of the street canyons leads to both an increase of the incoming shortwave radiation but also to a reduction of the incoming longwave radiation. The shading effect dominates for the street canyons with aspect ratios above 0.5. Here, positive sensitivities of up to 0.8 K/m are found. Slightly negative or slightly positive sensitivities appear in the other street canyons.

(a)   (b)
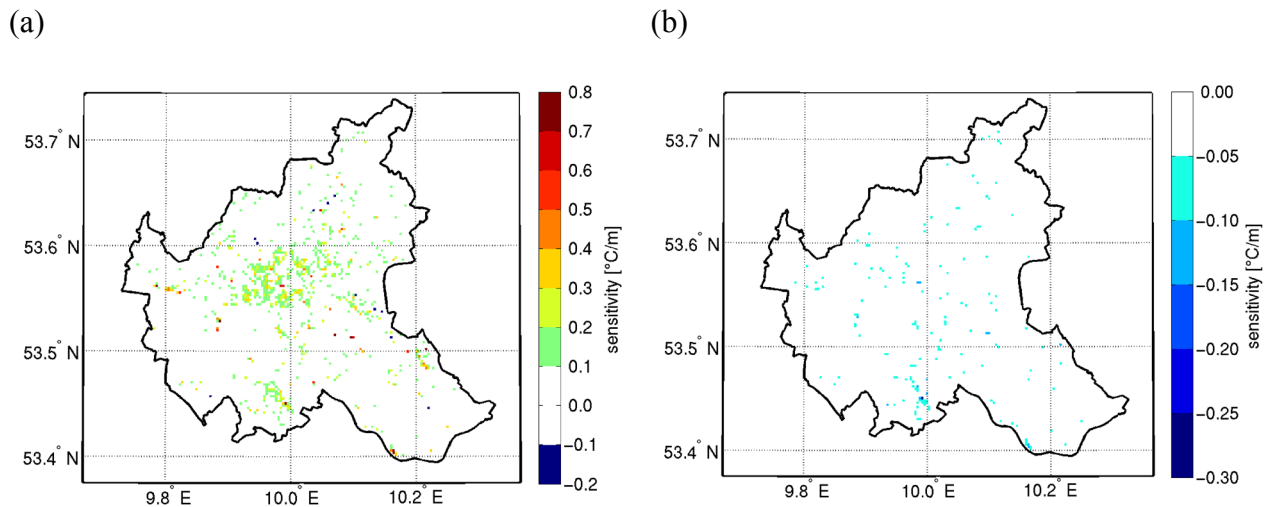
Figure 3-14: Tangent linear sensitivity of PT on street canyon width. (a): average over NOON, (b): average over LATE. Note the different colour scales.

The difference of PT between a scenario with each building 5 m higher and PT obtained with the original building heights is displayed in Figure 3-15. The difference of PT is positive for LATE (Figure 3-15b), because higher buildings lead to an increase of the incoming longwave radiation. The differences are highest (up to 0.4 K) in areas with relatively low buildings. If the buildings are low, an increase of the building height by 5 m has more impact than if the buildings are high. For NOON (Figure 3-15a), higher buildings lead to a considerable decrease of PT of up to 2.4 K mainly in areas near the centre of the city. PT can increase by up to 1.6 K after an increase of the building heights by 5 m in areas mainly located in the outer parts of the city.

The difference of PT obtained for the scenario with building heights increased by 5 m is scattered against the aspect ratio of the street canyons in Figure 3-16 to investigate the impact of building height more in detail. For NOON (Figure 3-16a), a positive difference of PT is found for all street canyons with an aspect ratio below 0.5, whereas the difference of PT is negative for street canyons with an aspect ratio above 0.5. The lower the building heights, the more the difference of PT depends on the aspect ratio. The largest positive and the largest negative differences are obtained for buildings that are lower than 10 m. The differences of PT are only slightly negative (0 K to -0.5 K) for buildings higher than 20 m.

These results are highly dependent on the elevation angle of the sun. Therefore, different results would appear in other seasons, because then the street canyons with high aspect ratio are nearly totally shaded. Higher buildings would not lead to more shading in this case. The complexity of the results depicts the challenge to create a climatology of PT and its sensitivities in urban areas.

For LATE (Figure 3-16b), the largest increases of PT are obtained for the grid points with

relatively low aspect ratio. If the aspect ratio is high, an increase of the building heights has only little impact on PT.

(a)   (b)
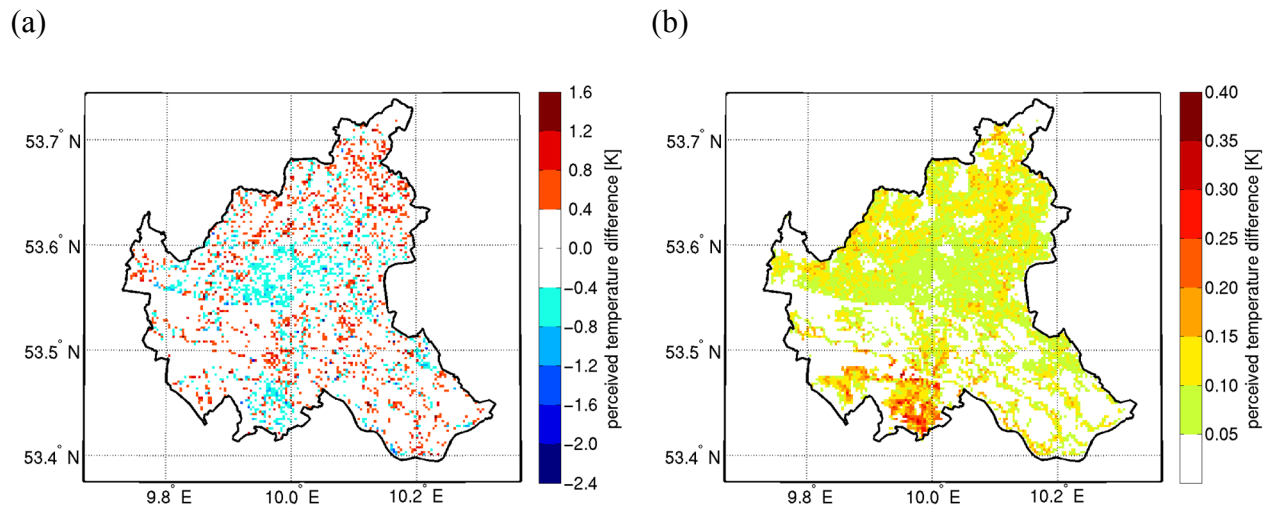
Figure 3-15: Difference between PT obtained when increasing each building height by 5 m and PT obtained with the original building heights. (a): average over NOON, (b): average over LATE. Note the different colour scales.

(a)   (b)
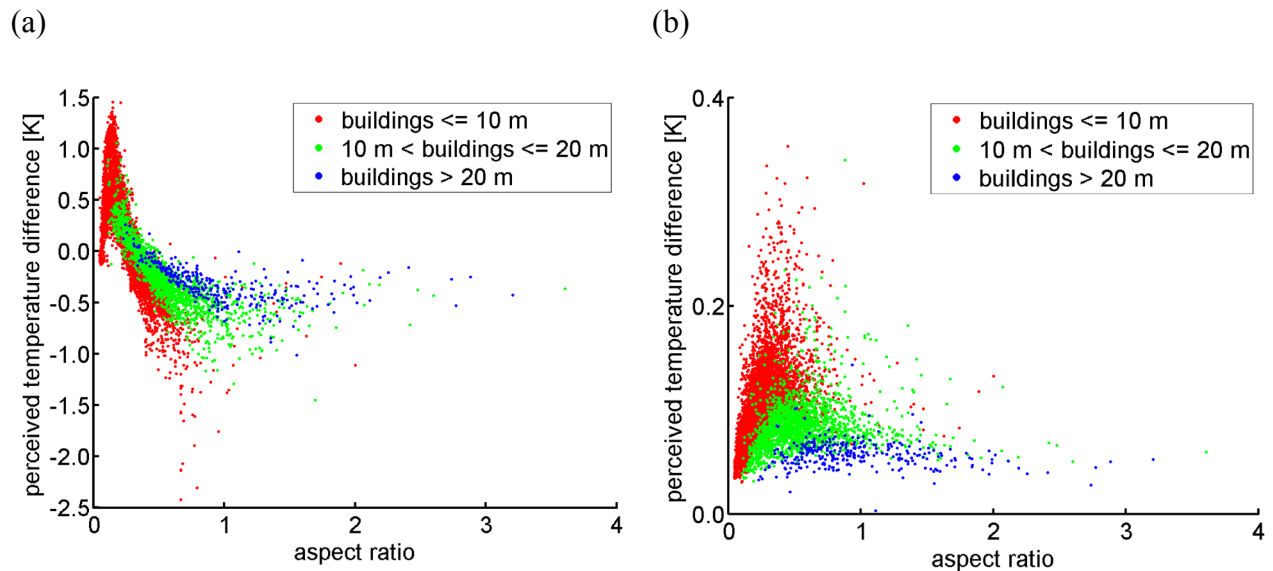
Figure 3-16: Difference between PT obtained when increasing each building height by 5 m and PT obtained with original building heights as a function of the aspect ratio of the street canyons of the respective grid cell. (a): average over NOON, (b): average over LATE.

3.3.5   Generality of the results for the summer season

The sensitivities of PT have been discussed in Section 3.3.4 for one meteorological situation. In this section, it is briefly discussed to which degree the presented results hold for the other 12 meteorological situations selected by Hoffmann (2012). No situations with cold stress occur, because all meteorological situations are in the summer season. Therefore, the sensitivities of PT can only be investigated for situations with thermal comfort and heat stress.

The sensitivity of PT on air temperature is between 0.6 °C/°C and 0.8 °C/°C as long as PT is in the "comfort possible" class. The situation is more complex if heat stress occurs: the sensitivity of PT on air temperature is higher (1.0 °C/°C to 1.4 °C/°C) for situations with high water vapour pressure than for situations with low water vapour pressure (0.6 °C/°C to 1.0 °C/°C) Therefore, the result presented in Section 3.3.4 is only representative for warm and humid conditions. In warm and dry conditions, the sensitivity of PT on air temperature is low.

The results for the other meteorological situations are very similar to the results presented in the Figures 3-11 to 3-13 for the sensitivities of PT on water vapour pressure, wind speed and mean radiant temperature. The sensitivities of PT are higher for situations with heat stress than for situations with thermal comfort. Furthermore, the absolute value of the sensitivity of PT on wind speed is generally small if the wind speed is high, but can become very large (down to -10 °C/(m/s)) if the wind speed is lower than 1 m/s.

The results for the other meteorological situations agree well with the results discussed in Section 3.3.4 for the sensitivity of PT on street canyon width and on the height of the buildings. For NOON, the reduction of PT due to 5 m higher buildings in street canyons with an aspect ratio above 0.5 is obtained for each of the 13 meteorological situations. Also, the sensitivity of PT on the street canyon width is positive in street canyons with an aspect ratio higher than 0.5 for each of the 13 meteorological situations. For LATE, broader street canyons slightly decrease PT and higher buildings slightly increase PT.

3.4   Discussion

The results give several hints on how to plan adaptation measures to climate change with respect to the target variable PT. They also indicate how accurate different input variables need to be known in order to achieve a desired accuracy in PT. However, the reader has to keep in mind the restrictions due to the limited number of investigated meteorological situations, the neglect of non-linear effects, the offline usage of the BEP and the neglect of radiation modification by urban canopy vegetation.

3.4.1 Hints for planning adaptation measures to climate change

For situations with heat stress and humid conditions, the sensitivity of PT on air temperature is higher than for situations with thermal comfort. Therefore, in such meteorological situations, an increase of air temperature due to regional climate change leads to the largest increase of PT in areas where heat stress already occurs. This result also means that a reduction of air temperature by adaptation measures has a higher impact on PT for situations with heat stress compared to situations with thermal comfort. However, one has to carefully assess if the adaptation measures that reduce air temperature during the day (e.g. more water surfaces or more parks within the urban area) lead to an increase in water vapour pressure, since PT has been found to be very sensitive to water vapour pressure for situations with heat stress. Another important result is the very high sensitivity of PT on wind speed for situations with low wind speeds. This could be important, if the structures in the city are changed (e.g. higher buildings). Planners should avoid creating locations with particularly low wind speeds. If the wind speed is high, changes in wind speed do not have a high influence on PT.

After sunset, the sensitivities of PT on street canyon width and building heights are relatively small. For this reason, higher buildings would only lead to a slight increase of PT after sunset. However, this result might be subject to change if the temperature of the walls is calculated dynamically by implementing BEP into METRAS. For NOON, a broadening of the street canyons leads to an increase of PT in the street canyons with an aspect ratio above 0.5. An increase of the building heights by 5 m leads to a reduction of PT down to -2.5 K, if the other meteorological variables do not change. In street canyons with an aspect ratio below 0.5, higher buildings tend to increase PT.

The results give a hint that the increase of PT due to regional climate change can be considerably reduced for NOON by shading due to the higher buildings, at least for the street canyons with relatively high aspect ratio. However, the complexity of the obtained results expressed by the large range of PT differences for one given aspect ratio indicates that urban planning should be made specific for each site. It has to be pointed out that a reduction of wind speed due to higher buildings could cancel out the benefit of shading, at least for situations with low wind speed.

3.4.2 Required accuracy of different input variables for PT

The sensitivities calculated in the present study indicate how accurate the different input variables need to be known in order to achieve a desired accuracy of PT. If an accuracy of 1 °C of PT is desired, the air temperature needs to be known with an accuracy of about 1 °C. The water vapour pressure needs to be known with an accuracy of about 2.5 hPa for situations with heat stress and with an accuracy of 5 to 10 hPa for situations with thermal comfort. The wind speed needs to be

known very precisely (to about 0.1 m/s) if the wind speed is below 1 m/s. This can be expected to be very challenging. The higher the wind speed, the lower is the required accuracy. For situations with wind speeds of about 3 m/s, errors of about 1 m/s are allowed. Errors larger than 1 m/s are allowed for wind speeds higher than 3 m/s. The mean radiant temperature needs to be known with an accuracy of about 3 °C for situations with heat stress, whereas an accuracy of 10 °C is sufficient for situations with thermal comfort. For LATE, the width of the street canyons needs to be known with an accuracy of about 10 m. A much better accuracy of up to 1 m is required if the situation at NOON is of interest. This might be more accurate than state of the art datasets characterising urban morphology can provide. The building heights do not need to be known with a better accuracy than 5 m if only the situation for LATE is of interest. For NOON, the building heights need to be known with an accuracy better than 5 m in order to achieve an accuracy of 1 °C for PT.

3.5 Conclusions and outlook

The sensitivities of PT on air temperature, water vapour pressure, wind speed, mean radiant temperature, street canyon width and building heights have been calculated for 13 meteorological situations during the summer season. Simulation results of the mesoscale model METRAS applied for a domain covering the city of Hamburg at 250 m horizontal resolution have been used to provide meteorological input data. Shading and radiation trapping due to the buildings has been calculated off-line using the radiation modification routines from BEP. Results give several hints on how to plan adaptation measures to climate change and indicate how accurate the different input variables need to be known in order to achieve a desired accuracy of PT.

Additional influences on PT as for example the sensitivity on the albedo and the emissivity of the walls and the ground could be determined with the same methodology, because adaptation measures to climate change could consist in changing these physical characteristics by using different materials. The changes of the results after a full implementation of the BEP into METRAS should be investigated. The temperature of the wall and the ground would then be calculated with the modified radiation fields and therefore depend on the street direction due to the different exposure to the sun. This might considerably change the results. The sensitivities of PT should be investigated in other seasons, because here also situations with cold stress would occur. In other seasons, the sensitivities on characteristics of the urban morphology will be different, because the elevation angle of the sun is lower. The by far most challenging effort would be to differentiate not only the PT program and the BEP but the whole METRAS code. This would allow considering for the non-linear effects of adaptation measures.

4 Change of perceived temperature in future climate

4.1 Introduction

In this chapter, the projected change of PT in future climate is determined for the city of Hamburg in Northern Germany. The climate change signals for PT and air temperature are compared. The changes in the frequency of PT values with respect to the thermal sensation scale defined by Staiger et al. (2011) are determined. The thermal sensation scale defines the thermo-physiological meaning of the PT values. The climate change signals are defined as the differences between the future time periods 2036-2065 and 2071-2100, and the reference time period (1971-2000).

Similar studies have been carried out for other regions. Thorsson et al. (2011) have investigated the changes in outdoor human thermal comfort for the city of Gothenburg (Sweden) based on the IPCC-AR4 simulations of ECHAM5 and found an increase of the mean radiant temperature slightly stronger than the increase of air temperature. Human thermal comfort expressed by PET was found to improve in all seasons except JJA due to reduced cold stress. A strong increase of situations with heat stress was found in JJA. Endler and Matzarakis (2011) have investigated the changes in human thermal comfort measured by PET for the Black Forest in Southwest Germany based on the same CLM and REMO simulations analysed in this thesis. They found an average annual increase of PET very similar to the average annual increase of air temperature, a decrease of days with cold stress and a small increase of days with heat stress.

This chapter is structured as follows: the data selection and preparation is described in Section 4.2, the changes of the climatological annual cycles of air temperature and PT are discussed in Section 4.3, the changes of the frequency of PT values with respect to the thermal sensation scale in Section 4.4. Conclusions are drawn in Section 4.5.

4.2 Data selection and preparation

Hourly or at least 3-hourly data of near-surface air temperature, water vapour pressure, wind speed and mean radiant temperature are required for the calculation of PT to capture the daily cycle. Large biases in these variables in the RCM simulation results are not acceptable, because the absolute values of PT need to be known. These are relevant for the thermal sensation scale. The evaluation results from Chapter 2 indicate which input variables are reasonably simulated by the RCMs. However, the total cloud cover has been evaluated instead of the mean radiant temperature, because no long-term observations of all the required radiation fields have been available. Further, only the PDF of the daily averages has been evaluated whereas hourly values

are used for PT. Shortcomings of the RCMs to simulate the diurnal cycle might therefore deteriorate the results.

In Chapter 2, a strong overestimation of total cloud cover in JJA has been detected for CLM. This can be expected to lead to too low shortwave radiation values. In addition, air temperature has a cold bias in JJA and SON. Further, relative humidity is considerably overestimated in all seasons. For this reason, CLM output is not used for the calculation of PT. In the REMO simulations, the relative humidity is overestimated in DJF and JJA and in the realisations REMO-1 and REMO-2, a too high frequency of 0 °C air temperature is simulated. This error is mostly removed in the REMO-3 simulation. The overestimation of relative humidity could lead to problems in situations with heat stress, because the sensitivity of PT on water vapour pressure is high in these situations. The other input variables are simulated well by REMO. For this reason, we decide to base the investigation on REMO data. The simulation results for the SRES-A1B scenario are used for future climate. Three realisations of the present climate as well as the A1B scenario are available. The data for the first two realisations of present climate (Jacob, 2005a; Jacob et al., 2009a) and the A1B scenario (Jacob, 2005b; Jacob et al., 2009b) have been downloaded from the CERA database. The data for the third realisation have been directly provided by Rechid (2012; personal communication) for usage within KLIMZUG-NORD.

The preparation of the data is described briefly as follows. Air temperature in 2 m above ground is used directly. Water vapour pressure in 2 m above ground is calculated from dew point temperature in 2 m above ground with the formula given by Lawrence (2005). Wind speed in 1 m above ground is estimated from wind speed in 10 m above ground assuming a logarithmic wind profile (neutral conditions) and using the roughness length from REMO. This accounts for the lower wind speed in 1 m above ground compared to 10 m above ground, but not for the effect of atmospheric stability. Wind speed in 1 m above ground is therefore underestimated for situations with unstable stratification and overestimated for situations with stable stratification.

The mean radiant temperature for an upright standing human being is calculated using the program developed by DWD (DWD, 2011; personal communication) based on the upward and downward shortwave and longwave radiation fluxes. The upward longwave and shortwave radiation fluxes at the surface are directly used. The downward longwave and shortwave radiation fluxes at the surface are calculated based on the upward radiation fluxes and the net radiation fluxes at the surface. The prepared input data are used to calculate PT for every hour and every grid point in Hamburg Metropolitan Region with the program developed by DWD.

In this chapter, results for the KLIMZUG-NORD model region Hamburg defined by Rechid et al. (2013) are shown. For the interpretation of the results one needs to keep in mind that the calculated PT is valid for a person standing in an open area (unmodified radiation fluxes). In the

presence of building structures and high vegetation, the radiation fluxes are modified and will impact PT as it has been shown in Chapter 3. The results are analysed separately for the time periods 10:00 to 16:00 local time (NOON) and 21:00 to 24:00 local time (LATE). This accounts for the differences that can be expected for human thermal comfort during the day and after sunset.

4.3 Climatological annual cycle

The projected change of the climatological annual cycle of air temperature and PT is displayed in Figure 4-1 for 2036-2065 and in Figure 4-2 for 2071-2100. The differences between the climate change signals of PT and air temperature are mainly small, confirming Endler and Matzarakis (2011). However, for all three realisations and both future time periods PT increases more than air temperature for NOON in JJA. For 2036-2065, PT increases by 1.5 K to 2.5 K. This is about 0.5 K more than the projected increase of air temperature (1.0 K to 2.0 K). For 2071-2100, PT increases by 2.5 K to 3.5 K compared to an increase of air temperature of 1.5 K to 2.5 K.

The larger increase of PT compared to air temperature in JJA for NOON cannot be attributed to changes in wind speed, because these are very small (not shown). Furthermore, the increase of the mean radiant temperature is smaller than the increase of air temperature, which is due to a slight decrease of shortwave incoming radiation in future climate (not shown). The reason for the increase of PT stronger than the increase of air temperature is the more frequent occurrence of humid conditions combined with PT in the heat stress range. The climate change signal for relative humidity is shown in Figure 4-3. During JJA, the relative humidity increases for NOON (Figure 4-3a), but not for LATE (Figure 4-3b). It has been shown in Chapter 3 that the sensitivity of PT on air temperature is higher than 1 °C/°C for situations with heat stress and humid conditions.

For LATE in JJA, PT increases along with air temperature, because situations with heat stress are rare and the relative humidity is not increasing (Figure 4-3b).

(a)   (b)
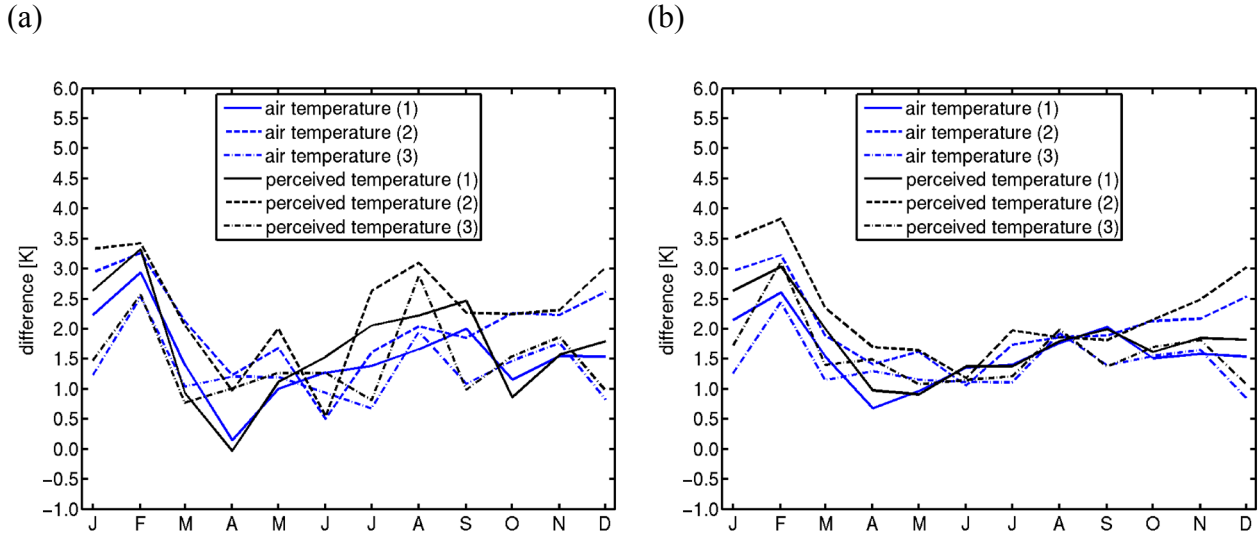
Figure 4-1: Difference of the climatological annual cycle between 2036-2065 and 1971-2000 for air temperature in 2 m above ground simulated by REMO (blue) and PT calculated based on REMO results (black). (a): average over all hourly values between 10:00 and 16:00 local time and (b): average over all hourly values between 21:00 and 24:00 local time. The bracketed numbers denote the realisation.

(a)   (b)
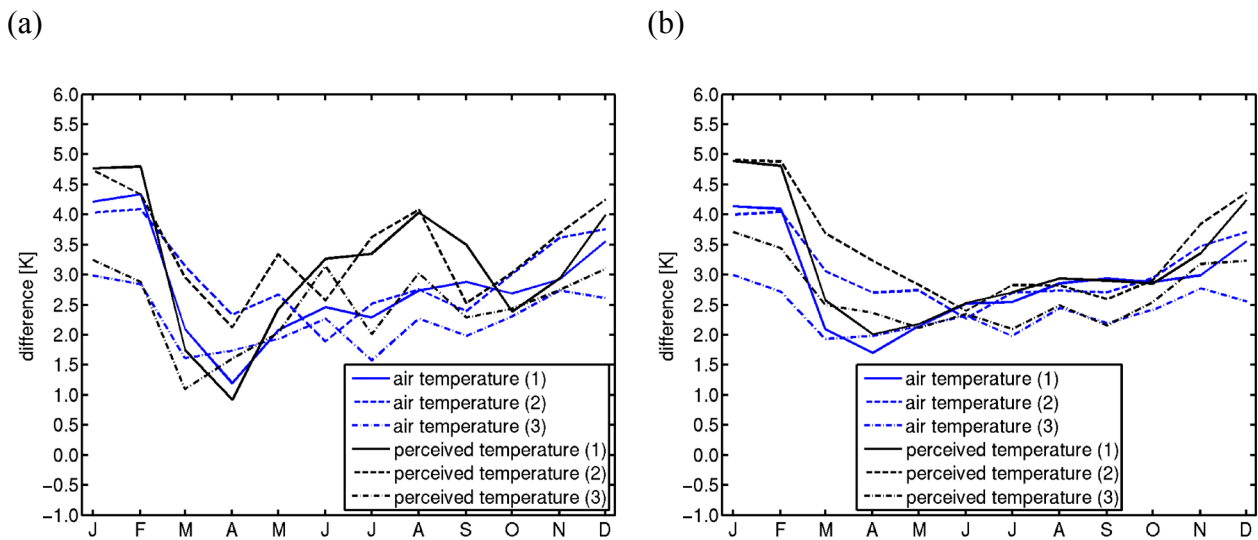
Figure 4-2: Same as Figure 4-1, but for the difference between 2071-2100 and 1971-2000.
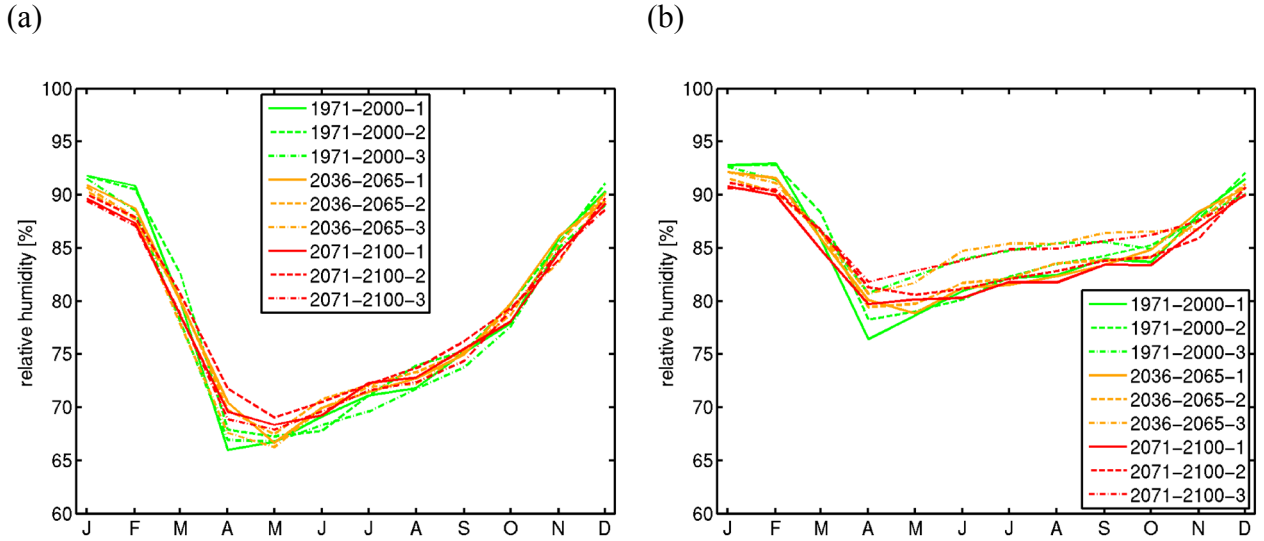
Figure 4-3: Climatological annual cycle of relative humidity in 2 m above ground simulated by REMO. (a): average over all hourly values between 10:00 and 16:00 local time and (b): average over all hourly values between 21:00 and 24:00 local time. The numbers denote the realisation.

4.4 Frequency of PT values with respect to the thermal sensation scale

In this section, the frequency of PT values with respect to the thermal sensation scale defined by Staiger et al. 2011 is investigated for present and future climate.

In DJF (Figure 4-4), PT is most frequently in the "slight cold stress" class in present climate, especially for LATE. A transition is projected in future climate. For both NOON (Figure 4-4a) and LATE (Figure 4-4b), PT is most frequently in the "comfort possible" class for 2071-2100. This is due to a very strong decrease of the frequency of days with air temperature below 0 °C in the RCM results, which is due to an enhanced circulation in the forcing GCM ECHAM5. Heat stress does never occur, not in present and not in future climate. The comparison of REMO-3 with REMO-1 and REMO-2 reveals differences in present climate. The frequency for "slight cold stress" is higher for REMO-1 and REMO-2 than for REMO-3. The reason is the unrealistic frequent occurrence of 0 °C air temperature. All these situations will result in a PT below 0 °C, because the mean radiant temperature is mostly lower than air temperature in DJF. The situations will therefore be attributed to the "slight cold stress" class of the thermal sensation scale. For REMO-3, the frequency of air temperature well above 0 °C is higher, leading to a higher frequency of PT in the comfort possible class. In future climate, the difference between REMO-3 and REMO-1 and REMO-2 is smaller.

In MAM (Figure 4-5), PT is in the "comfort possible" class for about 80% of the hours for NOON and for about 65% of the hours for LATE in present climate. For NOON, both cold stress

and heat stress can occur, whereas heat stress is very improbable for LATE. Only very small changes are projected for NOON. The frequency of events with cold stress is slightly reduced and the frequency of events with heat stress is slightly increased, but the absolute values are still low. Also in future climate, thermal comfort is achievable during about 80% of the hours. The reason for this result is that the climate change signal can mainly be compensated by an adaptation of clothing. For LATE, similar to DJF, a shift from situations with cold stress to situations with thermal comfort is found.

In JJA (Figure 4-6), cold stress does not occur in the investigated time periods. For NOON (Figure 4-6a), thermal comfort is achievable for about 60% of the hours in present climate, heat stress occurs for the rest of the hours. The frequency of "slight heat stress" is the second largest (25%). However, also "extreme heat stress" can occur in JJA. A shift from situations with thermal comfort to situations with heat stress is projected in future climate. The frequency of the two classes with largest heat stress is projected to increase by a factor of two to three. For REMO-3, a higher frequency of thermal comfort is obtained, which is due to a higher simulated total cloud cover compared with REMO-1 and REMO-2. For LATE (Figure 4-6b), thermal comfort is found for more than 98% of the hours in present climate. This is due to the missing shortwave radiation leading to relatively low mean radiant temperatures. In future climate, a very slight shift from situations with "comfort possible" to situations with "slight heat stress" is found. Heat stress is still not projected to be problematic in future climate for LATE. However, the modification of radiation due to the presence of buildings is neglected here. Furthermore, one has to recall that only the outdoor thermal comfort is assessed in this study.

The results for SON (Figure 4-7) are very similar to the results for MAM. For NOON (Figure 4-7a), thermal comfort is achievable for about 85% of the hours and the climate change signal can mainly be compensated by an adaptation of clothing. For LATE (Figure 4-7b), a shift from situations with "slight cold stress" to situations with "comfort possible" is projected in future climate.

(a)
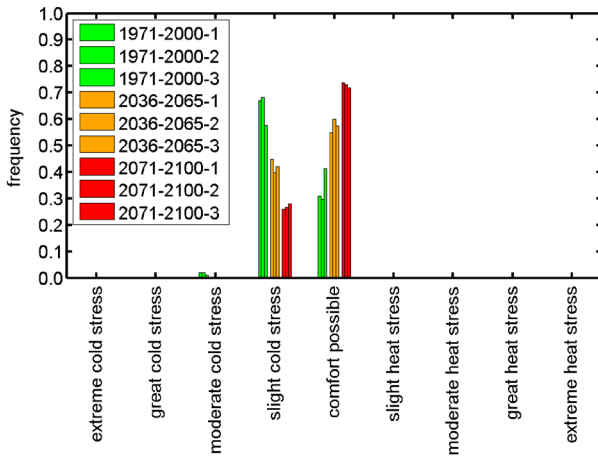
(b)
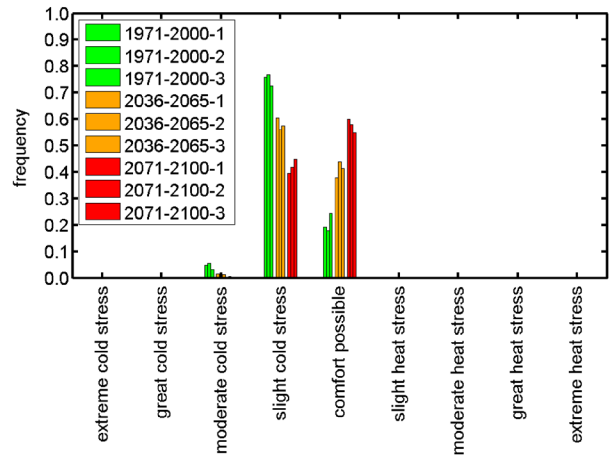
Figure 4-4: Frequency of PT values calculated based on REMO data with respect to the thermal sensation scale in DJF for (a): NOON and (b): LATE.

(a)
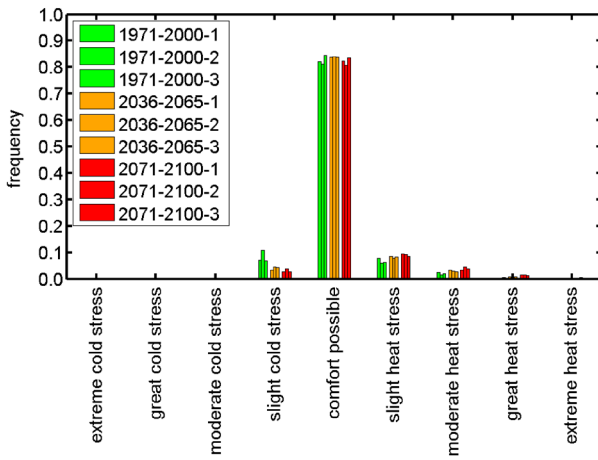
(b)
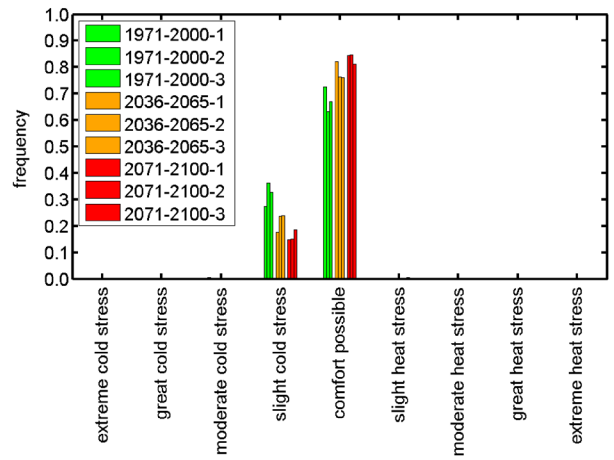
Figure 4-5: Same as Figure 4-4, but for MAM.

(a)
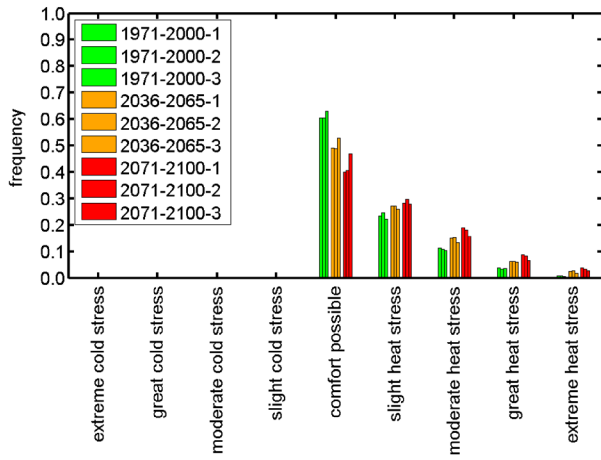
(b)
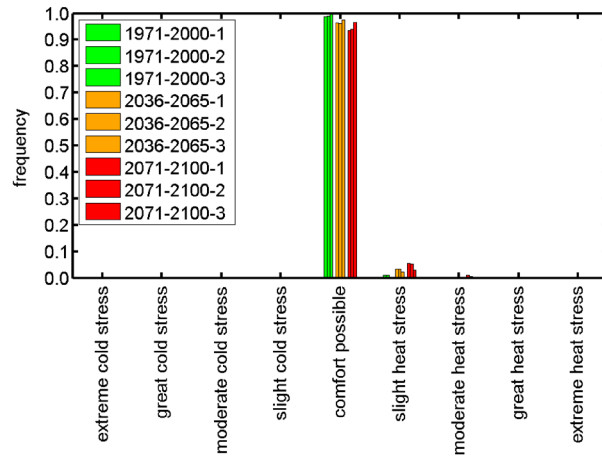
Figure 4-6: Same as Figure 4-4, but for JJA.

(a)
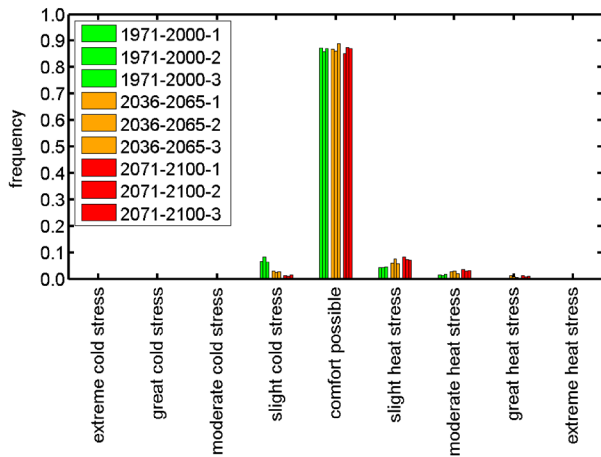
(b)
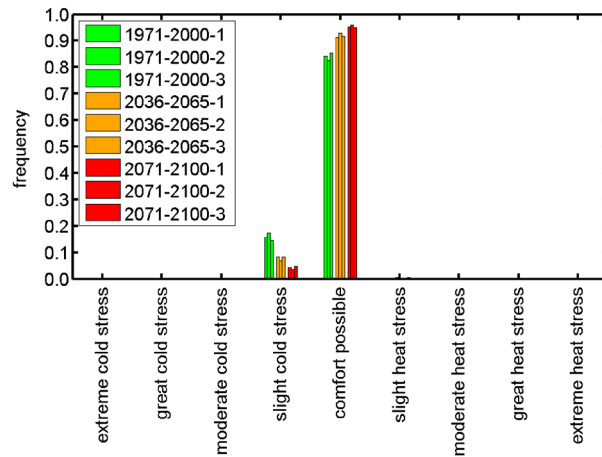
Figure 4-7: Same as Figure 4-4, but for SON.

4.5 Conclusions

In this chapter, the projected change of PT in future climate has been investigated using results of the RCM REMO for the SRES-A1B scenario. PT is increasing mainly along with air temperature, because the climate change signals in wind speed and relative humidity are relatively small. The only exception is found for JJA during NOON: here the increase of PT is 0.5 K to 1.0 K stronger than the increase of air temperature. This can be attributed to an increasing relative humidity in situations with occurrence of heat stress. The analysis of the frequency of PT values with respect to the thermal sensation scale reveals a very pronounced reduction of cold stress in DJF and at least for LATE in MAM and SON. Situations with heat stress become more frequent for NOON in JJA. Here, the frequency of great and extreme heat stress is increasing by a factor of two to three. In MAM and SON, the climate change signal can be mainly compensated by an adaptation of clothing.

The results of this study rely only on one RCM. In future studies it should be investigated if the main features found in the REMO data are also found in other RCM simulation results. The main focus should be on the stronger increase of PT compared to air temperature in JJA, because it is very relevant for occurrence of heat stress in future climate. It should also be investigated whether the slight decrease of incoming shortwave radiation in JJA is also simulated by other RCMs. An increase of shortwave radiation could severely aggravate the thermal stress in JJA. Further, the climate change signals need to be investigated in complex building environments leading to more complex changes in the mean radiant temperature than for a human being standing in an open area. This has for example been made by Thorsson et al. (2011).

5 Downscaling heavy summer precipitation for the present

It is plausible that the characteristics of precipitation will change in future climate. Figure 5-1a displays the 1th to 99th percentiles of daily precipitation amounts for days with more than 1 mm precipitation in the summer season (JJA). The percentiles are based on simulation results of the RCMs CLM and REMO for an area covering Hamburg Metropolitan Region and the time period 1971-2000, which is used here as a reference period. The projected difference of these percentiles between the future time period 2071-2100 and the reference period for the A1B, A2 and B1 greenhouse gas emission scenarios is shown in Figure 5-1b.

(a)   (b)
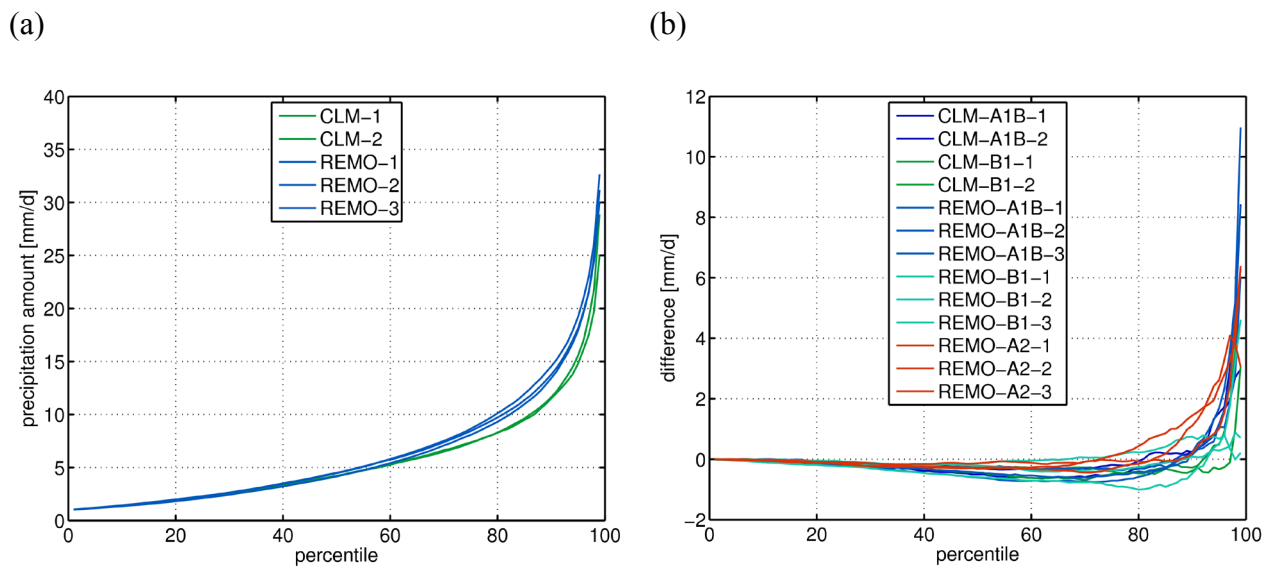
Figure 5-1: (a) Simulated 1th to 99th percentiles of precipitation amounts on days with more than 1 mm precipitation in JJA by the RCMs CLM and REMO for 1971-2000 and (b) projected difference of these percentiles between 2071-2100 and 1971-2000 for different greenhouse gas emission scenarios and realisations. This figure has been adapted from a contribution to Rechid et al. (2013).

A similar characteristic of climate change is resulting for all scenarios, both RCMs and all realisations. The difference is negative for the 20th to 60th percentiles of the precipitation amounts, corresponding to 2 mm/d to 5 mm/d in the reference period. The difference is positive for the 95th to 99th percentiles, corresponding to 20 mm/d to 30 mm/d in the reference period. A transition zone with positive or negative differences is located between the 60th and the 95th percentile. The differences between the single simulations depict the uncertainty due to the choice of the RCM, the emission scenario and the internal climate variability. A similar climate change signal is found for 2036-2065, but less pronounced (not shown). This result is further confirmed by Rudolf (2011), who found an increase of heavy precipitation in future climate

based on analyses of the larger ensemble of RCM simulation results conducted in the framework of the ENSEMBLES project.

Hamburg Metropolitan Region needs to adapt to the projected increase of heavy summer precipitation. The adaptation could be achieved by increasing the capacities of the urban drainage system, reducing the run-off by green roofs or reducing the fraction of sealed surfaces within the city (e.g. Hellmers and Hüffmeyer, 2013). However, urban areas can modify precipitation themselves (literature summary in Section 6.2). Therefore, the present study focuses on the modification of heavy precipitation by the city of Hamburg. This includes studies on the impact of adaptation measures on precipitation development. To be able to quantify the impact of small-scale changes in surface cover, the surface characteristics have to be properly resolved and the heavy precipitation needs to be simulated in a realistic manner with an atmospheric model at horizontal resolutions in the order of 1 km.

Observed heavy summer precipitation events (Section 5.1) have been downscaled with the mesoscale atmospheric model METRAS (Section 5.2) to a domain covering Hamburg Metropolitan Region at 2 km horizontal resolution. The focus on present climate allows to evaluate the simulation results against routine observations made by DWD. The main goal of this chapter is the description of the setup and adaptation of the METRAS model (Section 5.3) as well as the evaluation of simulation results (Section 5.4). The impact of topography on the simulated precipitation is then investigated in Chapter 6.

5.1 Selected meteorological situations

Schlünzen et al. (2010) have found higher daily precipitation amounts at the DWD stations northeast of Hamburg in situations when they are located downwind of the urban area compared to situations when they are located upwind of the urban area. The selected meteorological situations cover those days within the summer season (JJA) with a daily precipitation amount exceeding 25 mm/d ("heavy precipitation") at one of the DWD stations within the urban area of Hamburg or its northeastern surroundings during 1982-1998. A precipitation amount of 25 mm/d corresponds to about the 97th percentile of observed daily summer precipitation amounts for days with more than 1 mm/d. The threshold of 25 mm/d is chosen, because precipitation events exceeding 25 mm/d can cause flooding in the urban area of Hamburg due to failure of the drainage system. Only stations with less than 5% missing data have been used for the selection of the meteorological situations. The considered stations are marked with red dots in Figure 5-2.
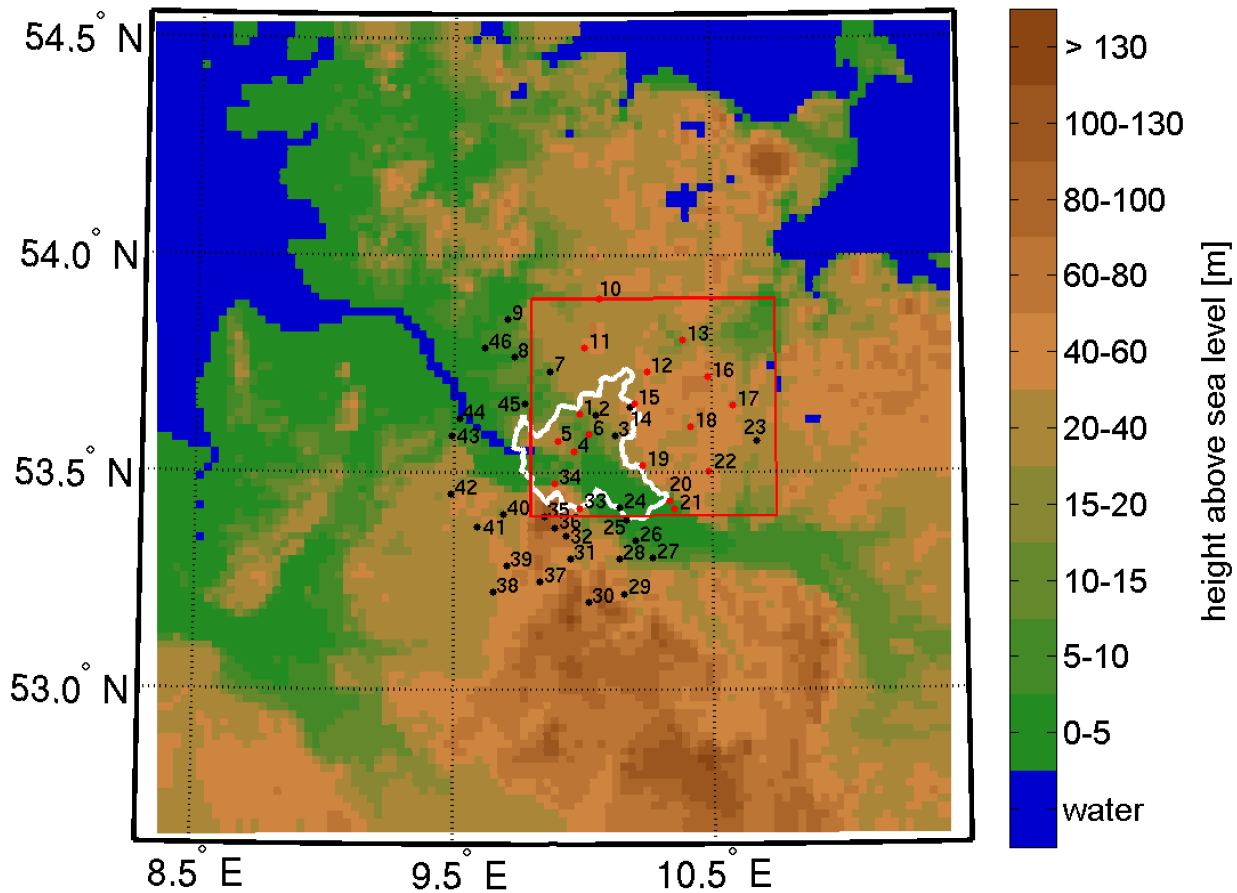
Figure 5-2: Location of the DWD stations reporting daily precipitation amounts used for selection of the meteorological situations (red dots) as well as for the evaluation of simulated daily precipitation amounts (black and red dots) within the model domain covering Hamburg Metropolitan Region at 2 km horizontal resolution. The white contour line displays the border of the federal state Hamburg.

Two main reasons motivate to focus on daily precipitation. First, most of the stations report daily precipitation amounts. Simulated sub-daily precipitation amounts can therefore not be evaluated. Secondly, the spatial representativeness of sub-daily precipitation amounts is very low (Ertl, 2010; Bohnenstengel et al., 2011), rendering an evaluation against station observations very challenging. The time period 1982-1998 has been selected to best use the available data. Many DWD stations reporting daily precipitation amounts have been closed after 1998 leading to a decrease of the number of available observations after 1998 (Ertl, 2010). Further, the METRAS model is nested into the ERA-Interim reanalysis data (Dee et al., 2011), which start in 1979. The NOAA optimum interpolation sea surface temperatures (SST) with 0.25° spatial resolution (OISST, Reynolds et al., 2007) are used to prescribe the SST values in METRAS; these become available only for dates after September 1981. The hourly DWD data used for evaluation of air temperature, specific humidity, wind speed and wind direction in the model domain are only

available after 1981 for this thesis. The location of these stations within the model domain at 2 km resolution is shown in Figure 5-3a. Finally, the surface cover map of the domain is based on relatively recent data. The combination of all these factors motivated to start the analysis in 1982 and not earlier.

A total of 82 heavy precipitation events have been detected matching the described selection criteria. In 8 cases, heavy precipitation is found on two consecutive days. METRAS is integrated for each heavy precipitation event from one day before to one day after the day with the observed heavy precipitation. Therefore, only 74 meteorological situations need to be downscaled.

The wind rose of the prevailing ERA-Interim wind direction in 700 hPa is displayed for the selected meteorological situations in Figure 5-3b. Burian and Shepherd (2005) point out that the 700 hPa level is the steering level for convective storms. A dominance of the wind directions west and southwest appears. The selected target stations are therefore located downwind of the urban area for most of the selected meteorological situations. A more detailed analysis of the synoptic situations related with heavy precipitation events is not carried out here, but could nevertheless give valuable mechanistic understanding on the triggering of heavy summer precipitation in Hamburg Metropolitan Region.

(a)   (b)
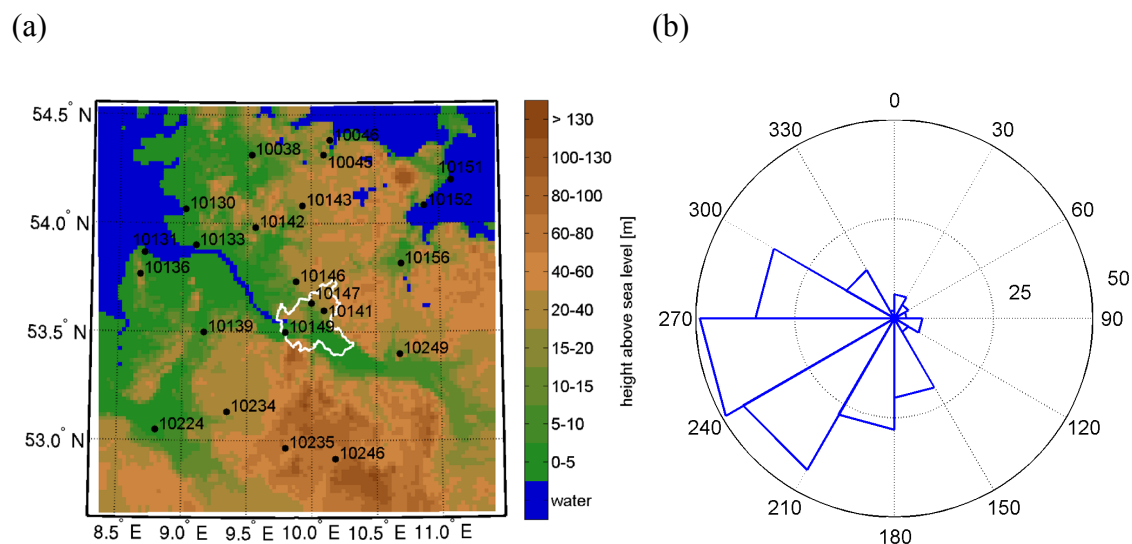
Figure 5-3: (a) Location of the DWD stations used for evaluation of hourly values of air temperature, specific humidity, wind speed and wind direction. (b) Wind rose in 700 hPa based on the ERA-Interim data for the selected meteorological situations.

5.2 METRAS model

5.2.1 General aspects

The mesoscale atmospheric model METRAS used for downscaling of the summer heavy precipitation events has first been described by Schlünzen (1990). The most recent version is documented in Schlünzen et al. (2012a,b). The model is based on the fundamental physical conservation laws for momentum, mass and energy as well as the ideal gas law. The equations are discretised on an Arakawa-C grid and solved in flux form. The coordinate system follows the terrain. The prognostic variables are the three components (u,v,w) of the wind vector, the potential temperature (θ), the specific humidity (q_v), as well as the specific cloud (q_c) and rain water contents (q_r). The equations are Reynolds-averaged, meaning that the solution is representative for the ensemble average over all possible realisations of turbulent flow. Those characteristics of the model that are most important for the present study are described in detail.

The anelastic approximation is applied for elimination of fast travelling sound waves.

The potential temperature and the specific humidity are split into a time independent large scale part and a time dependent deviation. The total pressure p is split into 3 parts (Equation (5-1)). The large scale pressure p_0 is hydrostatically balanced with the large scale density ρ_0 (Equation (5-2)). The acceleration due to gravity is denoted by g. The pressure deviation p_1 is hydrostatically balanced with the density deviation $\tilde{\rho}$ (Equation (5-3)). In the model equations, the density deviation $\tilde{\rho}$ is neglected except in the buoyancy term (Boussinesq approximation). The pressure deviation p_2 results from dynamic effects. The time dependent change of the pressure deviation p_2 ($\widehat{p_2}$) is diagnosed under the assumption of a divergence-free flux of the air mass (Equation (5-4)). The time step is denoted by Δt. At the top of the model domain, the pressure deviation p_1 as well as the horizontal average of the pressure deviation p_2 are assumed to be zero (Equation (5-5)). In the Equations (5-2) to (5-4), additional factors resulting from the transformation into the terrain following coordinate system have been left out for better readability.

$$p = p_0 + p_1 + p_2 \qquad\qquad (5\text{-}1)$$

$$\frac{\partial p_0}{\partial z} = -g\rho_0 \qquad\qquad (5\text{-}2)$$

$$\frac{\partial p_1}{\partial z} = -g\tilde{\rho} \qquad\qquad (5\text{-}3)$$

$$\nabla^2 \widehat{p_2} = \frac{1}{\Delta t} \nabla \cdot \rho_0 \vec{v} \tag{5-4}$$

$$p_1^{top} = \overline{p_2^{top}} = 0 \tag{5-5}$$

5.2.2 Parameterisation of sub-grid scale processes

The impact of sub-grid scale turbulence is parameterised using a first order closure scheme. The turbulent fluxes at the first model level in 10 m above ground are calculated separately for each sub-grid scale surface cover class using the Monin-Obukhov similarity theory. Then they are aggregated over the entire grid cell applying the flux aggregation method including Blending height (von Salzen et al., 1996). Above the first model level, the exchange coefficients are calculated for the case of stable and neutral stratification with the local mixing-length closure (Lüpkes and Schlünzen, 1996). For unstable stratification, the non-local effects of turbulence generation are parameterised with the non-local closure described also by Lüpkes and Schlünzen (1996). The non-local closure scheme accounts for the effect of turbulence in the upper boundary layer due to plumes generated near the surface.

The radiation is parameterised with a two-stream approximation taking into account absorption and reflection of longwave and shortwave radiation due to the presence of water vapour and liquid water. The details can be found in Schlünzen et al. (2012b).

There is no parameterisation for convection in clouds in METRAS. Precipitation can only occur due to explicit formation of clouds and rain. Therefore, reliable results for precipitation can only be expected at horizontal resolutions of a few kilometres and finer. The cloud microphysics is parameterised with a liquid-only Kessler scheme (Kessler, 1969); the implementation into METRAS is described in Schlünzen et al. (2012b). The basic idea of the Kessler scheme is to solve prognostic equations for the cloud water content (Equation (5-6)) and the rain water content (Equation (5-7)). In METRAS, the equations are solved in flux form. The local change of cloud water density is caused by divergence of the cloud water density flux, condensation of water vapour to cloud water or evaporation of cloud water to water vapour (Q_{COND}), autoconversion of cloud droplets to rain droplets (Q_{AUTO}) and accretion of cloud droplets by rain droplets (Q_{ACCR}). The terms Q_{AUTO} and Q_{ACCR} appear as source terms in the prognostic equation for the rain water density. The evaporation of rain droplets falling through subsaturated air is considered as the sink term Q_{EVAP} in this equation. Additionally, a local change in the rain water density can occur due to the divergence of the sedimentation velocity of the rain droplets V_{SED} (solved in flux form). The terms Q_{COND} and Q_{EVAP} also appear in the prognostic equation for the water vapour density (Equation (5-8)). In addition, the latent heat released or uptaken during condensation and evaporation causes local changes in air temperature. The term α^* denotes the grid volume.

$$\frac{\partial \rho_0 \alpha^* q_c}{\partial t} = -\nabla \cdot \rho_0 \alpha^* q_c \vec{v} + Q_{COND} - Q_{AUTO} - Q_{ACCR} \qquad (5\text{-}6)$$

$$\frac{\partial \rho_0 \alpha^* q_r}{\partial t} = -\nabla \cdot \rho_0 \alpha^* q_r \vec{v} + \frac{\partial \rho_0 \alpha^* q_r V_{SED}}{\partial z} + Q_{AUTO} + Q_{ACCR} - Q_{EVAP} \qquad (5\text{-}7)$$

$$\frac{\partial \rho_0 \alpha^* q_v}{\partial t} = -\nabla \cdot \rho_0 \alpha^* q_v \vec{v} - Q_{COND} + Q_{EVAP} \qquad (5\text{-}8)$$

The complex processes involved in the formation of clouds and precipitation are represented in a simplified manner when using the Kessler scheme. The main simplifications have been reviewed by Doms and Herbert (1985). The most important simplification is the neglect of cloud ice, snow and hail/graupel. Many processes with involved ice phase are therefore not captured. The effects of solution and curvature on the saturation specific humidity for water vapour with respect to the cloud droplets are neglected. The Kessler scheme strictly distinguishes between cloud water and rain water. A possible break-up of rain droplets to sizes in the cloud droplet range is neglected. Condensation only increases the cloud water content but not the rain water content. For the calculation of the conversion terms in the Equations (5-6) to (5-8), the rain droplet spectrum is assumed to follow a distribution after Marshall and Palmer (1948).

Gilmore et al. (2004) have investigated the difference between the Kessler liquid-only scheme and the Lin-Farley-Orville scheme that includes ice microphysics for strong convective storms simulated with the Straka atmospheric model. They find stronger updrafts in the middle of the troposphere for the scheme including ice microphysics. The physical reason is the additional latent heat release during freezing and during deposition of water vapour onto ice particles. According to Gilmore et al. (2004), this result is consistent with other studies. Due to intensified updrafts and lower sedimentation velocities of the snow particles, the precipitation falls out further away from the updraft region if the ice microphysics is included. The total amount of simulated precipitation increases by 40%. Although the reported differences between the microphysical schemes might strongly depend on the meteorological conditions, the results from Gilmore et al. (2004) have to be kept in mind, simply because heavy summer precipitation is investigated in the present study.

The calculation of the conversion terms in the Equations (5-6) to (5-8) is briefly described. Condensation and evaporation are assumed to take place simultaneously. The amount of water to condensate or evaporate is calculated with the method of saturation adjustment described for example in Kong and Yau (1997). The saturation adjustment technique takes into account the change in the saturation specific humidity due to the change in air temperature caused by condensation or evaporation. The specific humidity after the saturation adjustment (q_v^{ADJ}) is the saturation specific humidity (q_v^{SAT}) with respect to the air temperature (T) changed by ΔT due to

the latent heat uptaken or released during evaporation or condensation (Equation (5-9)). The left hand side of Equation (5-9) is Taylor expanded to the first order (Equation (5-10)). The change of specific humidity due to condensation or evaporation (Δq_v) is linked to the change of air temperature by Equation (5-11). With the formula for the saturation specific humidity implemented in METRAS (Equation (5-12)), the expression for Δq_v can be obtained after modest algebraic manipulations (Equation (5-13) and Equation (5-14)). In Equation (5-13) it is assured that not more than the entire available cloud water content evaporates. The term Δq_v is symbolised in the Equations (5-6) and (5-8) by Q_{COND}.

$$q_v^{ADJ} = q_v^{SAT}(T + \Delta T) = q_v + \Delta q_v \tag{5-9}$$

$$q_v^{SAT}(T + \Delta T) \cong q_v^{SAT}(T) + \frac{\partial q_v^{SAT}(T)}{\partial T} \Delta T \tag{5-10}$$

$$\Delta T = \frac{\Delta q_v l_{21}}{c_p} \tag{5-11}$$

$$q_v^{SAT}(T) = q_v^0 \, exp\left(\frac{4028(T - 273.16)}{(273.16 - 38.33)(T - 38.33)}\right) \tag{5-12}$$

$$\Delta q_v = max\left(\frac{q_v - q_v^{SAT}}{\beta}, -q_c\right) \tag{5-13}$$

$$\beta = 1 + \frac{4028 \, l_{21} q_v^{SAT}}{c_p(T - 38.33)^2} \tag{5-14}$$

The amount of cloud water content converted into rain water content by autoconversion ($AUTO$) per time step is calculated using Equation (5-15). The autoconversion starts for cloud water contents exceeding 10^{-3} kg/kg and is not allowed to become negative. In the Equations (5-6) and (5-7), the autoconversion is symbolised by Q_{AUTO}. The magnitude of the autoconversion is determined such that the cloud water content would be reduced to the threshold value within 1000 s. According to Doms and Herbert (1985), different but reasonable values for these thresholds or the usage of more sophisticated approaches in the calculation of the autoconversion do not lead to qualitative differences in cloud formation and precipitation.

$$AUTO = \Delta t \, max\left(10^{-3}s^{-1}\left(q_c - 10^{-3} \, \frac{kg}{kg}\right), 0\right) \tag{5-15}$$

The accretion of cloud droplets by rain droplets is calculated according to Doms and Herbert (1985) assuming that the rain droplets follow a Marshall-Palmer distribution and that all cloud

droplets on their pathway are collected (collection efficiency equal to 1). The amount of cloud water content to be converted to rain water content by accretion per time step is given by Equation (5-16). In the Equations (5-6) and (5-7), the accretion is symbolised by Q_{ACCR}.

$$ACCR = \Delta t\ 934.63\ q_c \sqrt{\frac{1.29}{\rho_0}} (10^{-3}\rho_0 q_r)^{0.875} \qquad (5\text{-}16)$$

The amount of rain water content to evaporate per time step when the rain droplets are falling through subsaturated air (Equation (5-17)) is calculated following Doms and Herbert (1985), neglecting the effects of solution and curvature. The evaporation depends on the subsaturation S (Equation (5-18)), a factor characterising the droplet spectrum (Equation (5-19)) and a ventilation factor required for large droplets (Equation (5-20)). The evaporation is limited to the total rain water content. In the Equations (5-7) and (5-8), the evaporation of rain droplets is symbolised by Q_{EVAP}.

$$EVAP = \Delta t\ max\left(-\frac{10^3}{\rho_0} S A_t F_v \sqrt{10^{-3}\rho_0 q_r},\ -q_r\right) \qquad (5\text{-}17)$$

$$S = \frac{100\ (q_v - q_v^{SAT})}{q_v^{SAT}} \qquad (5\text{-}18)$$

$$A_t = \frac{2.623 \cdot 10^{-3}\rho_0 10^{-3} q_v^{SAT}}{1 + 1.282 \cdot 10^{10} 10^{-3}\rho_0 q_V^{SAT} T^{-2}} \qquad (5\text{-}19)$$

$$F_v = 0.78 + 80.73(10^{-3}\rho_0 q_r)^{0.225} \qquad (5\text{-}20)$$

The sedimentation velocity of the rain droplets is calculated after Doms and Herbert (1985) as a mass weighted average over the sedimentation velocities of the rain droplets of different sizes, again assuming a Marshall-Palmer distribution (Equation (5-21)). The dependency of the sedimentation velocity on the droplet size is obtained from empirical relationships.

$$V_{SED} = 68.81 \sqrt{\frac{1.29}{\rho_0}} (10^{-3}\rho_0 q_r)^{0.1905} \qquad (5\text{-}21)$$

An error in the scheme for cloud microphysics has been detected during the setup of the simulations presented in this chapter. The error is described in detail in Appendix A and has been removed before the simulations have been conducted. The simulation results are therefore not affected by this error.

5.2.3 Lower boundary conditions

The wind components at the lower boundary are defined as being zero (no-slip condition; Schlünzen et al., 2012b).

A prognostic equation is solved for the surface energy budget (Equation (5-22)) to calculate the surface temperature T_S per surface cover class (Schlünzen et al., 2012b). The surface energy budget consists of the shortwave (B_S) and longwave (B_L) radiation budget at the surface, the sensible and latent heat flux as well as the ground heat flux. The sensible heat flux is obtained from the friction velocity u_* and scaling value for temperature θ_*, the latent heat flux from the friction velocity and the scaling value for humidity q_*. The roughness of the surface impacts both sensible and latent heat flux. The latent heat flux is further influenced by the soil moisture availability. The ground heat flux is calculated assuming a restoring of the difference between the surface temperature and the temperature of the soil in the depth of the daily temperature wave $T_s(-h_\theta)$ within one day. The thermal conductivity of the soil is denoted by v_S, the thermal diffusivity by k_S. The depth of the daily temperature wave h_θ is determined from the thermal diffusivity and the duration of one day (L_{day} = 86400 s) (Equation (5-23)). The temperature of the soil in the depth of the daily temperature wave is kept constant over the entire integration of the model and within the grid cell. This approach is only valid for short-term integrations (e.g. few days). A more sophisticated treatment of the soil would be necessary for long-term integrations.

$$\frac{\partial T_S}{\partial t} = \frac{2\sqrt{\pi}k_S}{v_S h_\theta}\left(B_S + B_L + c_P\rho_0 u_*\theta_* + l_{21}\rho_0 u_* q_* - \sqrt{\pi}v_S\frac{T_S - T_s(-h_\theta)}{h_\theta}\right) \tag{5-22}$$

$$h_\theta = \sqrt{L_{day}\,k_s} \tag{5-23}$$

In the simulations presented here, the anthropogenic heat flux of about 8.5 W/m² in JJA when averaging over the federal state Hamburg (Petrik et al., 2013) is neglected. Lin et al. (2011) found that the anthropogenic heat is important for heavy precipitation over Taipei. However, the anthropogenic heat flux is much higher in this city (about 200 W/m²).

The specific humidity at the surface q_S is calculated with the method suggested by Deardorff (1978). At each time step, q_S is adjusted towards its saturation value q_S^{SAT} (but not higher) with a proportionality factor α between 0 and 1 that represents the soil moisture availability (Equations (5-24) and (5-25)). The air near the surface is saturated for α equal to 1. For α equal to 0, q_S is equal to the specific humidity in 10 m above ground (q_v^{10m}).

A prognostic equation is solved for the soil moisture availability taking into account the

evaporation and precipitation P (Equation (5-26)). Here, ρ_w denotes the density of water, ρ_s the density of the air at the surface and W_k the depth of the column of available water at saturated soil. The initial values used for α and the values used for W_k for the different surface cover classes are described in Schlünzen et al. (2012a). A shortcoming of this simple treatment of soil moisture with only one parameter for the soil moisture availability is the limited possibility for parameterisation of standing water or puddles immediately after a precipitation event (Deardorff, 1978).

$$q_S = \alpha q_S^{SAT}(T_S) + (1 - \alpha)q_v^{10m} \tag{5-24}$$

$$q_S <= q_S^{SAT}(T_S) \tag{5-25}$$

$$\frac{\partial \alpha}{\partial t} = \frac{l_{21}\rho_s u_* q_* + P}{\rho_w W_k} \tag{5-26}$$

With the described calculation of the meteorological variables at the lower boundary, the surface cover classes in urban areas are characterised to be different from rural or vegetated areas by their higher roughness, higher thermal diffusivity and conductivity as well as by the reduced soil moisture availability. No urban canopy parameterisation is used for the parameterisation of the impact of buildings on the meteorological variables at grid points above the surface. Also, the radiation trapping is neglected. This might influence the urban precipitation impact. Lei et al. (2008) find higher precipitation for Bombay when the urban canopy parameterisation TEB is used.

A value of 1.5 mm is assumed for W_k for the sealed surfaces like asphalt, concrete and buildings. This accounts for the formation of shallow pools after a precipitation event. After a longer dry period, these pools have dried out and the evaporation from the sealed surfaces is zero.

The surfaces in urban areas are represented by two classes of buildings (buildings lower than 11.5 m, buildings higher than 11.5 m), the classes asphalt, concrete, brick/pavers, gravel and steel, as well as vegetation classes (different kinds of trees, bushes and grassland). Urban canopy vegetation needs to be included, because its neglect can deteriorate model results in studies dealing with urban climate (Grimmond et al., 2011). The separation between sealed surfaces and vegetated surfaces is tailored to the flux-aggregation method, which allows a calculation of the fluxes separately for surface cover classes with very different physical properties. The fractions of the different surface cover classes within Hamburg Metropolitan Region have been derived by Flagg et al. (2012). Maps with the occurrence of different surface cover groups in the domain at 2 km horizontal resolution are displayed in Section 6.3.1.

5.2.4 Nesting in large scale model results

For an adequate simulation of realistic meteorological situations in a high resolution, the mesoscale model needs to be nested into results of another model or analysis data covering a larger area. This is the only way how information about changes of the prognostic variables at the boundary of the limited area model can be transferred to it. For METRAS, a one way nesting is achieved by introduction of an artificial forcing term into the prognostic equations. This forcing term relaxes the unforced prognostic variable ψ_u to the corresponding variable in the forcing data ψ_c (Equation (5-27)). The selection of the magnitude and shape of the forcing factor δ depends on the purpose of the investigation. The shape of the forcing factor in the x- direction is given by Equation (5-28). The symbol ji denotes the index of the grid, $NX1$ is the total number of grid points in x- direction. The forcing factor has a maximum value at the boundary of the domain and decreases towards the centre of the domain. The usage of the hyperbolic tangent function assures a smooth transition from the boundary towards the centre of the domain. In y- direction, the same shape of the forcing factor is used (not shown). For the z- direction, the forcing factor has the lowest value near the surface and increases towards the top of the model (Equation (5-29)). In Equation (5-29), $NX3$ denotes the number of grid points in z-direction. The total forcing factor is given as the maximum of the forcing factors for the different directions and multiplied with the parameter δ_0 (Equation (5-30)). A minimum forcing factor δ_{min} can be specified if it is desired to force the solution within the entire model domain. Detailed information on the choice of the parameters δ_0, A, NH, NV, δ_{min}, as well as on the forced variables will be given in Section 5.3.

$$\psi_f = \psi_u(1 - \delta) + \delta\psi_c \qquad (5\text{-}27)$$

$$\delta(ji) = max\left(\left(1 - tanh\left(\frac{A(ji - 1)}{NH - 3}\right)\right), \left(1 - tanh\left(\frac{A(NX1 - ji)}{NH - 3}\right)\right)\right) \qquad (5\text{-}28)$$

$$\delta(jk) = 1 - tanh\left(\frac{A(NX3 - jk)}{NV - 3}\right) \qquad (5\text{-}29)$$

$$\delta(ji, jj, jk) = max(\ \delta_0\ max(\ \delta(ji), \delta(jj), \delta(jk)\ )\ ,\ \delta_{min}) \qquad (5\text{-}30)$$

It should be noted that the introduction of the forcing term can have severe implications, because the conservation laws are no longer fulfilled in the zone with strong forcing. Therefore, the forcing can be an artificial source or sink for the forced variable (e.g. Davies, 1976).

In order to avoid reflection of gravity waves at the model top, the Rayleigh damping technique is applied to the vertical wind component. The formulation of the Rayleigh damping is similar to the formulation of the forcing (Equation (5-31)). The vertical wind component is forced towards

w_0 (0 m/s) with a forcing factor R_d rapidly increasing towards the top of the model (Equation (5-32)). The Rayleigh damping is only applied for the five highest model levels.

$$w_d = w_u(1 - R_d) + R_d\, w_0 \tag{5-31}$$

$$R_d(jk) = 0.2^{NX3-jk+1} \tag{5-32}$$

5.2.5   Initialisation of the model

The details of the model initialisation are described in Schlünzen et al. (2012b). From the forcing data, the surface pressure at the reference point is derived. Furthermore, vertical profiles of the friction-free horizontal wind components, air temperature and relative humidity are calculated as average over all grid points with an orography below 10 m in the METRAS model domain. These vertical profiles determine the basic state and are used to integrate a one-dimensional version of METRAS until the wind fields are stationary. After the start of the three-dimensional version of METRAS, the one-dimensional profile is extended to the entire model domain with the orography set to zero. The orography grows within one minute simulation time to its final value calculating the full model equations (diastrophism) but reconstructing the basic state to heights above sea level. At the end of diastrophism, the three-dimensional basic state adjusted to the orography is kept constant for the rest of the model integration. Before 40 minutes simulation time the forcing factor is zero. After a simulation time of 40 minutes, a constant forcing factor that is linearly increasing from zero to the final value δ_0 (0.01 s^{-1}) is applied in the entire model domain. This value is reached after 90 minutes of simulation time. Then the forcing factor is linearly changed from the constant forcing factor to the shape described in the Equations (5-28) to (5-30). The final value of the forcing factor is reached after 150 minutes of simulation time.

5.3   Adaptation of METRAS

In this section, the setup of the METRAS model for the simulations and necessary adaptations are described.

METRAS is applied in hindcast mode and forced at the boundaries with ERA-Interim reanalysis data. These have been obtained by Dee et al. (2011) by assimilation of different types of observational data (for example from stations, radiosondes, buoys, aircrafts, satellites, etc.) into the ECMWF Integrated Forecast System (IFS, release Cy31r2). The horizontal resolution is about 79 km. Due to the assimilation of the observations it can be expected that the ERA-Interim data perform well, when comparing them with the station data used for model evaluation in the present study. However, Dee et al. (2011) report that no near-surface observations of wind over land have been assimilated. The ERA-Interim data have been downloaded from the CERA

database (ECMWF, 2009a).

5.3.1 Model setup

The ERA-Interim data at about 79 km horizontal resolution and available every 6 hours are used to force a simulation covering Northern Germany, parts of the North Sea, the Baltic Sea and Southern Scandinavia at 15 km horizontal resolution (domain D1, Figure 5-4). The results of domain D1 are used to force a simulation covering parts of Northern Germany at 4 km horizontal resolution (domain D2; black lines in Figure 5-4). The final target domain D3 covers Hamburg Metropolitan Region at 2 km horizontal resolution (red lines in Figure 5-4).

For the present study, the domains have been chosen to be relatively small. It is well known that the larger the model domain is, the larger the deviation becomes between the meteorological situation simulated by the mesoscale model from that in the forcing data (e.g. Schmitt, 2011). Large deviations of the meteorological situations are not desired, because the goal of the downscaling is to capture heavy precipitation events located in an area of about 60 km x 60 km. Therefore, only about 10 to 15 grid points separate the border of the parent nest from the border of the respective child nest to account for the effects of the nesting.
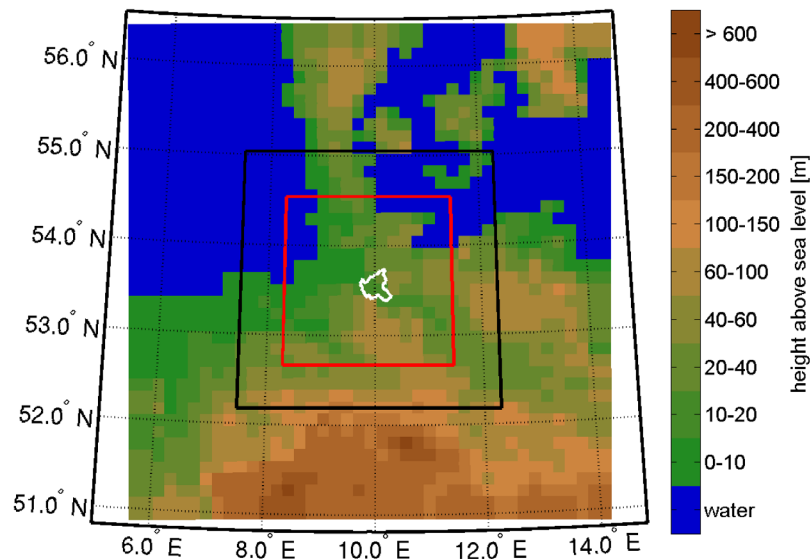
Figure 5-4: Orography of METRAS domain D1 (15 km horizontal resolution). The grid cells with a fraction of water larger than 50% are in blue. The boundaries of domain D2 (4 km horizontal resolution) and domain D3 (2 km horizontal resolution) are outlined with the black and red lines respectively. The white contour line displays the border of the federal state Hamburg.

Different values for the parameters in the forcing factor (Equations (5-28) to (5-30)) are used for each domain and also different variables are forced (Table 5-1). For domain D1, the horizontal

wind components, potential temperature and specific humidity are forced. The vertical wind component is not forced, because it is diagnosed from the hydrostatic approximation in the ECMWF model, which is inconsistent with the non-hydrostatic METRAS model. The cloud and rain water contents from ERA-Interim are not forced, because cloud formation is highly parameterised in the ECMWF model.

Tests with METRAS showed that the wind fields were not well simulated in domain D1 when forcing them only at the boundary. This might be due to the differences in the formulation of METRAS (non-hydrostatic, pressure diagnostic) and the ECMWF model (hydrostatic, prognostic equation for the surface pressure). For this reason, the horizontal wind components but not the potential temperature and the specific humidity are strictly forced towards the wind components from ERA-Interim for domain D1. This is technically achieved by setting the minimum forcing factor δ_{min} to 10^{-3} s^{-1} for the horizontal wind components. With this method, METRAS can calculate the vertical wind component and the pressure field consistent with its formulation based on the horizontal wind components in the ERA-Interim data. The price to be paid is the loss of mesoscale variability of the wind fields within domain D1. The gain lies in much more reliable synoptic flow fields (not shown here).

For the domains D2 and D3, METRAS is forced by the corresponding coarser METRAS output (D2 by D1, D3 by D2). Therefore, for these domains, the vertical wind component as well as the cloud and rain water contents are also forced, because these are prognostic variables in METRAS. In contrast to domain D1, the value of the minimum forcing factor is very small in the domains D2 and D3, allowing METRAS to evolve nearly freely. This is crucial for the feasibility of scenario studies, because the differences of the METRAS results obtained for different surface cover scenarios are only reliable if the model can develop its own solution.

Table 5-1: Dimensions of the grid in x-, y-, vertical direction (NX1, NX2, NX3), forced variables and parameters in Equations (5-28) to (5-30) for the three domains. Note that the minimum forcing factor only applies to the wind components.

Domain	Resolution	$NX1$	$NX2$	$NX3$	Forced variables	δ_0(s^{-1})	A	NH	NV	δ_{min}(s^{-1})
D1	15 km	41	42	34	u, v, θ , q_v	10^{-2}	0.4	5	5	10^{-3}
D2	4 km	78	80	34	u, v, w, θ , q_v, q_c, q_r	10^{-2}	0.4	4	5	10^{-9}
D3	2 km	103	105	34	u, v, w, θ , q_v, q_c, q_r	10^{-2}	0.4	4	4	10^{-9}

The vertical resolution near the surface is 20 m, meaning the first model level is located at 10 m

above ground. The vertical resolution is kept constant over the first 100 m and increases with 17.5% per grid cell to a final value of 1000 m. There are 18 model levels below 1000 m. In 1500 m above ground, the vertical resolution is about 250 m. The top of the model is located at 11 km above ground. With the chosen vertical grid, the influence of the Rayleigh damping starts at about 7 km above ground.

The daily precipitation values used for evaluation of simulation results have been downloaded by Hoffmann (2009; personal communication) via the WebWerdis portal of DWD and are integrated values for the time period from 6:00 UTC to 6:00 UTC. The distribution of the precipitation within the 24 hours is not known. In the simulations, the precipitation could be shifted to another day due to a delay or acceleration of the passage of a front in METRAS compared to reality. For this reason, also the day before and the day after the observed heavy precipitation event are simulated for each meteorological situation. The simulated time period is explained for the example of 27 August 1989. The time period when the "heavy precipitation" has been observed is from 27 August 1989 6:00 UTC to 28 August 1989 6:00 UTC. In order to account for the spin-up of the nested model system, the simulation for domain D1 is started for 25 August 1989 16:00 and conducted until 29 August 1989 8:00. The simulation for domain D2 is started with a delay of 3 hours compared to the simulation for domain D1 in order to not interfere with the initialisation procedure described in Section 5.2.5. The simulation for domain D3 is therefore started for 25 August 1989 22:00. The evaluation of the simulation results against DWD data starts for 26 August 1989 6:00 and ends 29 August 1989 6:00. In the evaluation, the 26 August 6:00 to 27 August 6:00 will be named Day 1, the 27 August 6:00 to 28 August 6:00 Day 2 and the 28 August 6:00 to 29 August 6:00 Day 3.

The SST values provided with the ERA-Interim data have not been used, because they turned out to be too coarse. Indeed, the water surfaces close to the coasts and especially in the mudflats at the shore of the North Sea heat up relatively quickly in early summer compared with the centre of the North Sea and the Baltic Sea. Due to the coarse horizontal resolution, the ERA-Interim SST are more representative for the centre of the North and the Baltic Sea than for the coasts. The daily NOAA OISST (Reynolds et al., 2007; 0.25° horizontal resolution) have used been instead.

For each selected meteorological situation, the average of the daily SST over the entire integration period has been calculated. The SST values close to the shore have been used for estimation of the water temperatures of lakes and rivers within the domain. An increase of the inland water temperatures from North to South is considered by applying a linear interpolation of the SST between the North Sea, the Baltic Sea and the Mediterranean, following the idea of Bungert (2008). However, the inland water temperatures are reduced with a lapse rate of -0.0065 K/m for water surfaces not located at sea level. The soil temperature in the depth of the daily temperature wave $(T_s(-h_\theta))$ is set to the interpolated water temperature of the

corresponding grid cell. Note that the described method for estimation of the inland water temperatures is tailored to the relatively small domain of interest and also the summer season.

The second order centred differences scheme is used for momentum advection. The short waves in the wind fields are damped with a Shapiro 7-point filter. The advection of scalar quantities is solved by a second order upstream scheme, because first order upstream might be too diffusive in many situations (Schoetter, 2010). This could negatively affect the formation of clouds.

5.3.2 Consideration of average pressure tendency

As described in Section 5.2, the pressure deviations p_1 and $\overline{p_2}$ are set to zero at the model top in the standard version of the model. A change in pressure at the model top due to synoptic scale forcing is therefore not accounted for. In past model applications, biases in the order of 10 hPa have been found for pressure in single simulations. Even though absolute levels of pressure are rarely of interest in mesoscale model applications, biases in pressure reduce the precision of the model, because the pressure is used for transformations between model variables. For example the potential temperature of the forcing is calculated based on the pressure of the forcing data. A bias in real temperature is therefore induced, if the pressure in the mesoscale model differs from the pressure in the forcing data.

To improve the model, the domain averaged pressure tendency in the forcing data at the model top is prescribed to the pressure deviation p_1 (Equation (5-33)). The time of initialisation is denoted by t_{init}.

$$\overline{p_1^{top}(t)} = \overline{p_{force}^{top}(t)} - \overline{p_{force}^{top}(t_{init})} \qquad (5\text{-}33)$$

The formulation of METRAS does not allow to prescribe the pressure tendency at each grid point because this would change the gradients of the pressure deviation p_1 and as a consequence cause artificial circulations. In Section 5.4.3, the benefit obtained from this model adaptation will be discussed.

5.3.3 Initialisation of soil moisture dependent on previous days

In case of cold starting METRAS, the soil moisture availability for the different surface cover classes needs to be initialised in an appropriate way. The soil moisture from the ERA-Interim data cannot be used due to inconsistencies in the soil parameterisations of METRAS and the ECMWF model. In the default model setup, the soil moisture availability is set to values representing soils that receive regular precipitation.

In the present study, a simple approach for the soil moisture initialisation developed by Schlünzen (2012; personal communication), is tested. Based on the vertical profile used for initialisation of the three-dimensional model (Section 5.2.5), the one-dimensional model is integrated for the "number of dry days" that is prescribed by the modeller. During this integration, the budget equations for temperature and humidity at the surface are solved for all surface cover classes occurring in the model domain, and the soil moisture availability is reduced in all surface cover classes according to the simulated evaporation (Equation (5-26)). The formation of clouds and precipitation is not allowed. At the end of the integration, the modified values for the soil moisture availabilities are passed to the three-dimensional model.

In the present study, the "number of dry days" is defined as the number of days before the initialisation day with less than 2 mm/d precipitation when averaged over the stations displayed in Figure 5-2. One day is added for technical reasons to the "number of dry days". The "number of dry days" is not allowed to be larger than 10. A histogram of the "number of dry days" used for the selected meteorological situations is shown in Figure 5-5. For about half of the meteorological situations, the "number of dry days" is 1 or 2, meaning that the soil moisture availability is not much changed compared to starting the model with the default values. At the other end, the "number of dry days" is 10 for 9 meteorological situations. In these cases, the soil moisture availability will be much lower compared to the default model setup.
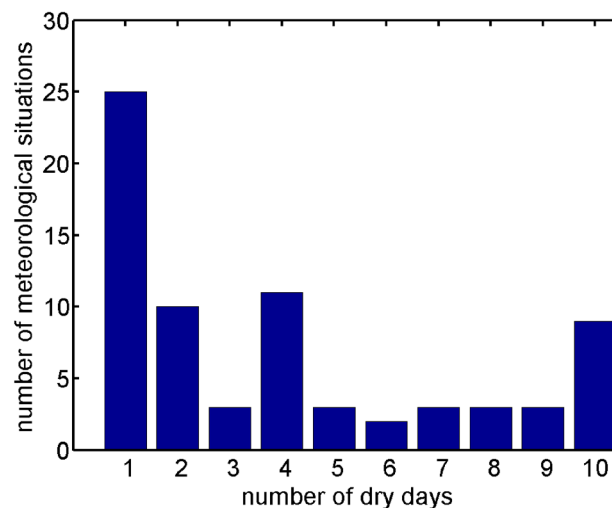
Figure 5-5: Histogram of the "number of dry days" used for initialisation of soil moisture availability.

The applied methodology has several weak points. First, the "number of dry days" is in reality not the same at each grid point in the model domain. Second, the evaporation is calculated based on the meteorological conditions at the initialisation grid point allowing for a diurnal cycle, but the large-scale meteorological conditions are kept unchanged. In reality, the meteorological

conditions might have changed during the dry period, leading to different values of soil moisture availability. In Section 5.4.3, the benefit from the described soil moisture initialisation compared with the standard model setup will be analysed.

5.3.4 Treatment of cloud and rain water content

In past model applications, the cloud and rain water contents from the forcing data have been added to the specific humidity of the forcing data leading to oversaturation at some grid points. In the context of the present study, it has been discovered that this approach can lead to unphysical growing of clouds during the initialisation phase. As described in Section 5.2.5, the forcing data are prescribed at each grid point in the model domain during the initialisation phase. At each grid point with oversaturation, the water vapour excess immediately condensates to cloud water (Equation (5-13)). Dense stratiform clouds can therefore form within the initialisation phase, because the specific humidity is forced back towards the oversaturated value. This can cause large errors in particular simulations. The described problem can also occur at the lateral boundaries during the entire model integration, because here a strong forcing is applied. This can lead not only to the formation of artificial clouds but also to artificial precipitation at the boundaries, reaching values of more than 100 mm/d.

Several measures have been taken to avoid the described problems. In domain D1, the cloud and rain water content from the ERA-Interim data are no longer added to specific humidity and no longer used. This means that no clouds enter the domain D1. Therefore, the clouds have to grow within this domain. In the domains D2 and D3, the cloud and rain water contents of the domains D1 and D2, respectively, are not added to specific humidity but are forced themselves. Further, the formation of clouds and precipitation is no longer allowed during the initialisation phase. This avoids the creation of artificial clouds or wetting of the soil due to artificial precipitation.

With the described model adaptations, the largest errors due to the formation of artificial clouds and precipitation at the lateral boundaries or during the initialisation phase have been removed. However, problems still occurred in some simulations because the interpolation of specific humidity and air temperature from the grid of the parent nest to the grid of the respective child nest can lead to oversaturation. Further, small differences between the solutions of the mesoscale model (for example 1 K lower air temperature compared with the forcing data) can lead to the formation of stratiform clouds if the air in the forcing data is close to saturation. For this reason, Equation (5-27) is modified for the case of specific humidity to ensure that the specific humidity in METRAS (q_{vf}) is no longer forced to values higher than 99% of its saturation value q_{vf}^{SAT} (Equation (5-34)). It needs to be pointed out that this threshold is arbitrary and a compromise between removing a part of the water vapour and risking the deterioration of the simulation results due to artificial formation of stratiform clouds.

$$q_{vf} = q_{vu}(1 - \delta) + \delta \, min(q_c, 0.99 \, q_{vf}^{SAT}) \qquad\qquad (5\text{-}34)$$

5.3.5 Interpolation of the forcing wind components

The ERA-Interim data are available every 6 hours, which is a much coarser temporal resolution than the time step used in METRAS (1 s to 10 s). The forcing data are interpolated linearly in time between two forcing times. For the thermodynamic variables, this can lead to inconsistencies resulting for example in values of the relative humidity larger than 100%, a problem that has already been tackled in Section 5.3.4.

For the wind components, a systematic error appears due to the time interpolation. In case of rapid changes of the wind direction, the time interpolation of the u- and v-wind components of the forcing data will lead to an artificial reduction of the wind speed. To solve this problem, the wind speed and wind direction of the forcing data for the two forcing times before and after the model time are calculated. The wind speed and wind direction of the forcing are linearly interpolated in time. Finally, the u- and v-wind components of the forcing data are calculated from the time interpolated wind speed and wind direction of the forcing data. With this method, the magnitude of the wind vector in the forcing data is preserved.

The chosen methodology involves interpolation of the u- and v-wind components of the forcing data from the vector grid points of the Arakawa-C grid to the scalar grid points to calculate the wind speed and wind direction. After time interpolation, the u- and v-wind components of the forcing have to be interpolated to the vector grid points. Precision might be lost due to this double interpolation. This might deteriorate the solution in situations with relatively stationary wind fields. However, an improvement can be expected in meteorological situations with rapidly changing wind direction. Tests showed a slight improvement of the simulated wind direction and wind speed (not shown).

5.4   Evaluation of simulation results

Evaluation of simulation results is split into two parts. Simulated hourly values of air temperature, specific humidity, wind speed and wind direction are evaluated against hourly routine observations taken by DWD, being space and time consistent. The routine observations have been provided by DWD for model evaluation purpose. The location of the stations is displayed in Figure 5-3a. Simulated daily precipitation values are evaluated against daily precipitation values observed by DWD at the stations shown in Figure 5-2, being space consistent.

METRAS aborted for 2 out of the 74 selected meteorological situations: once in domain D1 and

once in domain D2. Large errors of the simulated meteorological variables have been detected for domain D1 in both cases. This might be due to shortcomings of the ERA-Interim data for these meteorological situations and, therefore, the analysis is reduced to the remaining 72 meteorological situations.

5.4.1   Evaluation of hourly values

Simulated air temperature, specific humidity, wind speed and wind direction in 10 m above ground are taken for the evaluation. This corresponds to the simulated values at the lowermost model level, a vertical interpolation is not needed. The time series is extracted from the METRAS grid cell closest to the DWD station, but not horizontally interpolated to the position of the station. No altitude correction has been applied. Simulated air temperature and specific humidity in 10 m above ground are compared to the observations in 2 m above ground. This height inconsistency accounts for some differences, for example in air temperature. Bedbur (2012) compared the measured air temperature in 2 m above ground to the measured air temperature in 10 m above ground at the Hamburg Weather Mast. The RMSE for air temperature is 0.5 K for stable stratification and 0.35 K for unstable stratification. The BIAS is 0.37 K for stable stratification and -0.31 K for unstable stratification. These values have to be kept in mind for interpretation of evaluation results.

In order to assure an objective model evaluation, the evaluation measures bias (BIAS), root mean square error (RMSE), hit rate (HITR) and skill variance (SKVAR) as defined by Schlünzen and Sokhi (2008) (Table 5-2) are calculated separately for each selected meteorological situation and each DWD station. A weighted average of the evaluation measures obtained for the single stations is calculated for each selected meteorological situation. The weights are the number of measurements available at the different stations. The weighted averages obtained with this method for the 72 selected meteorological situation will be displayed as crosses in the Figures 5-6 and 5-8 to 5-10.

The evaluation measures are calculated for the results of METRAS domain D3 (METRAS-D3; 2 km horizontal resolution) and for the ERA-Interim data after being interpolated in space and time to force the simulation for domain D1. Only the same measurement sites are considered in the evaluation. The ERA-Interim data interpolated in space and time are named hereafter as the "Forcing". Additionally, the evaluation measures are calculated for a forecast obtained by using the DWD observations of the initialisation day as persistence forecast for the days simulated ("Persistence"). Very high errors appear for Persistence in some meteorological situations. Therefore, only the median of the 72 averaged evaluation measures will be shown for Persistence.

Table 5-2: Evaluation measures for mesoscale models considered in the present study. The symbols M_i and O_i denote the simulated and observed meteorological variable at hour i, N is the total number of observations, $\bar{M}$ is the model result averaged over all hours with observations. For HITR, the values of the desired accuracy DA have been chosen according to Cox et al. (1998) to be ± 2 K for air temperature, ± 1 g/kg for specific humidity, ± 1 m/s for wind speed, $\pm 30°$ for wind direction and ± 1.7 hPa for pressure. One has to note that DA denotes a desired accuracy and not the uncertainty of the observational data as it has been used in Chapter 2.

Abbreviation	Denomination	Formula	Optimum value
BIAS	Bias	$BIAS = \dfrac{1}{N}\sum_{i=1}^{N}(M_i - O_i)$	0
RMSE	Root mean square error	$RMSE = \sqrt{\dfrac{1}{N}\sum_{i=1}^{N}(M_i - O_i)^2}$	0
HITR	Hit rate	$HITR = \dfrac{1}{N}\sum_{i=1}^{N}\begin{cases} 1 & if \ \lvert M_i - O_i\rvert \le DA \\ 0 & else \end{cases}$	1
SKVAR	Skill variance	$SKVAR = \dfrac{\sum_{i=1}^{N}(M_i - \bar{M})^2}{\sum_{i=1}^{N}(O_i - \bar{O})^2}$	1

To quantify the significance of differences in the performance between METRAS-D3, Forcing and Persistence, a bootstrap resampling (10000 resamples) is applied to the median of the averaged evaluation measures obtained for the 72 meteorological situations. In the Tables 5-3 to 5-6, the median of the evaluation measures as well as the 5th and the 95th percentile of the resampled medians (90% confidence interval) are displayed. A difference between the median of the evaluation measures for two different models (e.g. METRAS-D3 and Forcing) is called significant if the 5th percentile of the resampled medians of the evaluation measures for METRAS-D3 is higher than the 95th percentile of the resampled medians of the evaluation measures for Forcing or vice versa.

If possible, evaluation results obtained in the present study are compared to evaluation results obtained for other mesoscale model applications of similar horizontal resolution. A literature summary has been compiled by Conrady (2010). However, one has to keep in mind that the comparison with other studies is not always justified, because the model applications differ in domain size, simulated meteorological situation and characteristics of the model domain. Further, for some of the studies the evaluation measures are calculated for forecasts, whereas in the

present study, METRAS is applied in hindcast mode forced with reanalysis data.

For the interpretation of the evaluation results it needs to be considered that the station data are subject to measurement errors and lack spatial representativity. Lengfeld and Ament (2012) investigated the representativity with a network of 13 stations at distances of 140 m to 370 m for a site dominated by different types of cropland in Western Germany during the summer season. They report an RMSE of 0.86 K for air temperature and of 0.67 g/kg for specific humidity if one station is used to represent a transect of about 2.3 km length. Even though the results might not be the same for each surrounding of a DWD station, they indicate that an RMSE lower than about 1 K for air temperature and about 0.7 g/kg for specific humidity cannot be expected without using model output statistics.

Evaluation results for air temperature are shown in Figure 5-6, the values for the medians of the averaged evaluation measures in Table 5-3. The Forcing performs very well. The absolute value of the BIAS is below 1 K for nearly all simulations, the median value of the BIAS is 0.0 K. The median value of the RMSE is 1.5 K. The median value of the HITR is 0.83. This shows that the air temperature of Forcing is mainly within the desired accuracy. It has to be mentioned that the routine observations used for evaluation might have been partly assimilated during the creation of the ERA-Interim reanalysis. Nevertheless, the evaluation indicates that, at least close to the surface, the quality of Forcing is high, despite its coarse spatial resolution and the linear interpolation between 6-hourly output times. However, due to the coarse resolution and the interpolation in time, Forcing significantly underestimates the variance of the time series (the median value of the SKVAR is 0.75).

(a)

(b)

(c)

(d)
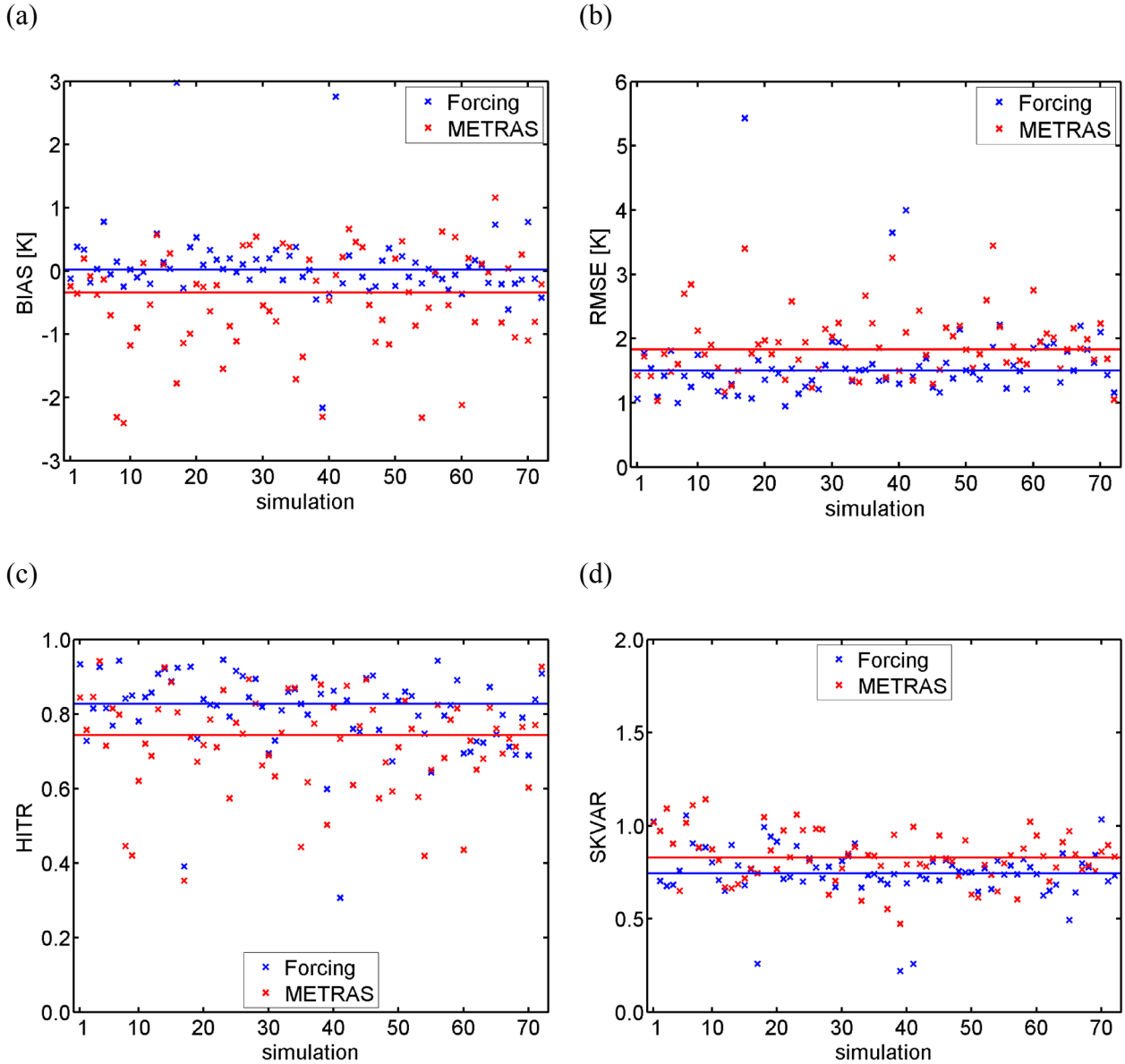
Figure 5-6: Model evaluation measures (a) BIAS, (b) RMSE, (c) HITR and (d) SKVAR for air temperature simulated for METRAS-D3 (red crosses). The evaluation measures obtained for Forcing are shown for comparison (blue crosses). Each cross denotes the weighted average of the evaluation measures obtained for the different DWD stations within domain D3 for one of the 72 meteorological situations. The median of the averaged evaluation measures is displayed with the red (METRAS-D3) and blue lines (Forcing).

Table 5-3: Median (bold) and 5% to 95% confidence interval for the different evaluation measures calculated for air temperature. The BIAS and RMSE have been rounded to 0.1 K, the HITR and SKVAR to 0.01.

Model	BIAS [K]			RMSE [K]			HITR			SKVAR		
METRAS-D3	- 0.5	**- 0.3**	- 0.2	1.8	**1.8**	1.9	0.72	**0.74**	0.76	0.80	**0.83**	0.84
Forcing	- 0.1	**+0.0**	+0.1	1.4	**1.5**	1.5	0.82	**0.83**	0.84	0.73	**0.75**	0.77
Persistence	- 0.1	**+0.6**	+1.1	3.0	**3.2**	3.4	0.43	**0.47**	0.50	0.82	**0.95**	1.05

Evaluation indicates that METRAS-D3 results are slightly more deviant from observations than Forcing. The main reason for the deviations is an underestimation of air temperature during the day leading to an average BIAS of about -1 K for 12:00 local time. This is highlighted by Figure 5-7, which displays the BIAS averaged over all meteorological situations as a function of the local time. The negative BIAS during the day can partly be due to usage of air temperature in 10 m above ground instead of air temperature in 2 m above ground. However, the BIAS of -0.31 K reported by Bedbur (2012) for unstable stratification is too low to explain the full negative BIAS obtained for the results of METRAS-D3 at 12:00 local time. The main reason for the negative BIAS is the occurrence of situations with too pronounced stratiform clouds reducing the solar insulation during the day. This can lead to a BIAS of down to -2.5 K for some meteorological situations; Figure 5-6a). As a consequence, the median value of the BIAS for METRAS-D3 (-0.3 K) is significantly negative, and the median value of the RMSE for METRAS-D3 (1.8 K) is significantly higher than the median value of the RMSE of Forcing. Also the median value of the HITR for METRAS-D3 is significantly lower than the median value of the HITR for Forcing. The median value of the SKVAR of METRAS-D3 is significantly improved compared to the median value of the SKVAR of Forcing, but significantly lower than the optimum value of 1. The mesoscale model METRAS adds variability to the time series compared with the coarsely resolved and time interpolated Forcing. The median values of the RMSE and HITR for METRAS-D3 and for Forcing are significantly better than for Persistence. For METRAS-D3, the median value of the BIAS is significantly worse than for Persistence. The median value of the SKVAR is closer to the optimum value of 1 for Persistence than for METRAS-D3 and Forcing.

For SKVAR, METRAS-D3 performs slightly worse than the median of other evaluation studies summarised in Conrady (2010). For RMSE, METRAS performs clearly better than the median from other evaluation studies (2.4 K) and is close to the 10th percentile of the best models (1.5 K). For the BIAS, METRAS-D3 performs close to the median value of the BIAS obtained in other model applications. Finally, it is mentioned that the lowest values of the RMSE obtained for single meteorological situations (Figure 5-6b) are about 1.0 K for both METRAS-D3 and

Forcing. This is very close to the value reported by Lengfeld and Ament (2012) as the best possible value of the RMSE for comparison with one single station in a transect of about 2.3 km length. Even though more than one station is used for evaluation, the values for the RMSE cannot cancel out.
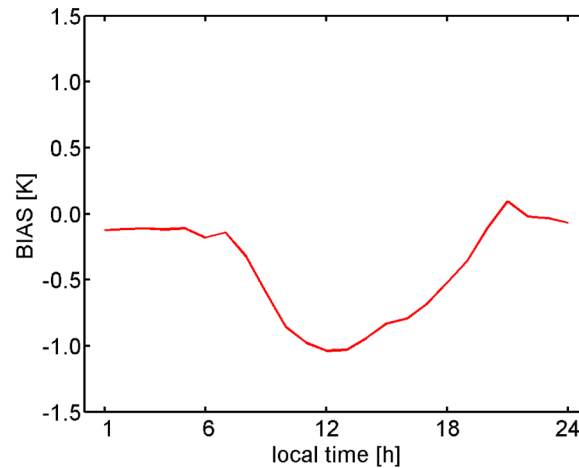
Figure 5-7: BIAS of air temperature as a function of local time for METRAS-D3 averaged over all stations and selected meteorological situations.

Evaluation results for specific humidity are displayed in Figure 5-8, the median values of the evaluation measures in Table 5-4. Similar to air temperature, very good evaluation measures are obtained for Forcing with a median value of the BIAS of +0.1 g/kg and a median value of the RMSE of 0.8 g/kg. The specific humidity for METRAS-D3 (median value of the BIAS of 0.0 g/kg) is slightly lower than for Forcing, which is physically consistent with the lower air temperature. The median values of the RMSE and HITR for METRAS-D3 are slightly but significantly worse than for Forcing, but clearly and significantly better than for Persistence (Table 5-4). In contrast to METRAS-D3 and Forcing, Persistence significantly underestimates the specific humidity, which is due to the selection of the meteorological situations. These become systematically more humid during the course of the integration, because heavy precipitation occurs on Day 2 in the observations. The variance of the time series is slightly but significantly underestimated by both METRAS-D3 and Forcing, but both are significantly better than Persistence. The comparison of the median value of the BIAS with the values summarised in Conrady (2010) shows that METRAS-D3 performs very close to the median BIAS for other mesoscale model applications. The lowest values of the RMSE obtained from Forcing and METRAS-D3 for single meteorological situations are between 0.6 g/kg and 0.7 g/kg (Figure 5-8b), which is again very close to the best possible value reported by Lengfeld and Ament (2012).

(a)

(b)

(c)

(d)
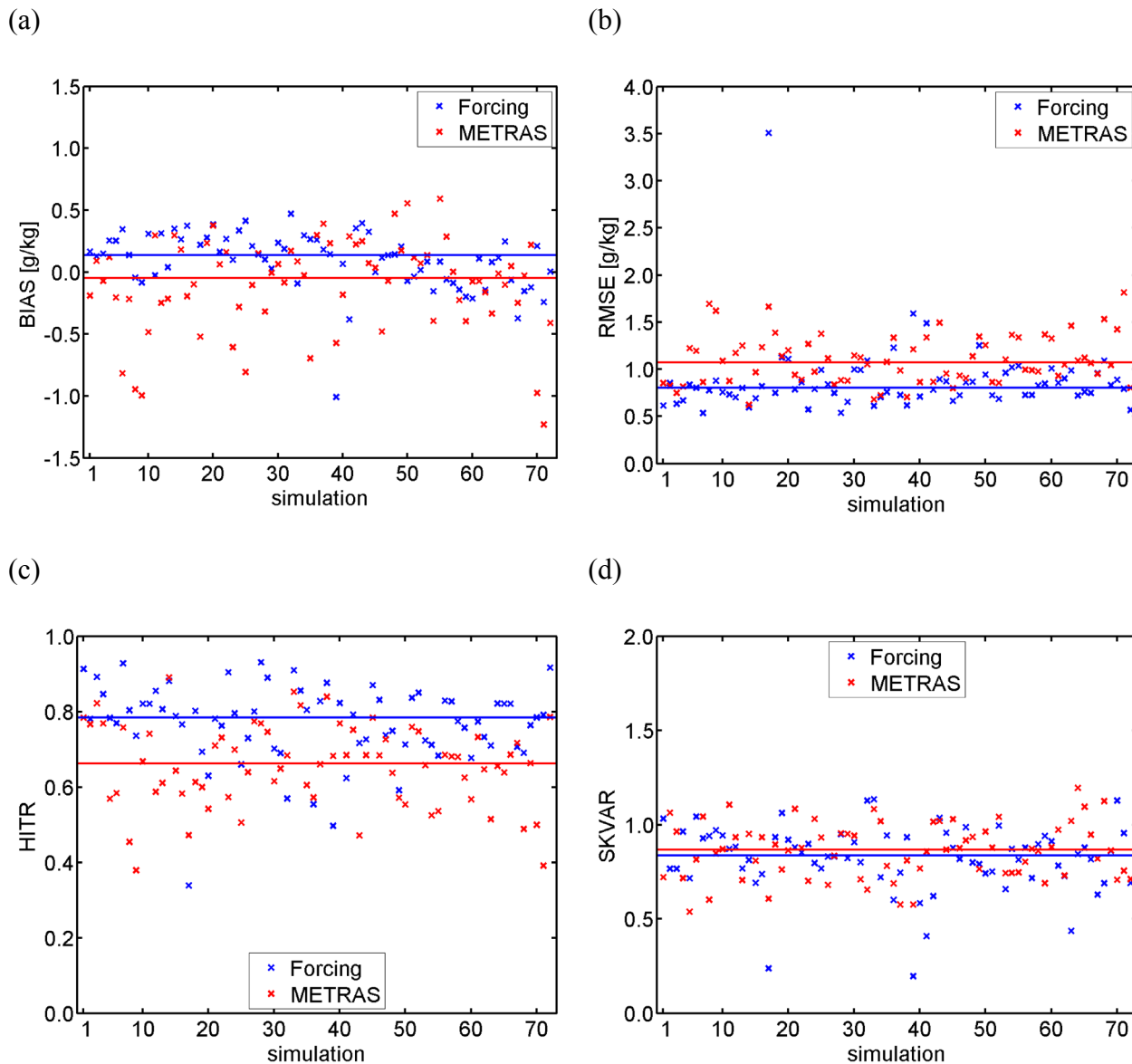
Figure 5-8: Same as Figure 5-6, but for specific humidity.

Table 5-4: Same as Table 5-3, but for specific humidity. The BIAS and RMSE have been rounded to 0.1 g/kg.

Model	BIAS [g/kg]			RMSE [g/kg]			HITR			SKVAR		
METRAS-D3	- 0.1	**+0.0**	+0.0	1.0	**1.1**	1.1	0.64	**0.66**	0.68	0.84	**0.87**	0.88
Forcing	+0.1	**+0.1**	+0.2	0.8	**0.8**	0.8	0.77	**0.78**	0.80	0.82	**0.84**	0.88
Persistence	- 0.7	**- 0.4**	- 0.3	1.6	**1.8**	1.9	0.37	**0.42**	0.43	0.63	**0.69**	0.75

Evaluation results for wind speed are shown in Figure 5-9, the median values of the evaluation measures are summarised in Table 5-5. The median value of the BIAS is strongly and significantly negative for Forcing. This is nearly entirely corrected in METRAS-D3 resulting in a strong and significant improvement of the median value of the BIAS. Also, the median value of the RMSE and the median value of the HITR are slightly but significantly better for METRAS-D3 than for Forcing. The comparatively weak performance of Forcing could be due to the neglect of near-surface observations of wind from land stations during the creation of the ERA-Interim reanalysis.

The median value of the HITR for wind speed is relatively low for both METRAS-D3 and Forcing. The simulated wind speed is within the desired accuracy of 1 m/s in less than 50% of the hours. Therefore, a desired accuracy of 1 m/s for wind speed is judged to be very challenging for the models. Nevertheless, both Forcing and METRAS-D3 perform significantly better than Persistence, except for the median value of the BIAS. Similar to air temperature and specific humidity, the variance of the time series is slightly but significantly underestimated by METRAS-D3. Consistent with the underestimation of the absolute values of wind speed, the variance of the time series of wind speed is strongly underestimated by Forcing. The median value of the BIAS in wind speed from other mesoscale model applications is mainly positive (Conrady, 2010). Therefore, the median value of the BIAS for METRAS-D3 is closer to the optimum value of 0 m/s than the median value of the BIAS for other mesoscale model applications. The median value of the RMSE is very close to the median value of the RMSE of other mesoscale model applications, the median value of the SKVAR is slightly worse.

Evaluation results for wind direction are displayed in Figure 5-10, the median values of the evaluation measures in Table 5-6. Only the HITR and RMSE have been calculated for wind direction. The median value of the RMSE for METRAS-D3 is significantly higher than the median value of the RMSE for Forcing. Correspondingly the median value of the HITR is significantly lower for METRAS-D3 than for Forcing. Both evaluation measures are strongly and significantly better than for Persistence. The comparison of the median value of the RMSE with the values from Conrady (2010) shows that METRAS-D3 performs better than the 10th percentile of the values for the RMSE obtained from other mesoscale model evaluation studies.

(a)   (b)

(c)   (d)
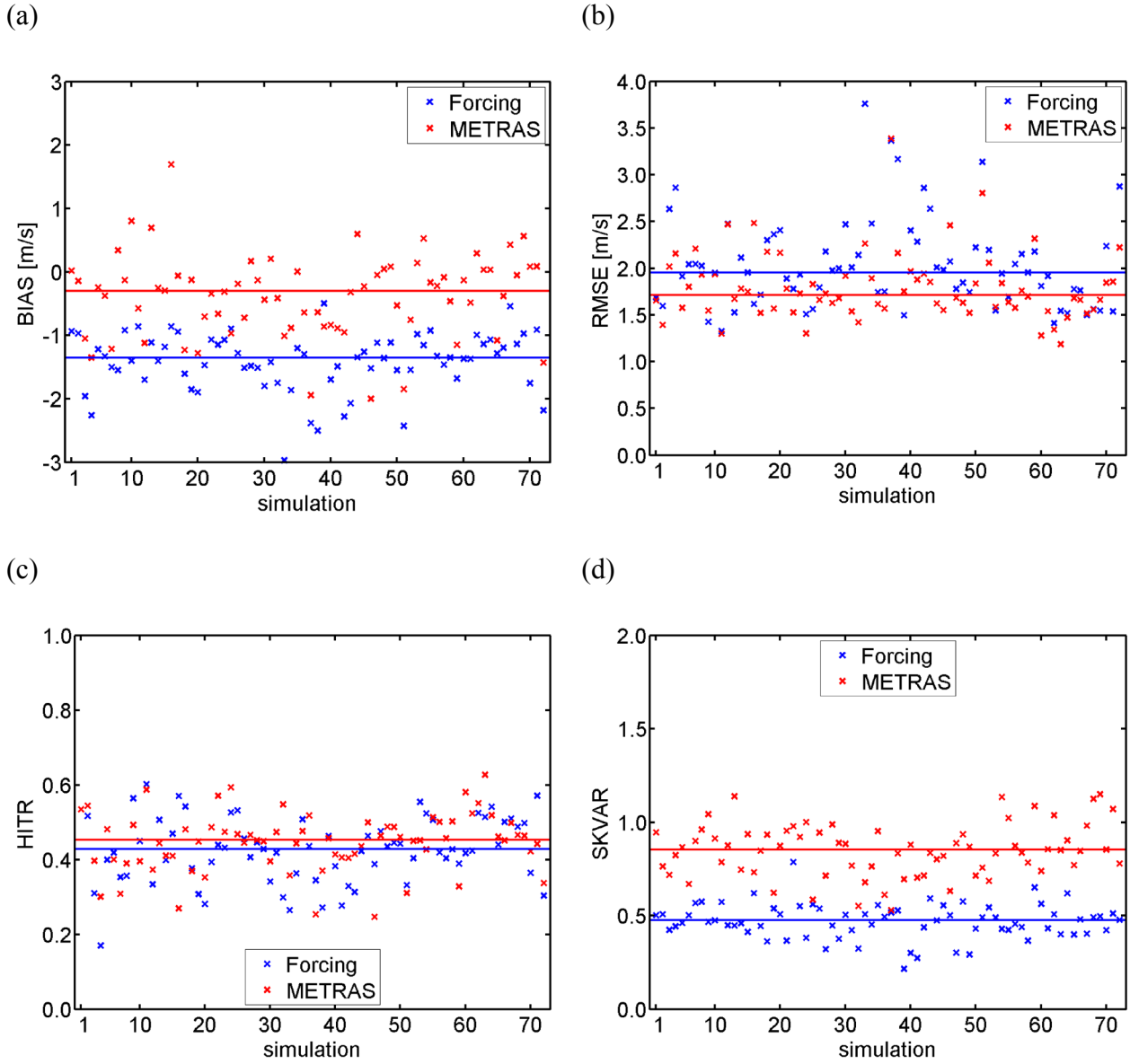
Figure 5-9: Same as Figure 5-6, but for wind speed.

Table 5-5: Same as Table 5-3, but for wind speed. The BIAS and RMSE have been rounded to 0.1 m/s.

Model	BIAS [m/s]			RMSE [m/s]			HITR			SKVAR		
METRAS-D3	-0.4	**-0.3**	-0.2	1.7	**1.7**	1.8	0.45	**0.45**	0.46	0.83	**0.85**	0.87
Forcing	-1.4	**-1.4**	-1.3	1.9	**2.0**	2.0	0.42	**0.42**	0.44	0.45	**0.47**	0.49
Persistence	-0.3	**-0.1**	+0.0	2.1	**2.2**	2.3	0.26	**0.28**	0.29	0.70	**0.73**	0.79

(a) (b)
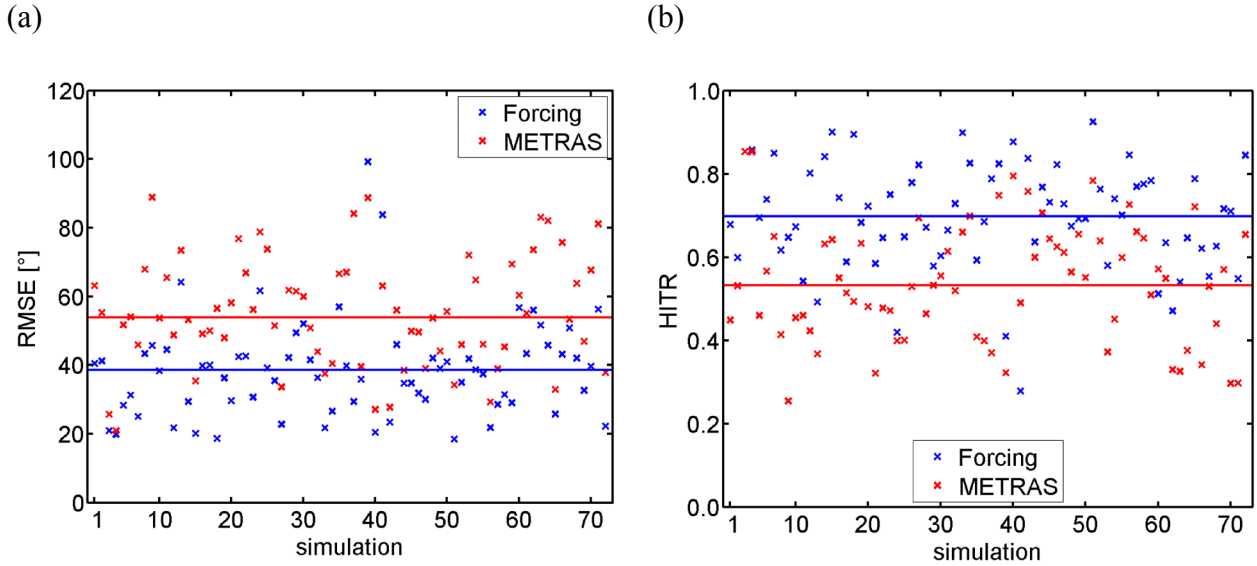
Figure 5-10: Same as Figure 5-6, but for (a) RMSE and (b) HITR for wind direction.

Table 5-6: Same as Table 5-3, but for RMSE and HITR for wind direction. The RMSE has been rounded to 1°, the HITR to 0.01.

Model	RMSE [°]			HITR		
METRAS-D3	52	**54**	56	0.51	**0.53**	0.56
Forcing	35	**38**	40	0.68	**0.70**	0.73
Persistence	90	**93**	98	0.21	**0.26**	0.30

5.4.2 Evaluation of daily precipitation values

Similar to air temperature, daily precipitation values at the METRAS grid cell that is closest to the DWD station are used for evaluation.

It is investigated how often the criterion of more than 25 mm/d is actually met at one of the target stations at Day 2. The target stations are the measurement sites that were used for the selection of the meteorological situations. The target stations are displayed with the red dots in Figure 5-2. Day 1 and Day 3 are also investigated to account for possible errors in timing of heavy precipitation. Due to the low spatial representativity of daily precipitation amounts it is possible that a heavy precipitation event is simulated in the area in between the target stations, but not at the location of the stations. Therefore, it is also calculated how often 25 mm/d precipitation is simulated at least in one grid cell of a control domain surrounding the stations. The location of the control domain is depicted by the red lines in Figure 5-2. The obtained number of events with

heavy precipitation is shown in Table 5-7.

Table 5-7: Number of events (out of 72 possible) with precipitation above 25 mm/d or above 10 mm/d at one of the stations used for the selection of the meteorological situations or at least in one grid cell in the control domain depicted in Figure 5-2. In the last row, it is denoted how often the criterion is met at least at one of the 3 days.

	>= 25 mm, station	>=25 mm, domain	>= 10 mm, station	>= 10 mm, domain
Day 1	6	12	17	24
Day 2	21	32	38	48
Day 3	10	22	23	38
at least one day	31	43	51	63

The criterion is met most often at the day with observed heavy precipitation (Day 2). This gives general confidence in the setup of the model. However, the criterion used for the selection of the meteorological situations is precisely achieved only in 21 out of 72 simulations. In 32 out of 72 simulations the more tolerant criterion of 25 mm/d precipitation within the control domain at Day 2 is achieved. If also Day 1 and Day 3 are included, heavy precipitation is obtained in 43 out of 72 simulations. Therefore, heavy precipitation is obtained in about 60% of the simulations within the control domain for at least one of the simulated days. These heavy precipitation events can be investigated in further scenario studies.

The comparatively low number of events with more than 25 mm/d can be due to the horizontal resolution of 2 km which might limit the intensity of convective cells. The meteorological situations have been selected based on the exceedance of 25 mm/d in point-scale observations whereas the METRAS-D3 results represent an average over an area of at least 2 km x 2 km. Due to filters and numerical dispersion, the effective resolution of the model is even lower. The difference between the point-scale observations of heavy precipitation and the area-averaged model result can account for the differences between simulated and observed precipitation (Bohnenstengel et al., 2011).

The exceedance of 10 mm/d precipitation is also investigated. In the simulations carried out, an exceedance of 10 mm/d is simulated for 48 out of 72 simulations at Day 2 and even for 63 out of 72 simulations for at least one of the three simulated days. This result shows that an event with more than 10 mm/d is simulated within the control domain for more than 85% of the selected meteorological situations.

The spatial distribution of the simulated daily precipitation amounts is displayed in Figure 5-11 as average over all simulated days (3 x 72) per station. The average precipitation amount is considerably underestimated at nearly all the stations. This is no surprise, because at least for the target stations (station numbers mainly between 1 and 20), heavy precipitation occurs at least at one of the stations for every selected meteorological situation at Day 2. As it has been shown, METRAS simulates heavy precipitation only in about 60% of the selected meteorological situations resulting in the underestimation of the average precipitation amounts, especially for the target stations.

Figure 5-11 reveals that for the stations located in the south of the model domain in the area with low hills of up to 150 m (station numbers 20 to 40), more precipitation is simulated than in the northeast of the domain. This pattern is not found in the observation data. The reason for the wrong pattern of the average precipitation amount could be the triggering of convection due to orography in the south and southeast of the model domain, a forcing that is nearly missing in the northwest of the domain, because here the air is advected over the water surfaces or over very flat land with little surface heterogeneity. In contrast, the convective cells can form relatively fast in the southeast of the model domain, triggered by small-scale orography induced updrafts and downdrafts.
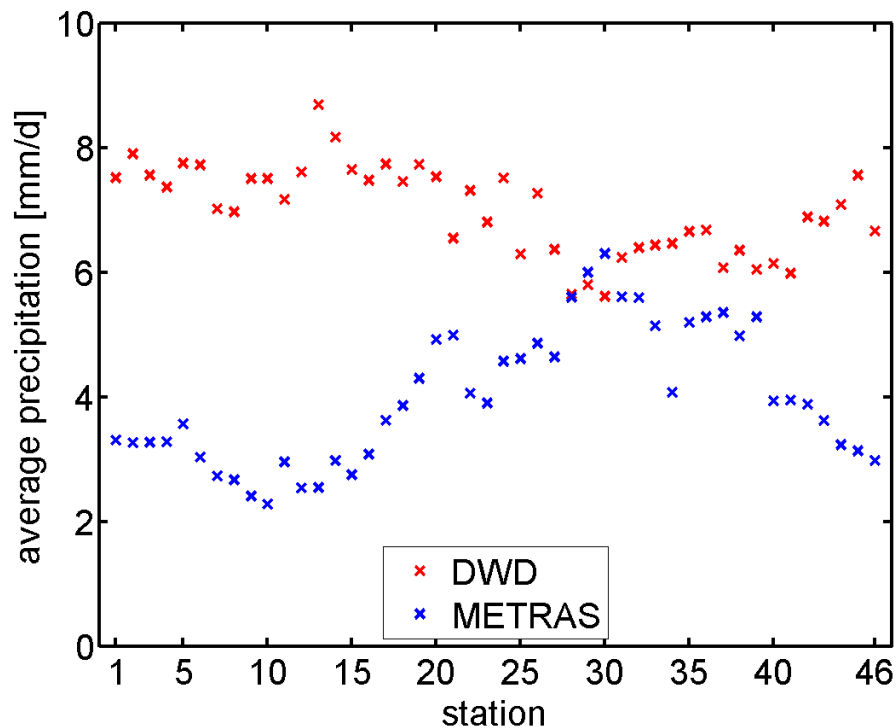
Figure 5-11: Average daily precipitation over all simulated days (3 x 72) observed at the DWD stations (red crosses) and simulated by METRAS (blue crosses). The location of the stations is displayed in Figure 5-2.

The representativity of the simulated precipitation is compared to the representativity of observed precipitation. For this purpose, the conditional probability that a precipitation amount exceeding a certain threshold is simulated at station B, if a precipitation amount exceeding the same threshold is simulated at station A, is calculated. The results for the conditional probabilities have been averaged over 4 km bins in the distance between the stations in order to eliminate the noise. The conditional probabilities are displayed in Figure 5-12 for the thresholds 1 mm/d, 5 mm/d, 10 mm/d, 15 mm/d and 25 mm/d, and are compared to the corresponding conditional probabilities obtained for the DWD data.
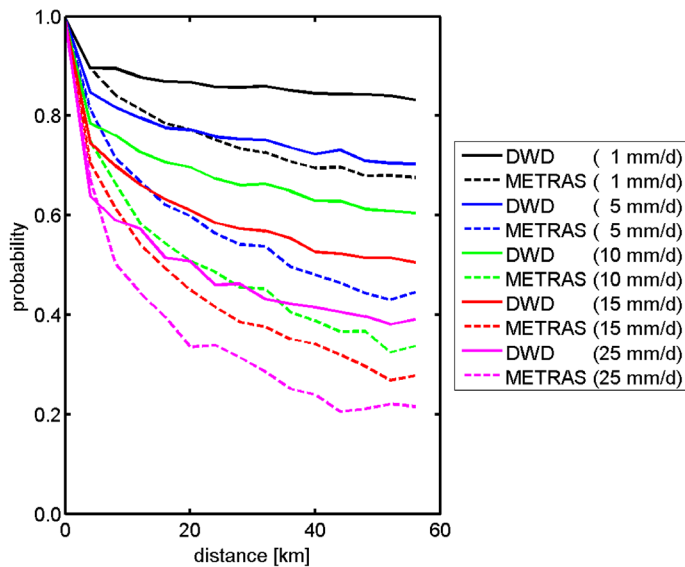
Figure 5-12: Conditional probability that a daily precipitation amount exceeds a threshold at station B if the daily precipitation amount has exceeded the same threshold at station A as a function of the distance between the stations A and B. The probabilities have been averaged over bins of 4 km in the distance between the stations.

By definition, the conditional probability is 1 for a distance of 0 km between the stations. Apart from this, the conditional probability decreases with increasing distance between the stations. For the selected meteorological situations, the representativity of precipitation exceeding the threshold of 1 mm/d is high in the DWD data. The conditional probability is above 80% even at a distance of 50 km between two stations. The higher the threshold for daily precipitation, the lower is the representativity. The conditional probability is reduced to about 40% for the threshold of 25 mm/d and a distance of 50 km between the stations.

For all thresholds, the representativity of the simulated precipitation is lower than the representativity of the observed precipitation. For the threshold of 25 mm/d, the conditional probability is only 20% for a distance of about 50 km when based on model results, but 40% when based on observations. This result is partly due to the fact that heavy precipitation events

are simulated in the south of the domain while they are not in the northwest of the domain. The lower representativity of simulated precipitation as well as the lack of "heavy precipitation" in about 40% of the selected meteorological situations contribute to the total underestimation of precipitation.

5.4.3 Impact of model adaptation on model skill

In this section, the impact of the model adaptation on model skill is quantified. The simulations have been repeated without consideration of the average pressure tendency at the model top for domain D1 and without soil moisture initialisation for the domains D1 and D2. The simulations have not been repeated for domain D3 due to the high computational costs.

The median value of the RMSE for pressure is significantly reduced (by more than a factor of two) if the average pressure tendency at the model top is considered (Table 5-8). The median value of the HITR for pressure is significantly increased, but still low, because the model is not able to simulate the pressure within the desired accuracy of 1.7 hPa in many meteorological situations. The median value of the BIAS for pressure is not significantly changed. However, in contrary to the observed pressure, the simulated pressure has not been converted to mean sea level pressure. This might explain the negative BIAS of pressure. No significant difference of the median values of the evaluation measures is detected for the variables air temperature, specific humidity, wind speed and wind direction. Therefore, it can be concluded that the consideration of average pressure tendency at the model top is not crucial, except if the simulated values of pressure are of interest.

Table 5-8: Median and 5% to 95% confidence interval of the model evaluation measures for pressure obtained with and without consideration of the average pressure tendency at the model top for domain D1. The values for the BIAS and the RMSE have been rounded to 0.1 hPa, the values for the HITR to 0.01.

Model setup	BIAS [hPa]			RMSE [hPa]			HITR		
consideration of average pressure tendency (cases in Section 5.3.2)	-2.6	**-2.4**	-2.3	2.5	**2.7**	3.0	0.25	0.32	0.37
no consideration of average pressure tendency (original model)	-3.6	**-2.8**	-2.0	6.2	**6.8**	7.2	0.18	0.21	0.24

When using the default values for the soil moisture availability from Schlünzen et al. (2012a), corresponding to soils that receive regular precipitation, the specific humidity is significantly overestimated (Table 5-9). With the soil moisture initialisation described in Section 5.3.3, the median value of the BIAS for specific humidity is significantly reduced by 0.1 g/kg. The median

values of the RMSE and HITR for specific humidity are not significantly changed by the soil moisture initialisation. No significant change of the median values of the evaluation measures is detected for the other meteorological variables. The relatively low impact of soil moisture initialisation might be due to the very moist meteorological situations that have been downscaled. A larger improvement of the simulated specific humidity can be expected for meteorological situations with less precipitation.

Table 5-9: Median and 5% to 95% confidence interval of the model evaluation measures for specific humidity obtained with and without soil moisture initialisation for domain D2. The values for the BIAS and the RMSE have been rounded to 0.1 g/kg, the values for the HITR to 0.01.

Model setup	BIAS [g/kg]			RMSE [g/kg]			HITR		
soil moisture initialisation (cases in Section 5.3.3)	0.0	**0.1**	0.1	1.1	**1.1**	1.1	0.64	0.66	0.67
no soil moisture initialisation (original model)	0.1	**0.2**	0.2	1.1	**1.1**	1.1	0.63	0.66	0.67

5.5 Conclusions

In this chapter, heavy summer precipitation events between 1982 and 1998 have been downscaled with the mesoscale atmospheric model METRAS to a domain covering Hamburg Metropolitan Region at 2 km horizontal resolution. The selection of the meteorological situations as well as the setup and adaptation of METRAS has been described. The simulation results have been evaluated against routine observations made by DWD.

The median values of the BIAS are very small for air temperature, specific humidity and wind speed. The median values of the RMSE for air temperature and wind direction are lower than the median values of the RMSE reported from other mesoscale model evaluation studies. The median values of the RMSE for specific humidity and wind speed are close to the median values of the RMSE reported from other mesoscale model evaluation studies. The variance of the time series is slightly underestimated for air temperature, specific humidity and wind speed. This could result from the relatively small model domain or, at least for air temperature and specific humidity, from using the simulated variables in 10 m above ground for comparison with observations made in 2 m above ground.

An event with more than 25 mm/d precipitation is simulated within the control domain in about 60% of the selected meteorological situations. Further, an event with more than 10 mm/d is simulated in about 85% of the selected meteorological situations. This is judged to be a reasonable result as given the coarse resolution of the forcing data, the meteorological phenomenon leading to a heavy precipitation event (e.g. cold front) might not be captured in the

forcing data for all of the selected meteorological situations. Further, it cannot be expected that the observed point-scale heavy precipitation is fully captured by the results of the mesoscale model representing an area-averaged value. Finally, the usage of the Kessler liquid-only scheme for the cloud microphysics might partly explain the underestimation of heavy precipitation.

A shortcoming of the model setup is revealed by the evaluation of the pattern of average daily precipitation amounts. More precipitation is simulated in the hilly south of the domain compared to the flat northwest of the domain. This is in contrast to what was observed during those episodes. One reason is the formation of convective cells leading to precipitation in the parts of the model domain with more orography, whereas in flat areas with little surface heterogeneity, the formation of the convective cells is not triggered and thus slower. To solve this problem, the simulations would need to be conducted for a larger domain, which has not been possible due to computational costs. Another possible solution could be the implementation of stochastic physics (e.g. Bouttier et al., 2012).

In future studies, the shortcomings of the spatial distribution of simulated precipitation should be further investigated. Last but not least, simulated precipitation should be evaluated against radar observations in order to better evaluate its space-time characteristics.

6 Impact of topography on heavy summer precipitation

6.1 Introduction

In this chapter, the impact of topography on simulation results for the heavy summer precipitation events downscaled in Chapter 5 is quantified. It is well known that urban areas can impact precipitation. The literature is briefly summarised in Section 6.2. To quantify the impact of adaptation measures on precipitation, plausible scenarios for future surface cover are developed. These are introduced in Section 6.3. In addition to calculating quite plausible surface cover change scenarios, the total impact of orography and of non-natural surface covers shall be investigated. In total, four scenarios are simulated: one with the orography removed, one with all non-natural surface covers replaced by natural surface covers and two plausible urban development scenarios.

For the different scenarios, the changes of the surface fluxes, the air temperature and relative humidity in 10 m above ground, the inversion height, the vertical velocity in the height of the clouds, the integrated water vapour and the integrated cloud water are calculated (Section 6-4). Finally, the changes of the precipitation amounts and the exceedances of the thresholds 25 mm/d and 10 mm/d are determined (Section 6-5).

The conclusions are drawn in Section 6.6.

6.2 Urban impact on precipitation

6.2.1 General findings

Following Shepherd (2005), urban areas can impact precipitation in various ways. The wind field can be modified due to the higher roughness of urban areas compared with rural areas. This can lead to convergence of the wind field in the boundary layer resulting in updrafts, mainly windward of the urban area. The surface energy budget in urban areas differs from rural areas (e.g. larger sensible heat fluxes, smaller latent heat fluxes at the surface). For many cities, this leads to the formation of an urban heat island. The result is a higher instability of the boundary layer compared to rural areas, which might result in updrafts enhancing or initiating convection. Finally, the aerosol concentrations are usually higher in urban areas than in rural areas. This can modify the clouds. Most studies reviewed by Shepherd (2005) report an enhancement of precipitation downwind of urban areas. However, after Shepherd (2005) there are also studies reporting a reduction of precipitation downwind of urban areas or studies that conclude that the investigated urban area does not change precipitation.

In the literature, the urban impact on precipitation is quantified by analysis of rain gauge data, radar observations, satellite bound precipitation measurements, as well as numerical modelling. For the present study, it is of particular interest how the numerical modelling has been conducted in other studies. One very striking point is the low number of simulated meteorological situations. Niyogi et al. (2006), Lin et al. (2011), Miao et al. (2011), Niyogi et al. (2011) simulated only one meteorological situation. Shem and Shepherd (2009) and Zhang et al. (2009) simulated two meteorological situations. Matheson and Ashie (2008) simulated eight meteorological situations. In the specified studies, the precipitation has been evaluated against radar data, and the performance of the model has been usually judged to be good. Matheson and Ashie (2008) and Niyogi et al. (2006) report problems with the timing and location of precipitation.

Inamura et al. (2011) point out that results from only few meteorological situations are misleading, because differences between a "no urban" scenario and a reference scenario can be due to the non-linearity of the atmospheric processes and might be wrongly attributed as urban impact. For this reason, Inamura et al. (2011) have simulated a total of 10 meteorological situations with heavy precipitation observed in the area of Tokyo and a wind direction from the southeast using 3 to 5 different reanalysis datasets with the RAMS model. They have found an increase of the ensemble averaged precipitation downwind of the city of Tokyo, but a decrease in single simulations. This confirms their hypothesis that the investigations on the urban precipitation impact with numerical models should not be based on a few meteorological situations only. From the 44 simulations carried out, only 24 reproduced the wind direction from southeast, the others have been rejected. Considerable deviations between simulated and observed precipitation have been found for several simulations. The study of Inamura et al. (2011) is the most similar to the present study and indicates that if a large number of simulations is carried out, not all simulations produce the heavy precipitation as desired. This is consistent with the results obtained in Chapter 5.

6.2.2   Results for Hamburg

The impact of the city of Hamburg on precipitation has been investigated by Hoffmann (2009) and Schlünzen et al. (2010) by analysing daily precipitation amounts observed at the 46 stations displayed in Figure 5-2. Daily average wind directions observed at station 1 have been used to define sectors downwind and upwind of the urban area as well as the rest. The reference point to define the sectors has been chosen to be located at 53°34'45''N and 10°1'24''E. A significant enhancement of precipitation has been detected for the stations north of the city, parts of the stations east of the city and parts of the stations southeast of the city, on days when they are located downwind of the urban area. The absolute difference between the median values of the precipitation amounts observed at upwind and downwind stations is relatively low (only up to 1 mm/d). However, the difference corresponds to at least 10% of the daily precipitation amount.

Ertl (2010) investigated the robustness of the method applied by Hoffmann (2009) and Schlünzen et al. (2010). He concludes that the obtained result is similar if days with snowfall (highly uncertain measurements) are excluded from the analysis. The results are not much changed if the days with a high variability of the wind direction are left out. Ertl (2010) further investigated the seasonal cycle of the urban impact on precipitation. He concludes that the enhancement of precipitation downwind of Hamburg is only found in September and between November and March. No statistically significant impact of Hamburg on precipitation is found during the summer season. He also showed that the position of the reference point does not highly impact the results as long as the reference point is kept within the urban area.

Trusilova et al. (2009) investigated the impact of urban areas on precipitation in Europe with MM5 at 10 km horizontal resolution. The simulations have been conducted for six times January and six times July (2000-2005). Hamburg has been in the model domain. A slight increase of precipitation due to the urban surfaces is found in winter, whereas a slight decrease of precipitation is found in summer. The authors point out that the coarse resolution might influence the results, because precipitation is highly parameterised in the model.

6.3   Selected scenarios

The scenario surface cover was only applied in domain D3 at 2 km horizontal resolution, which is still covering the whole Hamburg Metropolitan Region (Figure 5-2).

6.3.1   Reference scenario - REFR

The reference surface cover has been applied for the simulations described in Chapter 5. The orography is not shown here, because it has already been displayed in Figure 5-2.

The land-use and surface cover datasets as well as the methodology applied for the creation of physically meaningful surface cover data as input for METRAS are described in Flagg et al. (2012).

The background surface cover is given by the top-down "European Commission programme to Coordinate Information on the Environment" (CORINE) dataset from 2006. After Flagg et al. (2012), the dataset is obtained from satellite based remote sensing data and covers the European Union at 100 m horizontal resolution. The CORINE data have only been used as background for the parts of domain D1 located outside of Northern Germany.

Higher resolved datasets have been used for Northern Germany and especially for Hamburg. The bottom-up dataset "Amtliches Topographisch-Kartographisches Informationssystem" (ATKIS) relying on a digital basic map is used for the German Federal States Lower Saxony, Bremen,

Hamburg, Schleswig Holstein, Mecklenburg-West Pomerania and Saxony-Anhalt, which are fully or partly included by the domains D2 and D3. After Flagg et al. (2012), the resolution of the ATKIS data is 2 m to 5 m and the data have been retrieved between 2007 and 2009. Information on building outlines has been retrieved for the larger cities from the "Digitale Stadtgrundkarte" (DSKG), which consists of laser scan data and records on buildings. After Flagg et al. (2012), the accuracy of the building outlines is usually better than 1 m. The DSKG dataset is dated from 2007 to 2009. For Hamburg, the bottom-up Biotope dataset compiled by the "Behörde für Stadtentwicklung und Umwelt" (BSU) is available and used additionally. The Biotope dataset contains detailed information on the presence of 392 different habitat types within the city borders of Hamburg. After Flagg et al. (2012), the horizontal resolution of the Biotope dataset is 2 m to 5 m and the data have been retrieved between 2000 and 2009.

The background orography is based on the Shuttle Radar Topography mission (SRTM) data. This top-down dataset has been obtained by remote sensing from space. The horizontal resolution is 3" (about 90 m in South-North direction) and the dataset is dated from 2004 (Flagg et al., 2012). Similar to CORINE, the SRTM data have only been used as background data for the areas outside of Northern Germany. For the German Federal States in Northern Germany, the "Digitales Geländemodell 5 m" (DGM5) data, which is part of the ATKIS data at 5 m horizontal resolution have been used. The DGM5 data have been retrieved from aircraft measurements.

The large number of original land-use and surface cover classes from the different datasets has been converted by Flagg et al. (2012) to a dataset containing only surface cover classes. All land-use classes have been assigned a fraction of existing or newly defined surface cover classes. After this step, the surface cover classes have been aggregated by Flagg et al. (2012) to a set of about 50 surface cover classes that can be reasonably distinguished by their physical characteristics in mesoscale model applications: the so-called METRAS-50 classes. The GRITOP pre-processor (Spensberger and Schlünzen, 2010) calculates the fraction of the METRAS-50 classes within each METRAS grid cell. The fractions are rounded to 1%.

With the land-use data employed, the surface covers from 2000 to 2009 are implicitly assumed. For the heavy precipitation events simulated between 1982 and 1998, possible differences in surface cover would need to be considered between 1982 to 1998 and 2000 to 2009. However, the development of realistic surface cover datasets for the past is beyond the scope of this thesis and would require additional research, as e.g. done by Daneke (2012).

For the purpose of display, the 36 surface cover classes occurring in domain D3 have been grouped into "water", "bare surfaces", "grassland, cropland", "trees, forests" and "sealed surfaces". The fractions of these surface cover groups are displayed in Figure 6-1, except for the "bare surfaces", because these appear only at very few grid points. The main water bodies in the

domain are the North Sea and the Baltic Sea (Figure 6-1a). The river Elbe, which passes through the city of Hamburg and the river Weser passing through the city of Bremen are recognisable. Some larger lakes are located in the northern and eastern part of the domain.

The non-water surface covers in the domain consist mainly of grassland and cropland (Figure 6-1b). Larger forests are located in the south of the domain (Figure 6-1c). Apart from these forests, many trees (street trees, trees in parks) are located within the urban area of Hamburg. The "sealed surfaces" group (Figure 6-1d) depicts the large cities in the domain: Hamburg in the centre, Bremen and Bremerhaven in the western part of the domain, Kiel and Lübeck in the northeast of the domain and Lüneburg, 40 km southeast of Hamburg. At 2 km horizontal resolution, the fraction of "sealed surfaces" hardly exceeds 60% at any grid cell in the domain. The reason is that the cities in Northern Germany are relatively green with a lot of street trees, courtyard vegetation and parks. Further, many water surfaces are located within the urban areas.

As shown by Flagg et al. (2012), only a small part of Hamburg is covered by buildings higher than 20 m. This is important because Carraca and Collier (2007) report that high-rise buildings are particularly important for the initiation of convection by urban areas.

The surface cover data presented here give a hint that the impact of Hamburg on precipitation might be relatively small: neither are the buildings very high nor is the sealed fraction of the surfaces very large. Instead, a lot of parks and street trees are located in the urban area. This reduces potential changes in simulated meteorological variables when replacing the non-natural surface covers with natural surface covers.
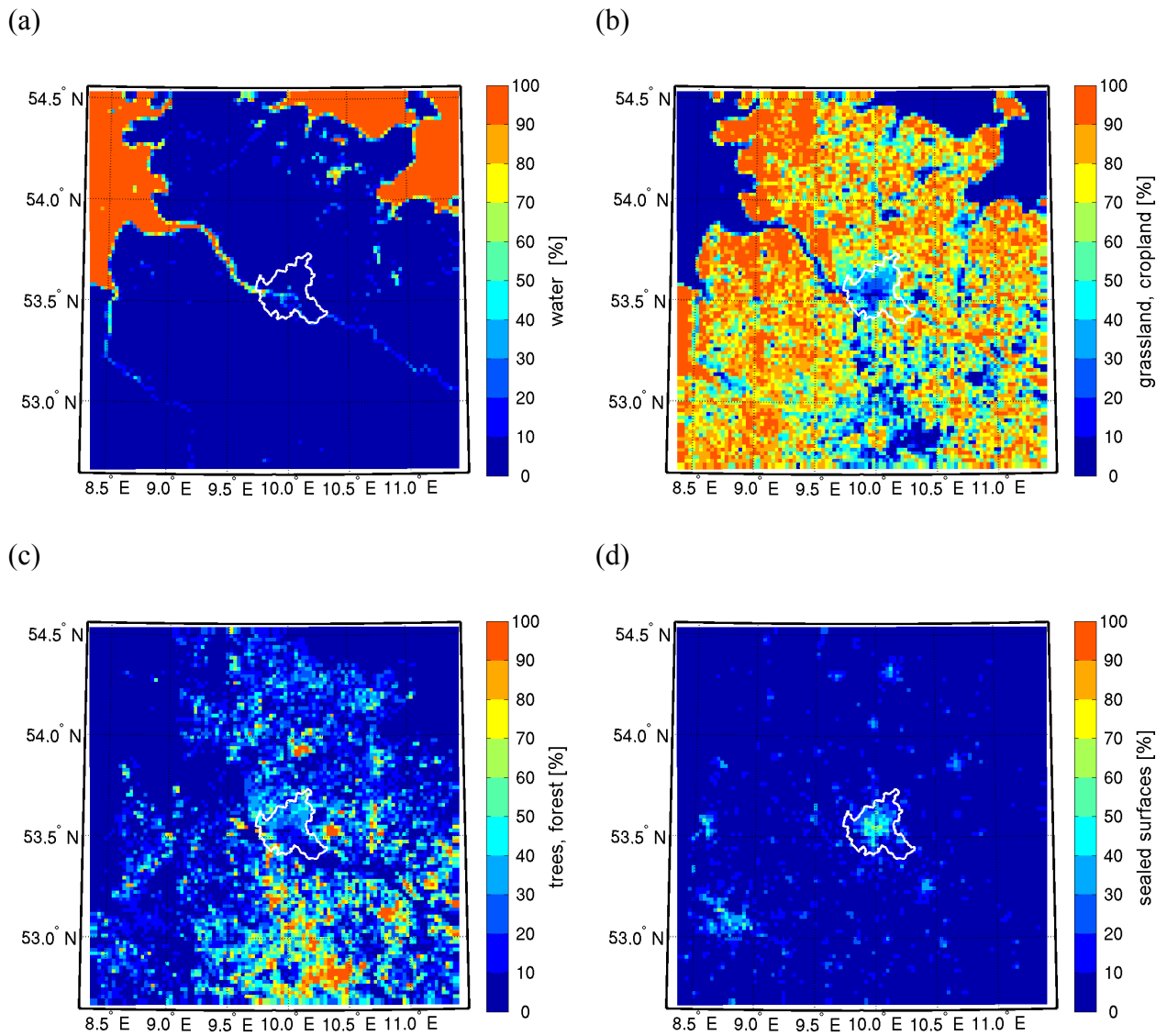
Figure 6-1: Percentage of the grid cells of METRAS domain D3 (2 km horizontal resolution) covered by the surface cover groups (a) "water", (b) "grassland, cropland", (c) "trees, forest" and (d) "sealed surfaces". Note that at a few grid points also bare surfaces like beaches or bogs occur. This surface cover group is not shown here. The white contour line depicts the border of the federal state Hamburg.

6.3.2 Scenario without orography - NOORO

The simulations for domain D3 are repeated without orography (scenario NOORO). The surface cover is kept as shown in Figure 6-1. The simulation results for domain D2 (with orography included) have to be extrapolated with respect to the flat orography in order to obtain forcing data for domain D3. The potential temperature simulated for domain D2 is extrapolated by assuming a lapse rate of the potential temperature of 0.0035 K/m, the specific humidity simulated for domain D2 is kept constant below the orography, the wind components simulated for domain D2 are extrapolated assuming a logarithmic wind profile (0.1 m roughness length). The cloud and rain water contents simulated for domain D2 are set zero below the orography. The pressure below the orography is calculated with the extrapolated air temperature and specific humidity assuming the validity of the hydrostatic assumption.

With the new forcing data, METRAS is initialised at the same grid point as for the reference simulations. However, for the NOORO simulations, the vertical profile used for the model initialisation is slightly different from the reference simulations, because the part of the atmosphere below the orography of the forcing data had to be extrapolated. This problem did not appear for the other scenarios. METRAS has been initialised with the same vertical profile as for the reference simulations.

6.3.3 Scenario without non-natural surface covers - NOURB

The simulations are repeated without the non-natural surface covers (NOURB). All non-natural surface cover classes (low buildings, high buildings, asphalt, concrete, brick/pavers, gravel and steel) have been replaced by natural surface covers. The non-natural surface cover classes have been assigned to the "sealed surfaces" group displayed in Figure 6-1d, except for gravel and brick/pavers. Note that here the denomination "non-natural" surface cover does not apply to surface covers like cropland, orchards and so on.

The non-natural part of each grid cell has been attributed to one of the classes cropland, deciduous forest, coniferous forest, short grass, long grass, short bushes, heath and bare ground. The probability that one of the specified classes is selected is given by the frequency of occurrence of this class in domain D3. The water surfaces are kept the same.

6.3.4 Scenario CliSAP compact city - CLICC

Daneke (2012) simulated plausible changes of land-use in Hamburg Metropolitan Region for 2050 with the dynamic land-use model Metronamica for three scenarios. In the present study, only the "CliSAP compact city" (CLICC) scenario is investigated, because the projected changes in land-use are the largest for this scenario. The main assumption made by Daneke (2012) for the

CLICC scenario is that the local government adopts a "compact city" strategy. The growth of Hamburg is focussed on the inner parts of the city. In the surroundings of the city, new structures are only built near public transport stations. In this scenario, the population of the city of Hamburg increases by 10%. A constant population is assumed by Daneke (2012) in the remaining part of Hamburg Metropolitan Region. Based on these assumptions, the scenario land-use has been simulated by Daneke (2012) with the Metronamica model. The changes in land-use have been transferred by Flagg (2012; personal communication) into changes of the METRAS-50 surface cover classes.

6.3.5   Scenario KLIMZUG S3 – KLIS3

Three scenarios for the future development of Hamburg Metropolitan Region have been developed within the project KLIMZUG-NORD (Kunert et al., 2013). Plausible adaptation measures based on the assumptions made in these scenarios (e.g. public finance, environmental consciousness, etc.) have been developed by Kruse et al. (2013). To represent the scenarios in the METRAS model, Linde (2012; personal communication) implemented 13 new surface cover classes and derived physical parameters for them. Details on these surface cover classes can be found in Appendix B. Linde et al. (2013) have investigated the impact of the three KLIMZUG scenarios on air temperature in 10 m above ground for the meteorological situations selected by Hoffmann (2012) to represent a strong UHI in different weather patterns in the summer season. The largest difference of air temperature in 10 m above ground has been obtained for the so-called scenario KLIMZUG S3 (KLIS3). For this reason, this scenario is selected for investigation in the present study. The most relevant assumptions of the KLIS3 scenario are the implementation of green roofs and the usage of materials for buildings and streets with higher albedo.

6.3.6   Surface cover fractions in all scenarios

In order to quantify the differences between the reference and scenario surface cover, the fractions of different surface cover groups averaged over the sector Hamburg defined by Figure 6-2 are shown in Table 6-1. In REFR, 20.2% of the area is actually sealed. In NORO, no changes in surface cover have been assumed. In NOURB, the sealed surface fraction is mainly replaced by cropland and grassland and to a smaller degree by trees and forests. The part of the bare surfaces containing gravel is also replaced by natural surfaces, leading to a decrease of the percentage of bare surfaces. In CLICC, the fraction of sealed surfaces increases by 0.5%, which is an absolute increase of about 2.5%. This represents the increase of population and industry within the city of Hamburg. In KLIS3, the sealed surfaces group (seen from the atmosphere) is reduced to 5.5%. The classic sealed surfaces are mainly replaced by buildings with green roofs (10%), and to a smaller degree by sealed surfaces with higher albedo (3.9%).

Table 6-1: Percentage of surface cover groups in the Hamburg sector depicted by Figure 6-2 for the different surface cover scenarios. The percentages have been rounded to 0.1%.

surface cover group	REFR	NOORO	NOURB	CLICC	KLIS3
water surfaces	5.4	5.4	5.4	5.4	5.5
bare surfaces	2.9	2.9	2.3	2.8	3.0
grassland, cropland	43.9	43.9	61.6	43.6	44.2
trees, forest	27.6	27.6	30.7	27.5	27.9
sealed surfaces	20.2	20.2	0.0	20.7	5.5
buildings with green roofs	0.0	0.0	0.0	0.0	10.0
sealed surfaces, higher albedo	0.0	0.0	0.0	0.0	3.9

6.4 Meteorological variables in scenarios

In this section, the impact of topography on meteorological variables is investigated. The focus is set on the surface fluxes, the air temperature and relative humidity in 10 m above ground, the inversion height, the integrated water vapour, the integrated cloud water, the vertical distribution of cloud water as well as the vertical wind in the height of the clouds.

In order to reduce the complexity of the data analysis, similar to Hoffmann (2009) and Schlünzen et al. (2010), the focus is mainly set on averages over sectors that are determined by the wind direction. The simulated wind direction in about 1400 m above ground is used for the determination of the location of the sectors. The cloud water density averaged over all simulations has its maximum in this height. Only the wind direction of the reference simulations is used. This is no major problem, because in the chosen height, the wind directions of reference and scenario simulations agree well. The median value of the RMSE of wind direction is below 5° if the wind direction from the reference simulations is used instead of the wind direction from the scenario simulations. For each output time (every half hour), the wind direction is calculated from the averaged wind components of the three hours before. The analysis is carried out for the time series over the three entire days that have been defined in Section 5.3.1 as Day 1, Day 2, and Day 3. The time series start and end at 7:00 local time, which is about 6:00 UTC.

The reference point is the same as in Schlünzen et al. (2010). The upwind and downwind sectors have an opening angle of 60° ($\pm$ 30° deviation of the wind direction). Only grid points with a maximum distance of 70 km to the reference point are included in the analysis. In contrast to Schlünzen et al. (2010), a new sector located over the city of Hamburg is defined. This Hamburg sector consists of all grid points located within 53.42° N to 53.70° N and 9.78° E to 10.20° E. The location of the sectors is displayed in Figure 6-2 for the example of a wind direction of 240°.
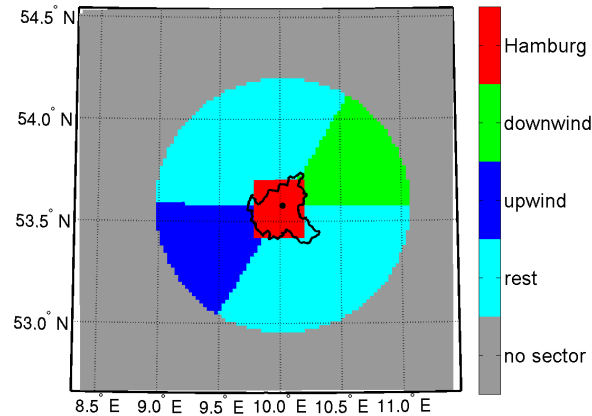
Figure 6-2: Location of the sectors for the example of a wind direction of 240°. The black dot depicts the position of the reference point.

The differences between scenario and reference simulations are subject to the non-linearity of the atmospheric processes. Even for very small topography changes, large differences between scenario and reference simulation can appear in single simulations, especially if clouds are changed. For this reason, the differences between single scenario and reference simulations are considered to be not reliable. Instead the analysis is based on the percentiles of the differences obtained for the 72 selected meteorological situations. For each scenario, the differences between the 72 scenario and the 72 reference simulations averaged over each sector have been sorted in ascending order. The 11th lowest difference (about the 15th percentile of the differences), the 11th largest difference (about the 85th percentile of the differences) and the 36th lowest difference (about the median of the differences) are extracted for each output time (half an hour). The time series obtained with this method will be displayed in the figures in the following sections. By leaving out the ten lowest and the ten largest differences between the scenario and the reference simulations it is made sure not to interpret large differences appearing in single simulations caused by the non-linearity of atmospheric processes.

6.4.1   Surface fluxes

The time series of the simulated fluxes of latent heat, sensible heat and momentum at the surface, averaged over the Hamburg sector (Figure 6-2) and all 72 reference simulations are displayed in Figure 6-3. All three fluxes depict a clear daily cycle with a maximum between 12:00 and 15:00 local time. During the day, the latent heat flux is higher than the sensible heat flux. This is due to the large fraction of vegetated surfaces and water surfaces within the urban area and the selected meteorological situations (very moist conditions). The average of the sensible heat flux becomes negative during night, when the stratification is stable.

(a)   (b)
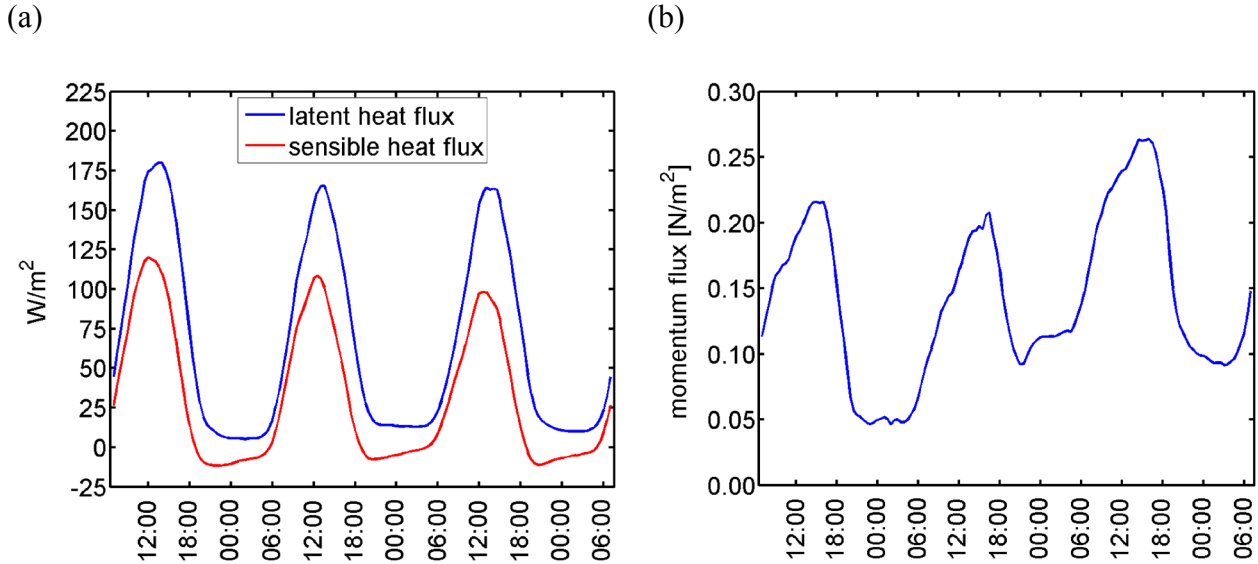
Figure 6-3: Time series (local time) of (a) the latent heat and sensible heat flux and (b) the momentum flux averaged over the Hamburg sector and all 72 reference simulations. The time series covers the Day 1, Day 2 and Day 3 as they have been defined in Section 5.3.1. Note that the "Days" start and end at 7:00 local time, because they have been tailored to the observations of daily precipitation.

The time series of the differences of the latent heat flux between scenario and reference simulations averaged over the Hamburg sector are displayed in Figure 6-4, the time series of the differences of the sensible heat flux in Figure 6-5 and the time series of the differences of the momentum flux in Figure 6-6.

For all three fluxes, the median of the differences is nearly zero for NOORO and CLICC. The lines for the 15th and 85th percentiles indicate that differences appear in some simulations, because a slightly different meteorological situation is simulated. However, the differences cancel out over all simulations. For NOORO, this is no surprise, because the surface cover is not changed compared to REFR. For CLICC, the result indicates that the surface cover changes are too small to induce a discernable change in the surface energy budget when averaging over the entire Hamburg sector. Larger differences appear at single grid points affected by large changes in surface cover (not shown).

For NOURB, a considerable modification of the surface energy budget is obtained. During the day, the median of the differences of the latent heat flux is up to 30 W/m^2 (Figure 6-4b), about 20% of the average latent heat flux in REFR. The median of the differences of the sensible heat flux is down to -10 W/m^2 (Figure 6-5b), about -10% of the reference sensible heat flux. The median of the differences of the momentum flux is down to -0.02 N/m^2 (Figure 6-6b), this is about -10% of the maximum reference momentum flux. The lines for the 15th and 85th percentiles indicate that in some meteorological situations, the differences between the fluxes can be about a

104

factor of two larger or smaller than the median of the differences. However, there are also meteorological situations with nearly no impact of the surface cover on the fluxes. During the night, the absolute differences of the fluxes are smaller than during the day.

For KLIS3 (Figure 6-4d), the increase of the latent heat flux is about half as large as for NOURB. This is mainly due to the green roofs. The decrease of the sensible heat flux for KLIS3 (Figure 6-5d) is nearly the same as for NOURB. This is achieved by the surface covers with higher albedo reflecting more solar radiation than in the reference scenario. The difference of the momentum flux is relatively small for KLIS3 (Figure 6-6d), because contrary to NOURB, the urban structures with their higher roughness are still present.

In the other sectors (upwind, downwind and rest), the surface cover changes for the different scenarios are much smaller than for the Hamburg sector. For this reason, the simulated changes in the surface fluxes are smaller than for the Hamburg sector, by a factor of three at least (not shown).

(a)

(b)

(c)

(d)
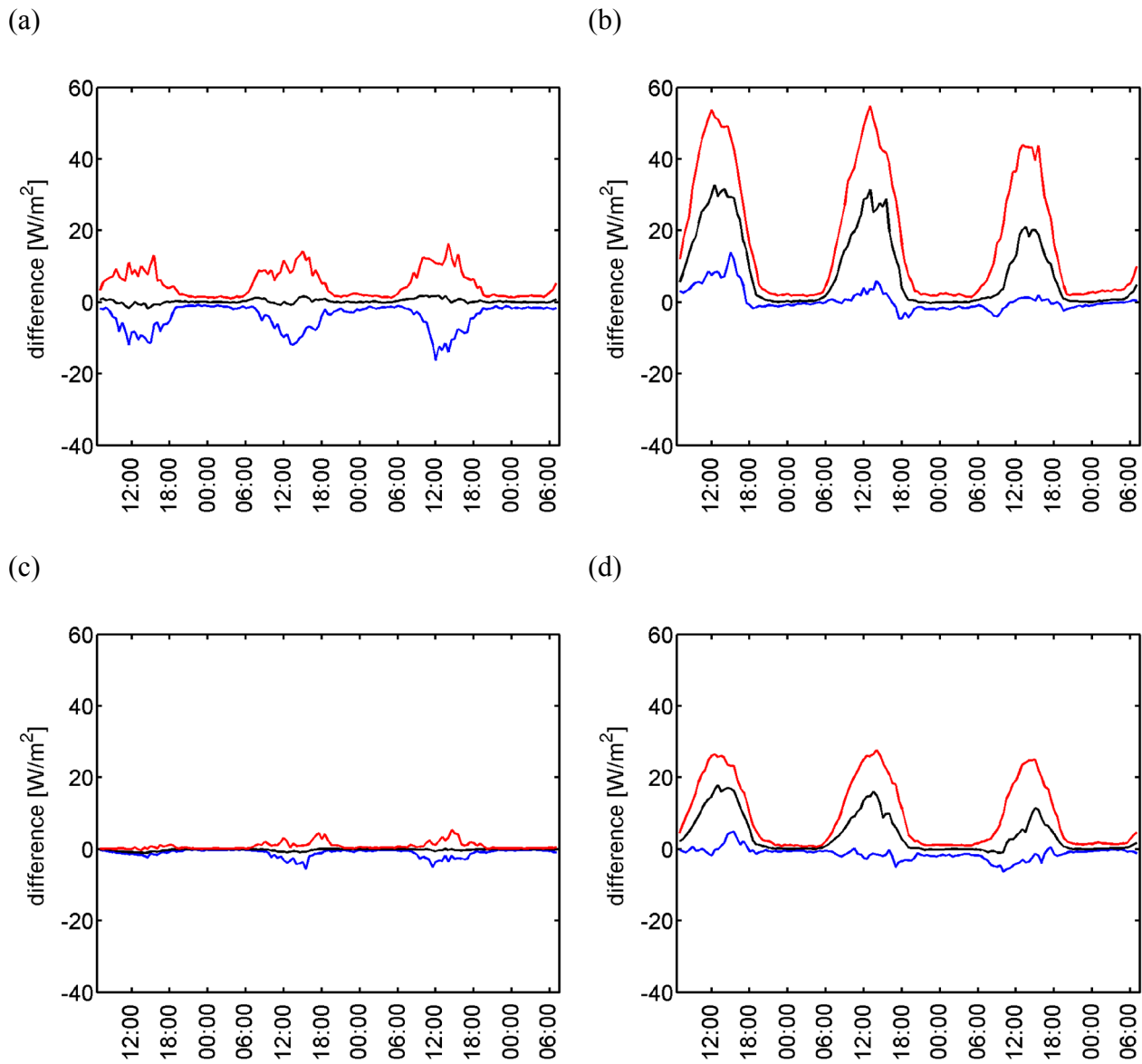
Figure 6-4: Time series of the median (black line), the 15th percentile (blue line) and the 85th percentile (red line) of the differences in the latent heat flux at the surface between (a) NOORO, (b) NOURB, (c) CLICC and (d) KLIS3, and the reference scenario (REFR) averaged over the Hamburg sector. The time series cover the Day 1, Day 2 and Day 3 as they have been defined in Section 5.3.1. Note that the "Days" start and end at 7:00 local time, because they have been tailored to the observations of daily precipitation.
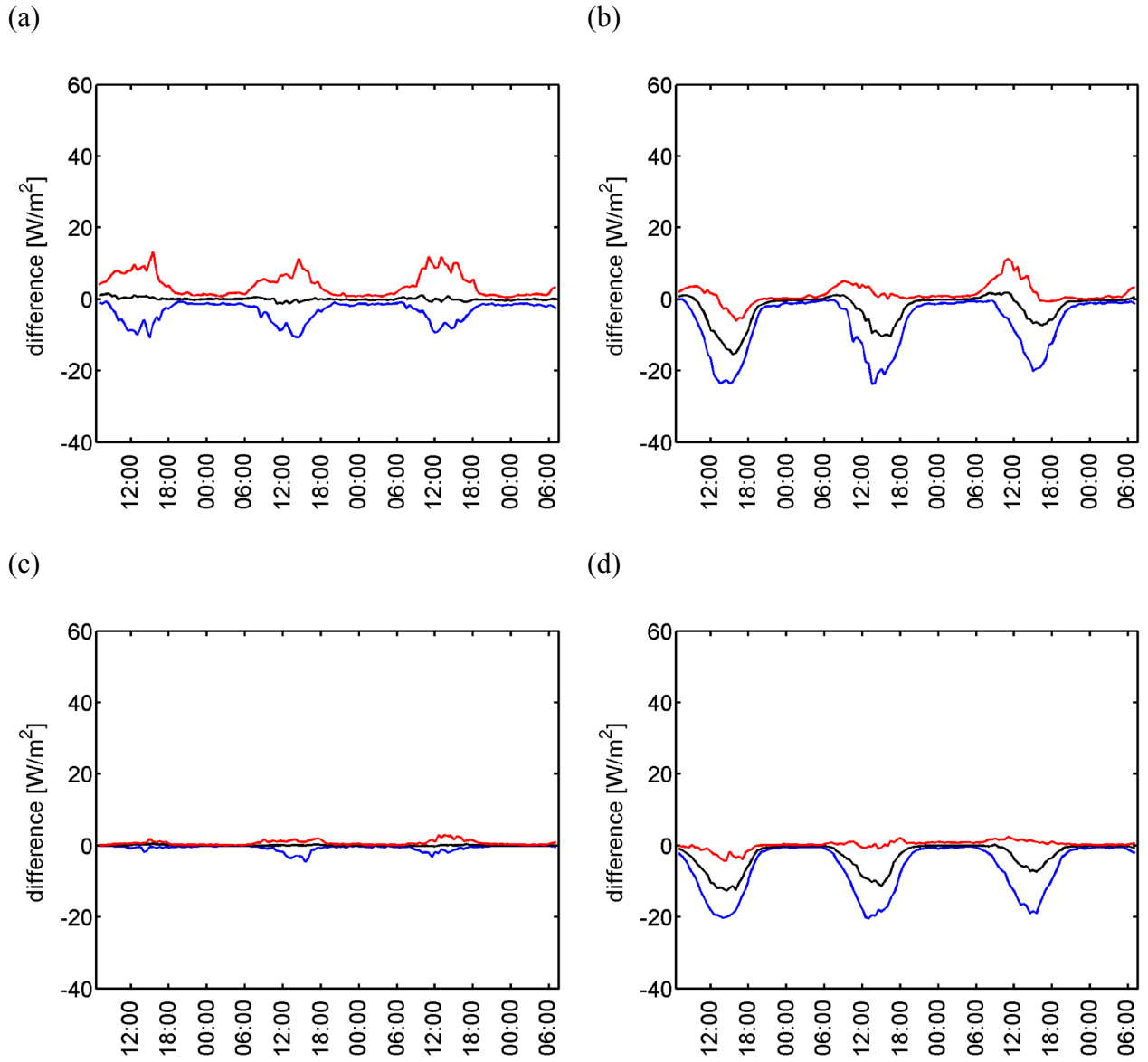
Figure 6-5: Same as Figure 6-4, but for the sensible heat flux at the surface for (a) NOORO, (b) NOURB, (c) CLICC and (d) KLIS3.
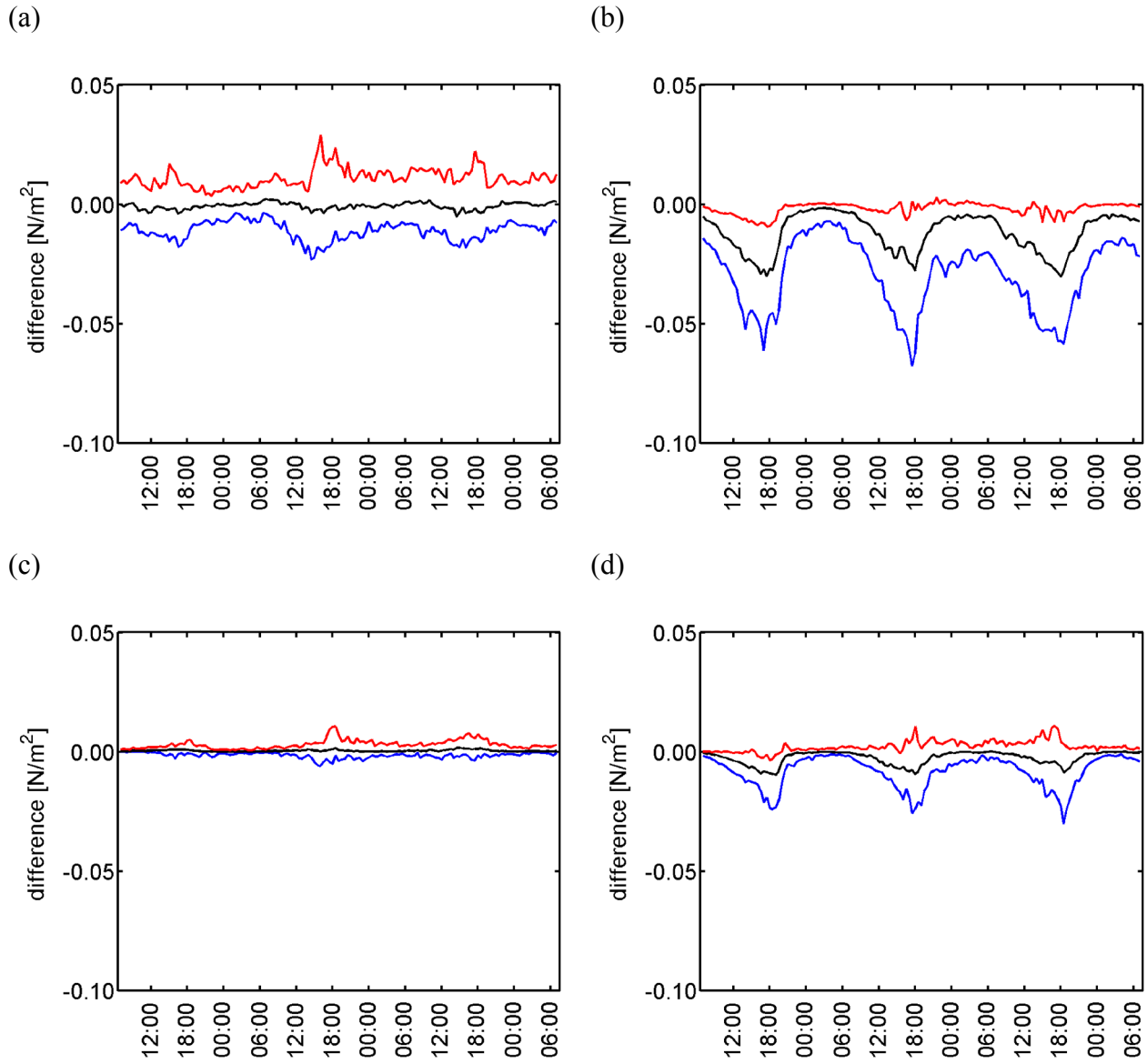
Figure 6-6: Same as Figure 6-4, but for the momentum flux at the surface for (a) NOORO, (b) NOURB, (c) CLICC and (d) KLIS3.

6.4.2 Air temperature and relative humidity in 10 m above ground

The time series of air temperature and relative humidity in 10 m above ground, averaged over all sectors and all reference simulations are displayed in Figure 6-7. The average amplitude of the daily cycle is about 6 K for air temperature and 25% for relative humidity. Air temperature is decreasing with time, relative humidity is increasing. This is due to the selection of the meteorological situations, which are all connected with heavy precipitation occurring on Day 2.

(a)   (b)
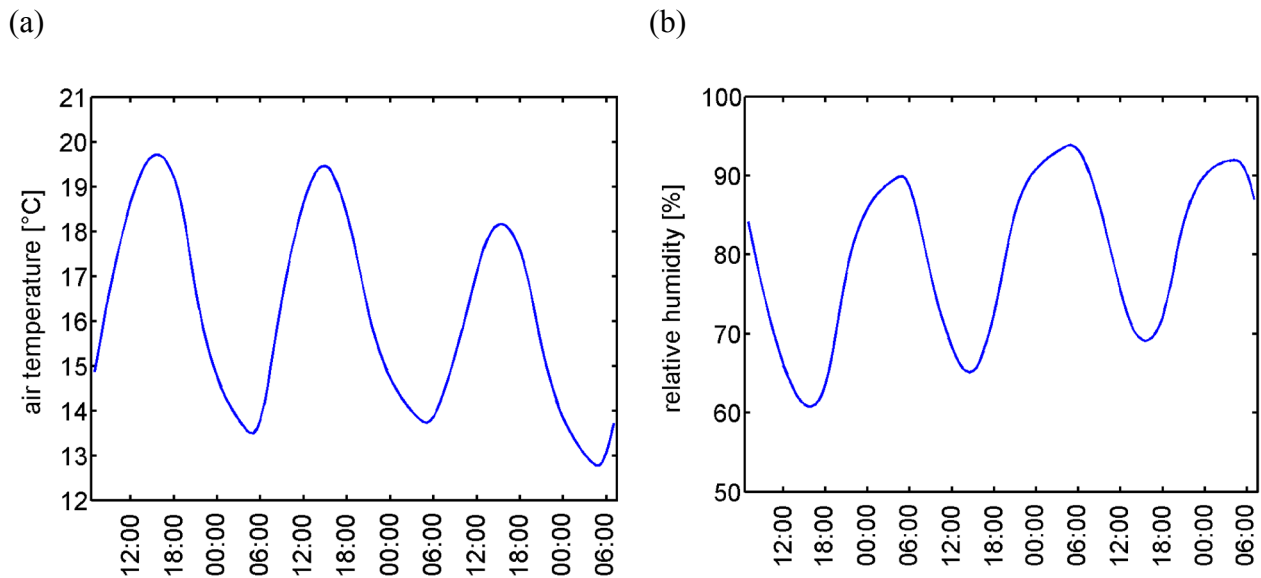
Figure 6-7: Time series of (a) air temperature and (b) relative humidity in 10 m above ground. The values have been averaged over all sectors and all 72 reference simulations. The time series cover the Day 1, Day 2, and Day 3 as defined in Section 5.3.1.

The time series of the differences between the scenario and the reference simulations for air temperature are shown in Figure 6-8 for the Hamburg sector. For NOORO (Figure 6-8a), the air temperature is slightly increased, because the domain is now located at sea level. For NOURB (Figure 6-8b), the median of the differences depicts a clear daily cycle with ~0 K in the morning (7:00 to 10:00 local time) and -0.2 K to -0.3 K in the evening (19:00 to 22:00 local time). The absolute value of the 15th percentile of the differences is about a factor of two larger than the median of the differences (-0.4 K to -0.6 K in the evening). The 85th percentile of the differences indicates that there are also meteorological situations with nearly no difference in simulated air temperature. Note that the differences are averaged over the sector Hamburg (Figure 6-2), with only about 20% sealed surfaces, and not representative for the maximum of the UHI located near the centre of the city.

For CLICC (Figure 6-8c), the differences of air temperature are very small, which is no surprise since the surface fluxes have not been changed noticeably in this scenario. For KLIS3

(Figure 6-8d), the absolute values of the differences of air temperature are about a factor of two lower than for NOURB.

In the other sectors, the differences for NOORO (increase of air temperature) and for CLICC (nearly no difference) are similar to the Hamburg sector (not shown). For NOURB, apart from the Hamburg sector, the largest differences are obtained for the downwind sector (not shown). Here, the daily cycle of the differences is about the same as for the Hamburg sector, the median of the differences of air temperature is down to -0.1 K in the evening (not shown). In the upwind and rest sectors, the median of the differences is only down to -0.05 K in the evening (not shown). For KLIS3, the results for the other sectors are similar to NOURB: the reduction of air temperature is about a factor of two lower in the upwind and rest sectors than in the downwind sector (not shown).

The time series of the differences between the scenario and the reference simulations are displayed in Figure 6-9 for relative humidity in 10 m above ground for the Hamburg sector. For NOORO (Figure 6-9a), the median of the differences is close to zero. For NOURB (Figure 6-9b), similar to air temperature, a pronounced daily cycle of the differences is found. The median of the differences is slightly positive in the morning (about 1%). In the evening, the median of the differences is higher (between 2% and 3.5%). This is partly due to the increased evaporation leading to higher specific humidity (not shown) and partly due to the reduction of air temperature. The line for the 85th percentile of the differences depicts that in some meteorological situations even larger differences of up to 6% occur. Similar to air temperature, there are also meteorological situations with no difference in simulated relative humidity. Again, the differences are negligible for CLICC (Figure 6-9c). For KLIS3 (Figure 6-9d), the differences are a factor of two lower than for NOURB.

In the other sectors, similar to the Hamburg sector, the median of the differences is zero for NOORO and CLICC (not shown). For NOURB and KLIS3, the daily cycle of the differences in the other sectors is similar to the Hamburg sector, but the amplitude is reduced by a factor of three (not shown).
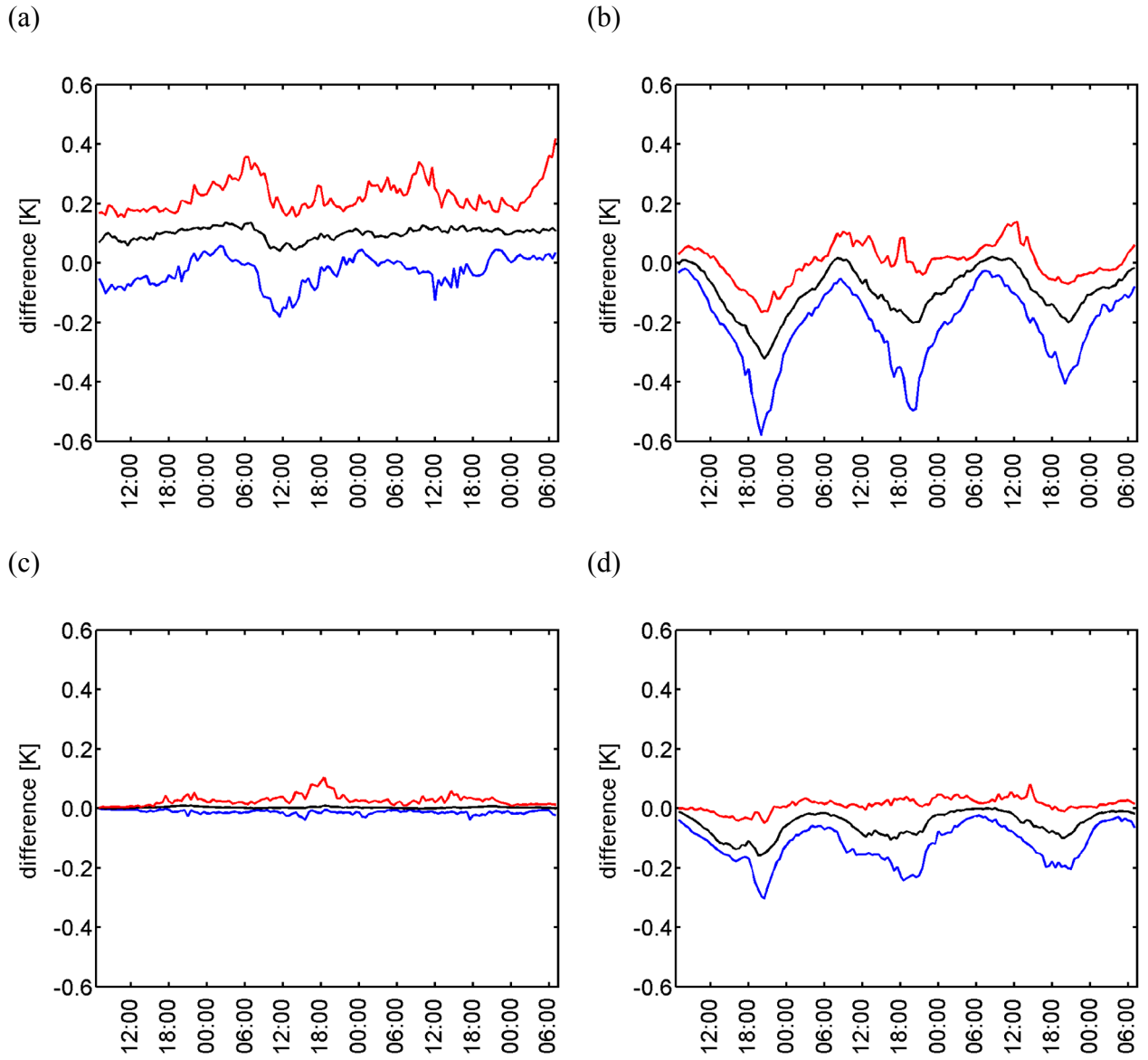
Figure 6-8: Same as Figure 6-4, but for air temperature in 10 m above ground for (a) NOORO, (b) NOURB, (c) CLICC and (d) KLIS3.
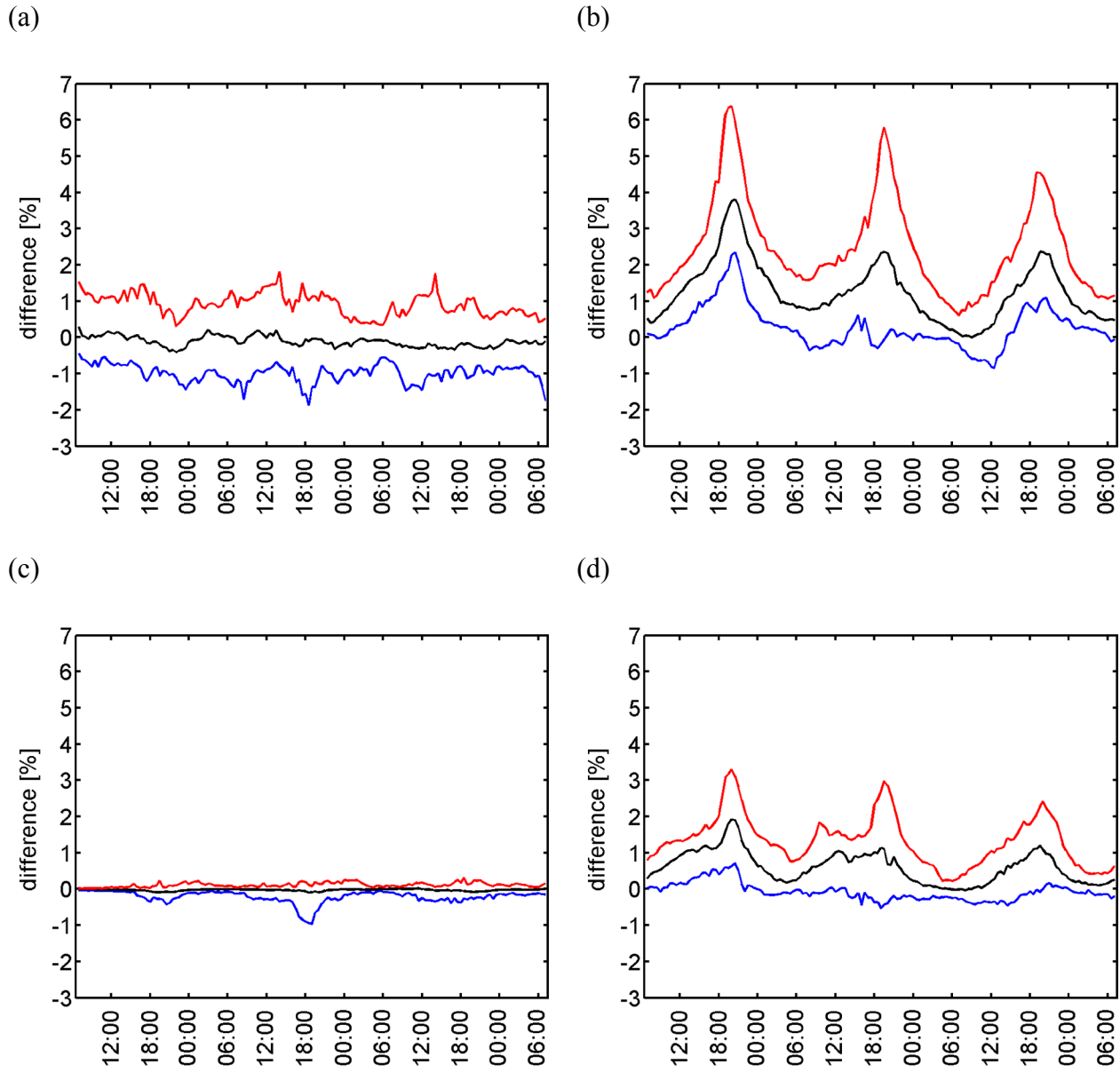
Figure 6-9: Same as Figure 6-4, but for relative humidity in 10 m above ground for (a) NOORO, (b) NOURB, (c) CLICC and (d) KLIS3.

6.4.3 Inversion height

The time series of inversion height averaged over the Hamburg sector and all reference simulations is displayed in Figure 6-10. The inversion height is defined as the height of the first model level with a vertical gradient of the potential temperature larger than 0.003 K/m. If this criterion is fulfilled at the lowest model level (10 m), an inversion height of 10 m is assumed. A strong daily cycle is simulated for inversion height with a minimum below 100 m from 20:00 to 6:00 local time and a maximum between 900 m and 1100 m from 12:00 to 16:00 local time.
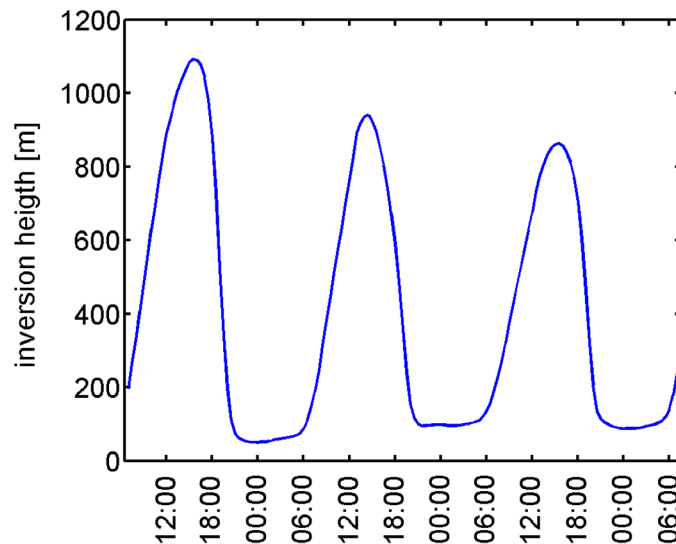
Figure 6-10: Same as Figure 6-7, but for inversion height.

The time series of the differences of inversion height are displayed for the Hamburg sector in Figure 6-11. For NOORO (Figure 6-11a) and CLICC (Figure 6-11c), the median of the differences is close to zero. For NOURB (Figure 6-11b), the median of the differences is between -50 m and -150 m; the largest reduction of the inversion height is obtained in the evening. Without the non-natural surface covers, a stable stratification is established earlier than with the reference surface cover. This effect can be very pronounced in some meteorological situations where a decrease of inversion height of more than 400 m is obtained (15th percentile of the differences). The line for the 85th percentile of the differences indicates that there are also meteorological situations with no difference of the inversion height. For KLIS3 (Figure 6-11d), the changes of inversion height are less pronounced than for NOURB. No clear signal is obtained for the 85th percentile and the median of the differences, the 15th percentile of the differences reaches -150 m to -250 m in the evening.

In the other sectors, the median of the differences is zero for the NOORO, CLICC and KLIS3 scenarios (not shown). For NOURB, the median of the differences is down to -20 m downwind of

113

the urban area, whereas in the upwind and rest sectors, the median of the differences is only down to -10 m (not shown).

(a)

(b)

(c)

(d)
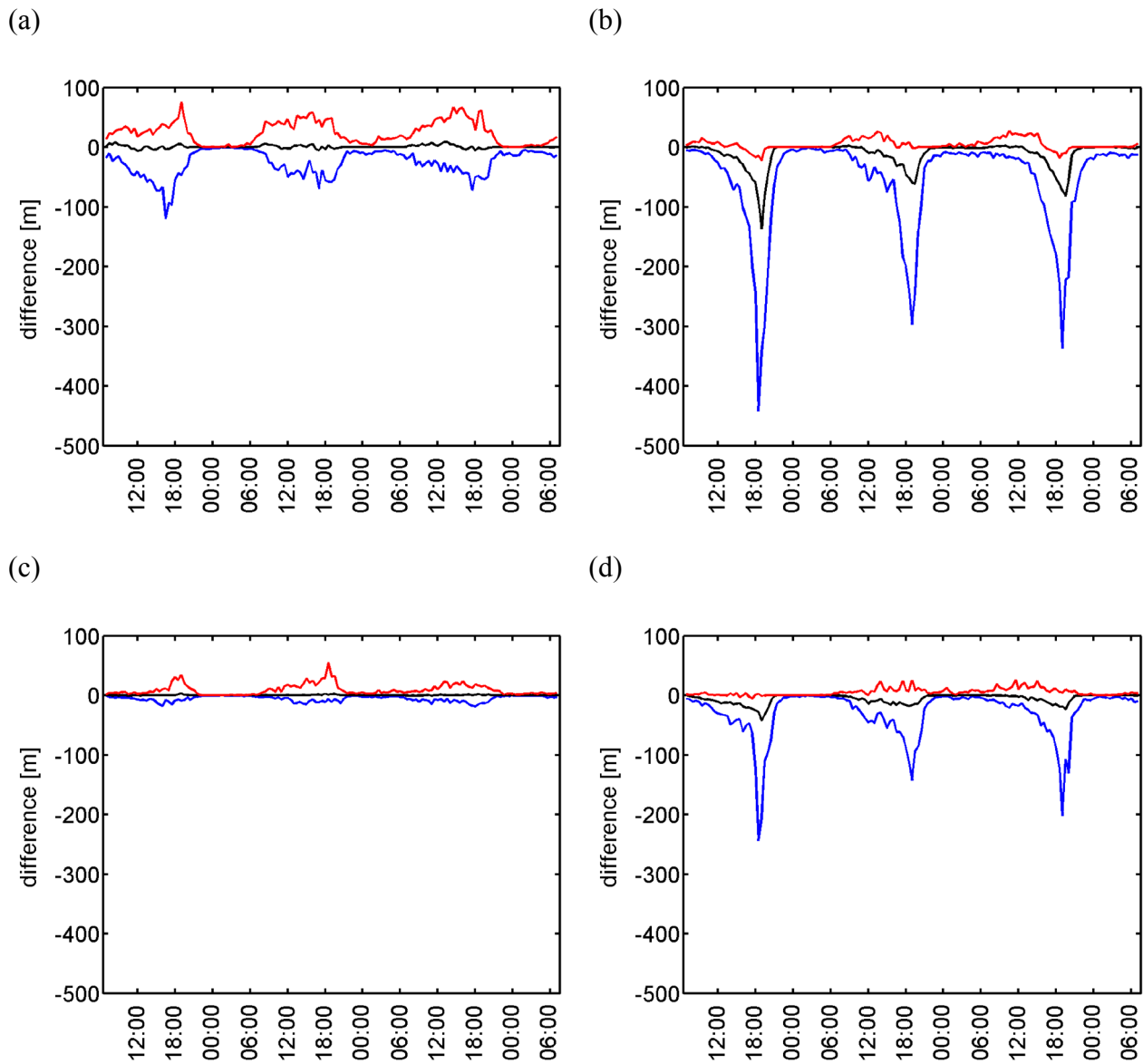
Figure 6-11: Same as Figure 6-4, but for inversion height for (a) NOORO, (b) NOURB, (c) CLICC and (d) KLIS3.

6.4.4 Integrated water contents

In order to quantify how variables related with the formation of clouds and precipitation are changed in the scenario simulations, the integrated water vapour and the integrated cloud water are investigated. The time series of the averages over all sectors and all reference simulations are displayed in Figure 6-12. Both integrated values are increasing from Day 1 to Day 2 and decreasing from Day 2 to Day 3. This is no surprise, since heavy precipitation has been observed on Day 2. The average integrated cloud water exhibits a double maximum on Day 2. The first maximum is at about 18:00 local time, the second at about 6:00 local time. This is consistent with the result from Bohnenstengel et al. (2011). A double maximum of precipitation amounts (one in the early morning and one in the early evening) has been found in an analysis of rain gauge data for a region in northeast Germany. Bohnenstengel et al. (2011) suggest that the maximum in the early evening is connected with formation of convective clouds due to diurnal heating, whereas the maximum in the early morning might be related with enhancement of stratiform clouds. The physical reason for the maximum of integrated cloud water in the early morning should be investigated in future studies.

(a)   (b)
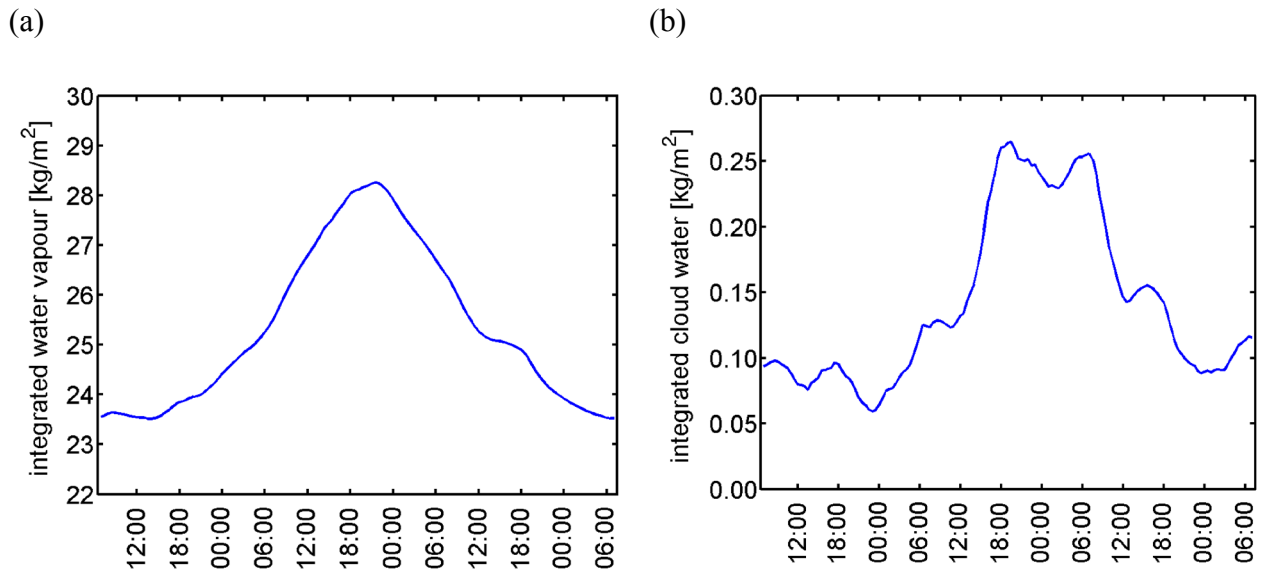
Figure 6-12: Same as Figure 6-7, but for (a) the integrated water vapour and (b) the integrated cloud water.

The time series of the differences of integrated water vapour are shown in Figure 6-13 for the Hamburg sector. For NOORO (Figure 6-13a), the median of the differences is slightly positive, because the height of the air column is increased after removing the orography. For NOURB (Figure 6-13b), the median of the differences is slightly positive (0.05 kg/m^2) between 12:00 and 18:00. However, this is only 0.2% of the average value for the reference scenario. Apart from the positive median of the differences, larger differences (up to 0.2 kg/m^2) in both directions can appear due to diverging solutions for the scenario simulations compared with the reference simulation. The differences between the NOURB and REFR simulations are largest around 18:00 and lowest around 6:00. This is consistent with the daily cycle of the changes in air temperature and relative humidity. The integrated water vapour is modified more in the early evening than in the early morning. For KLIS3 (Figure 6-13d), the median of the differences is only very slightly positive. For CLICC (Figure 6-13c), the median of the differences is very close to zero.

In all other sectors and for all scenarios, the median of the differences of the integrated water vapour is very close to zero (not shown).

The differences of the integrated cloud water averaged over the Hamburg sector are displayed in Figure 6-14. Obviously, the median of the differences is nearly zero for all scenarios. The lines for the 15th and 85th percentiles of the differences indicate that in some simulations the clouds are strongly modified to higher or lower ($\pm$ 30% of the average values for REFR) values of the integrated cloud water in the scenario simulations compared to the reference simulations. However, these differences cancel out over all simulations.

Similar to the integrated water vapour, the integrated cloud water is modified by the scenarios mainly in the evening (indicated by the lines for the 15th and 85th percentiles of the differences). However, the median of the differences between the scenarios is zero.

Similar to the Hamburg sector, the median of the differences of the integrated cloud water is very close to zero for the other sectors (not shown).

(a)

(b)

(c)

(d)
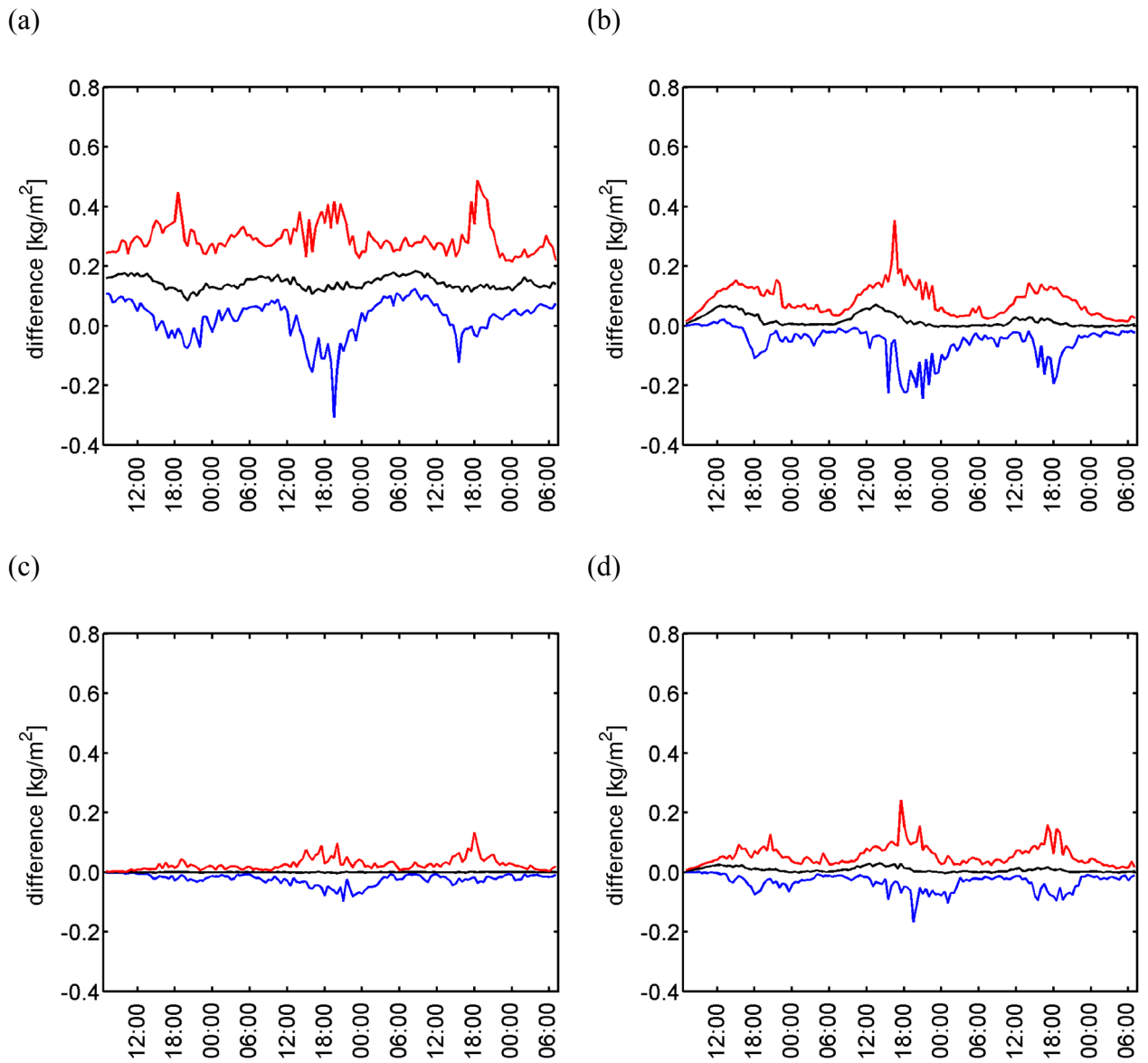
Figure 6-13: Same as Figure 6-4, but for the integrated water vapour for (a) NOORO, (b) NOURB, (c) CLICC and (d) KLIS3.
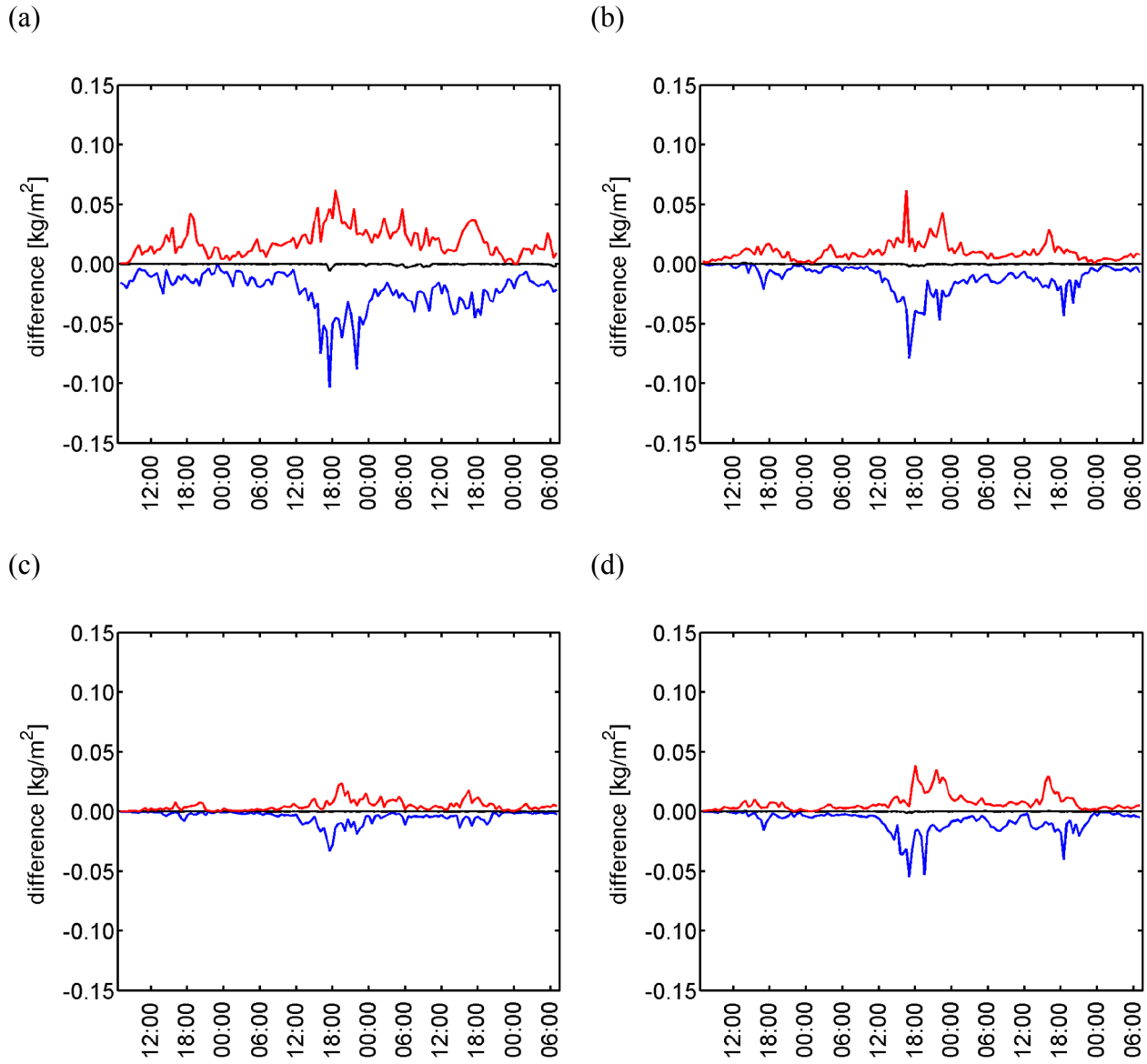
Figure 6-14: Same as Figure 6-4, but for the integrated cloud water for (a) NOORO, (b) NOURB, (c) CLICC and (d) KLIS3.

6.4.5   Vertical distribution of cloud water density and vertical wind component

The simulated vertical distribution of the clouds is investigated by calculating the average cloud water density over all grid points in the domain D3 and over all meteorological situations. To account for spin-up of the clouds and effects of the nesting, 15 grid points have been omitted at each lateral boundary. The obtained vertical profile is displayed in Figure 6-15 for all scenarios. Values of more than 0.01 g/m^3 are obtained for the average cloud water density between 250 m above ground and 6 km above ground. The differences between the averages of the reference and the scenario simulations are very small, which confirms the result from the previous section that there is no systematic difference of the integrated cloud water between the scenarios.
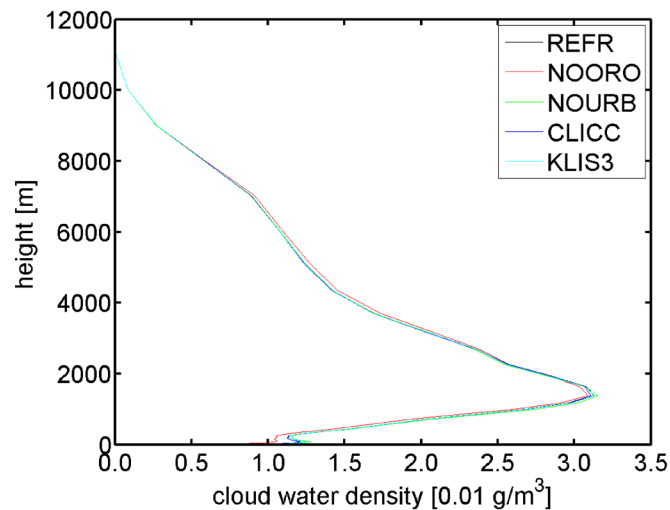
Figure 6-15: Vertical profile of the simulated cloud water density averaged over all simulations and the domain D3, except the boundaries. At each lateral boundary, 15 grid points have been omitted.

The impact of the topography changes on the vertical wind component in the height of the clouds is investigated. For this purpose, the average vertical wind component between 250 m above ground and 6000 m above ground is calculated for each simulation and each output time. The spatial distribution of the median of the averaged wind components is shown in Figure 6-16a. Updrafts and downdrafts are mainly induced in the areas with hills. This is consistent with the spatial distribution of average precipitation discussed in Section 5.4.2. The spatial distribution of the median of the differences between NOURB and REFR is displayed in Figure 6-16b. No clear spatial pattern can be found. The medians of the differences near the city of Hamburg or downwind of the city (in most of the simulations northeast of Hamburg) are not larger than the medians of the differences in the other parts of the domain. The result is similar for the other scenarios (not shown), except for NOORO where the updrafts and downdrafts due to the orography are removed (not shown).
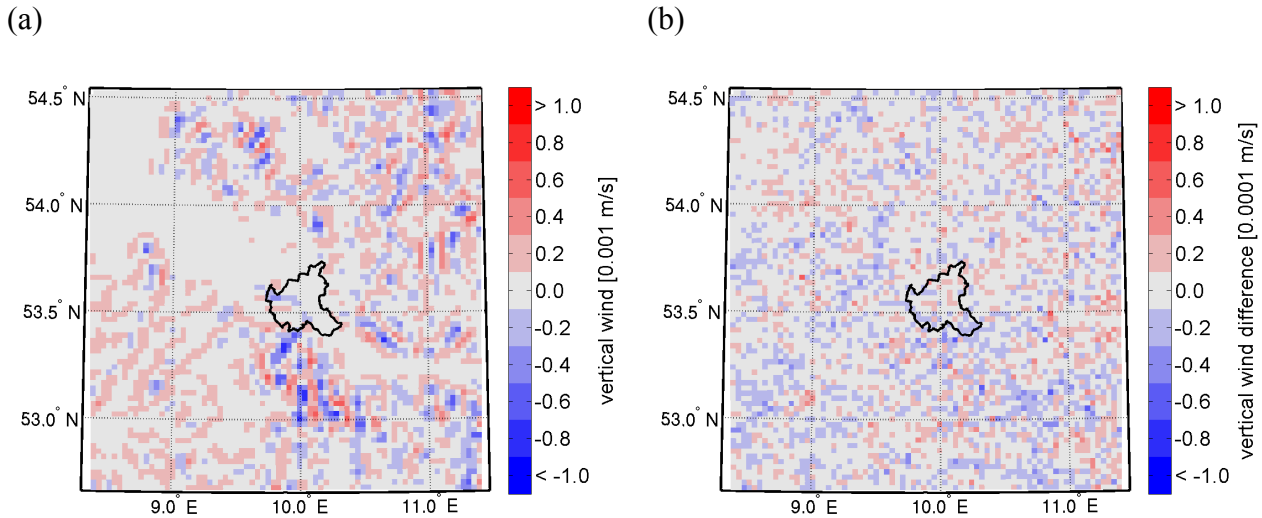
Figure 6-16: Spatial distribution of (a) the median of the vertical wind component averaged over 250 m above ground to 6000 m above ground and (b) the median of the differences of the vertical wind component between NOURB and REFR.

6.5 Heavy precipitation in scenarios

6.5.1 Threshold exceedances

Exceedances of the thresholds 25 mm/d and 10 mm/d are investigated in the different sectors. As daily precipitation amounts are investigated, the wind direction that determines the location of the sectors is calculated from the vector averaged wind components over the entire day (Day 1, Day 2, Day 3 respectively). For each meteorological situation, each of the three days and each sector, the percentage of grid points with the daily precipitation exceeding the thresholds is calculated. The differences between the percentages obtained for the scenario and the reference simulations are calculated. The median of these differences is calculated, and the 5% to 95% confidence interval of the median of the differences is estimated with bootstrap resampling (10000 resamples). The three consecutive days belonging to each of the 72 meteorological situations are resampled as blocks, because they are not independent. When calculating 90% confidence intervals, about 10% of the investigated differences will become statistically significant even though the samples have been drawn from the same basic population. For this reason, it also needs to be considered whether the obtained signals are physically meaningful.

The average percentage values of the threshold exceedances in the different sectors are shown in Table 6-2 for the reference simulations. The percentage of grid points with daily precipitation amounts exceeding the chosen thresholds is larger in the downwind sector than in the other sectors. However, this result cannot be interpreted as urban impact. Indeed, the convective cells are not so well developed in the upwind sector compared to the downwind sector, because they

are closer to the inflow boundary in the upwind sector. Note that for the investigation of daily precipitation values, the position of the sectors is different for each day and determined according to the prevailing wind direction (Figure 6-2).

Table 6-2: Percentage of grid points in the different sectors with the daily precipitation amount exceeding a certain threshold, averaged over all reference simulations. The values have been rounded to 0.1%.

	Hamburg	downwind	rest	upwind
more than 25 mm/d [%]	3.3	4.6	3.6	1.8
more than 10 mm/d [%]	10.7	14.7	12.0	7.8

In Figure 6-17, the median and the 5% to 95% confidence interval of the differences between scenario and reference simulations is displayed for the threshold of 25 mm/d. For the Hamburg sector (Figure 6-17a), a statistically significant decrease of heavy precipitation is obtained for NOORO. This is physically plausible, because removing the orography located in the south of Hamburg results in a reduced triggering of updrafts. The median value of the decrease is 0.5%, corresponding to a reduction of 15% of the total value simulated in REFR. Due to the large variability of heavy precipitation, the confidence intervals are relatively large. The difference of the median has to be about 10% of the reference value to become statistically significant. For NOURB, CLICC and KLIS3 no significant differences are obtained for the Hamburg sector. No significant difference is obtained downwind of Hamburg (Figure 6-17b). In the rest and upwind sectors (Figure 6-17c,d), the confidence intervals for the median of the differences are smaller than for the Hamburg and downwind sectors. This indicates that the differences between the reference and scenario simulations are smaller than in the sectors Hamburg and downwind, which is physically plausible, because the changes in surface cover are relatively small in these sectors and the sectors are not downwind of the urban area with changed surface cover. None of the differences is significant.

The spatial pattern of the differences of simulated precipitation between NOURB and REFR is shown in Appendix C for each of the 72 meteorological situations. Very large differences appear in single meteorological situations. However, these cancel out when analysing the ensemble of 72 meteorological situations.

The median and the 5% to 95 % confidence interval of differences for the threshold 10 mm/d is displayed in Figure 6-18. In the Hamburg sector (Figure 6-18a), the sign of the medians of the differences for NOORO, NOURB and CLICC is the same as for the threshold of 25 mm/d. However, none of the changes is significant. For KLIS3, the median value of the differences is significantly negative. This result is inconsistent with the increase for NOURB, because the

NOURB and KLIS3 scenarios have acted in a similar manner on the simulated meteorological variables. No significant difference is obtained for the other sectors, except for NOURB and the rest sector (Figure 6-18c). However, the difference is very small and not physically plausible. In case of movement of convective cells around the city, a decrease and not an increase of precipitation could be expected for the NOURB scenario in the rest sector.

(a)   (b)

(c)   (d)
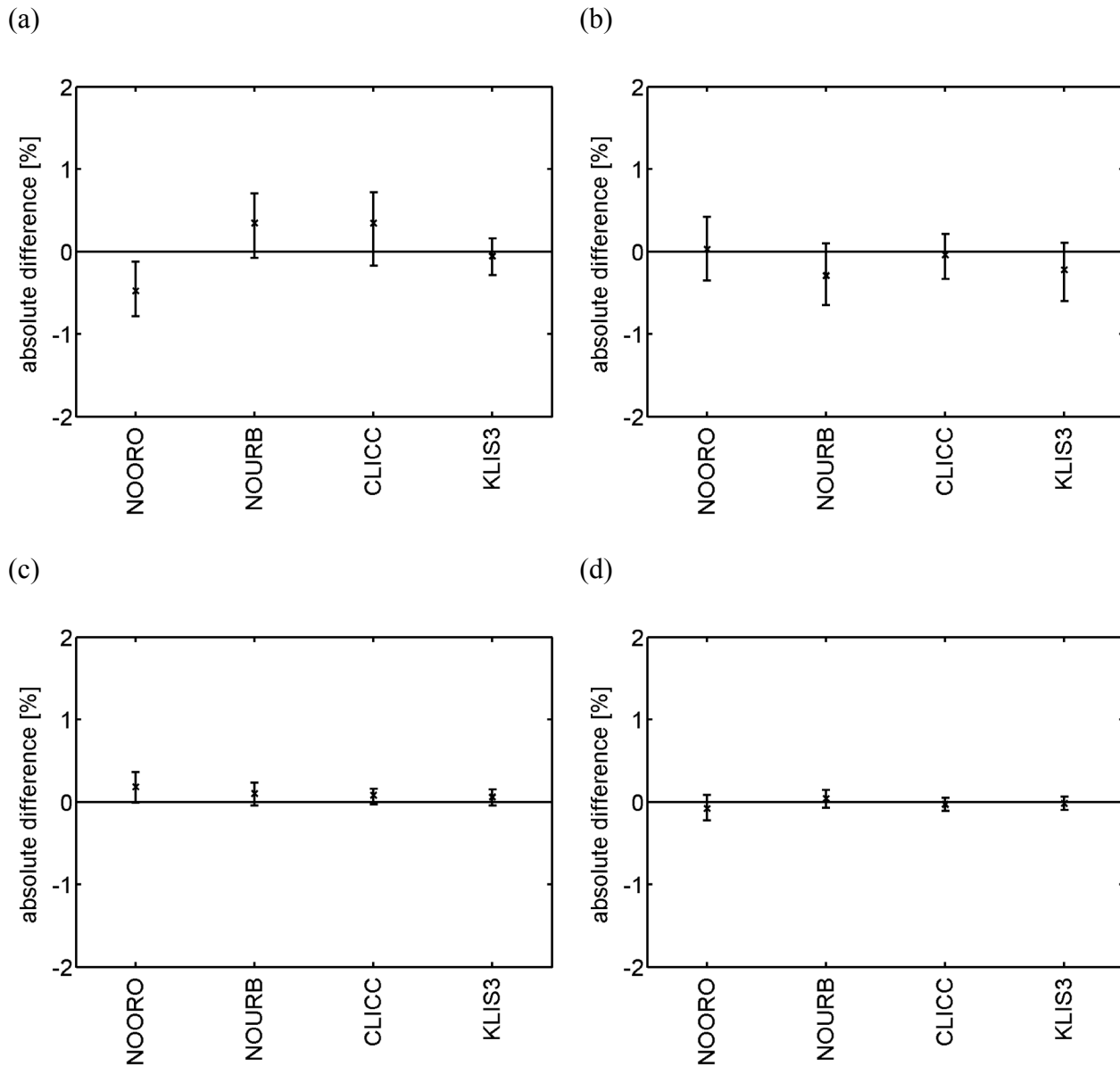
Figure 6-17: Median and 5% to 95% confidence interval of the differences between scenario and reference simulations of the percentage of grid cells with more than 25 mm/d precipitation in the sectors (a) Hamburg, (b) downwind, (c) rest and (d) upwind.

(a)

(b)

(c)

(d)
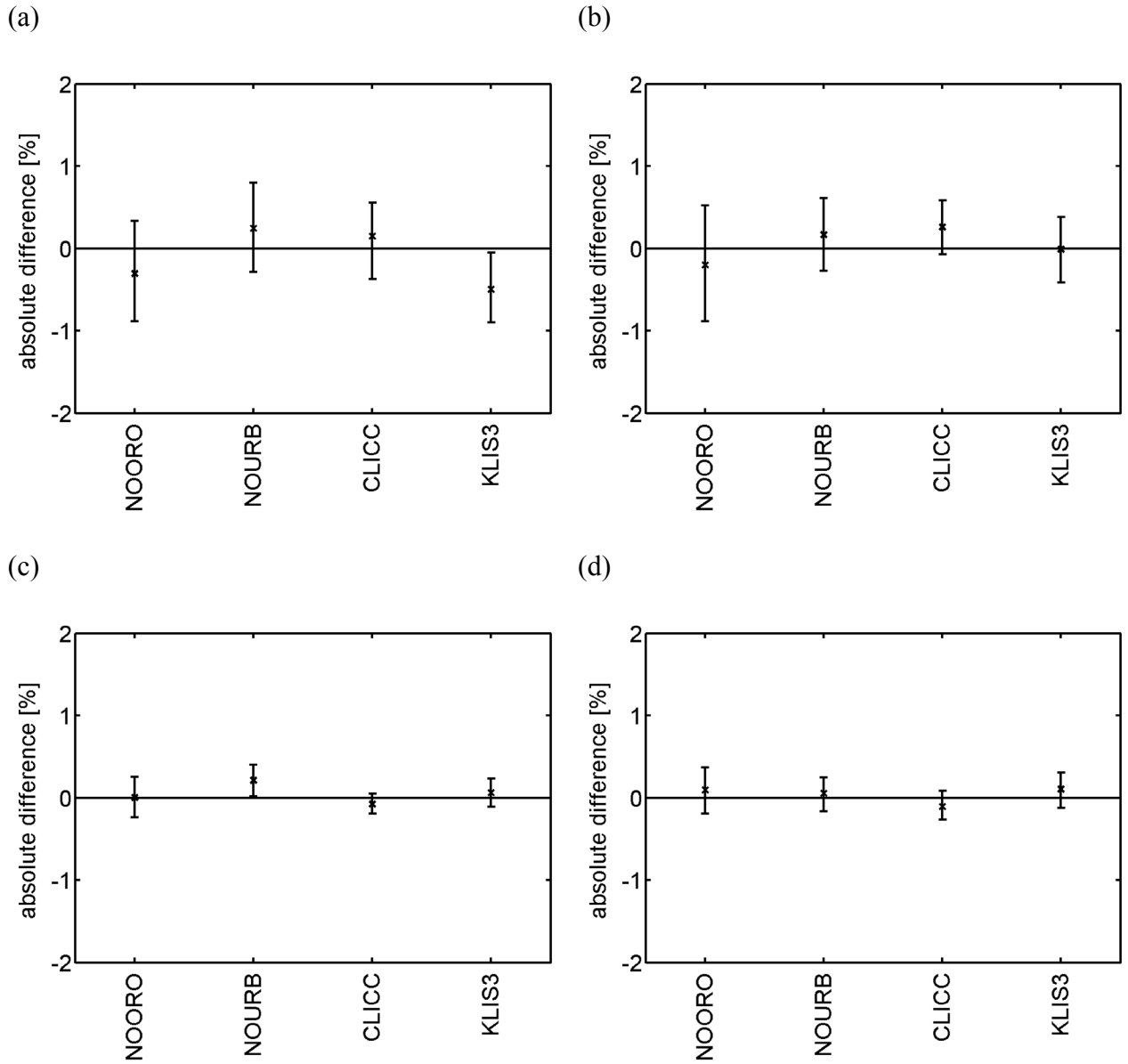
Figure 6-18: Same as Figure 6-17, but for the threshold 10 mm/d for (a) Hamburg, (b) downwind, (c) rest and (d) upwind.

6.5.2 Precipitation amounts

With the methodology described in Section 6.5.1, the differences of the average precipitation amounts at all grid cells with more than 1 mm/d precipitation are investigated. The absolute values of the average precipitation amounts averaged over the reference simulations are shown in Table 6-3. Again, the largest values are obtained for the downwind sector and the lowest values are obtained for the upwind sector. This is due to the spin-up of convective precipitation between the inflow boundary and the outflow boundary of the model domain.

Table 6-3: Average daily precipitation amount at all grid cells with more than 1 mm/d in the different sectors averaged over all reference simulations.

	Hamburg	downwind	rest	upwind
Average precipitation [mm/d]	6.3	7.7	7.6	5.8

The median and the 5% to 95% confidence interval of the differences of the average precipitation amounts are displayed in Figure 6-19. None of the changes is significant. For NOORO, the precipitation amounts are reduced for the Hamburg sector, but not significantly. The orography has therefore a larger impact on heavy precipitation than on average precipitation.
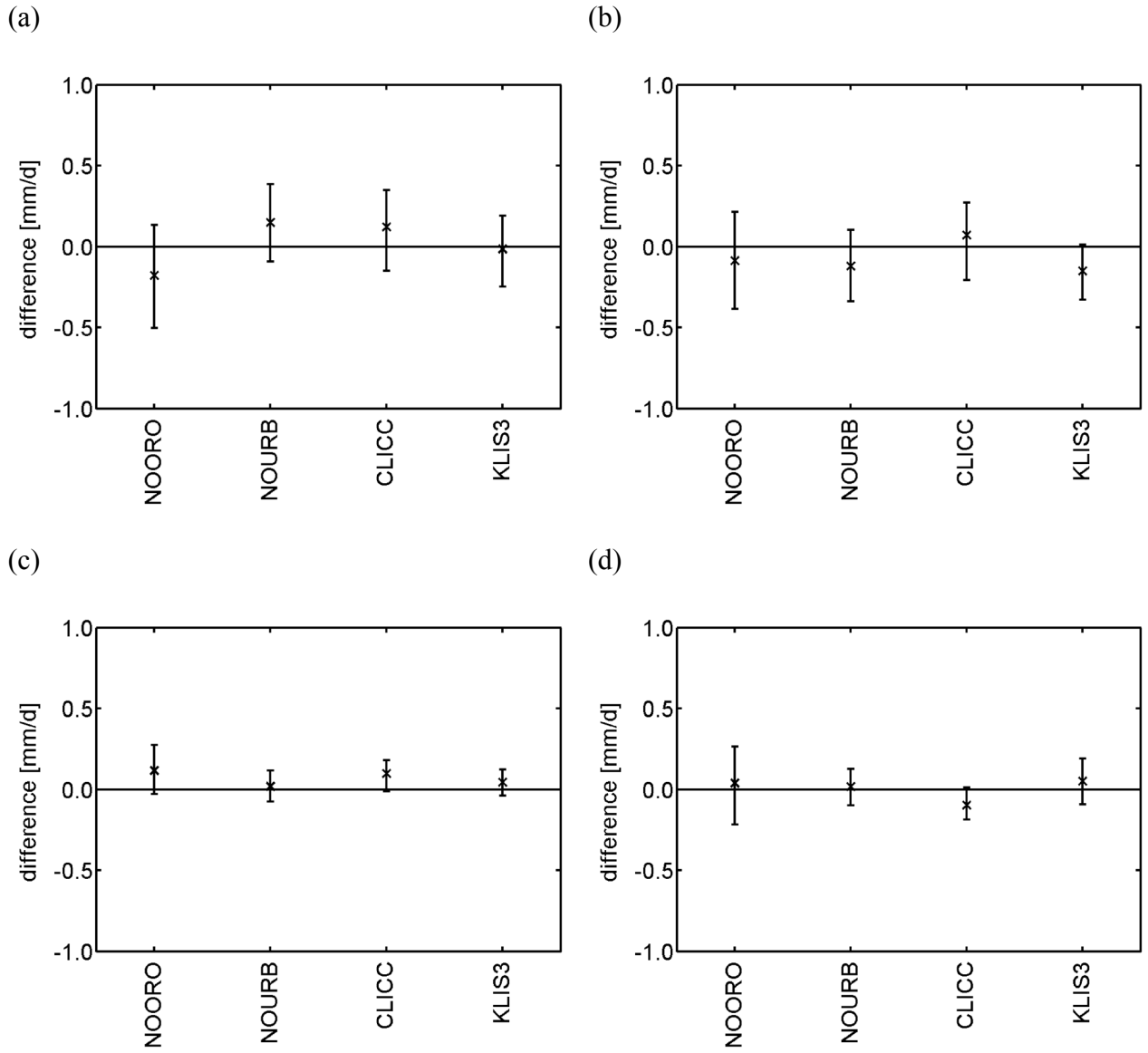
Figure 6-19: Same as Figure 6-17, but for the average precipitation amount at grid cells with more than 1 mm/d for (a) Hamburg, (b) downwind, (c) rest and (d) upwind.

6.6 Conclusions

In this chapter, the impact of topography on meteorological variables and heavy precipitation has been investigated by simulation of 72 heavy precipitation events during the summer season for different scenarios. One scenario consisted of removing the orography, one of replacing the non-natural surface covers by natural surface covers. Apart from these idealised scenarios, two plausible urban development scenarios have been implemented.

It has been shown that KLIS3 (green roofs and higher albedo) changes the surface fluxes as well as air temperature and relative humidity in 10 m above ground quite efficiently compared with NOURB (all non-natural surface covers removed). The differences of air temperature in 10 m above ground that have been quantified for KLIS3 by Linde et al. (2013) for meteorological situations representing a strong UHI (few clouds, small wind speed) therefore also appear in meteorological situations with heavy precipitation events.

The CLICC scenario, which consists only of a re-allocation of existing land-use types, and a slight increase of sealed surfaces does not impact the investigated meteorological variables, when averaging over the whole Hamburg sector.

The median of the differences between scenario and reference simulations is only very small for the integrated water vapour and the integrated cloud water. For this reason, it is not surprising that no statistically significant and physically meaningful change in heavy precipitation or average precipitation amounts is obtained within the urban area of Hamburg or downwind of the urban area. The only statistically significant and physically meaningful difference is obtained for NOORO in the Hamburg sector. Here, heavy precipitation is reduced when removing the orography. Apart from this, it needs to be mentioned that large differences of the simulated precipitation appear between scenario and reference simulations for single meteorological situations. However, these differences cancel out when averaging over all 72 selected meteorological situations. This clearly shows that results from only few simulations dealing with the impact of topography on heavy precipitation are not reliable, confirming Inamura et al. (2011).

The result obtained in the present study is consistent with the rain gauge data analysis by Ertl (2010). The relatively green city Hamburg with relatively low buildings does not alter the meteorological variables enough to noticeably influence precipitation. However, one needs to consider that parts of the urban impacts have been neglected in the simulations. The usage of an urban canopy parameterisation and the consideration of anthropogenic heat release could lead to an increase of the simulated UHI and possibly lead to an impact of Hamburg on precipitation in simulation results. Also, the impact of the neglected aerosols should be investigated.

7 Conclusions and outlook

The main research question of this thesis has been whether local adaptation measures can compensate for regional climate change in Hamburg Metropolitan Region. This question has been investigated for the target variables "perceived temperature" (PT) and "heavy precipitation" in the summer season. The conclusions of the thesis and the answer to the research question will be given in this chapter.

Simulation results of the RCMs CLM and REMO have been evaluated against observation based data. The Hit-Rate of the Percentiles (HRP) has been newly introduced as a measure for the evaluation of the probability density function of daily averages. The main benefit of the HRP is that it allows to account for the uncertainty of the observation based data. Evaluation results indicate that REMO simulates the meteorological input data required for the calculation of PT within the uncertainty of the observation based data, except for relative humidity in DJF and JJA. Major shortcomings have been detected for CLM, especially for relative humidity and total cloud cover. For this reason, simulation results of CLM have not been used for the calculation of PT.

The projected change of PT for the SRES-A1B scenario has been determined based on simulations results of REMO. PT is increasing mainly along with air temperature. The only exception is found for JJA around noon. Here, PT increases stronger than air temperature. The reason is an increase of relative humidity. The projected increase of PT in JJA is 1.5 K to 2.5 K for 2036-2065 and 2.5 K to 3.5 K for 2071-2100 compared to 1971-2000. The changes of the frequency of PT values with respect to the thermal sensation scale have been investigated. In DJF, MAM and SON, thermal comfort is improved in future climate due to a reduction of the frequency of hours with cold stress. Only in JJA around noon, thermal comfort is deteriorated in future climate due to an increase of the frequency of hours with heat stress. The frequency of great and extreme heat stress is increasing by a factor of two to three. Nearly no outdoor heat stress occurs after sunset. Based on these results, it can be concluded that adaptation measures with respect to the target variable PT in Hamburg Metropolitan Region should mainly focus on reducing the increase of PT around noon in JJA, but not in the other seasons. Similar results have been obtained by Thorsson et al. (2011) for the city of Gothenburg (Sweden) and are also stated by Kuttler (2011) for Western Germany.

In order to estimate the potential impact of adaptation measures, the sensitivities of PT on meteorological variables and urban morphology data have been determined. Meteorological input data for PT have been provided by simulation results of the mesoscale atmospheric model METRAS for meteorological situations in JJA. The modification of radiation due to the presence of buildings has been calculated with the Building Effect Parameterisation BEP. The highest

sensitivity of PT on air temperature, water vapour pressure, wind speed and mean radiant temperature has been obtained for situations with heat stress and humid conditions. The sensitivity of PT on wind speed is particularly high for low wind speed. In situations with heat stress (high sensitivity of PT), the projected increase of PT of about 2 K for 2036-2065 could be compensated by a reduction of the air temperature of about 1.5 K or a reduction of the mean radiant temperature of about 7 K. In meteorological situations with wind speed larger than 3 m/s, an increase of wind speed would only lead to a weak reduction of PT. However, in situations with very low wind speed (below 1 m/s), even a small increase of wind speed (e.g. by 0.5 m/s) can lead to a decrease of PT of more than 2 K. It has been shown that around noon, a decrease of PT of up to 2.5 K is obtained in street canyons with aspect ratios above 0.5 when increasing the building heights by 5 m. The reason for this reduction of PT is enhanced shading. However, the sensitivity of PT on building heights is very site-specific, because it depends on the orientation of the street canyons and on the building height.

Based on the calculated sensitivities, the main research question of the thesis can be answered with a "Yes" for the target variable PT. The sensitivities of PT on meteorological variables and urban morphology are sufficiently high to give good options for compensation of the projected increase of PT in JJA by a combination of local adaptation measures that reduce the mean radiant temperature, the air temperature and increase the wind speed. However, one has to note that this result is only valid for locations in the city of Hamburg close to buildings (e.g. within street canyons or on public places). In an open area with no possibility for enhanced shading or modification of wind speed, a reduction of PT would need to be achieved by a decrease of air temperature. Linde et al. (2013) have shown, that local adaptation measures cannot compensate for regional climate change with respect to air temperature in the city of Hamburg. Therefore, also the projected increase of PT in future climate cannot be compensated in open areas.

A lot of additional work is required to adequately implement the adaptation measures. For example it has been shown that increasing the building heights can lead to differences of PT with opposite signs in different street canyons. Therefore, general conclusions cannot be drawn and a more detailed analysis needs to be made for each site with building resolving models (as for example done by Fröhlich and Matzarakis, 2013). The simulation of an entire city like Hamburg with building resolving models is not possible with state of the art computational resources. For this reason, investigations based on results with parameterised building effects as presented in Chapter 3 could be used as "first guess" in order to determine possible locations where changes in urban morphology might have the largest impacts. These locations can then be investigated more in detail with building resolving models.

The sensitivities determined in Chapter 3 also highlight potential negative effects of adaptation measures. For example, an increase of the building height could lead to a reduction of wind

speed, which could cause a strong increase of PT in situations with low wind speed. Further, it should be investigated if adaptation measures like the implementation of green roofs lead to an increase of water vapour pressure overcompensating the benefit from the reduction of air temperature.

The next steps in planning adaptation measures with respect to the target human thermal comfort should be the following. Based on the calculated sensitivities it should be estimated which adaptation measure is the most efficient to change PT. The results can be expected to be location-specific. For example increasing the building heights might be the most appropriate for some locations in the city whereas shading due to deciduous trees might be more efficient for other locations. The impact of potential adaptation measures should be quantified in other seasons in order to not deteriorate human thermal comfort there. Especially, the sensitivity of PT on building height should be investigated for situations with a smaller elevation angle of the sun. The impact of adaptation measures on the indoor thermal comfort needs to be determined, because human beings spend most of their time within buildings. Finally, the measures used for the quantification of human thermal comfort need to be developed further. They should take into account the differences between population groups, not rely on the assumption of reasonable human behaviour and be tailored specifically to targets like morbidity, labour productivity, leisure activities and so on.

Meteorological situations with heavy summer precipitation have been downscaled with the mesoscale atmospheric model METRAS for present climate and present surface cover. Simulated daily precipitation amounts have been evaluated against rain gauge observations made by DWD. METRAS simulates heavy precipitation in 60% of the selected meteorological situations. This result is judged reasonable, because the point-scale rain gauge observations are compared to simulated precipitation amounts representing an area-average. Heavy precipitation can therefore be expected to be underestimated in simulation results. A serious shortcoming of the applied downscaling approach has been revealed by the evaluation of the spatial distribution of average precipitation amounts. Too low average precipitation amounts are simulated in the flat areas with little surface heterogeneity in the northwest of the domain. In these areas, less convection is triggered compared with the hilly areas in the south of the domain.

The impact of topography on simulated heavy summer precipitation has been investigated for two plausible urban development scenarios, as well as one scenario without orography and one scenario with all non-natural surface covers replaced by natural surface covers. It has been shown that only the surface fluxes and the meteorological variables near the surface are modified systematically in the surface cover scenarios. No systematic difference has been obtained for meteorological variables more directly related with precipitation (e.g. the integrated cloud water). No statistically significant and physically meaningful difference of heavy precipitation is obtained for

the scenarios with changed surface cover in Hamburg or downwind of Hamburg. A statistically significant decrease of heavy precipitation is obtained for Hamburg for the scenario without orography. This is physically plausible, because the orography located southwest of Hamburg might trigger heavy precipitation events. However, removing the orography southwest of Hamburg is only an academic scenario.

Based on the results obtained in this thesis, the main research question can be answered with a "No" for the target variable heavy precipitation. Plausible urban development scenarios are not a promising method to compensate for the projected increase in heavy summer precipitation due to regional climate change.

In future studies, the physical reason for the wrongly simulated spatial pattern of average precipitation amounts should be investigated more in detail. The confidence in the results obtained from scenario simulations would increase if this shortcoming of the downscaling approach would be fixed.

Not all urban effects have been considered in the simulations carried out in this thesis. The most important neglected effects are the radiation trapping and the anthropogenic heat release. It has been shown by Hoffmann (2012), that the urban heat island of Hamburg is underestimated by METRAS in simulations neglecting these effects. Therefore, including radiation trapping by using an urban canopy parameterisation like BEP and anthropogenic heat release could lead to a more realistic simulation of the strength of the urban heat island. With a stronger urban heat island, the impact of Hamburg on heavy precipitation could be higher. However, results from Ertl (2010) based on rain gauge observations indicate that the impact of Hamburg on precipitation is very small in JJA.

The effects of the aerosols on precipitation should be investigated. However, this can be expected to be very challenging, because the emissions of the relevant substances need to be known and the concentrations of the aerosols have to be simulated accurately by the atmospheric model. Further, the scheme for the cloud microphysics needs to be modified to allow for a consideration of the effects of the aerosols.

In future studies, it should be investigated whether additional sealing or increased building heights would lead to an impact of Hamburg on heavy precipitation. This could be a valuable information for urban planning.

Finally, the impact of Hamburg on heavy precipitation has only been investigated for the present climate. METRAS should be nested in simulation results of regional climate models to quantify the impact of Hamburg on heavy precipitation in future climate.

Acknowledgments

Appendix A   Error in scheme for cloud microphysics

The air temperature (T) needs to be calculated at several instances during model integration from the prognostic variable potential temperature (θ) (e.g. for the calculation of the specific humidity at saturation). The conversion from potential temperature to air temperature (Equation (A-1)) is made with the Exner function ($\Pi_{0,C}$, Equation (A-2)).

$$T = \theta \Pi_{0,C} \tag{A-1}$$

$$\Pi_{0,C}(jk,jj,ji) = \left(\frac{p(jk,jj,ji)}{10^5 \; Pa}\right)^{\frac{R_L}{c_p}} \tag{A-2}$$

A wrong formula ($\Pi_{0,W}$, Equation (A-3)) has been used for the Exner function at three instances in the scheme for cloud microphysics. Instead of the total pressure at the actual grid point $p(jk,jj,ji)$, the surface pressure $p_s(jj,ji)$ has been used. Further, the fraction is inverted. The error made by using this wrong Exner function is small near the surface and increases for higher model levels.

$$\Pi_{0,W}(jj,ji) = \left(\frac{10^5 \; Pa}{p_s(jj,ji)}\right)^{\frac{R_L}{c_p}} \tag{A-3}$$

The wrong Exner function has been used for the conversion from potential temperature to air temperature in the calculation of the saturation adjustment (Equation (5-14)). Therefore, in previous model versions, the formula given by Equation (A-4) has been used instead of the formula given by Equation (5-14).

$$\beta = 1 + \frac{4028 \; l_{21} q_v^{SAT}}{c_p (\theta \Pi_{0,W} - 38.33)^2} \tag{A-4}$$

Further, the wrong Exner function has been used for the calculation of the increment of potential temperature $\Delta\theta$ from the increment of air temperature ΔT resulting from the condensation of water vapour to cloud water, or the evaporation of cloud or rain droplets (Equation (5-11)). The wrong potential temperature increment is given by Equation (A-5).

$$\Delta\theta = \frac{\Delta T}{\Pi_{0,W}} \tag{A-5}$$

The impact of the error on simulation results has been tested for the 72 meteorological situations evaluated in Chapter 5. Evaluation results for air temperature, specific humidity, wind speed and wind direction for domain D2 are very similar when comparing a model version with the error included and a model version with the error fixed (not shown). Simulation results for daily precipitation amounts are strongly affected. After fixing the error, the precipitation amount averaged over all meteorological situations and all stations increases by about 6% for domain D1 and about 13% for domain D2 (not shown). Domain D3 has not been tested due to computational costs.

The simulation results analysed in Chapter 3 of this thesis are affected by the error. This is not judged problematic, because simulated precipitation values are not relevant for the results discussed in Chapter 3.

The simulation results presented in Chapter 5 and Chapter 6 are not affected by the error, because the corrected version of the scheme for cloud microphysics has been used.

Appendix B Surface cover classes for scenario KLIS3

The surface cover classes used to represent scenario KLIS3 as well as the physical parameters assigned to these surface cover classes (Table B-1) have been derived by Linde (2012; personal communication). Note that the "building" classes consist of buildings and adjacent sealed surfaces. Therefore, "buildings, partly unsealed" means that the sealed surfaces adjacent to the buildings (e.g. parking lots) are partly unsealed.

Table B-1: Surface cover classes and physical parameters derived by Linde (2012; personal communication) for scenario KLIS3.

class name	albedo	thermal diffusivity [m^2/s]	thermal conductivity [W/mK]	initial soil moisture availability	maximum depth of soil water [m]	momentum roughness length [m]
asphalt, higher albedo	0.20	2.3E-6	1.35	0.50	0.0015	0.00030
concrete, higher albedo	0.35	2.3E-6	1.81	0.50	0.0015	0.00030
brick/pavers, higher albedo	0.40	2.3E-6	0.90	0.02	100.000	0.00060
low buildings, higher albedo	0.60	1.4E-6	2.61	0.50	0.0015	0.60000
high buildings, higher albedo	0.60	2.3E-6	3.44	0.50	0.0015	1.20000
low buildings, green roof	0.20	1.4E-6	2.61	0.50	100.000	0.60000
high buildings, green roof	0.20	2.3E-6	3.44	0.50	100.000	1.20000
low buildings, partly unsealed	0.20	1.4E-6	2.61	0.05	0.05	0.60000
high buildings, partly unsealed	0.20	2.3E-6	3.44	0.05	0.05	1.20000
low buildings, higher albedo, partly unsealed	0.60	1.4E-6	2.61	0.05	0.05	0.60000
high buildings, higher albedo, partly unsealed	0.60	2.3E-6	3.44	0.05	0.05	1.20000
low buildings, green roofs, partly unsealed	0.20	1.4E-6	2.61	0.55	100.000	0.60000
high buildings, green roofs, partly unsealed	0.20	2.3E-6	3.44	0.55	100.000	1.20000

Appendix C   Differences of precipitation sum between NOURB and REFR

In the Figures C-1 to C-12, the difference of the simulated precipitation sum (Day 1, Day 2, and Day 3) between the scenarios NOURB and REFR is displayed for each of the 72 meteorological situations downscaled in Chapter 5. The difference is zero for few meteorological situations, because no precipitation is simulated. In most of the meteorological situations, the location of the simulated precipitation differs between NOURB and REFR. This results in areas with strongly increased precipitation amounts beneath areas with strongly reduced precipitation amounts. However, as it has been shown in Section 6.5, the differences obtained for the single meteorological situations cancel out when analysing all 72 meteorological situations. Therefore, wrong conclusions on a possible urban impact on precipitation could be drawn from the analysis of single meteorological situations.
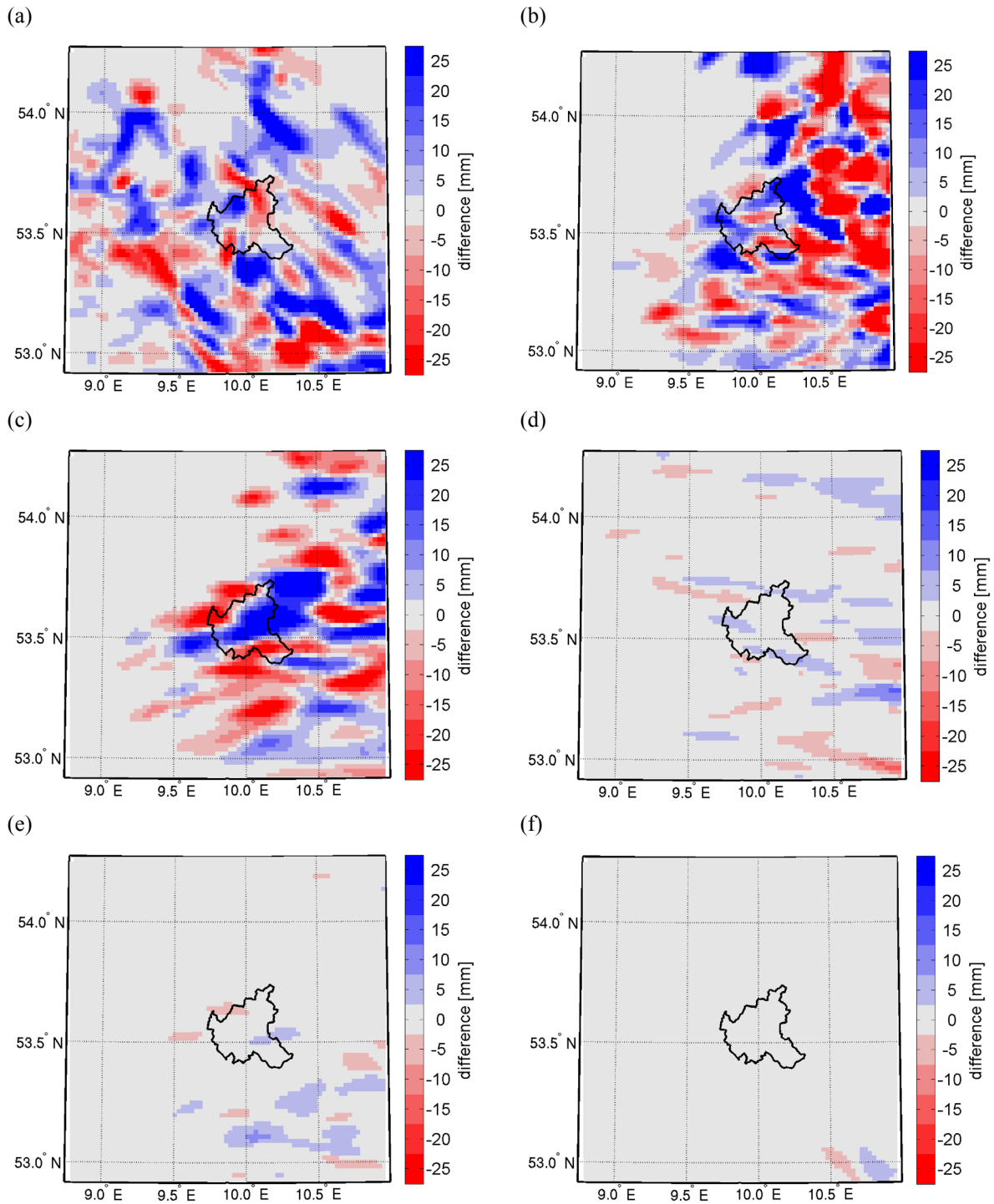
Figure C-1: Difference of the precipitation sum over Day 1, Day 2 and Day 3 between NOURB and REFR for heavy precipitation observed on (a) 19 June 1982, (b) 27 June 1982, (c) 29 June 1982, (d) 21 August 1982, (e) 26 August 1982 and (f) 29 June 1983. The black contour line displays the border of the federal state Hamburg.
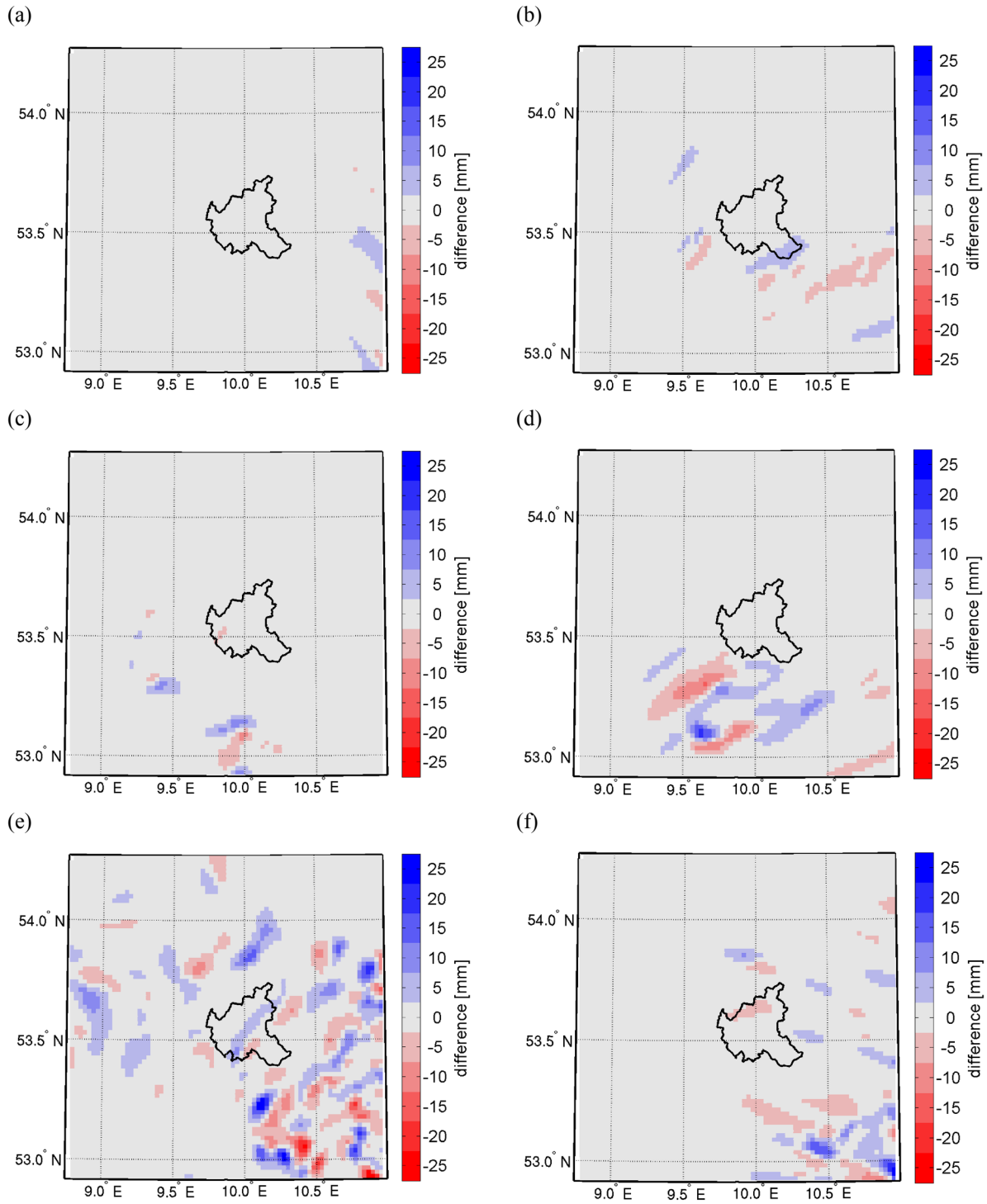
Figure C-2: Same as Figure C-1, but for heavy precipitation observed on (a) 13 June 1984, (b) 11 July 1984, (c) 3 August 1984, (d) 6 June 1985, (e) 20 June 1985 and (f) 22 July 1985.
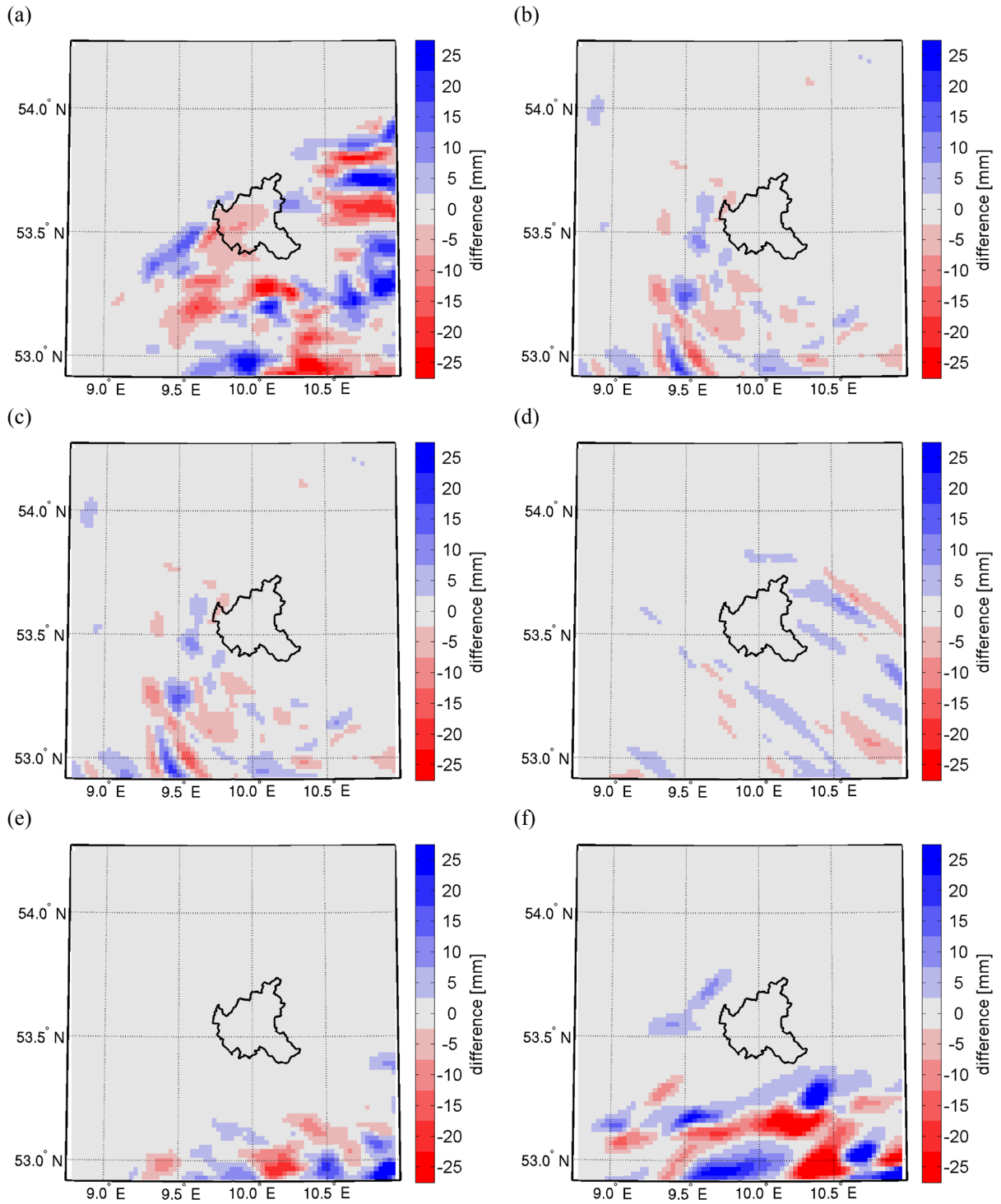
Figure C-3: Same as Figure C-1, but for heavy precipitation observed on (a) 16 August 1985, (b) 7 June 1986, (c) 10 July 1986, (d) 23 July 1986, (e) 30 June 1987 and (f) 11 July 1987.
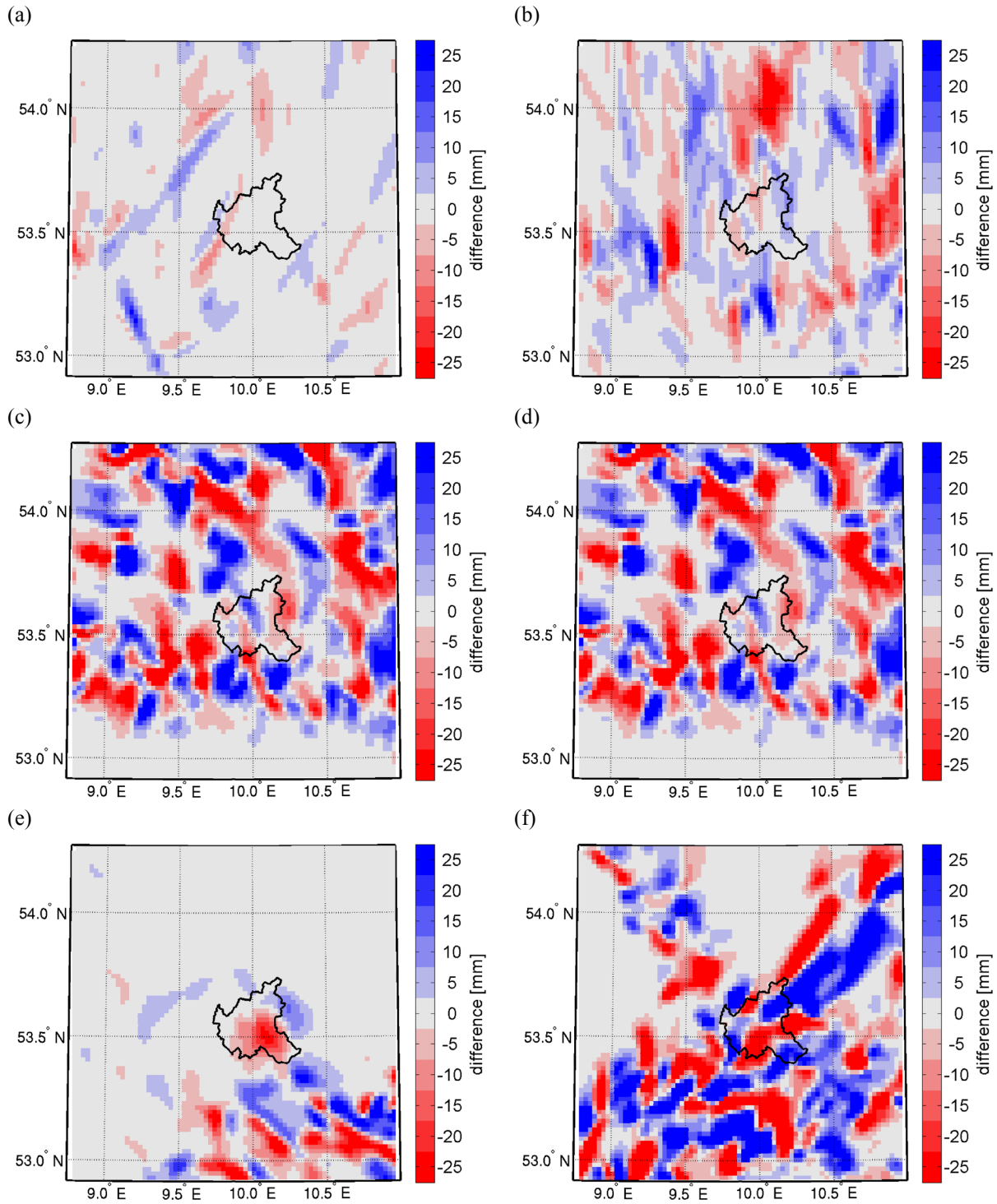
Figure C-4: Same as Figure C-1, but for heavy precipitation observed on (a) 15 July 1987, (b) 17 July 1987, (c) 20 July 1987, (d) 23 July 1987, (e) 29 July 1987 and (f) 28 June 1988.
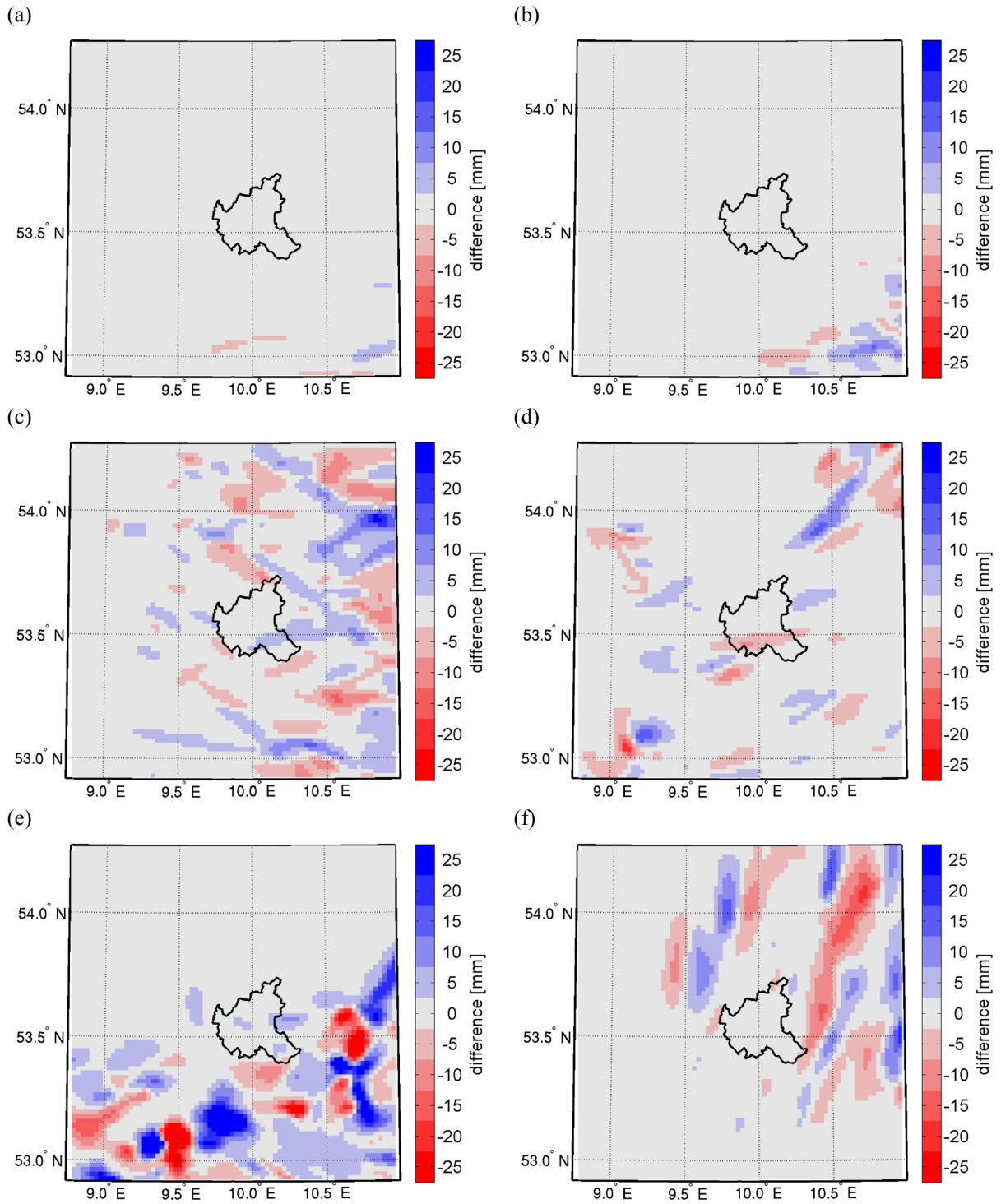
Figure C-5: Same as Figure C-1, but for heavy precipitation observed on (a) 22 July 1988, (b) 11 August 1988, (c) 21 August 1988, (d) 4 June 1989, (e) 7 June 1989 and (f) 27 June 1989.

141
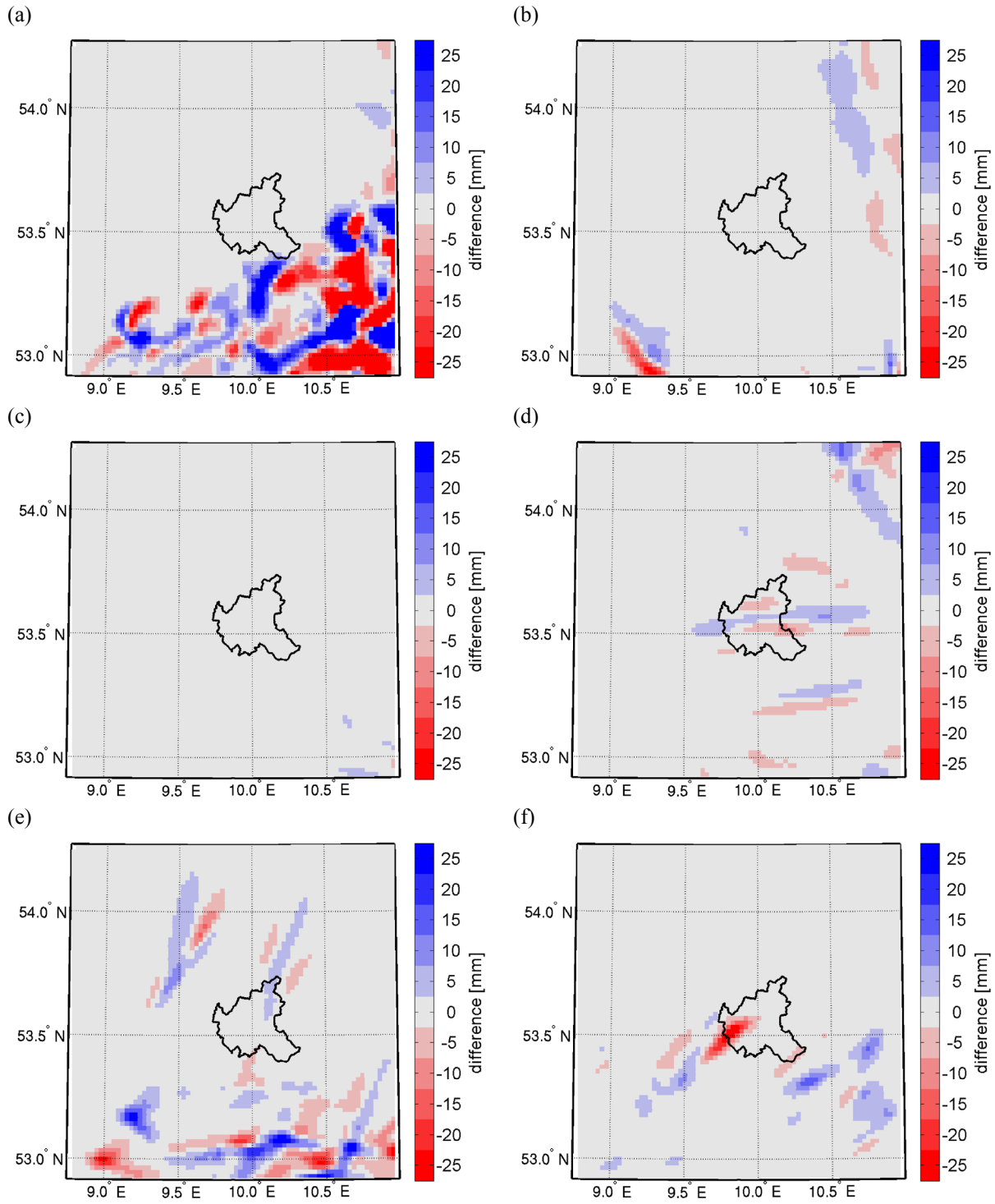
Figure C-6: Same as Figure C-1, but for heavy precipitation observed on (a) 8 July 1989, (b) 23 July 1989, (c) 27 August 1989, (d) 4 June 1990, (e) 27 June 1990 and (f) 14 August 1990.
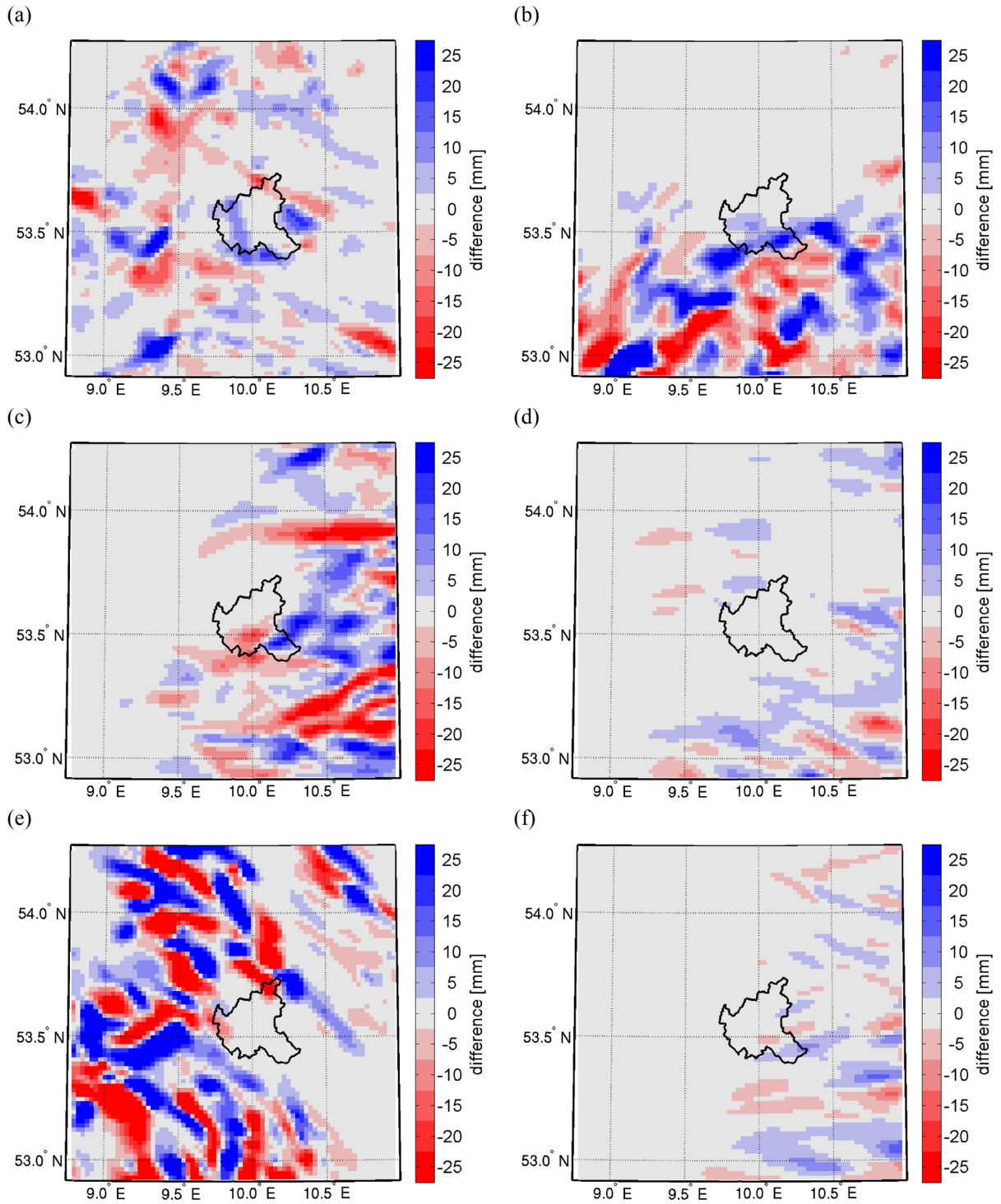
Figure C-7: Same as Figure C-1, but for heavy precipitation observed on (a) 19 August 1990, (b) 27 June 1991, (c) 1 July 1991, (d) 16 July 1991, (e) 1 August 1991 and (f) 17 August 1991.
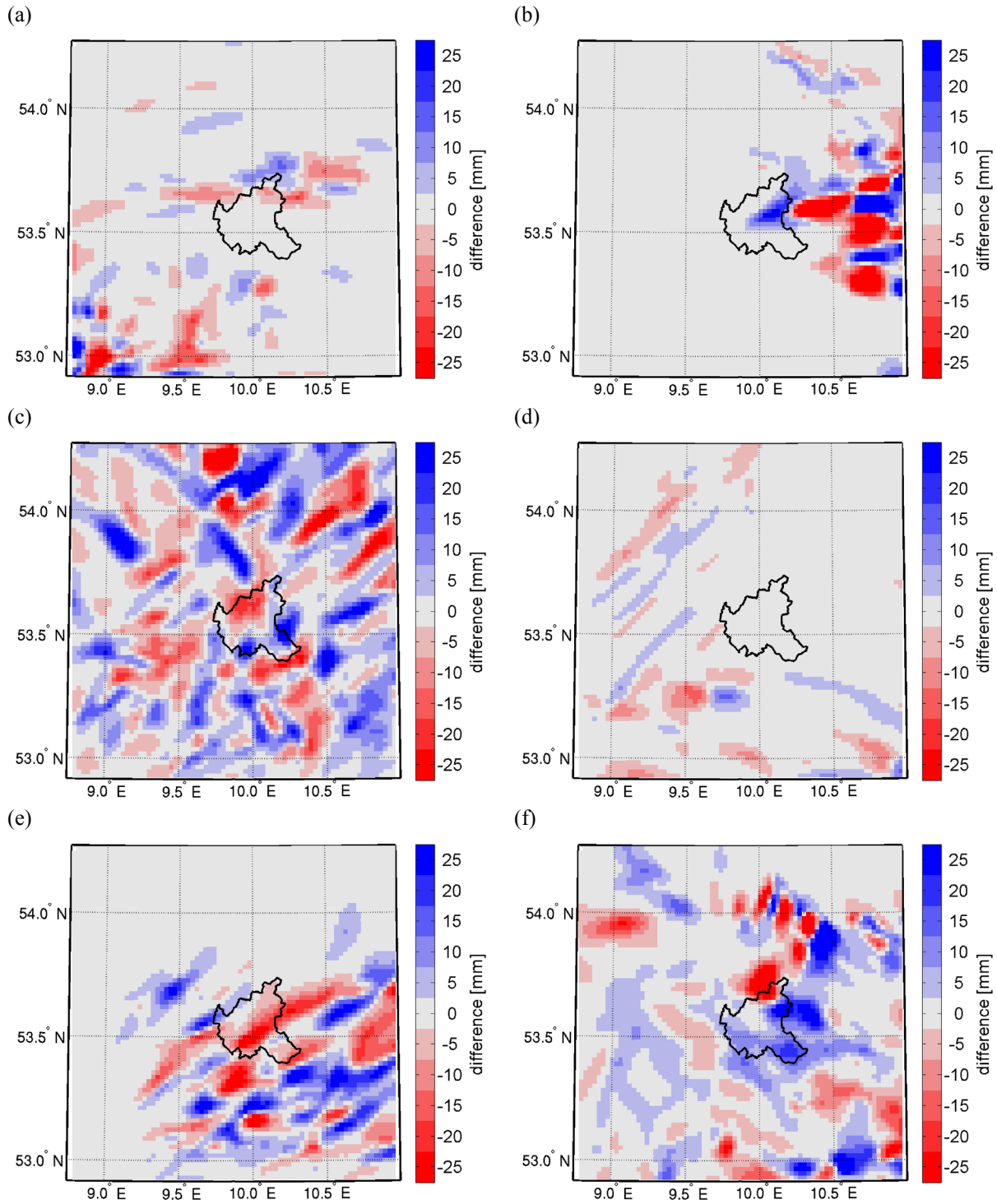
Figure C-8: Same as Figure C-1, but for heavy precipitation observed on (a) 4 July 1992, (b) 12 June 1993, (c) 20 July 1993, (d) 23 July 1993, (e) 15 August 1993 and (f) 7 July 1994.
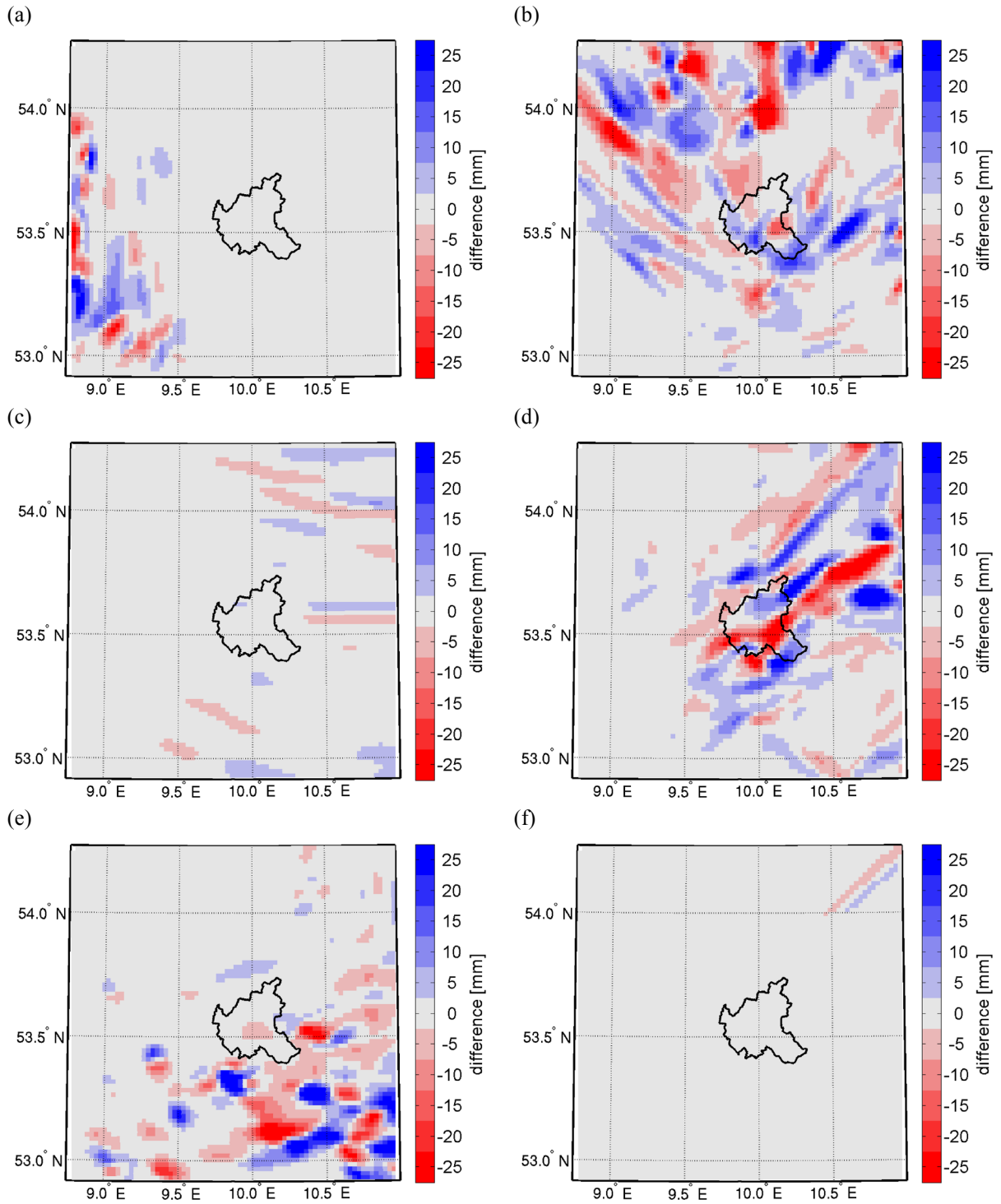
Figure C-9: Same as Figure C-1, but for heavy precipitation observed on (a) 14 July 1994, (b) 11 August 1994, (c) 14 August 1994, (d) 17 August 1994, (e) 25 August 1994 and (f) 21 July 1995.

145
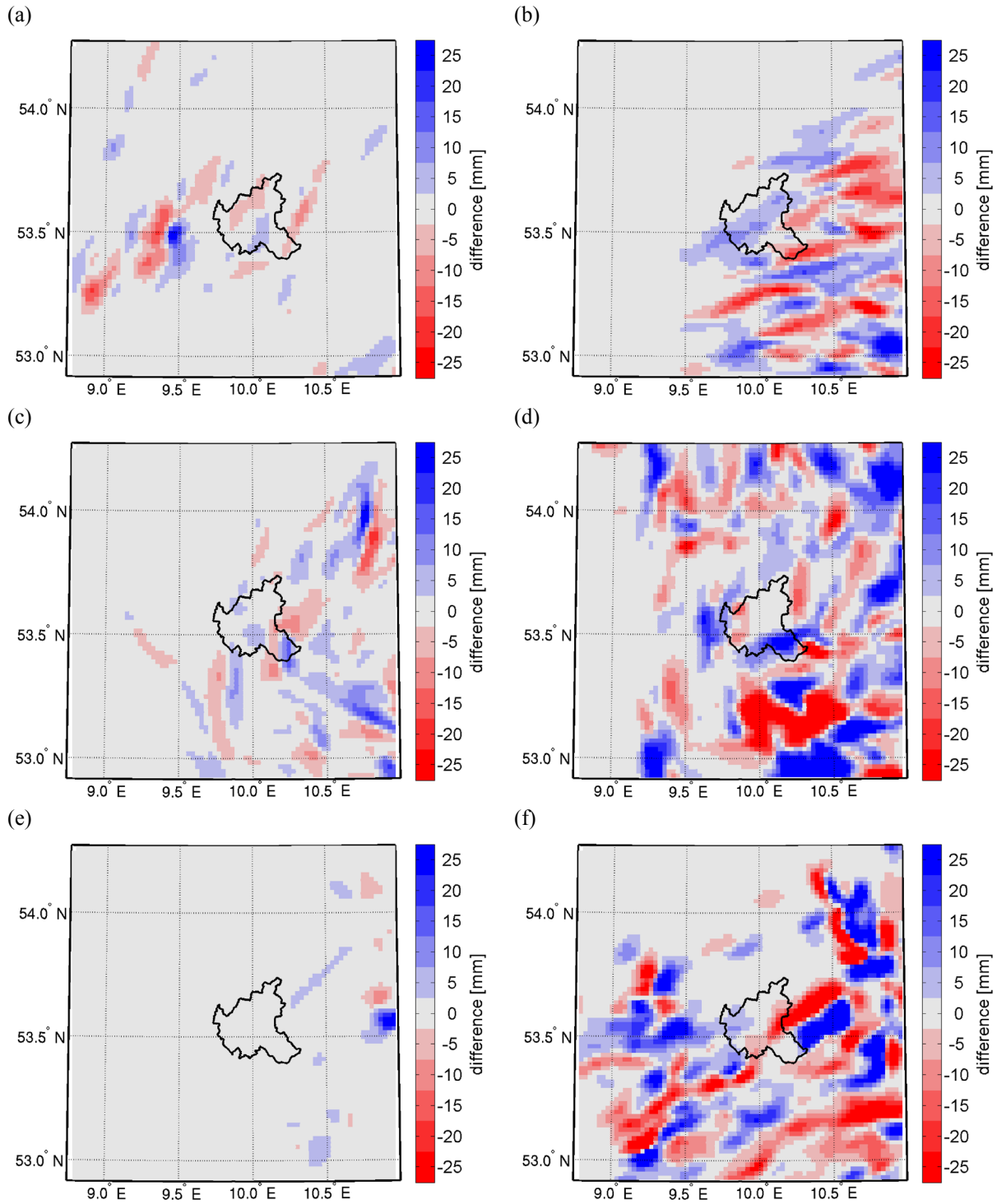
Figure C-10: Same as Figure C-1, but for heavy precipitation observed on (a) 23 August 1995, (b) 25 August 1995, (c) 27 August 1995, (d) 24 July 1996, (e) 28 August 1996 and (f) 12 June 1997.
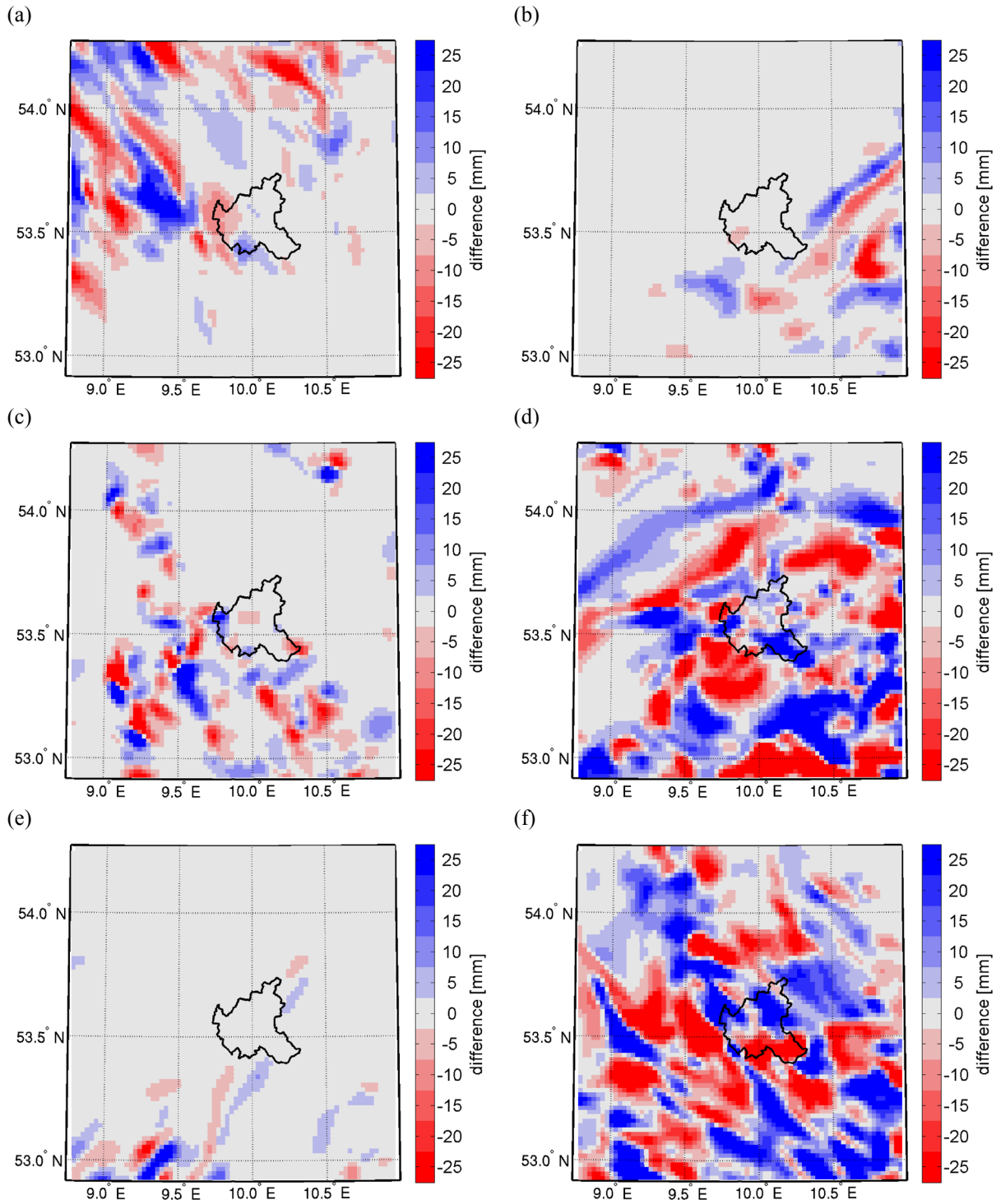
Figure C-11: Same as Figure C-1, but for heavy precipitation observed on (a) 27 June 1997, (b) 3 July 1997, (c) 15 July 1997, (d) 17 July 1997, (e) 20 July 1997 and (f) 25 July 1997.
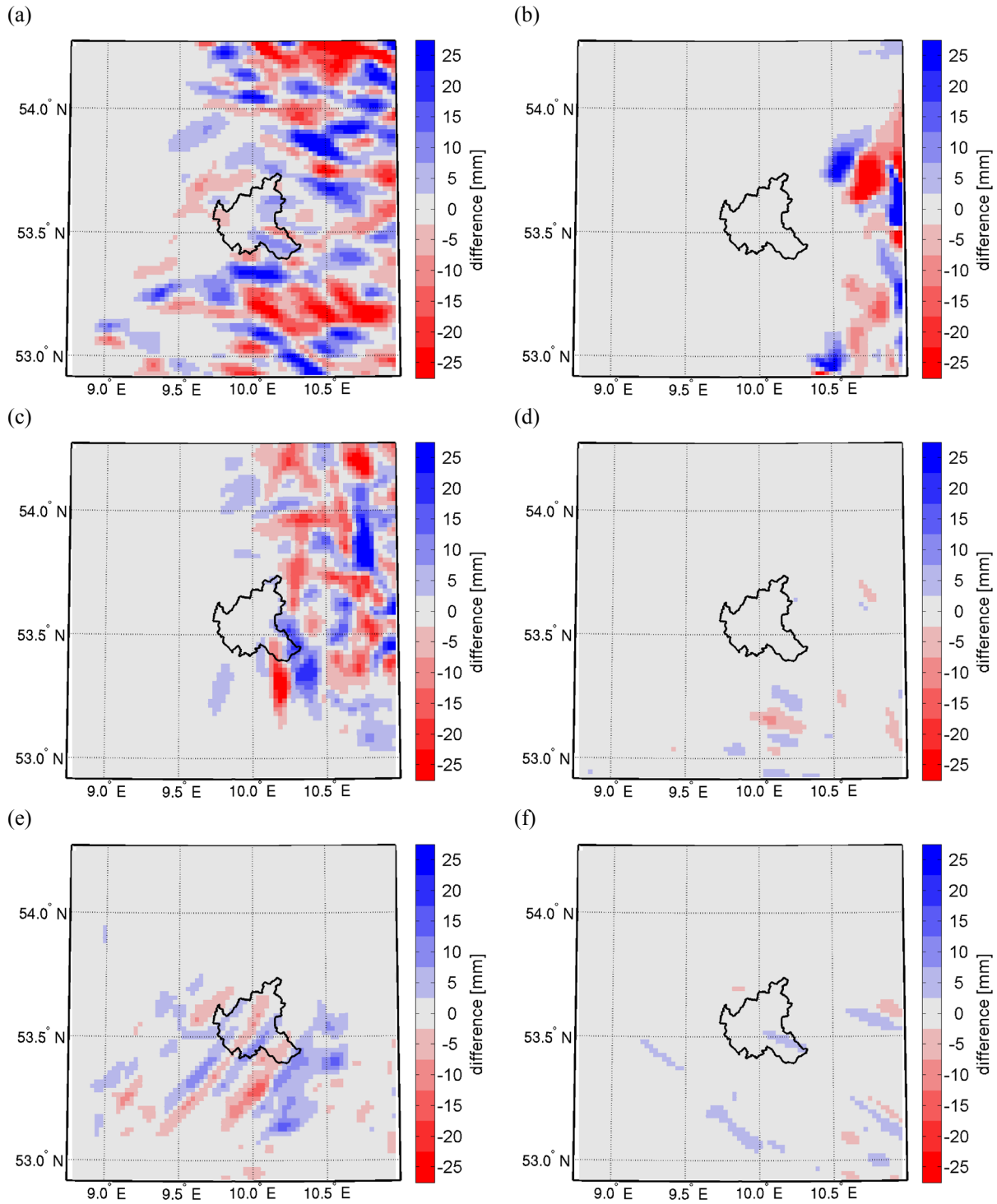
Figure C-12: Same as Figure C-1, but for heavy precipitation observed on (a) 31 July 1997, (b) 26 August 1997, (c) 28 August 1997, (d) 5 June 1998, (e) 25 June 1998 and (f) 23 August 1998.

List of important acronyms

AR4	Assessment Report 4 of the IPCC
ATKIS	Amtliches Topographisch-Kartographisches Informationssystem
BEP	Building Effect Parameterisation
BIAS	Bias
BMBF	Bundesministerium für Bildung und Forschung
BSU	Behörde für Stadtentwicklung und Umwelt
CERA	Climate and Environmental Data Retrieval and Archive
CLICC	Scenario CliSAP Compact City
CLM	Climate Local Model
CMIP	Coupled Model Intercomparison Project
CORDEX	Coordinated Regional Climate Downscaling Experiment
CORINE	Coordinate Information on the Environment
CRU	Climatic Research Unit
CTCO	Climatological Temporal Correlation
DA	Desired Accuracy
DGM5	Digitales Geländemodell 5 m
DJF	December, January, February
DSKG	Digitale Stadtgrundkarte
DWD	Deutscher Wetterdienst
ECA&D	European Climate Assessment and Data
ECHAM5	European Centre Hamburg Model Version 5
ECMWF	European Centre for Medium-Range Weather Forecasts
ENSEMBLES	ENSEMBLE-based Predictions of Climate Changes and their Impacts
ERA-40	ECMWF 40 years Reanalysis
ERA-Interim	ECMWF Interim Reanalysis
GCM	General Circulation Model
GPCC	Global Precipitation Climatology Centre
GRITOP	Gridded Topography
HITR	Hit-Rate
HRP	Hit-Rate of the Percentiles
IFS	Integrated Forecast System
IPCC	Intergovernmental Panel on Climate Change
JJA	June, July, August
KLIMZUG	Klimawandel in Regionen zukunftsfähig gestalten
KLIS3	Scenario KLIMZUG S3
LATE	Late (21:00 to 24:00 local time)
LGV	Landesbetrieb Geoinformation und Vermessung
MAM	March, April, May
MAMD	Mean Absolute Monthly Difference
MATLAB	Matrix Laboratory
METRAS	Mesoskaliges Transport- und Strömungsmodell

MM5	PSU/NCAR Mesoscale Model Version 5
MOST	Monin-Obukhov Similarity Theory
MPIOM	Max Planck Institute Ocean Model
NOAA	National Oceanic and Atmospheric Administration
NOON	Around noon (10:00 to 16:00 local time)
NOORO	Scenario without orography
NOURB	Scenario without non-natural surface covers
OISST	Optimum Interpolation Sea Surface Temperature
PDF	Probability Density Function
PET	Physiological Equivalent Temperature
PRUDENCE	Prediction of Regional Scenarios and Uncertainties for Defining European Climate Change Risks and Effects
PT	Perceived Temperature
RATV	Ratio of Temporal Variances
RCM	Regional Climate Model
REFR	Reference topography
REGNIE	Regionalisierung von Niederschlagshöhen
REMO	Regional Model
RMSE	Root Mean Square Error
ROD	Routine Observation Data
ROYA	Ratio Of Yearly Amplitudes
SKVAR	Skill Variance
SON	September, October, November
SRES	Special Report on Emissions Scenarios
SRTM	Shuttle Radar Topography Mission
SSC	Skill-Score
SST	Sea Surface Temperature
TAF	Transformation of Algorithms in Fortran
TS	Time Series
UHI	Urban Heat Island
UTC	Universal Time Coordinated

List of important symbols

α	Soil moisture availability
A	Constant in forcing factor
B_L	Budget of longwave radiation at the surface
B_S	Budget of shortwave radiation at the surface
c_p	Specific heat capacity of dry air
δ	Forcing factor
δ_0	Maximum value of the forcing factor
δ_{min}	Minimum value of the forcing factor
Δt	Time step
$\Delta \theta$	Difference of potential temperature
ΔT	Difference of air temperature
g	Acceleration due to gravity
h_θ	Depth of the daily temperature wave
ji	Grid index in x-direction
jj	Grid index in y-direction
jk	Grid index in z-direction
k_S	Thermal diffusivity of the soil
l_{21}	Specific heat of condensation/evaporation
L_{day}	Length of one day (86400 s)
M_i	Model result at time i
M_m	Model result for the mth month of the year
ν_S	Thermal conductivity of the soil
∇	Nabla operator
NH	Constant in forcing factor
NV	Constant in forcing factor
$NX1$	Number of grid points in x-direction
$NX2$	Number of grid points in y-direction
$NX3$	Number of grid points in z-direction
O_i	Observational data at time i
O_m	Observational data for the mth month of the year
ψ_c	Variable in forcing data

ψ_f	Forced prognostic variable
ψ_u	Unforced prognostic variable
p	Total pressure
p_0	Pressure of basic state
p_1	Thermodynamic pressure deviation
p_1^{top}	Thermodynamic pressure deviation at the model top
p_2	Dynamic pressure deviation
$\widehat{p_2}$	Temporal change of dynamic pressure deviation
p_2^{top}	Dynamic pressure deviation at the model top
p_{force}^{top}	Pressure at the model top in the forcing data
p_s	Surface pressure
$\Pi_{0,C}$	Exner function, correct
$\Pi_{0,W}$	Exner function, wrong
P	Precipitation
$P_{M,i}$	i[th] percentile of model data
$P_{O,i}$	i[th] percentile of observational data
$PDF_{M,i}$	Relative frequency of model data in the ith bin
$PDF_{O,i}$	Relative frequency of observational data in the ith bin
q_c	Specific cloud water content
q_r	Specific rain water content
q_S	Specific humidity at the surface
q_S^{SAT}	Specific humidity at saturation at the surface
q_v	Specific humidity
q_{vf}	Specific humidity, forced
q_{vu}	Specific humidity, unforced
q_{vf}^{SAT}	Specific humidity, forced, at saturation
q_v^{ADJ}	Specific humidity, saturation adjusted
q_v^{SAT}	Specific humidity at saturation
q_v^0	Specific humidity at saturation at 0 °C
q_v^{10m}	Specific humidity in 10 m above ground
q_*	Scaling value for specific humidity
Q_{ACCR}	Term representing accretion of cloud droplets by rain droplets
Q_{AUTO}	Term representing autoconversion of cloud droplets to rain droplets
Q_{EVAP}	Term representing evaporation of rain droplets

Q_{COND}	Term representing condensation and evaporation
ρ_0	Basic state air density
ρ_s	Air density at the surface
ρ_w	Water density
$\tilde{\rho}$	Deviation of air density
R_d	Rayleigh damping factor
R_L	Gas constant for dry air
t	Time
t_{init}	Time of model initialisation
θ	Potential temperature
θ_*	Scaling value for potential temperature
T	Air temperature
T_s	Surface temperature
u	Wind component in x-direction
u_*	Friction velocity
$U(P_{O,i})$	Allowed deviation for the ith percentile of observational data
v	Wind component in y-direction
$\vec{v}$	Three-dimensional wind vector
V_{SED}	Sedimentation velocity of rain droplets
w	Wind component in z-direction
w_0	Vertical wind component in Rayleigh damping (0 m/s)
w_d	Damped vertical wind component
w_u	Undamped vertical wind component
W_k	Depth of the column of available water at saturated soil

References

Adam, J.C. and D.P. Lettenmaier, 2003: Adjustment of global gridded precipitation for systematic bias. *J. Geophys. Res.*, **108,** D9, 14 pp.

Bedbur, G., 2012: Wie genau kann die Temperatur in 2 m Höhe über die Stabilitätsfunktionen aus der Temperatur in 10 m Höhe berechnet werden? Bachelorarbeit, Studiengang Meteorologie, Universität Hamburg, 36 pp.

Blazejczyk, K., Y. Epstein, G. Jendritzky, H. Staiger and B. Tinz, 2011: Comparison of UTCI to selected thermal indices. *Int. J. Biometeorol.*, **56 (3)**, 515-535.

BMBF, 2011: Klimawandel in Regionen. Anpassungsstrategien für sieben Regionen. Editors: Bardt, H., H. Biebeler, E. Chrischilles and M. Mahammadzadeh, 40 pp.

Bohnenstengel, S.I., K.H. Schlünzen and F. Beyrich, 2011: Representativity of in situ precipitation measurements – A case study for the LITFASS area in North-Eastern Germany. *J. Hydrol.*, **400**, 387-395.

Bouttier, F., B. Vie, O. Nuissier and L. Raynaud, 2012: Impact of stochastic physics in a convection-permitting ensemble. *Mon. Weather Rev.*, **140**, 3706-3721.

BSU, 2008: Versiegelungsdaten Hamburg 2008. Behörde für Stadtentwicklung und Umwelt, Hamburg.

Bungert, U.M., 2008: Einfluss der Nestung auf die Ergebnisse meteorologischer Modelle. Dissertation zur Erlangung des Doktorgrades der Naturwissenschaften im Department Geowissenschaften der Universität Hamburg, Universität Hamburg, 134 pp.

Burian, S.J. and J.M. Shepherd, 2005: Effect of urbanization on the diurnal rainfall pattern in Houston. *Hydrol. Process.*, **19**, 1089-1103.

Carraca, M.G.D. and C.G. Collier, 2007: Modelling the impact of high-rise buildings in urban areas on precipitation initiation. *Meteorol. Appl.*, **14**, 149-161.

Cheng V, E. Ng, C. Chan and B. Givoni, 2012: Outdoor thermal comfort study in a sub-tropical climate: a longitudinal study based in Hong Kong. *Int. J. Biometeorol.*, **56 (1)**, 43-56.

Christensen, J.H. and O.B. Christensen, 2007: A summary of the PRUDENCE model projections of changes in European climate by the end of this century. *Climatic Change*, **81**, 7-30.

154

Christensen, J.H., B. Hewitson, A. Busuioc, A. Chen, X. Gao, I. Held, R. Jones, R.K. Kolli, W.-T. Kwon, R. Laprise, V. Magaña Rueda, L. Mearns, C.G. Menéndez, J. Räisänen, A. Rinke, A. Sarr and P. Whetton, 2007: Regional Climate Projections. In: Climate Change 2007: The Physical Science Basis. Contribution of Working Group I to the Fourth Assessment Report of the Intergovernmental Panel on Climate Change (Solomon, S., D. Qin, M. Manning, Z. Chen, M. Marquis, K.B. Averyt, M. Tignor and H.L. Miller (editors)). Cambridge University Press, Cambridge, United Kingdom and New York, NY, USA, p. 850.

Christensen, J.H., F. Boberg, O.B. Christensen and P. Lucas-Picher, 2008: On the need for bias correction of regional climate change projections of temperature and precipitation. *Geophys. Res. Lett.*, **35**, L20709, 6 pp.

Conrady, C., 2010: Typische Werte statistischer Maßzahlen zur Evaluierung mesoskaliger Modelle. Bachelorarbeit, Studiengang Meteorologie, Universität Hamburg, 39 pp.

Cox, R., B.L. Bauer and T. Smith, 1998: A mesoscale model intercomparison. *Bull. Amer. Meteor. Soc.*, **79 (2)**, 265-283.

Daneke, C., 2012: Modellierung von Stadtentwicklungsprozessen am Beispiel Hamburgs unter Berücksichtigung stadtklimatologischer Aspekte. Dissertation zur Erlangung des Doktorgrades der Naturwissenschaften im Fachbereich Geographie der Universität Hamburg, 211 pp.

Daschkeit, A., 2011: Das Klima der Region und mögliche Entwicklungen in der Zukunft bis 2100. In von Storch, H. and M. Claussen (editors), Klimabericht für die Metropolregion Hamburg, DOI 10.1007/978-3-642-16035-6, Springer 2011, p. 61-90.

Davies, H.C., 1976: A lateral boundary formulation for multi-level prediction models. *Quart. J. R. Met. Soc.*, **102**, 405-418.

Deardorff, J.W., 1978: Efficient prediction of ground surface temperature and moisture, with inclusion of a layer of vegetation. *J. Geophys. Res.*, **83**, C4, 1889-1903.

Dee, D.P., S.M. Uppala, A.J. Simmons, P. Berrisford, P. Poli, S. Kobayashi, U. Andrae, M.A. Balmaseda, G. Balsamo, P. Bauer, P. Bechtold, A.C.M. Beljaars, L. van de Berg, J. Bidlot, N. Bormann, C. Delsol, R. Dragani, M. Fuentes, A.J. Geer, L. Haimberger, S.B. Healy, H. Hersbach, E.V. Holm, L. Isaksen, P. Kallberg, M. Köhler, M. Matricardi, A.P. McNally, B.M. Monge-Sanz, J.-J. Morcrette, B.-K. Park, C. Peubey, P. de Rosnay, C. Tavolato, J.-N. Thepaut, F. Vitart, 2011: The ERA-Interim reanalysis: configuration and performance of the data assimilation system. *Q. J. R. Meteorol. Soc.*, **137**, 553–597.

Dibike, Y.B., P. Gachon, A. St-Hilaire, T.B.M.J. Ouarda and Van T.-V. Nguyen, 2008: Uncertainty analysis of statistically downscaled temperature and precipitation regimes in Northern Canada. *Theor. Appl. Climatol.*, **91**, 149-170.

Doms, G. and F. Herbert, 1985: Fluid- und Mikrodynamik in numerischen Modellen konvektiver Wolken. Berichte des Instituts für Meteorologie und Geophysik der Universität Frankfurt/Main, p. 218-254.

ECMWF, 2009: ERA-Interim model level 00_6H. World Data Center for Climate. CERA-DB "ERAIN_ML00_6H" http://cera-www.dkrz.de/WDCC/ui/Compact.jsp?acronym=ERAIN_ML00_6H, last access on 29.05.2012.

ECMWF, 2009: IFS DOCUMENTATION - Cy33r1 Operational implementation 3 June 2008, PART II: DATA ASSIMILATION. European Centre for Medium-Range Weather Forecasts, Shinfield Park, Reading, RG2 9AX, England, 160 pp.

ECMWF, 2010: IFS DOCUMENTATION - Cy36r1 Operational implementation 26 January 2010, PART II: DATA ASSIMILATION. European Centre for Medium-Range Weather Forecasts, Shinfield Park, Reading, RG2 9AX, England, 168 pp.

Efron, B., 1979: Bootstrap methods: another look at the Jackknife. *Ann. Statist.*, **7,** 1-26.

Endler, C. and A. Matzarakis, 2011: Analysis of high resolution simulations for the Black Forest region from a point of view of tourism climatology – a comparison between two regional climate models (REMO and CLM). *Theor. Appl. Climatol.*, **103**, 427-440.

Ertl, 2010: Charakteristika und Repräsentativität von Niederschlag in Norddeutschland. Diplomarbeit im Fach Meteorologie, Meteorologisches Institut, Universität Hamburg, 153 pp.

Feldmann, H., B. Früh, G. Schädler, H.-J. Panitz, K. Keuler, D. Jacob and P. Lorenz, 2008: Evaluation of the precipitation for South-western Germany from high resolution simulations with regional climate models. *Meteorol. Z.*, **17 (4)**, 455-465.

Flagg, D.D., R. Schoetter, B.H. Fock, D. Grawe, P. Kirschner and K.H. Schlünzen, 2012: From land-use to surface cover for mesoscale atmospheric models. Submitted to *Theor. Appl. Climatol*.

Foley, A.M., 2010: Uncertainty in regional climate modelling: a review. *Prog. Phys. Geog.*, **34**, 647-670.

Fröhlich, D. and A. Matzarakis, 2013: Modeling of changes in thermal bioclimate: examples based on urban spaces in Freiburg, Germany. *Theor. Appl. Climatol.*, **111 (3-4)**, 547-558.

Fuentes, U. and D. Heimann, 2000: An improved statistical-dynamical downscaling scheme and its application to the Alpine precipitation climatology. *Theor. Appl. Climatol.*, **65**, 119-135.

Garratt, J.R., 1992: The atmospheric boundary layer. Cambridge University Press, p. 49-60.

Giering, R. and T. Kaminski, 1998: Recipes for adjoint code construction. ACM Transactions on Mathematical Software (TOMS), **24 (4)**, ACM New York, NY, USA, 35 pp.

Giering, R., T. Kaminski, R. Todling, R. Errico, R. Gelaro and N. Winslow, 2005: Generating tangent linear and adjoint versions of NASA/GMAO's Fortran-90 global weather forecast model. Volume 50 of Lecture Notes in Computational Science and Engineering. Springer, New York, NY, 273-282.

Gilmore, M.S., J.M. Straka and E.N. Rasmussen, 2004: Precipitation and evolution sensitivity in simulated deep convective storms: comparisons between liquid-only and simple ice and liquid phase microphysics. *Mon. Weather Rev.*, **132**, 1897-1916.

Giorgi, F., C. Jones and G.R. Asrar, 2009: Addressing climate information needs at the regional level: the CORDEX framework. *WMO Bulletin*, **58 (3)**, 9 pp.

Grawe, D., H.L. Thompson, J.A. Salmond, X.-M. Cai and K.H. Schlünzen, 2013: Modelling the impact of urbanisation on regional climate in the Greater London Area. *Int. J. Climatol.*, **33**, 2388-2401.

Grimmond, C.S.B, M. Blackett, M.J. Best, J.-J. Baik, S.E. Belcher, J. Beringer, S.I. Bohnenstengel, I. Calmet, F. Chen, A. Coutts, A. Dandou, K. Fortuniak, M.L. Goueva, R. Hamdi, M. Hendry, M. Kanda, T. Kawai, Y. Kawamoto, H. Kondo, E.S. Krayenhoff, S.-H. Lee, T. Loridan, A. Martilli, V. Masson, S. Miao, K. Oleson, R. Ooka, G. Pigeon, A. Porson, Y.-H. Ryu, F. Salamanca, G.J. Steenevold, M. Tombrou, J.A. Voogt, D.T. Young and N. Zhang, 2011: Initial results from phase 2 of the international urban energy balance model comparison. *Int. J. Climatol.*, **31**, 244-272.

Haylock, M.R., N. Hofstra, A.M.G. Klein Tank, E.J. Klok, P.D. Jones and M. New, 2008: A European daily high-resolution gridded data set of surface temperature and precipitation for 1950-2006. *J. Geophys. Res.*, **113,** D20119, 12 pp.

Hegerl, G.C., F.W. Zwiers, P. Braconnot, N.P. Gillett, Y. Luo, J.A. Marengo Orsini, N. Nicholls, J.E. Penner and P.A. Stott, 2007: Understanding and Attributing Climate Change. In: Climate Change 2007: The Physical Science Basis. Contribution of Working Group I to the Fourth Assessment Report of the Intergovernmental Panel on Climate Change (Solomon, S., D. Qin, M. Manning, Z. Chen, M. Marquis, K.B. Averyt, M. Tignor and H.L. Miller (editors)).

Cambridge University Press, Cambridge, United Kingdom and New York, NY, USA, p. 665.

Hellmers, S. and E. Pasche, 2011: Quantification of climate change impacts on flood probability in urban areas and adaptation measures using climate model data with a high spatial resolution and a semi-distributed rainfall runoff model. Proceedings, Exhibition and International Conference on Climate Impact, Flood Protection and Hydraulic Engineering, Hamburg, 12 pp.

Hellmers, S. and N. Hüffmeyer, 2013: Quantifizierung der Wirksamkeit von Anpassungsmaßnahmen aus wasserwirtschaftlicher Sicht. In Kruse, E., T. Zimmermann, A. Kittel, W. Dickhaut, J. Knieling, C. Sörensen (editors): Abschlussbericht Modellgebiet Wandse - Konzepte der Stadtentwicklung zur Klimaanpassung, ihre Wirkungen und Umsetzbarkeit. In preparation.

Höppe, P., 1999: The physiological equivalent temperature – a universal index for the biometeorological assessment of the thermal environment. *Int. J. Biometeorol.*, **43**, 71-75.

Hoffmann, P., 2009: Modifikation von Starkniederschlägen durch urbane Gebiete. Diplomarbeit im Fach Meteorologie. Meteorologisches Institut, Universität Hamburg, 117 pp.

Hoffmann, P. 2012. Quantifying the influence of climate change on the urban heat island of Hamburg using different downscaling methods. Dissertation zur Erlangung des Doktorgrades der Naturwissenschaften im Department Geowissenschaften, Universität Hamburg, 138 pp.

Hoffmann, P., O. Krueger and K.H. Schlünzen, 2012: A statistical model for the urban heat island and its application to a climate change scenario. *Int. J. Climatol.*, **32**, 1238-1248.

Hoffmann, P. and K.H. Schlünzen, 2012: Weather pattern classification to represent the urban heat island in present and future climate, accepted by *J. Appl. Meteorol. Climatol.*.

Hollweg, H.D., U. Böhm, I. Fast, B. Hennemuth, K. Keuler, E. Keup-Thiel, M. Lautenschlager, S. Legutke, K. Radtke, B. Rockel, M. Schubert, A. Will, M. Woldt and C. Wunram, 2008: Ensemble simulations over Europe with the regional climate model CLM forced with IPCC AR4 global scenarios. M&D Technical Report No. 3, 152 pp.

Huntley, B., Y.C. Collingham, S.G. Willis and R. E. Green, 2008: Potential impacts of climatic change on European breeding birds. *PLoS ONE*, **3 (1)**, e1439, 11 pp.

Hupfer, P. and W. Kuttler, 2006: Witterung und Klima: Eine Einführung in die Meteorologie und Klimatologie. B.G. Teubner Verlag GWV Fachverlag GmbH, Wiesbaden, p. 90.

Inamura, T., T. Izumi and H. Matsuyama, 2011: Diagnostic study of the effects of a large city on heavy rainfall as revealed by an ensemble simulation: a case study of central Tokyo, Japan.

J. Appl. Meteorol. Climatol., **50**, 713-728.

Jacob, D., 2001: A note to the simulation of the annual and inter-annual variability of the water budget over the Baltic Sea drainage basin. *Meteorol. Atmos. Phys.*, **77**, 61-73.

Jacob, 2005: REMO climate of the 20th century run, UBA project, 0.088 degree resolution, run no. 006210, 1h data. World Data Center for Climate. CERA-DB "REMO_UBA_C20_1_R006210_1H". http://cera-www.dkrz.de/WDCC/ui/Compact.jsp?acronym=REMO_UBA_C20_1_R006210_1H, last access on 10 May 2010.

Jacob, 2005: REMO A1B scenario run, UBA project, 0.088 degree resolution, run no. 006211, 1h data. World Data Center for Climate. CERA-DB "REMO_UBA_A1B_1_R006211_1H". http://cera-www.dkrz.de/WDCC/ui/Compact.jsp?acronym=REMO_UBA_A1B_1_R006211_1H, last access on 7 November 2012.

Jacob, D., L. Bärring, O.B. Christensen, J.H. Christensen, M. de Castro, M. Déqué, F. Giorgi, S. Hagemann, M. Hirschi, R. Jones, E. Kjellström, G. Lenderink, B. Rockel, E. Sánchez, C. Schär, S.I. Seneviratne, S. Somot, A. van Ulden and B. van den Hurk, 2007: An inter-comparison of regional climate models for Europe: model performance in present-day climate. *Climatic change*, **81**, 31-52.

Jacob, D., H. Göttel, S. Kotlarski, P. Lorenz and K. Sieck, 2008: Klimaauswirkungen und Anpassung in Deutschland: Erstellung regionaler Klimaszenarien für Deutschland mit dem Klimamodell REMO. Forschungsbericht 204 41 138 Teil 2, i.A. des UBA Dessau, 159 pp.

Jacob, D., E. Nilson, L. Tomassini and K. Bülow, 2009: REMO climate of the 20th century run, BFG project, 0.088 degree resolution, run no.2, 1h data. World Data Center for Climate. CERA-DB "REMO_BFG_C20_1H". http://cera-www.dkrz.de/WDCC/ui/Compact.jsp?acronym=REMO_BFG_C20_1H, last access on 10 May 2010.

Jacob, D., E. Nilson, L. Tomassini and K. Bülow, 2009: REMO A1B scenario run, BFG project, 0.088 degree resolution, 1h values. World Data Center for Climate. CERA-DB "REMO_BFG_A1B_1H". http://cera-www.dkrz.de/WDCC/ui/Compact.jsp?acronym=REMO_BFG_A1B_1H, last access on 7 November 2012.

Jacob, D., K. Bülow, L. Kotova, C. Moseley, J. Petersen and D. Rechid, 2012: Regionale Klimaprojektionen für Europa und Deutschland: Ensemble Simulationen für die Klimafolgenforschung. CSC Report 6, Climate Service Center, 51 pp.

Jendritzky, G., H. Staiger, K. Bucher, A. Graetz and G. Laschewski, 2000: The perceived temperature: The method of the Deutscher Wetterdienst for the Assessment of Cold Stress and Heat Load for the Human Body. Internet Workshop on Windchill, 03.-07. April 2000, hosted by the Meteorological Service of Canada, 23 pp.

Jones, R.N., 2000: Managing uncertainty in climate change projections-issues for impact assessment. *Climatic Change*, **45**, 403-419.

Jungclaus, J.H., N. Keenlyside, M. Botzet, H. Haak, J.-J. Luo, M. Latif, J. Marotzke, U. Mikolajewicz and E. Roeckner, 2006: Ocean circulation and tropical variability in the coupled model ECHAM5/MPI-OM. *J. Climate.*, **19**, 3952-3972.

Kay, A.L., H.N. Davies, V.A. Bell and R.G. Jones, 2009: Comparison of uncertainty sources for climate change impacts: flood frequency in England. *Climatic Change*, **92**, 41-63.

Kendon, E.J., D.P. Rowell, R.G. Jones and E. Buonomo, 2008: Robustness of future changes in local precipitation extremes. *J. Climate.*, **21**, 4280-4297.

Kessler, E., 1969: On the distribution and continuity of water substance in atmospheric circulation. Meteorological Monographs, American Meteorological Society, 82 pp.

Keuler, K., 2006: Quantifizierung von Ungenauigkeiten regionaler Klima- und Klimaänderungssimulationen (QUIRCS). QUIRCS Abschlussbericht, 156 pp.

Keuler, K., M. Lautenschlager, C. Wunram, E. Keup-Thiel, M. Schubert, A. Will, B. Rockel and U. Boehm, 2009: Climate Simulation with CLM, Climate of the 20th Century run no.2, Data Stream 2: European region MPI-M/MaD. World Data Center for Climate. DOI:10.1594/WDCC/CLM_C20_2_D2. http://dx.doi.org/10.1594/WDCC/CLM_C20_2_D2, last access on 10 May 2010.

Keuler, K., M. Lautenschlager, C. Wunram, E. Keup-Thiel, M. Schubert, A. Will, B. Rockel and U. Boehm, 2009: Climate Simulation with CLM, Climate of the 20th Century run no.3, Data Stream 2: European region MPI-M/MaD. World Data Center for Climate. DOI:10.1594/WDCC/CLM_C20_3_D2. http://dx.doi.org/10.1594/WDCC/CLM_C20_3_D2, last access on 10 May 2010.

Kim, J., K. R. Kim, B.-C. Choi, D.-G. Lee and J.-S. Kim, 2009: Regional Distribution of Perceived Temperatures Estimated by the Human Heat Budget Model (the Klima-Michel Model) in South Korea. *Adv. Atmos. Sci.*, **26 (2)**, 275-282.

Kong, F. and M.K. Yau, 1997: An explicit approach to microphysics in MC2. *Atmos.-Ocean*, **35 (3)**, 257-291.

Kotlarski, S., A. Block, U. Böhm, D. Jacob, K. Keuler, R. Knoche, D. Rechid and A. Walter, 2005: Regional climate model simulations as input for hydrological applications: evaluation of uncertainties. *ADGEO*, **5**, 119-125.

Kruse, E., J. Ziegler, N. Klostermann and J. Fink, 2013: Analyse der Stadtstrukturtypen und ihre weitere Entwicklung gemäß der sozio-ökonomischen Rahmenszenarien. In Kruse, E., T. Zimmermann, A. Kittel, W. Dickhaut, J. Knieling, C. Sörensen (editors): Abschlussbericht Modellgebiet Wandse - Konzepte der Stadtentwicklung zur Klimaanpassung, ihre Wirkungen und Umsetzbarkeit. In preparation.

Kunert, L., E. Rottgardt, R. Schoetter and E. Kruse, 2013: Sozio-ökonomische Entwicklungsszenarien sowie Strategien und Maßnahmen der Klimaanpassung abgeleitet aus den Rahmenszenarien. In Kruse, E., T. Zimmermann, A. Kittel, W. Dickhaut, J. Knieling, C. Sörensen (editors): Abschlussbericht Modellgebiet Wandse - Konzepte der Stadtentwicklung zur Klimaanpassung, ihre Wirkungen und Umsetzbarkeit. In preparation.

Kuttler, W., 2011: Climate change in urban areas. *Environmental Sciences Europe*, **23 (21)**, 15 pp.

Lautenschlager, M., K. Keuler, C. Wunram, E. Keup-Thiel, M. Schubert, A. Will, B. Rockel and U. Boehm, 2009: Climate Simulation with CLM, Climate of the 20th Century run no.1, Data Stream 2: European region MPI-M/MaD. World Data Center for Climate. Doi:10.1594/WDCC/CLM_C20_1_D2. http://dx.doi.org/10.1594/WDCC/CLM_C20_1_D2, last access on 10 May 2010.

Lawrence, M.G., 2005: The Relationship between Relative Humidity and the Dewpoint Temperature in Moist Air: A Simple Conversion and Applications. *Bull. Amer. Meteor. Soc.*, **86**, 225–233.

Legates, D.R. and C.J. Willmott, 1990: Mean seasonal and spatial variability in gauge-corrected, global precipitation. *Int. J. Climatol.*, **10**, 111-127.

Lei, M., D. Niyogi, C. Kishtawal, R.A. Pielke, A. Beltran-Przekurat, T.E. Nobis and S.S. Vaidya, 2008: Effect of explicit urban land surface representation of the simulation of the July 205 heavy rain event over Mumbai, India. *Atmos. Chem. Phys. Discuss.*, **8**, 8773-8816.

Lengfeld, K. and F. Ament, 2012: Observing Local-Scale Variability of Near-Surface Temperature and Humidity using a Wireless Sensor Network, *J. Appl. Meteor. Climatol.*, **51**, 30-41.

LGV, 2009: Digitale Stadtgrundkarte. Landesvermessungsamt Hamburg.

Lin, C.Y., W.C. Chen, P.-L. Chang and Y.-F. Sheng, 2011: Impact of the urban heat island effect on precipitation over a complex geographic environment in northern Taiwan. *J. Appl. Meteor. Climatol.*, **50**, 339-353.

Linde, M., P. Hoffmann, K.H. Schlünzen and R. Schoetter, 2013: Auswirkung der veränderten Stadtstrukturtypen auf die mittleren Sommertemperaturen. In Kruse, E., T. Zimmermann, A. Kittel, W. Dickhaut, J. Knieling, C. Sörensen (editors): Abschlussbericht Modellgebiet Wandse - Konzepte der Stadtentwicklung zur Klimaanpassung, ihre Wirkungen und Umsetzbarkeit. In preparation.

Lüpkes, C. and K.H. Schlünzen, 1996: Modelling the arctic convective boundary-layer with different turbulence parameterizations. *Boundary-Layer Meteorol.,* **79**, 107-130.

Marshall, J.S. and W.M. Palmer, 1948: The distribution of rain drops with size. *J. Meteor.*, **5**, 165-166.

Martilli, A., A. Clappier and M. W. Rotach, 2002: An Urban Surface Exchange Parameterisation for Mesoscale Models. *Bound.-Lay. Meteorol.*, **104**, 261-304.

Matheson, M.A. and Y. Ashie, 2008: The effect of changes of urban surfaces on rainfall phenomenon as determined by a non-hydrostatic mesoscale model. *J. Meteorol. Soc. Jpn.*, **86 (5)**, 733-751.

Matzarakis, A., M. Hämmerle, C. Endler, S. Muthers and E. Koch, 2012: Assessment of tourism and recreation destinations under climate change conditions in Austria. *Meteorol. Z.*, **21 (2)**, 157-165.

Mayer, H., J. Holst, P. Dostal, F. Imbery and D. Schindler, 2008: Human thermal comfort in summer within an urban street canyon in Central Europe. *Meteorol. Z.*, **17 (3)**, 241-250.

Meehl, G.A., C. Covey, T. Delworth, M. Latif, B. McAvaney, J.F.B. Mitchell, R.J. Stouffer and K.E. Taylor, 2007: The WCRP CMIP3 multimodel dataset. A new era in climate change research. *Bull. Amer. Meteor. Soc.*, **88**, 1383–1394.

Meehl, G.A., T.F. Stocker, W.D. Collins, P. Friedlingstein, A.T. Gaye, J.M. Gregory, A. Kitoh, R. Knutti, J.M. Murphy, A. Noda, S.C.B. Raper, I.G. Watterson, A.J. Weaver and

Z.-C. Zhao, 2007: Global Climate Projections. In: Climate Change 2007: The Physical Science Basis. Contribution of Working Group I to the Fourth Assessment Report of the Intergovernmental Panel on Climate Change (Solomon, S.,D. Qin, M. Manning, Z. Chen, M. Marquis, K.B. Averyt, M. Tignor and H.L. Miller (editors)). Cambridge University Press, Cambridge, United Kingdom and New York, NY, USA, p. 749.

Miao, S., F. Chen, Q. Li and S. Fan, 2011: Impacts of urban processes and urbanization on summer precipitation: a case study of heavy rainfall in Beijing on 1 August 2006. *J. Appl. Meteor. Climatol.*, **50**, 806-825.

Mitchell, T.D. and P.D. Jones, 2005: An improved method of constructing a database of monthly climate observations and associated high-resolution grids. *Int. J. Climatol.*, **25,** 693-712.

Murphy, J.M., B.B.B. Booth, M. Collins, G.R. Harris, D.M.H. Sexton and M.J. Webb, 2007: A methodology for probabilistic predictions of regional climate change from perturbed physics ensembles. *Phil. Trans. R. Soc. A*, **365**, 1993-2028.

Muthers, S., A. Matzarakis and E. Koch, 2010: Climate change and mortality in Vienna-A human biometeorological analysis based on regional climate modeling. *Int. J. Environ. Res. Public Health*, **7**, 2965-2977.

Nakicenovic, N., J. Alcamo, G. Davis, B. de Vries, J. Fenhann, S. Gaffin, K. Gregory, A. Gruebler, T.Y. Jung, T. Kram, E. L. La Rovere, L. Michaelis, S. Mori, T. Morita, W. Pepper, H. Pitcher, L. Price, K. Riahi, A. Roehrl, H.-H. Rogner, A. Sankovski, M. Schlesinger, P. Shukla, S. Smith, R. Swart, S. van Rooijen, N. Victor and Z. Dadi, 2000. Emissions Scenarios. Cambridge University Press, p. 3-11.

New, M., M. Hulme and P.D. Jones, 1999: Representing twentieth-century space-time climate variability. Part I: Development of a 1961-90 mean monthly terrestrial climatology. *J. Climate*, **12,** 829-856.

Niyogi, D., T. Holt, S. Zhong, P.C. Pyle and J. Basara, 2006: Urban and land surface effects on the 30 July 2003 mesoscale convective system event observed in the southern Great Plains. *J. Geophys. Res.*, **111**, D19107, 20 pp.

Niyogi, D., P. Pyle, M. Lei, S.P. Aryam, C.M. Kishtawal, M. Shepherd, F. Chen and B. Wolfe, 2011: Urban modification of thunderstorm: an observational storm climatology and model case study for the Indianapolis region. *J. Appl. Meteor. Climatol.*, **50**, 1129-1144.

Perkins, S.E., A.J. Pitman, N.J. Holbrook and J. McAneney, 2007: Evaluation of the AR4 climate models' simulated daily maximum temperature, minimum temperature and precipitation over Australia using probability density functions. *J. Climate*, **20**, 4356-4376.

Petrik, R., D. Grawe, U. Bungert and K.H. Schlünzen, 2013: Quantifying the impact of anthropogenic heat on the urban climate of Hamburg in the summer season. In preparation.

Piani, C., J.O. Haerter and E. Coppola, 2010: Statistical bias correction for daily precipitation in regional climate models over Europe. *Theor. Appl. Climatol.*, **99**, 187-192.

Piani, C., G. P. Weedon, M. Best, S. M. Gomes, P. Viterbo, S. Hagemann and J. O. Haerter, 2010: Statistical bias correction of global simulated daily precipitation and temperature for the application of hydrological models. *J. Hydrol.*, **395**, 199-215.

Randall, D.A., R.A. Wood, S. Bony, R. Colman, T. Fichefet, J. Fyfe, V. Kattsov, A. Pitman, J. Shukla, J. Srinivasan, R.J. Stouffer, A. Sumi and K.E. Taylor, 2007: Climate Models and Their Evaluation. In: Climate Change 2007: The Physical Science Basis. Contribution of Working Group I to the Fourth Assessment Report of the Intergovernmental Panel on Climate Change (Solomon, S., D. Qin, M. Manning, Z. Chen, M. Marquis, K.B. Averyt, M. Tignor and H.L. Miller (editors)). Cambridge University Press, Cambridge, United Kingdom and New York, NY, USA, p. 631.

Rechid, D., J. Petersen, R. Schoetter and D. Jacob, 2013: Klimaprojektionen für die Metropolregion Hamburg. In preparation.

Reynolds, R.W., T.M. Smith, C. Liu, D.B. Chelton, K.S. Casey and M.G. Schlax, 2007: Daily high-resolution-blended analysis for sea surface temperature. *J. Climate*, **20**, 5473-5496.

Rockel, B, A. Will and A. Hense, 2008: The Regional Climate Model COSMO-CLM (CCLM). *Meteorol. Z.*, **17**, 347-348.

Roeckner, E., G. Bäuml, L. Bonaventura, R. Brokopf, M. Esch, M. Giorgetta, S. Hagemann, I. Kirchner, L. Kornblueh, E. Manzini, A. Rhodin, U. Schlese, U. Schulzweida and A. Tompkins, 2003: The atmospheric general circulation model ECHAM5-Part 1, Model description. Max-Planck-Institut für Meteorologie, Report No. 349., 127 pp.

Roeckner, E., 2004: IPCC-AR4 MPI-ECHAM5_T63L31 MPI-OM_GR1.5L40 20C3M run no.2: atmosphere 6 hour values MPImet/MaD Germany. World Data Center for Climate. CERA-DB "EH5-T63L31_OM-GR1.5L40_20C_2_6H". http://cera-www.dkrz.de/WDCC/ui/Compact.jsp?acronym=EH5-T63L31_OM-GR1.5L40_20C_2_6H, last access on 29 March 2010.

Roeckner, E., M. Lautenschlager and M. Esch, 2006: IPCC-AR4 MPI-ECHAM5_T63L31 MPI-OM_GR1.5L40 20C3M run no.3: atmosphere 6 hour values MPImet/MaD Germany. World Data Center for Climate. "EH5-T63L31_OM-GR1.5L40_20C_3_6H". http://dx.doi.org/10.1594/WDCC/EH5-T63L31_OM-GR1.5L40_20C_3_6H, last access on 29 March 2010.

Roeckner, E., M. Lautenschlager and H. Schneider, 2006: IPCC-AR4 MPI-ECHAM5_T63L31 MPI-OM_GR1.5L40 20C3M run no.1: atmosphere 6 hour values MPImet/MaD Germany. World Data Center for Climate. "EH5-T63L31_OM-GR1.5L40_20C_1_6H". http://dx.doi.org/10.1594/WDCC/EH5-T63L31_OM-GR1.5L40_20C_1_6H, last access on 29 March 2010.

Rudolf, B. and U. Schneider, 2005: Calculation of gridded precipitation data for the global land-surface using in-situ gauge observations. Proceedings of the 2nd Workshop of the International Precipitation Working Group IPWG. EUMETSAT, ISBN 92-9110-070-6, ISSN 1727-432X, 231-247, 17 pp.

Rudolf, B., A. Becker, U. Schneider, A. Meyer-Christoffer and M. Ziese, 2010: On the most recent gridded global data set issued in fall 2010 by the Global Precipitation Climatology Centre (GPCC). GPCC Status Report, July 2010, 7 pp.

Rudolf, E.-M., 2011: Untersuchung von Starkniederschlägen der ENSEMBLES Regionalmodelle in der Metropolregion Hamburg. Bachelorarbeit, Studiengang Meteorologie, Universität Hamburg, 65 pp.

Schlünzen, K.H., 1990: Numerical studies on the inland penetration of sea breeze fronts at a coastline with tidally flooded mudflats. *Beitr. Phys. Atmosph.*, **63 (3/4)**, 243-256.

Schlünzen, K.H. and R.S. Sokhi (editors), 2008: Overview of tools and methods for meteorological and air pollution mesoscale model evaluation and user training. Joint report of COST action 728. WMO/TD-No. 1457, p. 70-73.

Schlünzen, K.H., P. Hoffmann, G. Rosenhagen and W. Riecke, 2010: Long-term changes and regional differences in temperature and precipitation in the metropolitan area of Hamburg. *Int. J. Climatol.*, **30 (8)**, 1121-1136.

Schlünzen, K.H., U. Bungert, D.D. Flagg, B.H. Fock, A. Gierisch, D. Grawe, P. Kirschner, C. Lüpkes, V. Reinhardt, H. Ries, R. Schoetter, C. Spensberger and M. Uphoff, 2012: Technical Documentation of the Multiscale Model System M-SYS. MEMI (METRAS, MITRAS,

MECTM, MICTM, MESIM). Technical Report 3, Meteorologisches Institut, KlimaCampus, Universität Hamburg, 129 pp.

Schlünzen, K.H, D.D. Flagg, B.H. Fock, A. Gierisch, C. Lüpkes, V. Reinhardt and C. Spensberger, 2012: Scientific documentation of the multiscale model system M-SYS. MEMI Technical Report 4, Meteorologisches Institut, KlimaCampus, Universität Hamburg, 146 pp.

Schmitt, R., 2011: Schneelast an Stromleitungen - Heute und in Zukunft. Masterarbeit am Fachgebiet Meteorologie, Universität Hamburg, p. 34.

Schoetter, R., 2010: Einflüsse von Quellkonfiguration und Modelleigenschaften auf simulierte Konzentrationsfelder. Diplomarbeit im Fach Meteorologie, Universität Hamburg, 127 pp.

Schoetter, R., P. Hoffmann, D. Rechid and K.H. Schlünzen, 2012: Evaluation and bias correction of regional climate model results using model evaluation measures. *J. Appl. Meteor. Climatol.*, **51**, 1670–1684.

Schoetter, R., D. Grawe, P. Hoffmann, P. Kirschner, A. Grätz and K.H. Schlünzen, 2013: Impact of local adaptation measures and regional climate change on perceived temperature. *Meteorol. Z.*, **22 (2)**, 117-130.

Scholten, A., B. Rothstein and R. Baumhauer, 2011: Critical parameters for mass-cargo affine industries due to climate change in Germany: impacts of low water events on industry and possible adaptation measures. In W.L. Filho (editors): The economic, social and political elements of climate change, climate change management. Springer-Verlag Berlin Heidelberg, 267-287.

Schubert, S., S. Grossman-Clarke and A. Martilli, 2012: A double-canyon radiation scheme for multi-layer urban canopy models. *Boundary-Layer Meteorol.*, **145 (3)**, 439-468.

Shem, W. and M. Shepherd, 2009: On the impact of urbanization on summertime thunderstorms in Atlanta: two numerical model case studies. *Atmos. Res.*, **92**, 172-189.

Shepherd, J.M., 2005: A review of current investigations of urban-induced rainfall and recommendations for the future. *Earth interact.*, **9**, 1-27.

Spensberger, C. and K.H. Schlünzen, 2010: GRITOP. Präprozessor zur Initialisierung von Topographiedaten für das Modell METRAS. METRAS technical report 8. Meteorologisches Institut, Universität Hamburg, 31 pp.

Spittlehouse, D.L. and R.B. Stewart, 2003: Adaptation to climate change in forest management. *J.E.M*, **4 (1)**, 1-11.

Staiger, H., G. Laschewski and A. Grätz, 2011: The perceived temperature-a versatile index for the assessment of the human thermal environment. Part A: scientific basics. *Int. J. Biometeorol.*, **56**, 165-176.

Swart, R., L. Bernstein, M. Ha-Duong and A. Petersen, 2009: Agreeing to disagree: uncertainty management in assessing climate change, impacts and responses by the IPCC. *Climatic Change*, **92**, 1-29.

Taylor, K.E., R.J. Stouffer and G.A. Meehl, 2012: An overview of CMIP5 and the experiment design. *Bull. Amer. Meteor. Soc.*, **93**, 485-498.

Thamer, H., J. Becker and A. von Maydell, 2009: KLIMZUG-NORD. Strategic approaches to climate change in the metropolitan Hamburg, 2 pp.

Thorsson, S., F. Lindberg, J. Björklund, B. Holmer and D. Rayner, 2011: Potential changes in outdoor thermal comfort conditions in Gothenburg, Sweden due to climate change: the influence of urban geometry. *Int. J. Climatol.*, **31**, 324-335.

Trusilova, K., M. Jung and G. Churkina, 2009: On climate impacts of a potential expansion of urban land in Europe. *J. Appl. Meteor. Climatol.*, **48**, 1971-1980.

Uppala, S.M., P.W. Kallberg, A.J. Simmons, U. Andrae, V. Da Costa Bechtold, M. Fiorino, J.K. Gibson, J. Haseler, A. Hernandez, G.A. Kelly, X. Li, K. Onogi, S. Saarinen, N. Sokka, R.P. Allan, E. Andersson, K. Arpe, M.A. Balmaseda, A.C.M. Beljaars, L. Van De Berg, J. Bidlot, N. Bormann, S. Caires, F. Chevallier, A. Dethof, M. Dragosavac, M. Fisher, M. Fuentes, S. Hagemann, E. Holm, B.J. Hoskins, L. Isaksen, P.A.E.M. Janssen, R. Jenne, A.P. Mcnally, J.-F. Mahfouf, J.J. Morcrette, N.A. Rayner, R.W. Saunders, P. Simon, A. Sterl, K.E. Trenberth, A. Untch, D. Vasiljevic, P. Viterbo and J. Woollen, 2005: The ERA-40 re-analysis. *Q. J. R. Meteorol. Soc.*, **131,** 2961-3012.

Van Pelt, S.C., P. Kabat, H.W. ter Maat, B.J.J.M. van den Hurk and A. H. Weerts, 2009: Discharge simulations performed with a hydrological model using bias corrected regional climate model input. *Hydrol. Earth Syst. Sci.*, **13**, 2387-2397.

Von Salzen, K., M. Claussen and K.H. Schlünzen, 1996: Application of the concept of blending height to the calculation of surface fluxes in a mesoscale model. *Meteorol. Z.*, **5**, 60-66.

Wilby, R.L., 2003: Past and projected trends in London's urban heat island. *Weather*, **58**, 251-260.

Wilks, D.S., 1995: Statistical methods in the atmospheric sciences. Acadamic Press, Elsevier, 465 pp.

Yang, D., D. Kane, Z. Zhang, D. Legates and B. Goodison, 2005: Bias corrections of long-term (1973-2004) daily precipitation data over the northern regions. *Geophys. Res. Lett.*, **32**, L19501, 5 pp.

Zhang, C.L., F. Chen, S.G. Miao, Q. C. Li, X. A. Xia and C.Y. Xuan, 2009: Impacts of urban expansion and future green planting on summer precipitation in the Beijing metropolitan area. *J. Geophys. Res.*, **114**, D02116, 26 pp.

168